A harmonic balance framework for the numerical simulation of non-linear wave energy converter models in random seas

Alexis Mérigaud

A thesis submitted for the degree of
Doctor of Philosophy

Faculty of Science and Engineering
Electronic Engineering Department
Maynooth University

Supervisor: **Prof. John V. Ringwood**
Head of the Department: Dr. Ronan Farrell

December 2018

Table of Contents

Abstract

Numerical simulation is essential, to assist in the development of wave energy technology. In particular, tasks such as power assessment, optimisation and structural design require a large number of numerical simulations to calculate the wave energy converter (WEC) outputs of interest, over a variety of wave conditions or physical parameters. Such challenges involve a sound understanding of the statistical properties of ocean waves, which constitute the forcing inputs to the wave energy device, and computationally efficient numerical techniques for the speedy calculation of WEC outputs. This thesis studies the statistical characterisation, and numerical generation, of ocean waves, and proposes a novel technique for the numerical simulation of non-linear WEC models.

The theoretical foundations, the range of validity, and the importance of the statistical representation of ocean waves are first examined. Under relatively mild assumptions, ocean waves can be best described as a stationary Gaussian process, which is entirely characterised by its *spectral density function* (SDF). Various *wave superposition* techniques are discussed and rigorously compared, for the numerical generation of Gaussian wave elevation time series from a given SDF. In particular, the *harmonic random amplitude* (HRA) approach can simulate the target statistical properties with perfect realism. In contrast, the *harmonic deterministic amplitude* (HDA) approach is statistically inconsistent (because the generated time-series are non-Gaussian, and under-represent the short-term statistical variability of real ocean waves), but can be advantageous in the context of WEC simulations since, if it can be verified that HDA results are unbiased, the HDA method requires a smaller number of random realisations than the HRA method, to obtain accurate WEC power estimates.

When either HDA or HRA are used for the generation of wave inputs, the forcing terms of WEC mathematical models are periodic. Relying on a Fourier representation of the system inputs and variables, the *harmonic balance* (HB) method, which is a special case of spectral methods, is a suitable mathematical technique to numerically calculate the steady-state response of a non-linear system, under a periodic input. The applicability of the method to WEC simulation is demonstrated for those WEC models which are described by means of a non-linear integro-differential equation. In the proposed simulation framework, the WEC output, in a given sea state, is assessed by means of many, relatively short, simulations, each of which is efficiently solved using the HB method.

A range of four case studies is considered, comprising a flap-type WEC, a spherical heaving point-absorber, an array of four cylindrical heaving point-absorbers, and a pitching device. For each case, it is shown how the HB settings (simulation duration and cut-off frequency) can be calibrated. The accuracy of the HB method is assessed through a comparison with a second-order Runge-Kutta (RK2) time-domain integration scheme, with various time steps. RK2 results converge to the HB solution, as the RK2 time step tends to zero. Furthermore, in a Matlab implementation, the HB method is between one and three orders of magnitude faster than the RK2 method, depending on the RK2 time step, and on the method chosen for the calculation of the radiation memory terms in RK2 simulations. The HB formalism also provides an interesting framework, for studying the sensitivity of the WEC dynamics to system parameter variations, which can be utilised within a gradient-based parametric optimisation algorithm. An example of WEC gradient-based parametric optimisation, carried out within the HB framework, is provided.

Declaration of authorship

I, Alexis Mérigaud, declare that this thesis entitled 'A harmonic balance framework for the numerical simulation of non-linear wave energy converter models in random seas', and the work presented in it, are my own. I confirm that:

- This work was done wholly or mainly while in candidature for a research degree at this University.
- Where any part of this thesis has previously been submitted for a degree or any other qualification at this University or any other institution, this has been clearly stated.
- Where I have consulted the published work of others, this is always clearly attributed.
- Where I have quoted from the work of others, the source is always given. With the exception of such quotations, this thesis is entirely my own work.
- I have acknowledged all main sources of help.
- Where the thesis is based on work done by myself jointly with others, I have made clear exactly what was done by others and what I have contributed myself.

Date: _____

Signature: _____

Acknowledgement

First and foremost, I would like to express my sincere gratitude to my supervisor, Prof. John V. Ringwood, for making me consider the idea of becoming a researcher, for giving me the opportunity to embark on this PhD journey, for the freedom I enjoyed throughout these four years, for the invaluable support, advice, and trust I received, and, no less importantly, for the countless 'these' and 'those' suppressed, and commas added, in my written work.

Many thanks to the staff members of the Electronic Engineering Department, in particular Ann Dempsey, Joanne Bredin, Denis Buckley and John Malocco, for their availability and kindness, and for the help they provided with a variety of administrative and technical issues.

I feel greatly indebted to Dr. Romain Genest, for his expert advise, help and encouragement, provided when they were most needed, to get a foot on the ladder in the early stages of my stay in Maynooth. I also thank Romain for his precious friendship, of course not forgetting Camille and her talent as a chef.

Special thanks to Prof. Frédéric Dias (University College Dublin), for kindly showing interest in my work and for his help and advise, which significantly contributed to building my confidence in the research directions I was following, as well as for the pleasurable collaboration on real-time ocean wave prediction.

To Dr. John Scanlan, I would like to express the gratitude of my most appreciative thankfulness, for the many hours spent exploring some of the finest literary works of the French and Irish nations, and even more importantly for his help, support and friendship throughout this PhD journey.

A warm *Thanks a mil'!* to present and former members of the COER group, for the fruitful discussions and collaborations, for the countless coffees and walks around the old campus, and for heaps of very random pub conversations: Jake Cunningham, Josh Davidson, Sébastien Dot, Nicolás Faedo, Marina Garcia-Abril, Paula Garcia-Rosa, Demián García-Violini, Giuseppe Giorgi, Tom Kelly, Jost Kemper, Sébastien Olaya, Francesco Paparella, Louis Papillon, Victor Ramos-Castro, Andrej Roessling, LiGuo Wang and Christian Windt. Very special thanks to Simone Giorgi for the LaTeX template used in this thesis, to Yerai Peña and Markel Peñalba-Retes for providing me with WAMIT and NEMOH hydrodynamic data, to Clément Auger, for his work on receding-horizon Fourier spectral control, and to the henceforth PhD Student Riccardo Novo, for his work on the ISWEC device.

My thoughts go to all of those, met throughout the past four years, whose friendship made Maynooth a second home. I am also deeply grateful to the old friends from France, for their constancy and support and, for those who could, for sharing with me a couple of adventures (and some 'coups durs'!) in Maynooth, Dublin, and the rest of Ireland.

Last but not least, I would like to thank my family and Claire, for their love and support, and for the unfailing enthusiasm with which they all embraced this Irish adventure.

Acronyms

ACF	Auto-Correlation Function.
AR	Auto-Regressive.
ARMA	Auto-Regressive Moving Average.
BEM	Boundary-Element Method.
CFD	Computational Fluid Dynamics.
COER	Centre for Ocean Energy Research.
DA	Deterministic Amplitude.
EA	Equal Area.
EADA	Equal Area wave superposition, with Deterministic Amplitude and random phases.
EARA	Equal Area wave superposition, with Random Amplitudes and phases.
FFT	Fast Fourier Transform.
FK	Froude-Krylov.
HB	Harmonic balance.
HDA	Harmonic superposition method with deterministic amplitudes and random phases.
HOS	High-order spectral method.
HPA	Heaving Point-Absorber.
HRA	Harmonic superposition with random amplitudes and phases.
IDE	Integro-differential equations.
IEC	International Electrotechnical Commission.
ISWEC	Inertial Sea Wave Energy Converter.
JONSWAP	Joint North Sea Wave Project.
LCOE	Levelised Cost Of Energy.
MA	Moving Average.
MEL	Mixed Eulerian-Lagrangian.
NH	Non-Harmonic.
ODE	Ordinary Differential Equation.
PDE	Partial Differential Equation.
PTO	Power take-off.
PS	Pseudo-spectral.
RA	Random Amplitude.
RANS	Reynolds-averaged Navier-Stokes.
RK	Runge-Kutta.
RK2	2^{nd}-order Runge-Kutta numerical integration scheme.
RMS	Root-mean-square.
RP	Random Perturbation.
RPDA	Random Perturbation wave superposition, with Deterministic Amplitude and random phases.
RPRA	Random Perturbation wave superposition, with Random Amplitudes and phases.
SDF	Spectral density function.
TD	Time-domain.

TS	Technical standard.
WEC	Wave energy converter.
WS	Wave superposition

List of symbols

A general convention adopted in this thesis is the use of the bold font style is used for multidimensional variables, such as matrices (e.g. $\mathbf{M}$ and $\mathbf{\Phi}$) and vectors (e.g $\mathbf{x}$ and $\boldsymbol{\theta}$). Vectors specified by means of two points, geometrically defined in the two- or three-dimensional physical space, are identified using the arrow notation, for example $\overrightarrow{GP}$. Finally, this section only lists the symbols used 'globally' through this thesis.

Greek Symbols

α	Vector of parameters in a WEC dynamical model.
δ	The Dirac delta function.
Δf	Frequency step.
Δt	Time step.
η	Free surface elevation.
ε_0	Spectral broadness parameter.
ϕ	The fluid velocity potential
Φ_k	Basis functions
Ψ_k	Basis functions
ω	Frequency (rad.)
γ	The peak enhancement factor of a JONSWAP spectrum.
μ	The fluid viscosity coefficient.
∇	Gradient operator, defined as $\begin{pmatrix} \frac{\partial}{\partial x} \\ \frac{\partial}{\partial y} \\ \frac{\partial}{\partial z} \end{pmatrix}$
ρ	Sea water density.
θ_p	Peak wave direction.
τ	A relative time (lag).
σ_x	Standard deviation of the random variable x.
ξ	Vector of hydrodynamic degrees of freedom.

Latin Symbols

b_{pto}	PTO damping coefficient.
$\mathbf{C}$	A damping matrix.
c_φ	The phase velocity.
c_g	The group velocity.
$C_{dis,l}$	Linear drag coefficient.
$C_{dis,q}$	Quadratic drag coefficient.
D	The dimension of a WEC dynamical model.
D_R	The dimension of the state-space approximation for the radiation memory terms.

e_{RMS}	Root-mean-square difference between two trajectories.
f	Frequency [Hz].
f_c	Cut-off frequency [Hz].
f_s	Sampling frequency [Hz].
$\mathbf{f}$	A generalised force.
$\mathbf{F}$	A force.
G	Gravity centre.
g	Gravitational acceleration.
H	The water depth
H_s	The significant wave height, estimated from wave time-series.
H_{m_0}	The significant wave height, estimated from the wave spectrum.
$\mathbf{H}_{xy}(\omega)$, or $\mathbf{H}_{xy}(f)$	The complex transfer function between variables x and y.
i	The imaginary unit.
$\mathbb{I}_n$	The identity matrix of dimension n
$\Im$	The imaginary part of a complex number.
$\mathbf{k}$	The wave vector
$\mathbf{K}(\tau)$	A convolution kernel
b_{pto}	PTO stiffness coefficient.
$\mathcal{L}$	The linear terms in the dynamical model of a WEC.
$\mathbf{M}$	An inertia matrix.
m_j	The spectral moment of order j.
$\mathbf{n}$	The non-linear terms in the dynamical model of a WEC.
$\mathbf{n}_P$	Unitary vector, normal to a surface at a point P.
N_t	Number of collocation points.
$\mathbf{N}_\alpha$	Number of parameters.
$\mathbf{N}_\omega$	Number of frequencies.
P	Absorbed power.
p	Pressure.
p_a	Atmospheric pressure.
$\mathbb{R}$	The set of real numbers.
R_{xx}	Auto-correlation function of the random process x.
$\Re$	The real part of a complex number.
$s_{\max}$	Spreading parameter in the Mitsuyasu directional spreading function.
S_{xx}	The spectral density function of the random process (or random field) x.
$\mathcal{S}_w$	Wetted surface.
$\mathcal{S}_w^0$	Mean wetted surface.
$\mathbf{S}$	A stiffness matrix.
t	A time instant.
T	A time duration.
T_p	The peak wave period of a wave spectrum.
T_e	The mean energy wave period of a wave spectrum.
$\mathbf{T}$	A torque.
$\mathbf{u}$	The fluid velocity field.
$\mathrm{var}[x]$	The variance of a random variable x
$\mathbf{x}$	The variables of a WEC dynamical model.

Others

$\langle . \rangle$	Mathematical expectation.

Chapter 1

Introduction

1.1 Introduction

With an estimated 300 to 400 GW wave power resource along European Atlantic coastlines, wave energy could be a significant contributor to carbon-free, renewable electricity production in Europe, in addition to providing opportunities for economic growth and for the creation of highly-qualified jobs [1]. Furthermore, possible uses of wave energy are not limited to electricity production for wholesale electricity markets, but also include the power supply of small-scale electrical networks on isolated islands, freshwater production through desalination, and the power supply of offshore platforms or measurement buoys [1]. An overview of the rich existing range of wave energy converter (WEC) patents, companies and operating principles, as well as a wide historical perspective on wave energy development, may be found in [2], and in the recent book from Babarit [1].

In spite of a tremendous diversity of concepts [2], the vast majority of, if not all WECs, feature one or more mechanical components, actuated under the effect of waves. As of today, it is estimated that the most advanced WEC technologies do not achieve more than 20% of the maximum power which could, theoretically, be captured by heaving mechanical structures of similar dimensions [1]. Improving WEC design through research, by increasing the amount of absorbed energy while limiting capital expenditure, is thus of primary importance, if wave energy is to one day fulfil its potential. To assist in the development of innovative wave energy technologies, numerical simulation is an essential tool for researchers and engineers [3], given the high cost generally associated with physical experiments.

1.2 Motivations: the challenges of WEC modelling and numerical simulation

This thesis is primarily concerned with the numerical simulation of WEC models, for applications where the calculation speed is highly important, including the following tasks[1]:

- WEC or WEC farm design based on optimisation, where the objective (or cost) function must be evaluated a large number of times through WEC simulations;
- WEC or WEC farm power assessment, which involves the calculation of WEC power output over several years of wave data [4], also involving a large number of numerical simulations;
- WEC or WEC farm fatigue analysis and reliability assessment, which may require probability analysis based on a large number of numerical simulations - see Chapter 14 of [3];

[1] The tasks enumerated here are not entirely distinct: for example, WEC power assessment could be embedded within a WEC optimisation algorithm, as part of the objective function evaluation.

- In the future, computationally efficient simulation tools will also be necessary for the real-time operation of WEC or WEC farms, including energy production forecasting for market participation, management of the WEC safe mode (to avoid structural damage, in case of dangerously high sea conditions), and predictive maintenance, as discussed in [5].

In general, numerical experiments require:

- An appropriate mathematical and numerical representation of the physical inputs to the WEC system, i.e. the *wave input* by which the WEC is actuated;

- A suitable *physical model*, sufficiently realistic for the application considered, and which mathematically represents the dynamical behaviour of the WEC system, usually in the form of a differential equation;

- An adequate *numerical simulation method*, which essentially aims to find the solution of the differential equation representing the physical model, subject to the forcing terms defined by the physical inputs.

Concerning the wave input, and for the aforementioned applications, ocean waves are usefully modelled as a Gaussian random process [6], with well-defined statistical properties. When wave-related quantities, such as the wave elevation or pressure forces, are numerically generated, it must be ensured that the simulated quantities are consistent with the statistical properties of the target wave random process.

In the tradition of naval and offshore engineering, linear hydrodynamic theory has been applied to WEC modelling since the 1970s, and has yielded a wealth of fundamental theoretical results, which can be best appreciated in [7]. Linear hydrodynamics permits the WEC dynamics be described and analysed in the frequency domain, allowing for highly efficient calculations of the WEC response in periodic wave signals. It is thus unsurprising to observe that linear hydrodynamic models generally form the basis of WEC design, optimisation, power assessment and performance analysis [8].

For most WEC concepts, maximum power capture cannot be reached, or even approached, if the WEC does not mechanically *resonate* in incoming waves, the WEC velocity being in phase with the wave excitation [7, 9]. Resonance can be achieved, either if the WEC size makes it resonate naturally in typical ocean waves, or if control strategies are applied, which modify the device response, so as to make it resonate artificially in incoming waves. The latter solution has received considerable attention in recent years, giving rise to many scientific publications [9]. One can further distinguish between real-time *optimal control*, whereby the control input is adjusted in real-time following the solution of an optimisation problem [10], and simpler *parametric control* strategies, whereby one or several parameters are tuned on a sea-state-by-sea-state basis, to enhance power absorption. Regardless of how it is achieved, resonance amplifies the WEC dynamical response, which violates the assumption of small motion, and thus invalidates the fundamental prerequisites underpinning linear hydrodynamics [11]. Accordingly, *non-linear* hydrodynamic models must be employed, to design and operate WECs capable of achieving optimal or near-optimal power absorption.

Unfortunately, non-linearities pose several challenges in the context of numerical WEC simulation. In addition to an increased modelling effort and mathematical complexity, non-linear hydrodynamic models do not lend themselves easily to computationally efficient output calculations; the traditional linear frequency-domain approach cannot be used, and time-domain numerical integration schemes are usually employed [3], which are relatively inefficient in comparison. The greater computational complexity of non-linear WEC models is problematic for those tasks, which require fast numerical simulations, and which are precisely the target applications for the work presented in this thesis.

1.3 Objectives and contributions: a harmonic balance simulation framework for wave energy applications

1.3.1 Thesis objective

In view of the preceding discussion, the main research direction for this thesis is the study of innovative numerical simulation methods, which would take advantage of a statistical perspective on ocean waves. New methods should accommodate non-linear WEC models, and present consistent benefits in terms of computational time or accuracy, with respect to existing approaches.

The main contributions of this thesis, directly aligned with the objective formulated above, are listed below in Section 1.3.2, and will be the subject of the remaining chapters of the present document. However, throughout the course of this thesis, several other research directions were followed, both *before* the main objective stated above was identified as such, and *after*, as natural developments, into the fields of real-time wave prediction and WEC optimal control, of the work presented in the following chapters. This supplementary material is briefly summarised in Section 1.3.3.

1.3.2 Principal contributions of the thesis

The first significant contribution of this thesis, with respect to the objective of Section 1.3.1, is a thorough study of the statistical properties of ocean waves, considered as a stochastic process, and the examination of how numerical wave simulation methods may, or may not, reflect those properties. This is the subject of Part I of this thesis. In particular:

- The criteria, for a wave signal generation method to be statistically realistic, are clearly formulated.
- It is shown that a commonly employed procedure, which consists of the superposition of harmonic sinusoids with random phases, and amplitudes derived deterministically from the wave spectrum (termed the HDA method in this thesis), is not statistically consistent but, if certain precautions are taken, can be useful to obtain quick estimates of statistical quantities of interest, such as the average energy in a given signal, or the power absorption of a WEC.
- In contrast, the method, consisting of superposing harmonic sinusoids with random phases, and amplitudes randomly generated from the wave spectrum (termed the HRA method in this thesis), is statistically correct; however, many or long simulations may be required to obtain accurate statistical estimates.
- Non-harmonic sinusoid superposition methods are also studied, and are shown to induce undesirable statistical inaccuracies.
- Therefore, to numerically generate time series of wave-related quantities (such as wave elevation or pressure forces), a pertinent alternative is to choose between HDA and HRA methods, depending on the target application.

The second main contribution of this thesis, contained in Parts II and III, is the introduction of the harmonic balance (HB) method, to the wave energy field. The proposed approach is a significant addition to the existing range of techniques, available to wave energy researchers and engineers, for the numerical simulation of non-linear WEC models. The HB technique belongs to the mathematical family of *spectral methods*. The approach is used to calculate, accurately and efficiently, the steady-state solution for a non-linear, time-periodic differential equation, by means of a Fourier expansion of the forcing input and solution. The proposed HB simulation methodology is thus able to exploit the synergy, between harmonic superposition methods, for wave input generation, and the HB mathematical technique, for the solution of the WEC dynamical

equations under the random forcing wave input. The specific contributions of this thesis, relative to the HB method, are listed as follows:

- The HB method is developed, for WECs described by means of non-linear integro-differential equations (IDEs). It is explained how the HB method results in the solution of a non-linear vector equation, termed the HB (or the HB residual) equation, where the unknown variables are the Fourier coefficients of the solution.
- It is studied how the Jacobian of the HB equation can be explicitly computed, in order to ensure a fast convergence to the HB solution.
- A number of WEC models, with smooth non-linearities, are successfully simulated using the HB method, for both one and several degrees-of-freedom models, as reported in this thesis: a flap-type WEC, a spherical WEC operating in heave, an array of cylindrical WECs also operating in heave, and a device operating in pitch, the ISWEC [12, 13].
- The tuning of the main HB parameters, namely the cut-off frequency and the duration of the simulated signal, is investigated in detail, taking into consideration the numerical accuracy of the HB method, and the appropriate statistical representation of the input wave signals.
- Most importantly, it is demonstrated that, for smooth non-linearities, the HB method can calculate the steady-state solution of non-linear WEC differential equations, between one and three orders of magnitude faster, and with better accuracy, than a standard 2^{nd}-order Runge-Kutta (RK2) [14] time-domain integration procedure. The HB method accuracy is evidenced by the fact that, as the RK2 time step decreases, the RK2 solution converges towards the HB solution.
- The possible issues associated with the HB method are highlighted, such as the absence of convergence, or the convergence to non-physical solutions.
- The solution of the sensitivity equation is shown to take a particularly simple form in the HB framework. It is explained how this can be advantageously used for gradient-based WEC optimisation.
- An application example is detailed, consisting of the parametric optimisation of the ISWEC device in a large range of sea states. Power assessment is another pertinent application of the HB method which, although not detailed in this thesis, has also been studied by the author.

1.3.3 Supplementary material

Other related research directions have led to the following contributions:

- The first works of the author, in the wave energy field, have highlighted the importance of non-linear hydrodynamic modelling for wave energy converters (WECs), particularly under resonant conditions [a,f].
- Various aspects of the operation of future commercial WECs or WEC farms have been explored. In particular, a literature review has been carried out on condition-based and predictive maintenance for renewable marine energies, including WECs [e]. The needs, requirements and techniques for medium-term ocean forecasting (from a few hours to a few days ahead) have been reviewed, in the context of WEC or WEC farm operation [g].
- The proposed HB method has a natural extension, in the domain of WEC power-maximising optimal control calculations; the HB equation can be used within a Fourier non-linear pseudo-spectral control approach, resulting in a smaller problem size, and making it possible to greatly improve the speed of calculating optimal WEC trajectories and control force [h]. However, this approach has only been applied to one-degree-of-freedom WEC models.

- The aforementioned control formalism has also led to the derivation of a set of useful theoretical results, relative to WEC optimal control, under various dynamical non-linear effects and constraint configurations. In particular, the dependence of the optimal control results on the different modelling terms has been studied [b].
- Assuming linear hydrodynamics, the robustness of different control architectures to various types of modelling errors has been investigated [d,m].
- The research, primarily dealing with the statistical aspects of ocean wave simulations, has also resulted in an innovative approach to real-time wave forecasting, based on statistical information contained in the wave spectrum [c,i,l]. Within the scope of Gaussian wave theory, the developed approach has been proven to be statistically optimal.
- It has been shown that the proposed pseudo-spectral WEC control formulation can be implemented within a real-time control framework, in a receding-horizon configuration, with the inclusion of real-time wave prediction, using the forecasting technique developed [j]. The influence of the length and shape of the receding-horizon window has been investigated.
- A study was carried out, articulating significant aspects of WEC real-time optimal control, including measurement noise, excitation force estimation, real-time wave forecasting, real-time non-linear optimal control calculations, and trajectory tracking [k]. The study shows that, in principle, under relatively realistic assumptions regarding the control setup, it should be possible to reach more than 90% of the optimal hydrodynamic power absorption.

1.3.4 List of publications related to the principal contributions of the thesis

1.3.4.1 Conference publications

[A] Alexis Mérigaud and John V. Ringwood. *Nonlinear frequency-domain WEC simulation: Numerical case studies and practical issues.* In Proceedings of the 11th European Wave and Tidal Energy Conference, Cork, Ireland, 2017.

[B] Riccardo Novo, Alexis Mérigaud, Giovanni Bracco, Sergei Sirigu, Giuliana Mattiazzo, and John. V. Ringwood. *Non-linear simulation of a wave energy converter with multiple degrees of freedom using a harmonic balance method.* In Proceedings of the 37th International Conference on Ocean, Offshore & Arctic Engineering (OMAE 2018), Madrid, Spain, 2018.

1.3.4.2 Journal publications

[C] Alexis Mérigaud and John V. Ringwood. *Free-surface time-series generation for wave energy applications.* IEEE Journal of Oceanic Engineering, 43(1), pp. 19-35, 2018.

[D] Alexis Mérigaud and John V. Ringwood. *A nonlinear frequency-domain approach for numerical simulation of wave energy converters.* IEEE Transactions on Sustainable Energy, 9(1), pp. 8694, 2017.

[E] Alexis Mérigaud and John V. Ringwood. *Power production assessment for wave energy converters: Overcoming the perils of the power matrix.* Proceedings of the Institution of Mechanical Engineers, Part M: Journal of Engineering for the Maritime Environment, 232(1), pp. 5070, 2018.

1.3.4.3 Publications in preparation

[F] Alexis Mérigaud and John V. Ringwood. *Non-linear, parametric optimisation of wave energy devices using gradient-based optimisation in a harmonic balance framework.*

1.3.5 List of publications related to the supplementary material

1.3.5.1 Conference publications

[a] Markel Penalba Retes, Alexis Mérigaud, Jean-Christophe Gilloteaux, and John V. Ringwood. *Nonlinear Froude-Krylov force modelling for two heaving wave energy point absorbers.* In Proceedings of the 11th European Wave and Tidal Energy Conference, Nantes, France, 2015.

[b] Alexis Mérigaud and John V. Ringwood. *Optimal trajectories, nonlinear models and constraints in wave energy device control*. In Proceedings the 20th IFAC World Congress, Toulouse, France, 2017.

[c] Alexis Mérigaud, James Herterich, Jason Flanagan, John V. Ringwood, and Frdric Dias. *Incorporating wave spectrum information in real-time free-surface elevation forecasting: Real-sea experiments.* In Proceedings of the 11th IFAC Conference on Control Applications in Marine Systems, Robotics, and Vehicles, Opatija, Croatia, 2018 (CAMS 2018), 2018.

[d] John V. Ringwood, Alexis Mérigaud, Nicolás Faedo, and Francesco Fusco. *Wave energy control systems: Robustness issues.* In Proceedings of the 11th IFAC Conference on Control Applications in Marine Systems, Robotics, and Vehicles, Opatija, Croatia, 2018 (CAMS 2018), 2018.

1.3.5.2 Journal publications

[e] Alexis Mérigaud and John V. Ringwood. *Condition-based maintenance methods for marine renewable energy*. Renewable and Sustainable Energy Reviews, 66, pp. 5378, 2016.

[f] Markel Penalba Retes, Alexis Mérigaud, Jean-Christophe Gilloteaux, and John V. Ringwood. *Influence of nonlinear FroudeKrylov forces on the performance of two wave energy points absorbers*. Journal of Ocean Engineering and Marine Energy, pp. 112, 2017.

[g] Alexis Mérigaud, Victor Ramos, Francesco Paparella, and John V. Ringwood. *Ocean forecasting for wave energy production*. Journal of Marine Research, 75(3), pp. 459505, 2017.

[h] Alexis Mérigaud and John V. Ringwood. *Improving the computational performance of nonlinear pseudo-spectral control of wave energy converters.* IEEE Transactions on Sustainable Energy, vol. 9, no 3, pp. 1419-1426, 2018.

[i] Alexis Mérigaud and John V. Ringwood. *Incorporating ocean wave spectrum information in short-term free-surface elevation forecasting.* IEEE Journal of Oceanic Engineering, pp. 114, 2018.

[j] Clément Auger, Alexis Mérigaud, and John V. Ringwood. *Receding-horizon pseudospectral control of wave energy converters using periodic basis functions.* IEEE Transactions on Sustainable Energy, 2018. In Press.

[k] Alexis Mérigaud and John V. Ringwood. *Towards realistic non-linear receding-horizon spectral control of wave energy converters.* Control Engineering Practice, 81, pp. 145-161, 2018.

[l] Yerai Peña-Sanchez, Alexis Mérigaud, and John V. Ringwood. *Short-term forecasting of sea surface elevation for wave energy applications: The AR model revisited.* IEEE Journal of Oceanic Engineering, 2018. In Press.

1.3.5.3 Submitted publications

[m] John V. Ringwood, Alexis Mérigaud, Nicolás Faedo, and Francesco Fusco. *On the sensitivity and robustness of wave energy control systems.* IEEE Transactions on Control Systems Technology. Revised version submitted June 2018.

1.3.5.4 Publications in preparation

[n] Alexis Mérigaud and John V. Ringwood. *Control-informed optimisation of a wave energy converter using pseudo-spectral optimal control and the notion of shadow costs.*

1.4 Thesis outline

This thesis consists of seven more chapters, organised into three parts, as follows:

- **Part I** is concerned with the statistical representation of ocean waves, with emphasis on the numerical generation of wave elevation time series, with appropriate statistical properties.
  - **Chapter 2** introduces the statistical representation of ocean waves, which usually takes the form of a Gaussian random process (if a single wave measurement point is considered) or a Gaussian random field (if the spatial distribution of the wave elevation is also examined). The underlying assumptions, and the range of validity of the Gaussian wave representation, are discussed. Modelled as a Gaussian process or Gaussian field, the statistical properties of ocean waves are entirely described by their spectral density function, or wave spectrum. The importance of the notion of a wave spectrum, in wave energy and other marine and offshore engineering applications, is highlighted.
  - **Chapter 3** devises methods for the numerical generation of wave elevation time series, with properties consistent with the Gaussian representation of ocean waves. In particular, various Gaussian process simulation methods, based on the idea of *harmonic superposition*, are rigorously compared. It is shown that, for most pertinent engineering applications, the so-called *harmonic superposition* methods are the most pertinent option. In harmonic superposition methods, wave time series are generated through a sum of sinusoidal signals, with random phases, and amplitudes derived from the wave spectrum.
- **Part II** introduces the HB method as a technique for calculating the steady-state response of WECs in random waves. The WEC models considered take the form of non-linear integro-differential equations.
  - In **Chapter 4**, the basic principles of WEC modelling are introduced. The variety of mathematical modelling approaches for hydrodynamic interaction, mooring systems and PTO systems is briefly reviewed, with an emphasis on the mathematical form taken by the resulting models. A reasonably generic WEC model formulation, in the form of a non-linear integro-differential equation, is proposed, which allows two challenging components, present in many WEC models, to be articulated: non-linear terms, and linear memory terms. How a wider range of WEC models could be developed under such a formalism is also discussed.
  - **Chapter 5** introduces the harmonic balance (HB) method and its application to the numerical simulation of WEC models for periodic wave inputs, and constitutes the core of this thesis. The fundamental features of the method are illustrated by means of a simple WEC model example. Combining the outputs from Chapters 3 and 5, a HB framework for WEC simulation in random seas is proposed, whereby several,

relatively short, simulation problems are efficiently solved using the HB method, in order to characterise the WEC output in a given sea state.

- **Part III** consists of several numerical case studies, which aim to demonstrate the accuracy, and illustrate the practical value, of the proposed simulation framework:
  - In **Chapter 6**, four case studies are presented, to give the reader a sense of how the HB method can be calibrated, and to assess the accuracy and computational gains which can be expected from using the HB method, with respect to widely employed RK2 time-domain numerical integration. It is found that the HB method provides computation gains of one to three orders of magnitude, while showing excellent accuracy compared to RK2 numerical integration.
  - While Chapter 6 is concerned with the validation and calibration of the HB method, **Chapter 7** details an application where the HB method can be used effectively, and which consists of the gradient-based, parametric optimisation of wave energy converters represented by non-linear models. The optimisation of three scalar parameters, governing the ISWEC power take-off system, is carried out as a numerical example.
- The conclusions of the foregoing parts are presented in **Chapter 8**.

Part I

Statistical aspects of ocean wave simulation

Chapter 2

Spectral description of ocean waves

2.1 Introduction

Ocean waves are random - at least wind-generated waves. Visually examining the water surface, it is impossible to anticipate the future wave pattern beyond the current wave, since two consecutive waves are never identical, with peaks and troughs following an apparently unpredictable sequence. Furthermore, even if it were possible to repeat the same atmospheric conditions (mean wind speed and direction, temperature, etc.) in a vast enough area around the location of interest, the precise time-history of the wave elevation would not be repeated. As formulated by Lord Rayleigh, quoted by Pierson [15], "the basic law of the seaway is the apparent lack of any law." Intuitively, the reason for the free-surface elevation randomness is that ocean waves are the result of a countless number of events and processes, whereby the wind - itself a random physical process - transfers energy to the sea, in a multitude of locations, directions and with varying strength. Therefore, when observed locally, the resulting waves cannot be reasonably accounted for through a deterministic description.

Randomness, however, does not mean that the wave elevation process behaves purely arbitrarily. In fact, except for special events such as wave breaking, which usually occur in shallow water or in extreme meteorological conditions, waves seem to follow sinusoidal, or pseudo-periodic patterns which, although they oscillate randomly, give the wave field an aspect of coherence and continuity. Furthermore, within a reasonably short time-window, e.g. 3 hours [16], the *average properties* of the wave field, such as the average crest-to-trough amplitude, average wave period, etc. don't usually show significant variation, thus defining a *sea state*. In other words, over a relatively short period (say, between several tens of minutes and several hours), it is possible to provide a *statistical description* of a sea state, as opposed to a wave-by-wave time history. In particular, under mild assumptions, the sea-state can be described as a Gaussian process, as detailed further in Sections 2.2 and 2.3.

Over its lifetime, any ship, or any offshore or coastal structure, experiences a long sequence of different sea states. The study of how the system of interest responds in specified sea states is then instrumental in naval, offshore and coastal engineering. In the case of WECs, the sea states do not only characterise the structural loads experienced by the devices (and thus their survivability) but also, importantly, determine the amount of energy absorbed by the WEC system. Numerical simulations, to calculate the WEC dynamical response and power production in a given sea state, thus constitute a centrepiece procedure in the development of wave energy technology.

For realistic simulations of WEC models, an appropriate representation of the forcing terms due to the waves is essential, which implies that:

- The statistical characterisation of the sea state is sufficiently accurate for the application considered, as discussed in this chapter;

- Time-series of the free-surface elevation[1] are generated through a numerical procedure, which appropriately reflects the statistical properties which define the sea-state of interest, as detailed in Chapter 3.

Chapter organisation

The rest of this chapter is organised as follows:

- Section 2.2 starts with a brief reminder of the physical, *deterministic* modelling of elementary waves propagating over the ocean surface, and depicts the train of thought which leads to a consistent *stochastic* description of wave fields. This stochastic description takes the form of a Gaussian process (when time series of the wave elevation are considered) or a Gaussian wave field (when the statistical properties of waves are also examined over a spatial domain). The statistical properties of Gaussian waves are entirely characterised by their spectral density function.

- Section 2.3 discusses the range of validity of the Gaussian wave model, as far as wave energy applications are concerned. It is pointed out that the Gaussian wave description should be accurate for the vast majority of WEC operating conditions, and thus a Gaussian random process may be used to model the wave input for WEC simulation.

- In the context of WEC power assessment, and assuming that the Gaussian wave model is valid, Section 2.4 highlights the need for an accurate characterisation of the wave spectral density function. The need for computationally efficient numerical methods for WEC simulation is highlighted, if one wants to avoid the use of over-simplified parametric representations of the wave spectral density function.

- The main developments and conclusions of this chapter are summarised in Section 2.5.

2.2 The Gaussian description of ocean waves and the notion of a wave spectrum

Many types of oscillations can be observed in the ocean, involving a variety of phenomena and time scales, such as storm surges, tidal oscillations, tsunami waves, infra-gravity waves, wind waves and capillary waves, in ascending order of the typical frequencies involved - the interested reader may find a brief typology of ocean wave phenomena in Chapter 1 of [16]. For wave energy extraction, the oscillations of interest are the most familiar *wind waves*, i.e. those waves which are generated by wind shear over the ocean surface, and have typical periods between 1 and 25 seconds. Wind waves belong to the category of gravity waves, in the sense that their propagation is mainly governed by gravity, as opposed to capillarity. Wind waves may be further categorised into different types of wave systems, namely *wind sea* and *swell*, the former being directly generated by the wind forces, with relatively low periods (typically lower than 10 seconds), while the latter are due to a gradual transfer of energy towards lower frequencies, i.e. larger periods, as waves propagate over long distances and time scales. Typical swell wave periods are between 10 and 25 seconds.

The following paragraphs introduce the theory of linear ocean waves, also called Airy's waves, which are the simplest available model to account for elementary gravity waves on water. It is then explained how a stochastic description of ocean waves can be built, starting from Airy's deterministic phenomenological description. More detailed developments may be found in the important articles by St Denis and Pierson [17] and by Pierson [15], in the books by Whitham [18]

[1] or any other relevant, wave-related physical quantity, such as the wave excitation force defined within the scope of linear hydrodynamics, as seen in Chapter 4

and Ochi [6], and in the didactic course entitled "The wave model", made available on-line by the European Centre for Medium-range Weather Forecasting (ECMWF)[2].

2.2.1 Deterministic description of elementary waves

Potential theory provides the basic framework for understanding ocean waves, although it excludes some special wave events, such as white-capping. Consider a body of water, described as a non-viscous, homogeneous, incompressible and irrotational fluid. The three-dimensional physical space is described by coordinates x, y and z, and by convention $z = 0$ corresponds to the mean water level at rest. Since, in potential theory, the flow is assumed irrotational, the velocity of water in each point can be written as the gradient of a potential field, $\phi(x,y,z,t)$, which satisfies the Laplace equation within the fluid domain, as well as boundary conditions, at the free surface $z = \eta(x,y,t)$ and at the sea bottom $z = -H$. The Laplace equation reads:

$$\frac{\partial^2\phi}{\partial x^2} + \frac{\partial^2\phi}{\partial y^2} + \frac{\partial^2\phi}{\partial z^2} = 0 \tag{2.1}$$

The free-surface boundary conditions for freely-propagating waves are, at $z = \eta$:

$$\frac{\partial\eta}{\partial t} + \nabla\phi.\nabla\eta = \frac{\partial\phi}{\partial z} \tag{2.2}$$

and

$$\frac{\partial\phi}{\partial t} + \frac{1}{2}(\frac{\partial\phi}{\partial z})^2 + g\eta = 0 \tag{2.3}$$

where Eq. (2.2) represents the fact that fluid particles cannot cross the free surface, and Eq. (2.3) (Bernoulli's equation) expresses the continuity of the pressure field at the interface between air and water.

Denoting H as the water depth, the no-flow boundary condition at the sea bottom is, at $z = -H$:

$$\frac{\partial\phi}{\partial z} = 0 \tag{2.4}$$

Linear wave theory assumes infinitesimally small wave amplitude, which allows the free-surface boundary conditions of Eqs. (2.2) and (2.3) to be linearised, by expressing them at $z = 0$ instead of $z = \eta$, and by neglecting quadratic contributions:

$$\frac{\partial\eta}{\partial t} = \frac{\partial\phi}{\partial z} \tag{2.5}$$

and

$$\frac{\partial\phi}{\partial t} + g\eta = 0 \tag{2.6}$$

Solutions to the Laplace equation (2.1), with boundary conditions (2.5), (2.6) and (2.4), are of the form:

$$\begin{cases} \eta(\mathbf{x},t) = \hat{\eta}e^{i(\mathbf{k}.\mathbf{x}-\omega t)} \\ \phi(x,y,z,t) = F(z)e^{i(\mathbf{k}.\mathbf{x}-\omega t)} \end{cases} \tag{2.7}$$

where $\mathbf{x} = \begin{pmatrix} x \\ y \end{pmatrix}$ denotes the horizontal position, $\mathbf{k} = \begin{pmatrix} k_x \\ k_y \end{pmatrix}$ is called the *wave number*, $\hat{\eta}$ is the complex wave amplitude and F is a scalar function of the depth z.

The Laplace equation (2.1) imposes $\frac{d^2F}{dz^2}(z) - |\mathbf{k}|^2F(z) = 0$. Together with the bottom boundary condition (2.4), this implies that F is of the form:

$$F(z) = C\cosh(|\mathbf{k}|(z+H)) \tag{2.8}$$

[2] https://www.ecmwf.int/en/learning/education-material/lecture-notes

Using the linearised Bernoulli equation (2.6), the constant C is found to be related to the wave amplitude $\hat{\eta}$ through $C = -\frac{ig}{\omega}\frac{\hat{\eta}}{\cosh(|\mathbf{k}|H)}$. Thus, $F(z)$ is given as:

$$F(z) = -\frac{ig}{\omega}\frac{\cosh(|\mathbf{k}|(z+H))}{\cosh(|\mathbf{k}|H)}\hat{\eta} \tag{2.9}$$

Eq. (2.5) imposes a relationship between the oscillation frequency ω and the wave number $\mathbf{k}$, called the *dispersion relation*:

$$\omega^2 = g|\mathbf{k}|\tanh(|\mathbf{k}|H) \tag{2.10}$$

Finally, a freely-propagating, linear wave with complex amplitude $\hat{\eta}$ is described as follows:

$$\begin{cases} \eta(\mathbf{x},t) = \hat{\eta}e^{i(\mathbf{k}.\mathbf{x}-\omega t)} \\ \phi(x,y,z,t) = -\frac{ig}{\omega}\frac{\cosh|\mathbf{k}|(z+H))}{\cosh(|\mathbf{k}|H)}\hat{\eta}e^{i(\mathbf{k}.\mathbf{x}-\omega t)} \end{cases} \tag{2.11}$$

where $\mathbf{k}$ and ω are related by the dispersion relation. In real conventions, with $\hat{\eta} = |\hat{\eta}|e^{i\varphi}$, Eq. (2.11) may be rewritten:

$$\begin{cases} \eta(\mathbf{x},t) = |\hat{\eta}|\cos(\mathbf{k}.\mathbf{x}-\omega t+\varphi) \\ \phi(x,y,z,t) = \frac{g}{\omega}\frac{\cosh|\mathbf{k}|(z+H))}{\cosh(|\mathbf{k}|H)}|\hat{\eta}|\sin(\mathbf{k}.\mathbf{x}-\omega t+\varphi) \end{cases} \tag{2.12}$$

In the case where the depth H is sufficiently large, with respect to the wavelength $1/|\mathbf{k}|$, to be considered infinite, the deep water dispersion relation is:

$$\omega^2 = g|\mathbf{k}| \tag{2.13}$$

The phase velocity measures the speed at which the crest of a single wave, with frequency ω, propagates horizontally. In deep water, the phase velocity is calculated as:

$$c_\varphi = \frac{\omega}{|\mathbf{k}|} = \sqrt{\frac{g}{|\mathbf{k}|}} = \frac{g}{\omega} \tag{2.14}$$

The group velocity measures the speed at which wave energy is transported by a wave train - see Chapter 11 of [18]. The group velocity is defined as $c_g = \frac{\partial\omega}{\partial|\mathbf{k}|}$ which, in deep water, becomes:

$$c_g = \frac{1}{2}\sqrt{\frac{g}{|\mathbf{k}|}} = \frac{1}{2}\frac{g}{\omega} = \frac{1}{2}c_\varphi \tag{2.15}$$

Thus, for linear, deep-water waves, the group velocity is half the phase velocity. Note that the dispersion relation is modified in the presence of current, or in the case of a slowly varying bottom profile $H(\mathbf{x},t)$. However, for the sake of simplicity this is not considered here. For more insight on the rich and difficult concept of group velocity, the reader is referred to Chapter 11 of [18].

The non-constant value of c_φ and c_g (across frequencies) indicates that deep-water waves are dispersive, i.e. that waves of different frequencies propagate at different speeds. This fact is essential to explain the randomness of ocean waves.

2.2.2 From a deterministic to a stochastic wave description

Eq. (2.12) describes an elementary wave, as first described by Airy - see the historical perspective on water wave theory presented by Craik [19]. However, from visual observation of the ocean surface, it is evident that Eq. (2.12) does not account for the complicated pattern of the water surface. In particular, considering the wave elevation at a single location, which is referred to as a *point measurement*, from Eq. (2.12) the time history of the free surface should be a simple sinusoidal function. Hence, a more sophisticated description is necessary to account for the actual ocean surface.

From the linearity of the governing equations, any superposition of solutions of the form (2.12), with various frequencies, phases and propagation directions, is also a solution to the linear equations (2.1), (2.5) and (2.6). The free-surface elevation for such a solution is given as:

$$\eta(\mathbf{x},t) = \sum_{n=1}^{N} A_n \cos(\mathbf{k}_n.\mathbf{x} - \omega_n t + \varphi_n) \tag{2.16}$$

where each pair $\mathbf{k}_n, \omega_n$ satisfies the dispersion relation.

It would be possible, locally, to approximate the ocean surface using a representation such as Eq. (2.16). Consider the simplified case of point measurements of the wave signal, $\eta(t)$, recorded at $\mathbf{x} = 0$ without loss of generality. The signal is first recorded for a finite duration. The recorded section can be approximated, with any arbitrary degree of accuracy, by means of Fourier series:

$$\tilde{\eta}(t) = \sum_{n=1}^{N} A_n \cos(\omega_n t + \varphi_n) \tag{2.17}$$

However, if Eq. (2.17) were used to predict the wave elevation at time instants t, beyond the section where the Fourier amplitudes and phases have been determined, it would soon be observed that the model $\tilde{\eta}$ no longer follows the actual wave elevation η. Thus, any finite-order Fourier approximation of the form (2.16) is only valid "locally", and has no descriptive capability beyond the horizontal space and the time period where the approximation has been carried out. Clearly, Eq. (2.16) is not yet a satisfactory model for an actual sea state.

In fact, as already suggested in Section 2.1, it is more useful to consider the actual sea surface as the result of uncountable, infinitesimal elementary random contributions, which originate from phenomena taking place at various instants in time and locations in the ocean - waves may indeed have travelled hundreds of kilometres before reaching the region where they are being observed. Therefore, a model which inherently represents the randomness of the wave elevation provides a better understanding of the phenomenon under study. In 1952, Pierson [20] gave rigorous mathematical consistency to such a point of view, by describing ocean waves using the theory of random noise, a theory which had been developed throughout the previous decade, in the field of telecommunication, by researchers such as Rice [21] and Wiener [22].

According to Pierson, the wave elevation in one point is now written as follows [15, 17]:

$$\eta(t) = \int_{\omega=0}^{\infty} \cos(\omega t + \varphi(\omega)) \sqrt{2 S_{\eta\eta}(\omega) d\omega} \tag{2.18}$$

which cannot be understood as an ordinary integral. Eq. (2.18) is the limit, when ω_{max} grows to infinity, of the following integral:

$$\int_{\omega=0}^{\omega_{max}} \cos(\omega t + \varphi(\omega)) \sqrt{2 S_{\eta\eta}(\omega) d\omega} \tag{2.19}$$

Eq. (2.19) is a *Fourier-Stieltjes* integral (see for example [23]) which is defined as:

$$\begin{aligned} &\lim_{\max|\omega_{k+1}-\omega_k|\to 0} \sum_{k=1}^{N} \cos(\omega'_k t + \varphi(\omega'_k)) \sqrt{2 S_{\eta\eta}(\omega'_k)(\omega_k - \omega_{k-1})} \\ &\text{with } \begin{cases} \omega_0 = 0 < \ldots < \omega_k < \omega_{k+1} < \ldots < \omega_N = \omega_{max} \\ \forall k,\ \omega'_k \in [\omega_{k-1}; \omega_k] \end{cases} \end{aligned} \tag{2.20}$$

where:

- $\varphi(\omega)$ is a random function of ω, uniformly distributed in $[0; 2\pi[$, and such that $\varphi(\omega)$ at all frequencies are statistically independent from each other;

- $S_{\eta\eta}(\omega)$ [m^2.s] is a positive function, called *spectral density function* (SDF), *energy spectrum*, or simply *spectrum*. It represents the mean squared amplitude of the waves with frequency ω;

- $\omega_0 = 0 < ... < \omega_k < \omega_{k+1} < ... < \omega_N = \omega_{max}$ forms an arbitrary partition, or 'net', of the interval $[0;\omega_{max}]$. The Fourier-Stieltjes integral (2.19) is the limit of the random sum in Eq. (2.20) as the net becomes infinitely refined.

Eq. (2.18) is a stochastic integral. The independence of the phases of all infinitesimal random components, combined with the central limit theorem, ensures that the resulting probability distribution of the wave process is Gaussian. Indeed, the central limit theorem states that, given a sequence of independent random variables X_i, and under specific conditions[3] on the variance of the X_i, the sum $\sum_{i=1}^{N} X_n$ tends to a normal distribution as N grows to infinity, even if the individual random variables X_i are not Gaussian (see any textbook on probabilities and statistics, such as [25]). This lays the foundation for the Gaussian statistical description of ocean waves.

Now considering the spatial distribution of the free surface, Eq. (2.18) is easily generalised to:

$$\eta(\mathbf{x},t) = \iiint_{\mathbf{k},\omega} \cos(\mathbf{k}.\mathbf{x} - \omega t + \varphi(\mathbf{k},\omega)) \sqrt{2S_{\eta\eta}(\mathbf{k},\omega) d\omega dk_x dk_y} \tag{2.21}$$

Since, following linear wave theory, the frequency ω and wave number $|\mathbf{k}| = \sqrt{\mathbf{k}_x^2 + \mathbf{k}_y^2}$ follow the dispersion relation, it is in general useless to describe the wave spectrum in 3 dimensions (ω, $\mathbf{k}_x$ and $\mathbf{k}_y$). Instead, the spectrum can be specified in terms of the wave number only as $S_{\eta\eta}(\mathbf{k})$, or as a function of frequency, ω, and direction of the wave vector, θ (while the wave number magnitude is governed by ω through the dispersion relation). With the latter possibility, and defining a directional spectrum $S_{\eta\eta}(\omega,\theta)$, in m^{2}s/rad, the wave field takes the form of the following Fourier-Stieltjes integral:

$$\eta(\mathbf{x},t) = \iint_{\omega,\theta} \cos\left[|\mathbf{k}|(\omega)(\cos(\theta)x + \sin(\theta)y) - \omega t + \varphi(\omega,\theta)\right] \sqrt{2S_{\eta\eta}(\omega,\theta) d\omega d\theta} \tag{2.22}$$

where $|\mathbf{k}|(\omega)$ and ω satisfy the dispersion relation. For each frequency ω, the directional and non-directional spectra are related through the following equation:

$$S_{\eta\eta}(\omega) = \int_{\theta=0}^{2\pi} S_{\eta\eta}(\omega,\theta) d\theta \tag{2.23}$$

In Eqs. (2.18) and (2.22), for each possible realisation of the random function $\varphi(\omega,\theta)$, there corresponds a function $\eta(\mathbf{x},t)$, which may then be termed a *realisation* of the underlying spectrum $S_{\eta\eta}(\omega,\theta)$. Therefore, as stressed by St Denis and Pierson [17], for a given SDF $S_{\eta\eta}(\omega,\theta)$, Eqs. (2.18) and (2.22) in fact represent *an infinity of realisations* of the random function $\eta(\mathbf{x},t)$, which are all generated following the same statistical properties.

Thus, the sea surface $\eta(\mathbf{x},t)$ is now described as a random function, indexed by time t and position $\mathbf{x}$, and generated through the random integrals of Eqs. (2.18) and (2.22). The basic properties of this random function are now presented in Section 2.2.3, while more details about random functions in general may be found in [23].

[3] In the case of Eq. (2.20), the random sequence X_i is not identically distributed; therefore Lindeberg's version of the central limit theorem must be employed, which requires that the variance of the X_i is finite and satisfies the so-called Lindeberg's condition - see [15] and Chapter 10 of [24].

2.2.3 The Gaussian sea state: fundamental properties

First of all, as already mentioned, $\eta(\mathbf{x},t)$ is a Gaussian random function, which formally means that, for any discrete set of points $\{(\mathbf{x}_1,t_1),...(\mathbf{x}_n,t_n)\}$, the set $\{\eta(\mathbf{x}_1,t_1),...\eta(\mathbf{x}_n,t_n)\}$ follows a multivariate Gaussian distribution. The Gaussian wave model implies, in particular, that the probability law followed by the free surface elevation, sampled at one location, is a normal random variable.

If $S_{\eta\eta}(\omega,\theta)$ remains constant over time, and over the horizontal space, then $\eta(\mathbf{x},t)$ is stationary and homogeneous, which means that the statistical properties of the function do not vary over time or in the horizontal space. Since $\eta(\mathbf{x},t)$ is Gaussian, stationarity and homogeneity reduce to the fact that the covariance between η, measured at any two points $(\mathbf{x}_1,t_1)$ and $(\mathbf{x}_2,t_2)$, only depends on the relative position $\mathbf{x}_2-\mathbf{x}_1$ and time t_2-t_1, which is called weak stationarity (resp. weak homogeneity) [25]. Thus, a covariance function $R_{\eta\eta}(\mathbf{r},\tau)$ can be defined, such that for all $(\mathbf{x}_1,t_1)$ and $(\mathbf{x}_2,t_2)$:

$$\langle\eta(\mathbf{x}_2,t_2)\eta(\mathbf{x}_1,t_1)\rangle = R_{\eta\eta}(\mathbf{x}_2-\mathbf{x}_1,t_2-t_1) \tag{2.24}$$

In particular, the variance, defined as the average $\langle\eta(\mathbf{x},t)^2\rangle$, is also equal to $R_{\eta\eta}(0)$, and does not depend on the location $\mathbf{x}$ or time t, and thus can be simply denoted $\langle\eta^2\rangle$, or more commonly σ^2.

Furthermore, the covariance function and the SDF constitute a Fourier transform pair, which is a property referred to as the Wiener-Khinchine theorem [23, 25]. The Wiener-Khinchine relation will be further detailed in Chapter 3, where it will be of particular importance.

Finally, another important property stems from the Gaussian representation of Eqs. (2.18) and (2.22), namely ergodicity [15], which means that statistics, based on time averages or space averages, are equal to statistics based on ensemble averages. For example, the variance, which is mathematically defined as the ensemble average $\langle\eta(\mathbf{x},t)^2\rangle$, can also be obtained by computing the time or space average of $\eta(\mathbf{x},t)^2$ for any specific realisation of $\eta(\mathbf{x},t)$:

$$\sigma^2 = \langle\eta^2\rangle = \lim_{T\to\infty}\frac{1}{T}\int_0^T \hat{\eta}(\mathbf{x}^*,t)^2 dt = \lim_{L_x,L_y\to\infty}\frac{1}{L_xL_y}\int_{x=0}^{L_x}\int_{y=0}^{L_y}\hat{\eta}(\mathbf{x},t^*)^2 dxdy \tag{2.25}$$

where $\hat{\eta}$ denotes a specific realisation of the function η, $\mathbf{x}^*$ in the second member of the equality indicates that time-integration is carried out at a fixed location $\mathbf{x}^*$, and t^*, in the third member of the equality, indicates that integration in the horizontal plane is carried out at fixed time t^*.

Assuming the stationary, homogeneous and ergodic Gaussian wave representation of Eqs. (2.18) and (2.22), the random function $\eta(\mathbf{x},t)$, i.e. the sea state, is *entirely characterised* by its SDF $S_{\eta\eta}(\omega,\theta)$. The Gaussian model thus provides a unified, elegant and relatively simple mathematical framework for the description of a random sea. In spite of its apparent simplicity, the Gaussian representation of random waves lends itself to a wealth of analysis which can be best appreciated in the book by Ochi [6]. In the field of wave energy, and other engineering applications, many parameters of interest can be derived from the wave spectrum, as a complement to those which can be directly estimated from wave time series. Such parameters will not be enumerated here; their definitions may be found in [26]. Only the most common parameters are introduced at this stage:

- For any integer j, the *spectral moment* of order j is defined as:

$$m_j = \int_{\omega=0}^{\infty}\omega^j S_{\eta\eta}(\omega)d\omega \tag{2.26}$$

  In particular, m_0, which is the area under the wave spectrum, measures the average energy of the random process, and is equal to the variance [25]. Therefore, the following equality holds:

$$m_0 = \sigma^2 = R_{\eta\eta}(0) \tag{2.27}$$

- The *significant wave height* H_s is defined as the average peak-to-trough height of the one third largest waves. Assuming a narrow-band spectrum, which means that the free surface elevation does not have any positive minima or negative maxima, the distribution of wave amplitudes follows a Rayleigh distribution, and H_s can be estimated directly from the wave spectrum (in which case it is usually denoted H_{m_0}) as:

$$H_s \approx H_{m_0} = 4.01\sqrt{m_0} \tag{2.28}$$

  In general, actual wave spectra are not narrow banded, which complicates the calculation of H_s; however the error in using the simplified Eq. (2.28) is an overestimation always smaller than 8% [6].

- The peak wave period, T_p, corresponds to the inverse of the frequency which has the highest energy in the wave spectrum, while the mean energy wave period, T_e, is calculated from the spectrum as:

$$T_e = \frac{m_{-1}}{m_0} \tag{2.29}$$

The Gaussian representations of Eqs. (2.18) and (2.22), with a given SDF $S_{\eta\eta}(\omega,\theta)$, remain valid over a period of time and a geographical area, where it can be reasonably assumed that the wave energy distribution, across frequencies and directions, remains constant - in other words, the stationarity and homogeneity assumptions are verified. In reality, the sea state slowly evolves in time and space. However, it is generally accepted that the sea state can be considered "locally" stationary, over durations less than 1 to 3 hours and distances of several kilometres, although the latter order of magnitude may be reduced in the case of a complex local bathymetry or coastline. Beyond such time and geographical scales, the variations in the statistical characterisations of the sea surface are generally dominated by slow changes in meteorological conditions while, on shorter scales, the dominant effect is the short-term variability of the random function η. The latter point is often relatively neglected or misunderstood by engineers and researchers, and will be exemplified in Chapter 3, using real wave data.

Thus, over a long period, the wave conditions in a given location can be modelled as a sequence of Gaussian wave spectra. Similarly, the wave conditions, encountered by a ship or an offshore structure throughout its life as discussed in 2.1, are usefully characterised by means of a large sequence of Gaussian wave spectra. Therefore, Gaussian wave fields form the fundamental tool to characterise wave loads in naval and offshore engineering, and to describe sea states in weather prediction models.

Before Section 2.4 provides more practical illustrations of ocean wave spectra, with a discussion on appropriate wave spectral representations in the context of wave energy, Section 2.3 discusses the range of validity of the Gaussianity assumption, as far as WEC systems are considered. Also note that hydrodynamic theory, which has only been the subject of a succinct presentation in the present section, is given more attention in Chapter 4, dedicated to the mathematical modelling of wave energy converters.

2.3 Beyond the Gaussian description

It is important to understand the limitations and the range of validity of the Gaussian description. In particular, two key assumptions may be questioned:

- Conceding that linear wave theory, as presented in Section 2.2, accurately describes ocean waves, and assuming that ocean waves are indeed generated by a large number of events, why should it be assumed that all the infinitesimal wave components have independent phases?

- If some of the assumptions of linear wave theory are violated, i.e., if some non-linear effects are taken into account in the physical description of waves, can the Gaussian model remain useful?

An initial answer to both questions is provided by empirical evidence. Based on observations at sea and laboratory tests, the consensus is that, quoting Ochi [6], *"waves can be considered a Gaussian random process even in severe seas if the water depth is sufficiently deep"*. In fact, the Gaussian wave description is successfully employed in practice, since it forms the basis of operational weather forecasting models, which consider that, for sufficiently short time scales (1 to 3 hours) and geographical spans (several kilometres), the sea is locally Gaussian, while the so-called *energy balance equation* describes how the wave spectrum slowly evolves in time and space[4].

The independence of the wave components also finds theoretical justifications, which are eloquently discussed by Hasselmann in Appendix B of [27]. The general idea relies on considering the wave field as a sum of uncountable, possibly interacting wave groups. Even if some of these wave groups were initially correlated, they subsequently propagate in time and space, at different speeds because of the dispersive nature of water waves, so that they eventually become separated, and the correlation between them can only be observed by indefinitely expanding the domain of analysis: *"The separations between dependent wave groups increase indefinitely with time, so that the statistical information disperses to infinity and can be recovered only by continually extending the spatial domain of the analysis"* [27]. Therefore, in practice, since a wave field is always examined over a limited domain, the observable wave properties are Gaussian.

As far as non-linearities are concerned, it is useful to distinguish broadly between "strong" non-linearities, which are incompatible with the Gaussianity assumption, and "weak" non-linearities, which do not necessarily contradict it.

Strongly non-linear sea states typically display a marked asymmetry between wave peaks and troughs, the latter being sharper while the former are relatively flat. Such patterns are typically observed in shallow waters, where the waves tend to lose their dispersive property, or in deep water in very strong sea states. The departure from Gaussianity in shallow water is discussed more precisely in Chapter 9 of [6]. An empirical separation law between Gaussian and non-Gaussian regimes is proposed, based on significant wave height and depth. For example, in a depth of 20m, a strong sea state with $H_{m_0} = 5$m separates Gaussian from non-Gaussian regimes. Similarly, in deeper water, strong seas and fast transient meteorological conditions may lead to non-Gaussian statistics, see for example [28]. In particular, the probability of occurrence of rogue waves may be explained by such departures from Gaussian statistics [28]. For non-Gaussian seas, the spectrum (which only measures second-order statistics) does not suffice for the complete characterisation of the random process under study. Higher-order spectral analysis (bi-spectrum, tri-spectrum) can be used, for example, in the study of random waves in shallow water [29]. Eventually, strongly non-linear waves may typically break, which is obviously not represented in any Gaussian model. As far as WECs are concerned, only the study of extreme conditions, or of specific WEC concepts operating in sufficiently shallow waters, may necessitate the modelling of non-Gaussian wave inputs.

Weak non-linearities are based on the idea that the solution of the linearised equations provides a satisfactory starting point, to describe small-but-finite disturbances of the free surface [30]. The non-linear wave field is then analysed by means of non-linear perturbations, in terms of a small (but finite) parameter, usually the wave steepness.

In particular, weak non-linearities account for resonant interactions between waves of different frequencies, which were first evidenced by Phillips [31, 32]. Two interacting waves, yielding a third wave at a frequency different from the first two waves, is referred to as three-wave interaction, while three waves, giving birth to a fourth one is called four-wave interaction, and so on. Phillips showed that three-wave interaction does not exist for deep-water gravity waves, so that four-wave

[4] https://www.ecmwf.int/en/learning/education-material/lecture-notes

interaction is the dominant non-linear process for those waves. Non-linear interactions amongst water waves have been studied at a *deterministic* level, i.e. by considering elementary interactions between a small number of waves, as well as from a *stochastic* point of view, i.e. by considering non-linear interactions in a random wave field with a broad spectrum [33]. The latter, stochastic, approach is referred to as *wave turbulence theory* [34]. Wave turbulence theory was pioneered by Hasselmann [35, 36, 37], who first proposed a model to calculate four-wave interactions in a random wave field. Four-wave interactions have been found essential to explain how the wave spectrum slowly evolves in time and space and, in particular, how the wave spectrum broadens to low frequencies which cannot be generated directly under the effect of wind [30]. As such, the computation of spectral energy transfers due to four-wave interactions is a challenging and crucial aspect of modern operational ocean weather forecasting models [5], referred to as 3^{rd} *generation* wave models. Note that, in numerical weather forecasting models, the other terms, namely wind forcing and wave dissipation, which govern the evolution of the wave spectrum in the energy balance equation, are also essentially non-linear phenomena.

In spite of their importance in the evolution of wave conditions, it is generally assumed that non-linear energy transfers take place over relatively large time and geographical scales, without significantly affecting the local Gaussian nature of the wave field, considering a small enough time and geographical range. Again, quoting Hasselmann [27]: *"The coupling between interacting wave groups which satisfy the resonance conditions leads to a small energy transfer and a weak statistical dependence between the wave groups. After interacting, the wave groups propagate away from one another and the statistical correlations disperse into a fine structure. The Gaussian hypothesis implies that the fine structure can be ignored for the development of the field forwards in time. Or in other words, in subsequent interactions (involving new sets of wave groups which interact for the first time) the interacting components can be regarded as statistically independent."*

Many other types of weakly non-linear wave phenomena exist, and their study is still a very active research area, with a rich literature (see, for example, reviews in [33] and [34]) with connections to other branches of theoretical physics, such as plasma waves and optics. Therefore, this brief discussion by no means constitutes a comprehensive review, but it merely emphasises the fact that a Gaussian statistical representation, if its limitations are correctly understood, is not incompatible with the presence of weak non-linearities.

Finally, strong non-linear effects may occur as a result of wave interaction with the WEC structure. However, such effects are to be distinguished from non-linearities in the undisturbed wave field. The modelling of non-linear fluid-structure interactions, discussed in Chapter 4, is not incompatible with the fact that the undisturbed, far-field waves, which essentially represent the independent forcing term for the system under study, are statistically Gaussian. Overall, it seems reasonable to assume that, for the vast majority of WEC concepts and operating conditions, the independent wave forcing terms can be modelled as a Gaussian statistical process.

2.4 Spectrum characterisation for wave energy applications

It has been explained, in Sections 2.2 and 2.3, why the fundamental characterisation of the wave input, for typical WEC operating conditions, takes the form of a Gaussian random function, of which the statistical properties are entirely specified by a SDF. Therefore, the statement formulated in the introduction of this chapter, that the WEC response should be studied in the *sea states* typically experienced throughout its lifetime, may now be rephrased more accurately by replacing "sea states" with "wave spectra". A realistic characterisation of the WEC response thus requires that the wave SDFs are represented with sufficient accuracy for the intended objective.

A particularly important task is *power production assessment*, or simply *power assessment*, which consists of evaluating the WEC or WEC farm power production over its lifetime, in a selected location. At the current development stage of WEC technologies, power assessment is essential to evaluate and compare the potential of various technologies at different locations [4, 38, 39, 40, 41, 42, 43, 44]. In the future, power assessment will also be instrumental in determining the

economic viability of specific wave energy projects. Power assessment may not only provide a raw figure for the average WEC power production, but may also, in a wider sense, include the study of the WEC production variability over different time, and geographical, scales [43, 45, 46, 47, 48].

In addition to power production, other aspects of the WEC performance may be analysed by means of numerical simulations, and thus also necessitate an appropriate wave spectral description: for example, dimensioning the device to ensure its survivability may be carried out through fatigue analysis using cycle counting, or by accurately assessing the probability of occurrence of some specific events (such as exceeding a given threshold of force or position), as discussed in Chapter 14 of [3]. Both approaches require a detailed statistical knowledge of the device dynamics over its lifetime, and therefore present challenges which are similar to those of power assessment. However, for the sake of simplicity, and because until now the bulk of the research effort on WEC technology has focused on power production, this section (2.4) focusses on how accurately wave spectra should be described, *in the specific context of power assessment*.

A comprehensive study on power assessment methodologies would also include a discussion on WEC physical modelling and numerical simulations. The detailed presentation of those topics is reserved for Part II (Chapters 4 and 5) of this thesis.

2.4.1 Real wave dataset

Throughout the remainder of this section, and in Chapter 3 of this thesis, a real wave dataset, kindly provided by the Irish Marine Institute, is used as a particular real-world case study. The Irish Marine Institute has wave elevation measurement buoys operating at several locations off the coast of Ireland. The dataset considered here consists of one year of wave data, recorded in a site off County Mayo in the West of Ireland, several miles away from the town of Belmullet[5]. Although the buoys record many variables, for the purpose of the present section, only free surface elevation data was used, and processed in order to obtain wave spectra.

The wave elevation data was originally organised into files corresponding to 30 minutes of wave elevation, recorded at a rate of $f_s = 1.28$ Hz. Unfortunately, there is a significant proportion of missing half-hourly files, approximately 30-40%, corresponding to periods of time where the buoy was not operating properly. A complete insight into the seasonal variability of the meteorological conditions would require significantly more data - typically 10 years of complete data. However, the dataset is large enough to provide meaningful examples.

Each 30-min wave elevation data file is processed, so as to obtain a 30-min wave spectrum estimate, in several steps:

- The thirty minutes of data are split into overlapping 3-min segments.
- In each segment, the signal is windowed through a tapered cosine function (or Tukey window) [49].
- The SDF is estimated for each segment, by means of an FFT.
- Finally, the SDF estimates in all segments are averaged to obtain the 30-min SDF.

Several remarks are appropriate. Firstly, the number of frequencies in the SDF is determined by the characteristics of the individual data segments. In particular, the cut-off frequency is determined as $f_{max} = \frac{1}{2\Delta_t} = \frac{1}{2} f_s = 0.64$Hz, and the frequency step is $\Delta_f = \frac{1}{T_{seg}} = 0.0056$Hz, where T_{seg} is the duration of individual data segments. Furthermore, it was found that the methodology and settings, used here to calculate the half-hourly spectra, are very similar to those used, within the WaveRider measurement buoys themselves, for the same purpose[6]. Finally, averaging the

[5] http://www.marine.ie/Home/site-area/data-services/real-time-observations/wave-buoys
Belmullet buoy: Wave DataWell Wave Rider "Berth B", Lat. 54.2339, Long. -10.1429, year 2010

[6] http://www.datawell.nl/Support/Documentation/Manuals.aspx

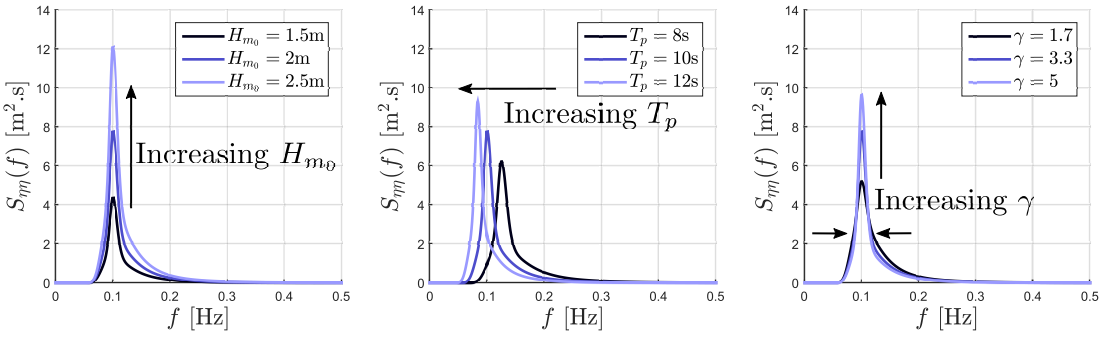

(a) $T_p = 10$s, $\gamma = 3.3$, varying H_{m_0} (b) $H_{m_0} = 2$m, $\gamma = 3.3$, varying T_p (c) $H_{m_0} = 2$m, $T_p = 10$s, varying γ

Figure 2.1: Examples of JONSWAP SDFs with varying parameters T_p, H_{m_0} and γ

SDF of all segments is essential to obtain spectral estimates which are less affected by short-term variability.

Once half-hourly wave spectra have been obtained, it is also easy to obtain hourly or 3-hourly wave spectra, depending on the intended objective. For example, hourly spectra are obtained by averaging every two consecutive half-hourly SDFs.

2.4.2 Parametric wave spectra

Actual ocean wave spectra, $S_{\eta\eta}(\omega,\theta)$, exhibit a variety of shapes. In particular:

- The spectrum can be more or less energetic, which corresponds to larger or smaller values of $S_{\eta\eta}(\omega,\theta)$, respectively.
- The spectrum can have a greater content in the low frequencies (long and slowly-oscillating waves) or, in contrast, in the high frequencies (short, quickly-oscillating waves).
- The spectrum may be uni-modal, which means that $S_{\eta\eta}(\omega,\theta)$ has only one spectral peak corresponding to one wave system, or multi-modal, when two or more wave systems are combined, thus resulting in a spectrum with two or more peaks. Multi-modal wave spectra may occur, for example, when swell waves (which have low frequencies) are combined with a wind sea (which has a high-frequency content).
- $S_{\eta\eta}(\omega)$ may be sharply concentrated around a peak frequency, or may be more broad-banded.
- $S_{\eta\eta}(\omega,\theta)$ may be strongly concentrated in one direction (long-crested waves) or exhibit strong directional spread (short-crested waves).

Physical considerations and empirical measurements have allowed the formulation of various parametric models for wave spectra, which represent spectral shapes under different idealised conditions, see for example Chapter 2 of Ochi's book [6]. For non-directional spectra, the most commonly encountered formulations are the Pierson-Moskowitz spectrum (for a fully-developed sea) [50], the Bretschneider spectrum (suitable for a developing sea) [51], and the JONSWAP formulation [52] for wind-generated seas with fetch limitations (the Pierson-Moskowitz spectrum is, in fact, a limit case of the JONSWAP formulation).

As an example, Fig. 2.1 shows non-directional wave spectra following the JONSWAP formulation. The JONSWAP formulation has three free parameters, usually taken as the peak wave period T_p, the significant wave height H_{m_0}, and a peak enhancement factor γ which can, in realistic conditions, take values between 1 and 6, with a typical default of 3.3 [6].

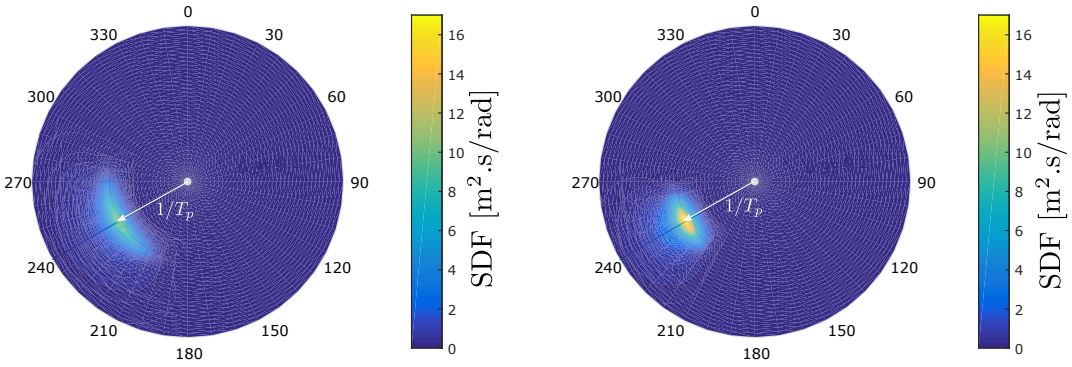

(a) $s_{\max} = 25$ (b) $s_{\max} = 75$

Figure 2.2: Examples of directional JONSWAP spectra with a Mitsuyasu spreading function, using two different spreading parameters $s_{\max}$ ($H_{m_0} = 2$m, $T_p = 10$s, $\gamma = 3.3$)

To account for the directional distribution of wave energy, analytical formulations are also available. The directional spectrum is often described by means of a parametric, directional spreading function, $D(\omega, \theta)$, such that:

$$S_{\eta\eta}(\omega, \theta) = D(\omega, \theta) S_{\eta\eta}(\omega) \tag{2.30}$$

where $S_{\eta\eta}(\omega)$ is the non-directional spectrum and, for each frequency ω,

$$\int_0^{2\pi} D(\omega, \theta) d\theta = 1 \tag{2.31}$$

so that Eq. (2.23) is verified. Several formulations exist for the spreading function $D(\omega, \theta)$, such as the *cosine-square*, *Mitsuyasu*, *Hasselmann* and *Borgman's* formulae [6]. In particular, the Mitsuyasu formula is widely used for engineering applications, and is considered reasonably realistic [53]. Denoting θ_p as the peak wave direction and $\omega_p = 2\pi/T_p$ the peak frequency, the Mitsuyasu directional spreading function is:

$$D(\theta, \omega) = \frac{2^{2s-1}}{\pi} \frac{\Gamma(s+1)^2}{\Gamma(2s+1)} |\cos(\frac{\theta - \theta_p}{2})|^{2s} \tag{2.32}$$

where the parameter s is frequency-dependent, with:

$$s = \begin{cases} s_{\max}(\omega/\omega_p)^5 & \text{for } \omega \leq \omega_p \\ s_{\max}(\omega/\omega_p)^{-2.5} & \text{for } \omega > \omega_p \end{cases} \tag{2.33}$$

The parameter $s_{\max}$ governs the concentration of the wave energy around the peak direction, and thus depends on the nature of the wave system considered. A large $s_{\max}$ value indicates a spectrum sharply concentrated around its mean direction. Values such as *"10, 25 and 75 for wind waves, swell with short decay distance, and swell with long decay distance, respectively"* [53], may be used. Fig. 2.2 shows two examples of directional spectra, obtained from a JONSWAP spectrum ($H_{m_0} = 2$m, $T_p = 10$s, $\gamma = 3.3$) and a Mitsuyasu spreading function with $s_{\max} = 25$ and $s_{\max} = 75$, respectively.

Parametric spectral formulations are extremely useful in practice. Indeed, they characterise the complete spectrum by means of several scalar values only - usually two. In particular, this simplifies the task of data storage, and eases the computations in numerical weather prediction

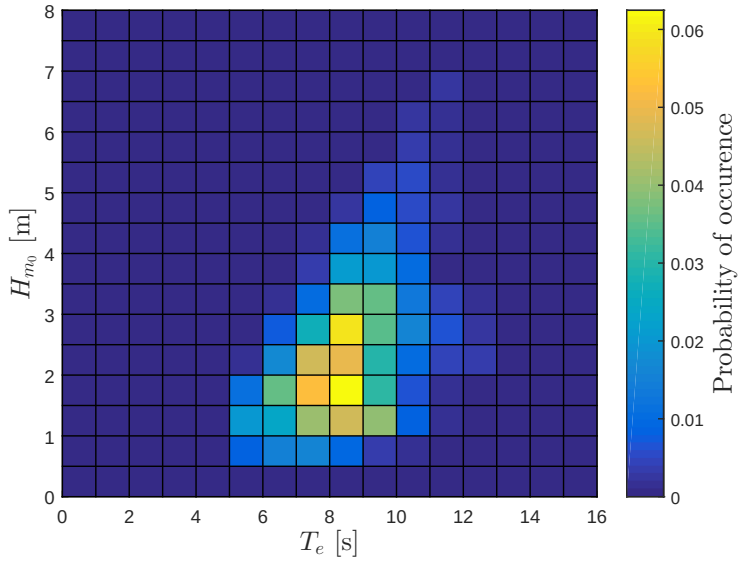

Figure 2.3: Example of scatter diagram showing the probability of occurrence for each hourly sea state, characterised by H_{m_0} and T_e

models. Furthermore, assuming a given spectral formulation, many statistical quantities can be derived using analytical formulae [6]. Finally, when it comes to measuring real ocean wave spectra, if a parametric formulation is assumed, the entire spectrum can be deduced from just two or three scalar parameters (for example m_0, T_p and θ_p), which are easily measurable using relatively simple devices and methods.

2.4.3 The power matrix approach

The most usual methodology for power production assessment of a given WEC at a specific site consists of calculating the convolution between the site *scatter diagram* and the device *power matrix*, see for example [4] and [38]. Such an approach characterises each sea state by means of only two parameters. The parameters recommended in the IEC standard TS 62600-101 [54], for wave energy resource assessment, are the significant wave height H_{m_0}, and the mean energy wave period T_e, as defined in Eqs. (2.28) and (2.29). A two-parameter representation implicitly assumes that all wave spectra, at the site of interest, can be described in a given parametric form characterised by two parameters, such as a Bretschneider spectrum, a Pierson-Moskowitz spectrum, or a JONSWAP spectrum with a fixed value for the peak enhancement factor γ.

The scatter diagram (or scatter table) has two entries corresponding to the two chosen spectral parameters. It represents, for each pair of parameters, the probability of occurrence of the corresponding sea state. The scatter diagram must be evaluated based on sufficiently long historical data, at least 10 years according to IEC TS 62600-101 [54, 55]. Such historical data may have been recorded at the site of interest (if a measurement device has been operating at the site for a sufficiently long time), or reconstructed from numerical ocean models [56], which is referred to as *hindcast* data [5]. An example of a scatter diagram is given in Fig. 2.3, which has been constructed from hourly wave spectra corresponding to the Belmullet wave dataset, although the record is far too short and incomplete to comply with the recommended 10 years.

The power matrix is a concise WEC representation, showing the WEC output, in terms of average power production, as a function of the two parameters describing the sea state. The value in each cell of the power matrix is computed through numerical simulations, where the wave spectrum has the chosen parametric shape, with height and period parameters corresponding to

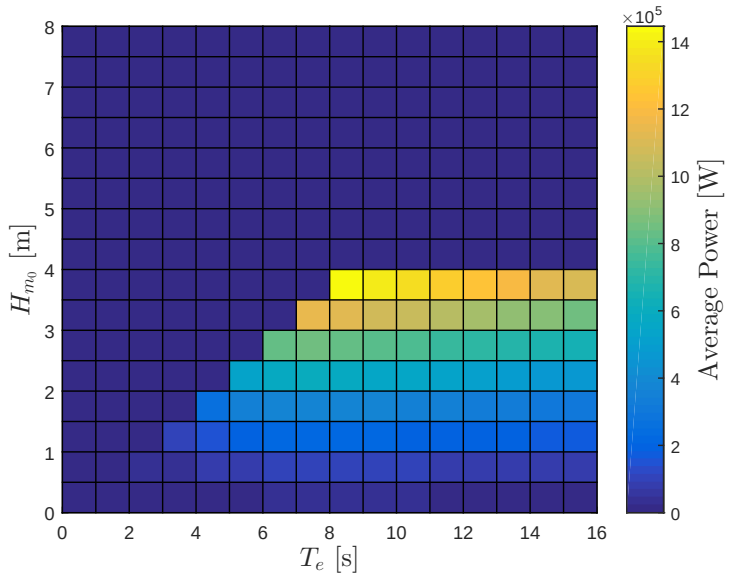

Figure 2.4: Example of power matrix

the cell indices. An example of a power matrix is shown in Fig. 2.4, which is an adaptation of the power matrix for the flap-type wave energy device studied in [57], and described in more detail in Chapter 5 of this thesis. A JONSWAP spectrum is assumed, with $\gamma = 3.3$. Note that the device operational range does not cover all sea states, in order to guarantee its physical integrity.

Denoting $p_{i,j}$ as the value in cell i, j of the scatter diagram, and $P_{i,j}$ as the value in cell i, j of the power matrix, the average annual power production can be simply computed as:

$$P_{\text{annual}} = \sum_i \sum_j p_{i,j} P_{i,j} \tag{2.34}$$

The power matrix approach has clear benefits:

- The approach only necessitates a characterisation of the wave input in terms of two parameters, and thus does not require the availability of hindcast data with a comprehensive description of each wave spectrum.

- Assuming that long enough hindcast data are available, with a comprehensive description of each wave spectrum, calculating the WEC output for each individual spectrum could be a computationally prohibitive task. In particular, as discussed in Chapter 4 of this thesis, when the WEC dynamical model is non-linear, numerical simulations are usually carried out using time-domain integration, which is relatively slow. In contrast, the power matrix approach only requires the WEC output to be calculated for each cell of the power matrix.

However, the power matrix approach is subject to significant limitations in terms of accuracy, since two-parameter wave spectra cannot reflect the variety of spectral shapes which are encountered in real seas. This is illustrated in Fig. 2.5, which shows three wave spectra, from the Belmullet dataset, along with JONSWAP spectra having the same (H_{m_0}, T_e) pairs (and $\gamma = 3.3$). Although the sea state on the left hand-side is reasonably well described by the JONSWAP shape, this is not the case for the two other sea states. In particular, bi- or multi-modal sea states are poorly represented.

In fact, in many locations, the sea condition is multimodal during a significant part of the year. For example, at the four locations studied in [4], namely North-West Denmark, North Spain,

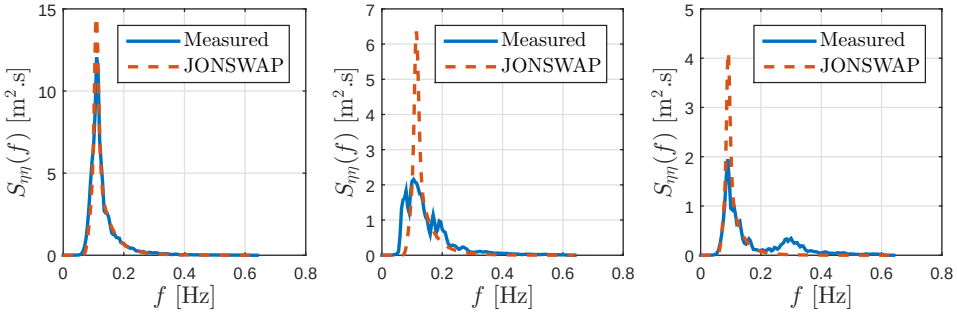

Figure 2.5: Three wave spectra recorded in Belmullet, along with JONSWAP spectra having the same H_{m_0} and T_e (with $\gamma = 3.3$)

Chile and West Ireland, unimodal sea states only represent from 45% to 60% of the total sea states recorded throughout the year. Finally, the directional spread of wave energy cannot be described in an omnidirectional spectrum formulation.

Given that the more energetic sea states are closer to theoretical spectral shapes (as also illustrated in Fig. 2.5), it could be assumed that the error in using a power matrix is relatively modest [46]. Furthermore, some WECs are insensitive to wave directionality and to the high-frequency content of the input wave spectrum, in which case a sea state characterisation through an omnidirectional, two-parameter, spectrum may be sufficient to predict the WEC output. But in a wide variety of cases, WECs are sensitive to the wave direction and, more often than not, are sensitive to the energy distribution across wave frequencies. Therefore, describing sea states as a simple (H_{m_0}, T_e) pair may lead to significant over- or underestimation of the WEC power output. In [4], it is shown that, for some of the WECs studied, the power output error, for a given spectrum describing a 3-hour sea state, could amount to as much as a 200 % overestimation of the true power production.

Within the scope of resource assessment, the errors for individual wave spectra may be averaged out when considering annual power production. However, even over such a long time scale, results of [4] tend to show that significant errors, of the order of 20 % of the true average annual power, may remain for some WEC types and geographical locations. The author of this thesis also carried out a study [57], regarding the limitations of the power matrix approach, where similar orders of magnitude are found.

In addition, the level of sophistication of current numerical ocean models makes it possible to describe local wave conditions much more precisely than through just two parameters. In state-of-the-art models such as in [56], sea states are described as discretised, full-directional spectra, with a spectral resolution of 30 frequencies and 24 directions, without assuming any predefined spectral shape or combination of spectral shapes. Therefore, it can be reasonably expected that, for the purpose of power assessment in a given location, hindcast data can be obtained featuring a comprehensive characterisation of each wave spectra.

Assuming availability of accurate hindcast data, two approaches can be identified to overcome the limitations of the power matrix approach:

- Run numerical simulations to obtain the WEC output *in each spectrum* of the historical or hindcast dataset;
- Adopt an improved, possibly multidimensional version of the power matrix approach, where the wave spectra are described by more than two parameters.

The former possibility can only be reasonably considered if an efficient numerical simulation method is available, which can be challenging if the WEC dynamical model is non-linear [3]. The second part of this thesis is dedicated to innovative numerical techniques which can address such

a challenge. The latter solution - improving the spectral parametrisation - is only briefly discussed in the following subsection (2.4.4).

2.4.4 Improved spectral parametrisations

A comprehensive approach would consist of describing the wave spectrum as the sum of a finite number of wave systems [58], each one being described through a standard spectral shape with two or three parameters, e.g. H_{m_0}, T_e and θ_p. Such an approach could provide an accurate and physically-meaningful description of any wave spectrum. But the number of possible parameter combinations of the multi-dimensional power matrix increases exponentially with the number of parameters, so that it may be computationally prohibitive to fill-in the multi-dimensional power matrix by means of experiments or numerical simulations. Additionally, many combinations of parameters would, in fact, never be met in the location considered, thus resulting in unnecessary computational overhead at the stage of calculating the cells of the multidimensional power matrix.

As a result, some authors have focused on more concise parametric sea state descriptions, suggesting only one or two more parameters in addition to H_{m_0} and T_e [59, 60]. For WECs, or WEC farms, which exhibit a strong sensitivity to the incident wave direction, the average direction of the main wave system may be a relevant additional parameter. Other suggested additional spectral parameters generally provide information about the wave spectrum directional spread [60], or about the wave spectrum frequency spread (or spectral bandwidth) [59, 60]. However, for the WECs tank-tested in [60], the directional spread only has a very minor impact on the WEC performance.

Concerning the energy spread of the wave spectrum across frequencies, it is suggested both in [60] and in [59] to use an additional parameter related to the spectral bandwidth of the spectrum. Indeed, spectral bandwidth has a strong influence on wave groups (i.e. groups of successive waves exceeding a given threshold) [6] which, in turn, may strongly influence power production [61]. Many different parameters exist, which measure the spectral bandwidth [6, 59]. For example, in [59], the spectral broadness ε_0, defined as

$$\varepsilon_0 = \sqrt{\frac{m_0 m_{-2}}{m_{-1}^2} - 1} \tag{2.35}$$

is found to be an interesting measure, which does not over-represent high frequencies and improves the accuracy of the WEC output power calculation. However, in general, the most appropriate spectral bandwidth parameter seems to depend on the WEC model considered [59].

Bandwidth parameters are particularly suitable for WECs with a broadband response [59], but may not be sufficient for any WEC and sea state, since even a triplet of values (wave height, wave period, spectral bandwidth) may still be the same for a range of significantly different sea states. In [4], for example, in the range of sea states studied, despite the fact that the WEC performance for a fixed (H_{m_0}, T_e) pair roughly follows a linear trend with respect to ε_0, it can also be seen that even with the same $(H_{m_0}, T_e, \varepsilon_0)$ triplet, significantly different power values can be obtained.

An interesting formulation is suggested in [46] where, for a given H_{m_0}, T_p pair, the spectral shape is characterised by two additional parameters, both taking continuous values between 0 and 1, and governing, respectively, the degree of bimodality and the degree of prevalence of swell over wind sea. Both parameters are directly computed from the omnidirectional spectrum, without resorting to any spectral partitioning method. The total number of parameters then remains relatively modest, and yet may allow the WEC power output to be assessed more accurately.

Another interesting method is the MaxDiss selection technique, used in [4]: the power matrix has 3 entries, namely H_{m_0}, T_p, and the broadness parameter ε_0. Within the historical wave data at a specific location, a limited number of spectra are chosen, which span the range of $(H_{m_0}, T_p, \varepsilon_0)$ triplets encountered at the site under study. Then, instead of assuming a JONSWAP spectral shape, the power matrix is built using the selected sea states, combined with an interpolation technique. The resulting power matrix is thus based on a more faithful representation of the spectra which

characterise the location, at moderate computational cost. However, the resulting WEC power matrix is site-specific, and the procedure would have to be carried out again for studies in other locations.

2.5 Summary

In order to develop wave energy technology, numerical WEC simulations in specified sea states are necessary. To generate realistic forcing terms for such simulations, consistent stochastic models for ocean waves are crucial, which are representative of average wave statistics, and also describe the short-term variability of real ocean waves.

This chapter has explained the theoretical foundations which lead to describing the sea state as a stationary, homogeneous, Gaussian random field, which reduces to a stationary Gaussian process when the wave elevation is considered at a single location. All the statistical properties of such a Gaussian random field are provided by its SDF. The Gaussian description of ocean waves does not explain the variety of strong non-linear wave phenomena observed in the ocean, and cannot account for the slow evolution of sea states in time and space. Nevertheless, the Gaussian assumption can be reasonably expected to hold for the vast majority of WEC operating conditions, and doubtlessly provides a fundamental framework to understand the short-term variability of wave records. In a non-Gaussian, stationary sea state, such as those which can occur in shallow waters and with strong meteorological conditions, spectral analysis can still be employed, although it does not provide a complete statistical characterisation of the wave process. Non-Gaussian sea states, however, will not be considered in the rest of this thesis.

Throughout its lifetime, a WEC will operate in a long series of sea states, i.e. SDFs, which can be modelled using historical data when available, or hindcast data from numerical weather prediction algorithms. In order to determine long terms statistics on the WEC behaviour, in particular for power assessment, simplified SDF representations are usually employed, to avoid running numerical WEC simulations across a large number of different sea states. Unfortunately, such approaches can yield erroneous estimates. However, if efficient numerical methods were available, WEC simulations in each sea state of the hindcast dataset could be achieved within a reasonable amount of time. This is the primary motivation to develop the innovative numerical methods for wave energy applications, which will be the subject of Part II of this thesis.

Most importantly, a clear working assumption can be established for the remainder of this work: the forcing term in numerical WEC models can be statistically described as a Gaussian process (possibly multivariate if there are several forcing terms). The numerical synthesis of such Gaussian wave inputs, with the statistical properties corresponding to a specified SDF, is discussed in Chapter 3.

At first glance, the outcome of this chapter may look somewhat lean: indeed, the notion of a wave spectrum could be considered common knowledge amongst researchers and engineers in the wave energy field. However, in practice, this notion is most often reduced to the simulation of the wave input as a finite sum of sinusoidal functions with random phases, and amplitudes derived from the wave spectrum. Such a simple, physically intuitive representation tends to conceal the more profound meaning of the wave spectrum, and the physical and statistical grounds upon which such a representation is based. Accordingly, the thorough discussion on the Gaussian wave representation and its range of validity, as far as WECs are concerned, justifies the length of this chapter.

Finally, the statistical view of ocean waves is not only fruitful for the purpose of realistic simulations. Although this is not directly related to the core topic of this thesis, the Gaussian representation can also be made the most of for real-time wave forecasting, a challenging task which has important prospects in many naval and offshore industries, including wave energy; applications include real-time WEC power-maximising control [9], helicopter landing, offshore heavy lifting, installation, access of personnel to offshore wind turbines, etc. The author of this thesis has proposed a method for real-time wave forecasting, entirely based on the Gaussian statisti-

cal representation, and which exploits the correlation structure between measured and predicted values of the wave elevation (or any other wave-related physical quantity) [62, 63]. Under the Gaussianity assumption, the proposed method has been proven to be statistically optimal (in a mean-square error sense), and can also provide a lower bound on the forecast error, with any given measurement configuration. Those developments, although they naturally stem from the work presented in Chapters 2 and 3, are beyond the scope of this thesis, which focusses on the sole task of WEC simulation.

Chapter 3

Simulation of Gaussian waves with specified spectrum

3.1 Introduction

Determining the output of a wave energy system in a specified wave spectrum (in terms, for example, of power absorption, or any other physical variable of interest), requires the generation of finite-duration wave time series, or *realisations*, which accurately reflect the statistical properties of the underlying sea state. Furthermore, as pointed out in Chapter 2, the assumption of a Gaussian sea is generally relevant for wave energy applications [6]. Therefore, this chapter focuses on the realistic generation of Gaussian wave time series from specified spectra, and discusses various methods to produce such time series.

Although the calculations and numerical examples provided in this chapter are for the generation of free-surface elevation (η) time-series, they can be readily extended to any other quantity related to the wave process through a linear relation, such as surface velocity, pressure, or excitation forces on marine structures. This is briefly discussed in Section 3.5 in the end of this chapter.

Furthermore, this chapter considers $\eta(t)$ as a *point* (i.e. univariate) random process, which describes the wave elevation at a single location. The generation of a spatially-distributed, Gaussian random wave *field* (as opposed to wave process), $\eta(\mathbf{x},t)$ is out of the scope of this thesis; however, the considerations developed in this chapter may be relatively easily extended to the more general case of a Gaussian random field.

Methods for Gaussian process generation can be broadly classified into those relying on a superposition of sinusoidal functions, with amplitudes determined from the wave spectrum (hereafter termed *wave superposition methods*, or WS), and those relying on the filtering of white noise through an AR, MA, or ARMA model (hereafter termed *filtering methods*) [64].

Filtering *vs* wave superposition methods

Filtering methods rely on the fact that a stationary Gaussian process can be modelled as the output of a linear system driven by white noise [25]. Once such a linear system has been identified, the simulation consists of generating an uncorrelated white noise sequence, which is subsequently filtered through the calculated linear filter. The choice of a linear filter, yielding a good approximation to the target process spectrum, is not unique. For example, the filter may be formulated either as an AR, MA, or more generally as an ARMA process. Furthermore, several methods exist to build an appropriate AR, MA or ARMA model, some of which are reviewed in [65] and [64]. Filtering techniques allow infinitely long time series to be generated, which accurately reproduce the stochastic properties of the target ocean wave spectrum. In particular, unlike harmonic superposition methods (as detailed further in Section 3.3), filtering methods are not subject to self-repetition

issues.

WS methods follow from the *spectral representation* of stationary processes, and from the Wiener-Khinchin relation, which states that the spectral density function (SDF) and the auto-correlation function (ACF) of a stationary random process are a Fourier transform pair [65, 66, 67, 68]. As will be further detailed in Sections 3.3 and 3.4, the random wave process is expressed as a finite sum of sinusoids, with *frequencies* spanning the target spectrum bandwidth, and *amplitudes* randomly derived from the target spectrum at the corresponding frequencies. As the frequency discretisation is refined (thus letting the number of components tend to infinity), the target process is perfectly approximated. Random wave simulation requires the generation of random amplitudes for each frequency component, and the application of an inverse discrete Fourier transform to obtain the time-series. How the spectrum is discretised, and how the random amplitudes are chosen, offer a number of options, which are discussed in Sections 3.3 and 3.4. WS, compared to filtering methods, shows several significant benefits from an engineering standpoint, including the following:

1. The methods are fast and simple - in particular, a time series with an arbitrarily small time step may be generated through Fourier transformation of the randomly-generated component amplitudes. The random amplitudes are directly derived from the wave spectrum, and no filter needs to be designed.

2. The methods are physically intuitive, in the sense that each individual wave component may represent an elementary wave, satisfying the wave propagation equations (see Chapter 2) - although here intuition can be sometimes misleading, since the Gaussian wave model relies on *an infinite set* of wave components, as opposed to a finite number of them: WS methods, which can merely approximate a finite-length realisation of the target wave spectrum, are not to be confused with the Fourier-Steltjes integrals of Eqs. (2.18) and Eqs. (2.22).

3. More importantly, representing a random wave signal through a superposition of sinusoids at different frequencies allows the calculation of the steady-state response of wave-driven, linear dynamical systems very efficiently in the frequency domain, without resorting to time-domain integration. In fact, as developed in Part II of this thesis, the frequency-domain wave input representation can also be made the most of, in calculating the response of *non-linear* systems.

In view of the aforementioned benefits, it comes as no surprise that WS methods are widespread in naval and offshore engineering, as well as in the wave energy field. WS will therefore be the focus of this chapter.

Wave superposition methods

WS methods may be further classified following two criteria:

- The frequency discretisation may be either *harmonic* (the frequency components are the multiples of a frequency step, or fundamental frequency, Δf), or *non-harmonic*;

- For a given discretisation of the spectrum (harmonic or non-harmonic), the amplitudes of the wave components may be chosen either *randomly* (with variance depending on the spectrum magnitude), or *deterministically* (in which case only the phase of the wave components is random). The random- and deterministic-amplitude variants are hereafter abbreviated as RA and DA, respectively.

RA WS methods can represent the randomness of sea waves as observed in nature [69, 70], while DA methods are statistically correct only when the number of frequency components tends to infinity [21]. However, DA has been deemed attractive by many engineers [71, 72], perhaps because it is somewhat more simple than WS, and because each random realisation produces

spectral estimates that closely match the target spectrum, thus possibly reducing the number or length of the simulations necessary to obtain an accurate estimate of a specific statistical quantity [73]. In 1984, Tucker et al. [71], in a controversial technical note, drew engineer's and researcher's attention to the "common mistake" consisting of using DA methods, claiming that using DA could result in erroneous estimates of wave statistics, especially wave group statistics. Nevertheless, later works by other researchers did not support their claim [74, 75, 76]: for various statistics, DA seems to produce unbiased estimates with respect to RA, although with less variance [76]. In more recent years, there has often seemed to be a lack of awareness about the implications of the choice of either RA or DA. The Det Norske Veritas guidelines, in 2011, promote the use of the theoretically correct method (RA) [77], while it is stated in a relatively recent report [78], from the European network Marinet (Marine Renewables Infrastructure Network for emerging Energy Technologies), that the DA method is the default approach for random wave generation in most experimental wave tanks. Finally, the implications of using either RA or DA methods in a wave energy context are studied in [79], although the statistical properties of the generated time series are not clearly specified.

Harmonic discretisation methods (either DA or RA) present the drawback of producing periodic time series with period $T_{per} = 1/\Delta f$, where Δf is the frequency step. Therefore, the length of generated signals is structurally limited to $T = 1/\Delta f$. In an era where the computational cost associated with WS could be an important factor to take into consideration, researchers proposed alternative WS methods to produce long, non-periodic time series, using only a relatively small number of frequency components, chosen in a non-harmonic way in order to avoid self-repetition of the generated signal [70, 75, 80, 81]. Although statistical distortion is suggested by the works of some authors [75, 82] as a result of non-harmonic WS, such methods are still considered in recent research [83, 84] and reports [78].

Chapter organisation

In view of the above discussion concerning WS methods, the rest of this chapter is organised in sections with the following objectives:

- Section 3.2 identifies, in a clear and rigorous way, the statistical properties which should be expected from the realistic random simulation of ocean waves with a specified spectrum. Special attention is given to finite-length estimation of 2$^{\text{nd}}$-order statistics, with practical illustrations by means of real wave data.

- In the light of the target statistical properties identified, Section 3.3 shows that harmonic WS methods are suitable for realistic random wave generation, and clarifies the differences between harmonic RA and DA simulated processes. Harmonic RA can realistically reproduce all desired statistical properties. Using DA, some realism is lost, but more accurate estimates of 2$^{\text{nd}}$-order statistics can be obtained using shorter, or fewer, simulations.

- Section 3.4 systematically analyses non-harmonic superposition methods, namely equal-area and random-perturbation techniques, in view of the aforementioned desired statistical properties, and rigorously examines the resulting statistical distortion.

- Section 3.5 discusses the results of the preceding sections, and formulates recommendations. More precisely, it is advocated that the alternative be simply between harmonic RA or DA, depending on the specific problem considered, while using non-harmonic WS techniques is not encouraged.

- Finally, the salient points and findings of this chapter are summarised in Section 3.6.

3.2 Problem specification: properties of finite-length wave records in Gaussian sea states

3.2.1 Probability law for a finite-length data record

Consider a stationary, ergodic Gaussian sea. Since it is a stationary, Gaussian random process [25], the wave elevation process is *entirely characterised* by its mean, which is assumed zero ($\langle\eta\rangle = 0$) and its ACF $R_{\eta\eta}$, defined as

$$R_{\eta\eta}(\tau) = \langle\eta(t)\eta(t+\tau)\rangle \tag{3.1}$$

which only depends on τ due to the process being stationary. $R_{\eta\eta}(\tau)$ and the wave spectral density $S_{\eta\eta}(f)$ are related through the Wiener-Khinchin relation:

$$S_{\eta\eta}(f) = 2\int_{-\infty}^{\infty} R_{\eta\eta}(\tau)\mathrm{e}^{-i2\pi f\tau}d\tau \tag{3.2}$$

and

$$R_{\eta\eta}(\tau) = \frac{1}{2}\int_{-\infty}^{\infty} S_{\eta\eta}(f)\mathrm{e}^{i2\pi f\tau}df \tag{3.3}$$

which can be reformulated as:

$$R_{\eta\eta}(\tau) = \int_{0}^{\infty} S_{\eta\eta}(f)\cos(2\pi f\tau)df \tag{3.4}$$

Examples of wave spectra, described in a JONSWAP parametric form (*Joint North Sea Wave Project*, [52]) are pictured on the left hand-side of Fig. 3.1. The corresponding ACFs, obtained through numerical integration of the Wiener-Khintchine relation of Eq. (3.4), are represented on the right hand-side of the figure. All three spectra in Fig. 3.1 have the same H_{m_0} and T_p values, but different peak enhancement factors γ.

Two remarks are appropriate. Firstly, the ACF of typical wave spectra consists of damped oscillations, fading out to zero after a few tens of seconds. As far as the discrete ACF is concerned, it means that it is possible to find a lag τ_{cor} such that for $\tau \geq \tau_{\mathrm{cor}}, R_{\eta\eta}(\tau) \approx 0$. As can be appreciated in Fig. 3.1, more sharply concentrated (or peaky) spectra have a larger correlation length. Secondly, it can be considered that the wave spectrum is zero above some frequency f_c - typically of the order of 0.5 Hz. This is reinforced by the fact that most marine devices, such as ships or WECs, act as low-pass filters, so that they are relatively insensitive to the high-frequency content of the wave spectrum.

In the remainder of this chapter, and unless otherwise specified, a JONSWAP spectrum with $H_{m_0} = 2m$, $T_p = 10$s and $\gamma = 1.5$ (shown in Fig. 3.1a) is retained as an illustrative example.

Now, consider a conceptual experiment where η is recorded over a finite duration T (either continuously or at regularly-spaced instants). Repeating the experiment many times, as illustrated in Fig. 3.2, it would be observed that the sequence $\eta(t)$, for $t \in [0;T]$, is never the same for any two experiments. More precisely, $\eta(t)$ is a stationary Gaussian random function of a discrete or continuous set $t \in [0;T]$ [23]. Furthermore, the covariance between the wave elevation measured at different instants separated by τ follows Eq. (3.4). The randomness of the experiment, and the statistical properties which characterise it, could be appreciated by considering the *ensemble* statistics, i.e. statistics obtained through averages over the set of experiments (as opposed to time-domain averaging).

Strictly speaking, when generating so-called 'realisations', corresponding to a given spectrum, the aim should be, in fact, to reproduce the above experiment, consisting of sampling free-surface

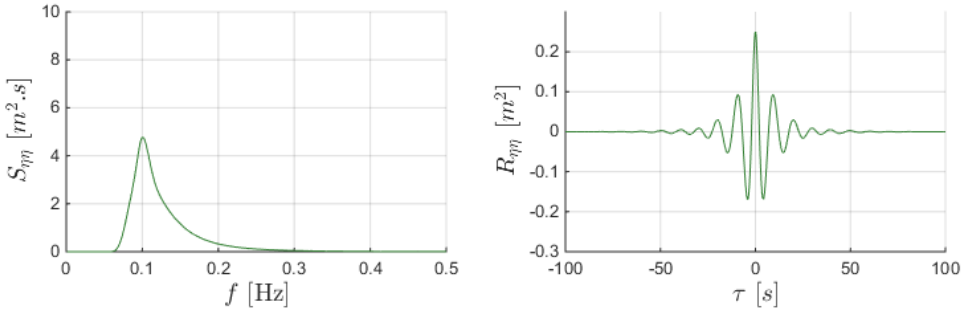

(a) $\gamma = 1.5$

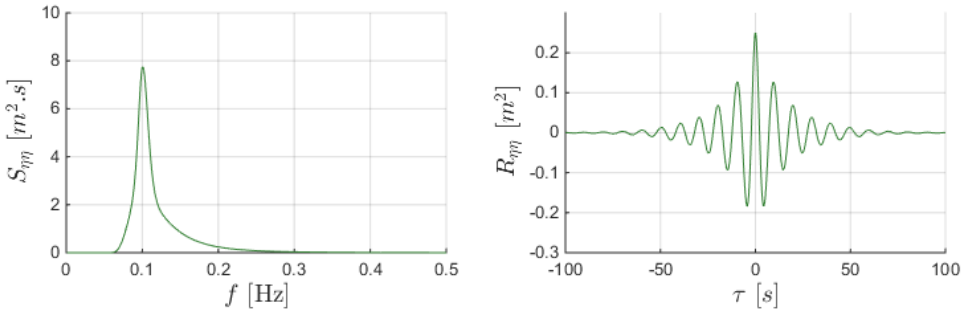

(b) $\gamma = 3.3$

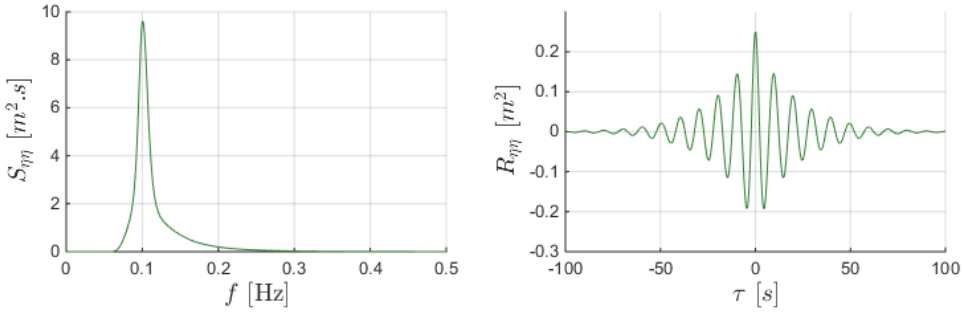

(c) $\gamma = 5$

Figure 3.1: SDF (left) and corresponding ACF (right), for JONSWAP spectra [52] with $H_{m_0} = 2m$, $T_p = 10$s, and three different peak enhancement factors.

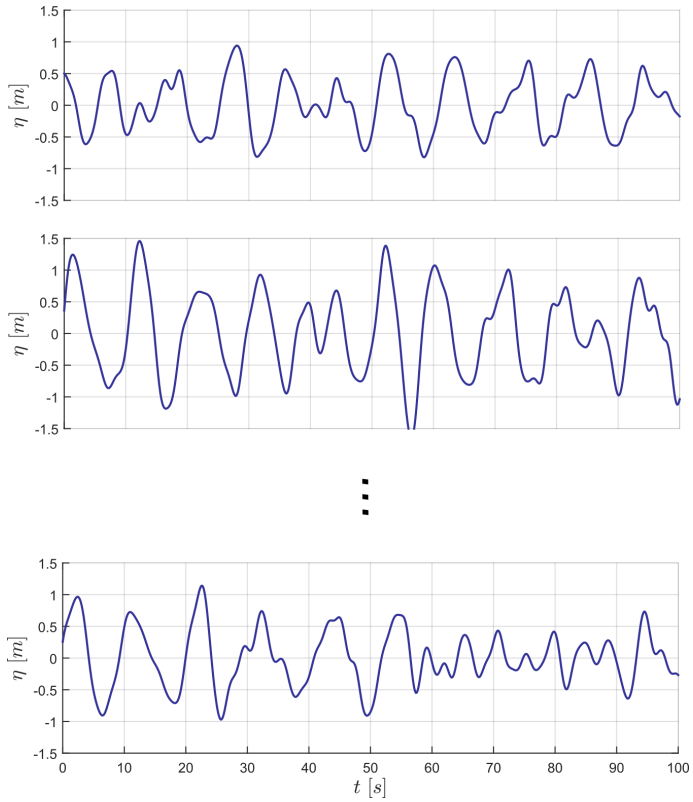

Figure 3.2: Illustrative example: free-surface elevation η being repeatedly sampled in the same sea state, over a duration $T = 100s$.

elevation values from a sea with the target spectrum. Therefore, two criteria are necessary and sufficient for the generated signal, $y(t)$, $t \in [0;T]$, to be an accurate representation of the target Gaussian sea:

- C1: The generated signal $y(t)$ should be a zero-mean Gaussian random function of $t \in [0;T]$;
- C2: The covariance function of the generated signal should satisfy Eq. (3.4) for all $\tau \in [0;T]$.

Similarly to the conceptual sampling experiment, the randomness of the generated signal can only be appreciated by repeated generation of the finite-length signal, whereby ensemble statistics can be characterised.

Note that, in addition to the two conditions C1 and C2 stated above, some authors have also deemed *ergodicity* as an important property to be satisfied by the generated signal [65, 67], which means that time-domain statistics (evaluated over an infinitely-long time horizon) should equal ensemble statistics (obtained through a large enough number of repetitions of the random experiment). However, formulated in the way chosen here, the ergodicity property does not matter, because only finite-length pieces of random signals are considered. Thus, the interest of the ergodicity property is more theoretical than practical and, in fact, C1 and C2 are sufficient to perfectly reproduce, in a statistical sense, the proposed sampling experiment.

The objectives of the random simulation are now explicitly formulated, and no other property is needed in addition to the two conditions C1 and C2 stated above, for a simulated wave signal to be representative of a given sea state.

3.2.2 Finite-length variance estimator in Gaussian sea states

In many engineering applications, important information is derived from the variance, or mean-square value, of certain physical variables. Examples include:

- Evaluation of the significant wave height H_{m_0}, derived from the variance of the wave elevation signal;

- Calculation of the mean-square difference between two simulated signals, or between predicted and measured signals;

- Calculation of the average power absorbed by WECs, usually obtained as a quadratic form on some of the WEC outputs, typically velocity, as will be detailed further in Section 3.5 and in Chapter 4.

Given a zero-mean signal x, recorded or simulated over a duration T, the mean-square value of the signal is evaluated as

$$\hat{\sigma}^2 = \frac{1}{T}\int_{t=0}^{T} x^2(t)dt \tag{3.5}$$

If x is a random signal, Eq. (3.5) is merely an estimate, which generally differs from the 'actual' variance σ^2. In particular, because the free-surface elevation η is a random process, quantities x which depend on η are also random, and hence $\hat{\sigma}^2$ differs from σ^2. However, repeating the calculation over many instances of the random signal x would provide a more accurate estimate of σ^2. The degree to which $\hat{\sigma}^2$ fluctuates around σ^2 determines the level of uncertainty associated with any given estimate $\hat{\sigma}^2$ and, in a Monte-Carlo framework, provides guidelines with respect to the number of experiments which should be carried out in order to obtain a reliable enough estimate.

Therefore, when carrying out experiments (either recorded or simulated) in a random sea, a good understanding of how finite-length estimates vary with respect to their average value is essential, since failing to do so may result in erroneous conclusions due to a particular instance, or set of instances, of the random sea.

In Eq. (3.5), the process x is not specified. However, in the following, the signal considered is the wave elevation itself, and therefore σ^2 (resp. $\hat{\sigma}^2$) corresponds to m_0 (resp. $\hat{m}_0$), the zeroth-order spectral moment of the wave elevation process (resp. its estimate).

If the finite-length simulated wave signal, y, accurately reflects the properties of a random sea, as clarified in Section 3.2, then $\hat{m}_0$ evaluated from y should, in general, not be equal to its statistical average m_0, but should instead exhibit some fluctuation around it, with the same magnitude as m_0 estimates would do in actual Gaussian seas. As will be seen in Sections 3.3 and 3.4, the different WS methods have contrasting properties in this respect. Therefore, prior to analysing the different WS methods, the properties of the finite-length estimator of the wave elevation variance in *actual* Gaussian seas are examined.

Of course, the above remarks, concerning the process variance, are also true for any other statistics (estimates of the spectrum of a signal, higher-order statistics, etc). Furthermore, in many applications, the variable of interest x is not η, but some other quantity which results from the waves, such as the pressure forces acting on a mechanical structure. However, it can be reasonably assumed that an appropriate representation of the randomness of η results in a suitable representation of the randomness of x. Therefore, focussing this section on η and its variance estimator $\hat{m}_0$ keeps the discussion relatively simple, but with fairly general significance.

Theoretical calculations

In this subsection, it is examined how finite-length estimates $\hat{m}_0$, in a stationary Gaussian sea, randomly differ from the actual m_0 of the underlying spectrum.

Assume that $\hat{m}_0$ is obtained through integration of the squared wave signal over a period of time T:

$$\hat{m}_0 = \frac{1}{T}\int_0^T \eta(t)^2 dt \tag{3.6}$$

The variance of $\hat{m}_0$ can be computed as:

$$\begin{aligned}\mathrm{var}[\hat{m}_0] &= \langle \hat{m}_0^2 \rangle - \langle \hat{m}_0 \rangle^2 \\ &= \langle \big(\frac{1}{T} \int_{t=0}^{T} \eta(t)^2 dt \big)^2 \rangle - m_0^2 \\ &= \langle \frac{1}{T^2} \int_{t_1=0}^{T} \int_{t_2=0}^{T} \eta(t_1)^2 \eta(t_2)^2 dt_1 dt_2 \rangle - m_0^2 \\ &= \frac{1}{T^2} \int_{t_1=0}^{T} \int_{t_2=0}^{T} \big(\langle \eta(t_1)^2 \eta(t_2)^2 \rangle - m_0^2 \big) dt_1 dt_2\end{aligned} \tag{3.7}$$

In the expression above, since for any t_1 and t_2, the random variables $\eta(t_1)$ and $\eta(t_2)$ are jointly Gaussian, Isserlis's theorem [85] may be applied, to yield:

$$\begin{aligned}\langle \eta(t_1)^2 \eta(t_2)^2 \rangle &= \langle \eta(t_1)^2 \rangle \langle \eta(t_2)^2 \rangle + 2 \langle \eta(t_1) \eta(t_2) \rangle^2 \\ &= m_0^2 + 2 R_{\eta\eta}(t_2 - t_1)^2\end{aligned} \tag{3.8}$$

Hence,

$$\mathrm{var}[\hat{m}_0] = \frac{2}{T^2} \int_{t_1=0}^{T} \int_{t_2=0}^{T} R_{\eta\eta}(t_2 - t_1)^2 dt_1 dt_2 \tag{3.9}$$

Using a change of variables on the integral on t_2, followed by a simple integration by parts, yields:

$$\begin{aligned}\mathrm{var}[\hat{m}_0] &= \frac{2}{T^2} \int_{t_1=0}^{T} \int_{t=-t_1}^{T-t_1} R_{\eta\eta}^2(t) dt dt_1 \\ &= \frac{2}{T^2} \Big(\Big[t_1 \int_{t=-t_1}^{T-t_1} R_{\eta\eta}(t)^2 dt \Big]_0^T - \int_{t_1=0}^{T} t_1 \big(R_{\eta\eta}(T - t_1)^2 - R_{\eta\eta}(-t_1)^2 \big) dt_1 \Big) \\ &= \frac{2}{T^2} \Big(T \int_{-T}^{0} R_{\eta\eta}(t)^2 dt + \int_{0}^{T} t_1 R_{\eta\eta}(T - t_1)^2 dt_1 - \int_{0}^{T} t_1 R_{\eta\eta}(t_1)^2 dt_1 \Big)\end{aligned} \tag{3.10}$$

Using the fact that $R_{\eta\eta}$ is even, and carrying out a change of variable in the second integral, gives:

$$\begin{aligned}\mathrm{var}[\hat{m}_0] &= \frac{2}{T^2} \Big(T \int_{0}^{T} R_{\eta\eta}(t)^2 dt + \int_{0}^{T} (T - t) R_{\eta\eta}(t)^2 dt - \int_{0}^{T} t R_{\eta\eta}(t)^2 dt \Big) \\ &= \frac{4}{T} \int_{0}^{T} (1 - \frac{t}{T}) R_{\eta\eta}(t)^2 dt\end{aligned} \tag{3.11}$$

Finally, again exploiting the evenness of $R_{\eta\eta}$, the following expression is obtained:

$$\mathrm{var}[\hat{m}_0] = \frac{2}{T} \int_{-T}^{T} (1 - \frac{|t|}{T}) R_{\eta\eta}(t)^2 dt \tag{3.12}$$

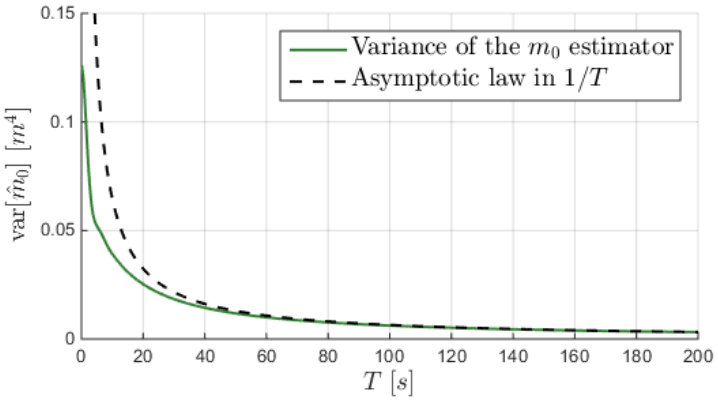

Figure 3.3: Variance of the m_0 estimator, $\hat{m}_0$, depending on the length of the estimation interval T

When T grows, and becomes significantly larger than the autocorrelation length of the process (beyond which $R_{\eta\eta}(t)$ is zero), the term $\frac{|t|}{T}R_{\eta\eta}(t)^2$ tends to zero for all t, so that Eq. (3.12) can be approximated as:

$$\begin{aligned}\mathrm{var}[\hat{m}_0] &\approx \frac{2}{T}\int_{-\infty}^{\infty} R_{\eta\eta}(t)^2 dt \\ &\approx \frac{1}{T}\int_{0}^{\infty} S_{\eta\eta}(f)^2 df\end{aligned} \tag{3.13}$$

where the second equality results from the Wiener-Khintchine (3.2) and Parseval's [6] theorems. Then, for large values of T, the variance of the m_0 estimator follows an asymptotic law in $\frac{1}{T}$, which can be found e.g. in [25], and is used in [61].

For the sea state pictured in Fig. 3.1a, Eq. (3.12) and its asymptotic approximation (3.13) are numerically computed, and compared in Fig. 3.3. Unsurprisingly, when m_0 is estimated over a very long period T of the signal, each estimate is always almost exactly equal to m_0, and hence the estimator variance tends to zero (asymptotically with $\frac{1}{T}$) when T tends to infinity. In contrast, when considered over a shorter time period, individual m_0 estimates can differ significantly from m_0.

It will also prove useful, in the next section, to have $\mathrm{var}[\hat{m}_0]$ expressed as a function of the SDF. Replacing $R_{\eta\eta}(t)$ in Eq. (3.11) with its expression given by the Wiener-Khinchine relation (3.3), it is straightforward to find that

$$\mathrm{var}[\hat{m}_0] = \frac{1}{2}\int_{-\infty}^{\infty}\int_{-\infty}^{\infty} S_{\eta\eta}(f)S_{\eta\eta}(f')\Lambda[\pi(f-f')T]^2 df df' \tag{3.14}$$

where

$$\Lambda[x] = \begin{cases} \frac{\sin(x)}{x} & \text{if } x \neq 0 \\ 1 & \text{if } x = 0 \end{cases} \tag{3.15}$$

The function $\Lambda[x]$ is represented in Fig. 3.4.

Note that, as an alternative to the above calculations leading to Eq. (3.12), which assume continuous sampling, a discrete-time analogue to Eq. (3.12) can be derived. Considering N regularly-spaced samples of η, the m_0 estimator is given as

$$\hat{m}_0 = \frac{1}{N}\sum_{n=1}^{N}\eta_n^2 \tag{3.16}$$

where $\eta_n = \eta(n\Delta t)$ and $N\Delta t$ is equivalent to the duration T in the continuous-time calculations of Eqs. (3.6) to (3.12). Then, using Isserlis's theorem [85] similarly to the continuous-time case, the

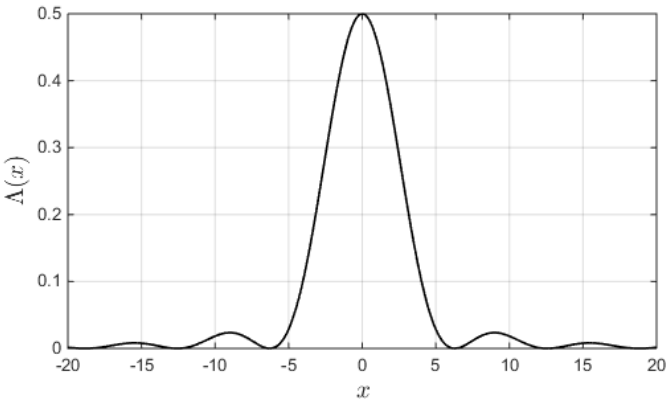

Figure 3.4: Function $\Lambda(x)$

variance of the estimator can be shown to be:

$$\text{var}[\hat{m}_0] = \frac{2}{N}\sum_{n=-N}^{N}(1-\frac{|n|}{N})R_{\eta\eta}(n\Delta t)^2 \tag{3.17}$$

which is the discrete-time analogue of Eq. (3.12), and is equivalent to the expression derived in [86].

Experimental validation using real wave data

The variability of $\hat{m}_0$ with respect to m_0 can be evidenced by means of real sea wave records, using the Belmullet dataset documented in Section 2.4.1. For the sake of illustration, a specific time period of 24 hours is chosen, during which the wave conditions show little evolution, so that the wave elevation process can be reasonably considered as a stationary Gaussian process, in spite of the relatively long dataset considered, well beyond the 30-min to 3-hour duration usually deemed compatible with the stationarity assumption. The 24 hour period starting on March 28$^{\text{th}}$, 2010, at 2:00 am, meets such requirements, as illustrated in Fig. 3.5, where it can be seen that the 3-hourly wave spectra undergo little change throughout the day.

Fig. 3.6 shows how the variance estimate, $\hat{m}_0$, calculated using Eq. (3.16), varies more when considered over shorter durations. When estimated every three hours, each estimate $\hat{m}_0$ remains close to the 24-h average (consistent with the weak variability of the 3-hourly spectrum, pictured in Fig. 3.5). In contrast, $\hat{m}_0$ measured every 10 minutes shows significant variability compared to the 24-h average.

Of course, in practice, the wave conditions (characterised by the wave spectrum) are never perfectly stationary, since the meteorological conditions rarely stop evolving completely - as governed by the energy balance equation, mentioned in Section 2.3. As discussed in Chapter 2, it is important to keep in mind that, for the wave elevation process to be considered as stationary, the duration under study must be small, compared to the rate at which meteorological conditions evolve.

Fig. 3.7 shows, in each 3-hour window, the empirical variance of the 10-min m_0 estimate (i.e. all the 18 ten-min $\hat{m}_0$, within each 3-hour window, are used to estimate the empirical var$[\hat{m}_0]$). The empirical var$[\hat{m}_0]$ is compared to a theoretical one, obtained by applying Eq. (3.13) to each 3-hourly spectrum, with an estimation interval $T = 10$ min. Assuming that the sea state is stationary over the whole day, the empirical and theoretical var$[\hat{m}_0]$ are also computed for the whole 24 hours of data (again for $T = 10$min). It can be seen that the empirical var$[\hat{m}_0]$, estimated every 3 hours, is consistent with, but does not exactly match the theoretical one, which can be attributed to two

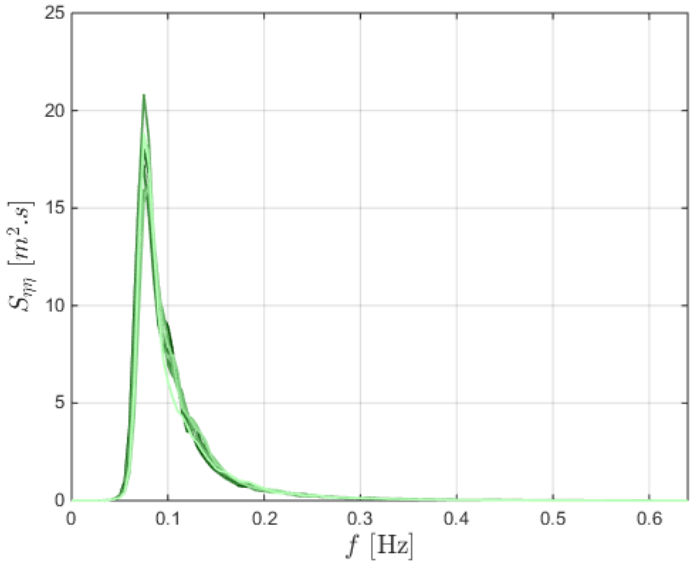

Figure 3.5: Eight consecutive 3-hourly wave spectra (Belmullet, starting 28 March 2010, 02:00). The lighter the colour, the more recent the spectrum.

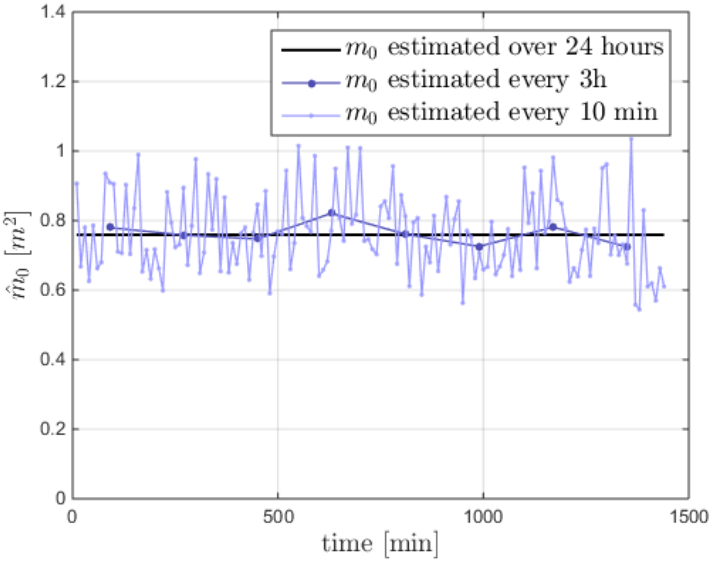

Figure 3.6: $\hat{m}_0$ estimated over 24-h, every 3 hours and every 10 minutes (Belmullet, starting 28 March, 2010, 02:00).

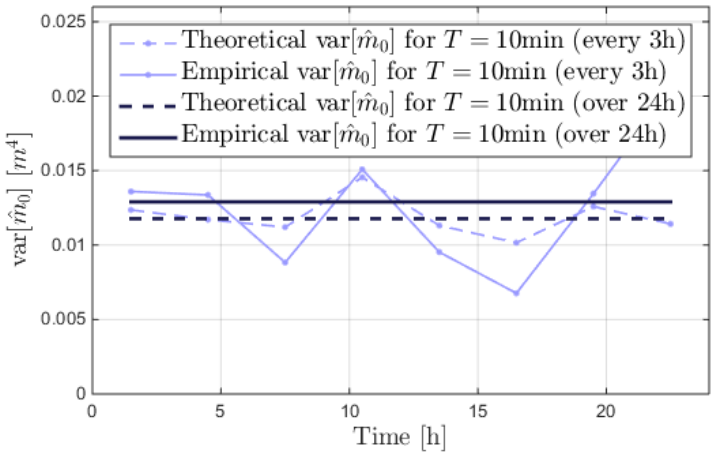

Figure 3.7: Theoretical and empirical variance of $\hat{m}_0$ for an estimation interval $T = 10$ minutes (Belmullet, starting 28 March 2010, 02:00).

reasons. Firstly, the empirical var$[\hat{m}_0]$ is estimated based on a limited number of points (18 in each 3 hours of data), so that it exhibits some variability compared to its average value (which is better approximated by the 24-hour value). Secondly, the sea condition is never exactly stationary, so that var$[\hat{m}_0]$ presents some variability, not only due to short-term estimations, but also due to the variability of the sea state (relatively small in this specific dataset). The second effect is reflected in the 24-hour empirical var$[\hat{m}_0]$ being slightly higher than the theoretical one, which would be obtained if the sea condition were perfectly stationary.

In order to illustrate the difference between the variability due to the change in wave conditions (i.e. in the wave spectrum) and the variability of $\hat{m}_0$ due to finite-duration sampling, Figs. 3.8 through 3.10 show another example, also based on data recorded at the Belmullet location, in which the meteorological conditions are rapidly evolving. It can be observed that:

- The 3-hourly $\hat{m}_0$ estimate varies relatively slowly, which corresponds to the gradual change in the wave spectrum as a result of the weather evolution.
- In contrast, $\hat{m}_0$, estimated every 10 minutes, shows an additional, 'noisy' variability, which adds to the slow pattern resulting from the weather evolution. As illustrated earlier, in Fig. 3.6, this noisy variability would exist, even if the weather conditions were not rapidly evolving, and is the result of $\hat{m}_0$ being estimated over finite-duration (10-min) samples.

Consistently with Eq. (3.13), var$[\hat{m}_0]$ is larger in more energetic sea states. Similarly to Fig. 3.7, Fig. 3.10 shows, in each 3-hour window, the empirical and theoretical variances of the 10-min m_0 estimate. Again, as in Fig. 3.7, empirical results differ to some extent from theoretical ones. In particular, due to the sea state evolving rapidly, the empirical $\hat{m}_0$ tends to present more variability then the theoretical $\hat{m}_0$, within each 3-hour period.

As seen in Figs. 3.7 and 3.10, the main limitation of empirical observations is that it is impossible to perfectly separate the effects of the sea state evolution from those due to the limited time duration over which spectral estimates are calculated. Overall, it is difficult to quantify accurately how the empirical statistical properties of the sea (such as var$[\hat{m}_0]$) should compare to theoretical ones, and some degree of discrepancy should always be expected between empirical and theoretical results. Nevertheless, real sea observations still clearly validate, at least qualitatively, the key points of this subsection.

In summary, for the statistically-realistic simulation of a stationary sea state, as defined in Section 3.2.1, the generated time series should have variability properties similar to the 28 March

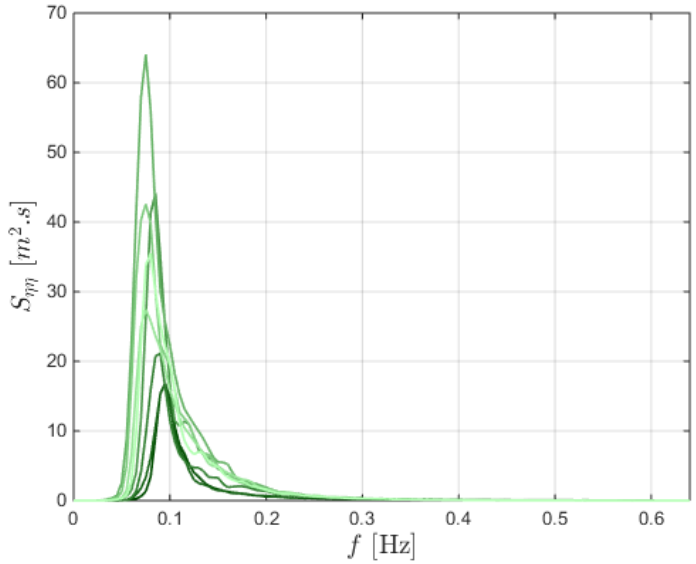

Figure 3.8: Eight consecutive 3-hourly wave spectra (Belmullet, starting 18 March 2010, 08:00). The lighter the colour, the more recent the spectrum.

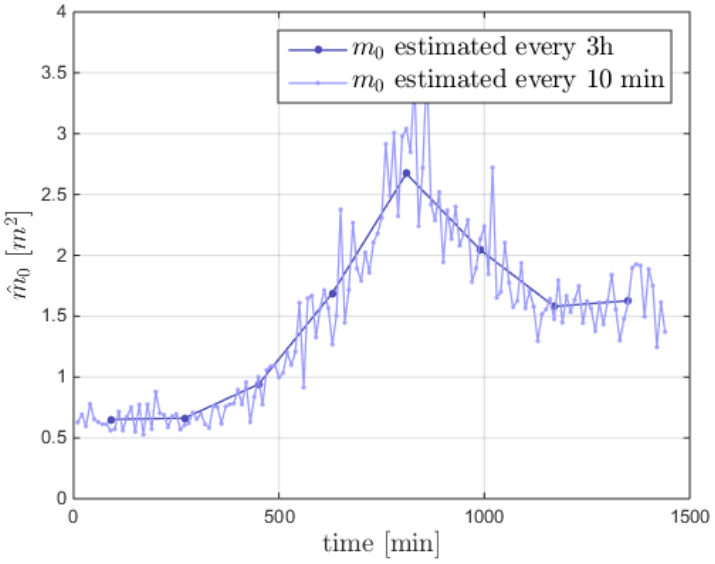

Figure 3.9: $\hat{m}_0$ estimated every 3 hours and every 10 minutes (Belmullet, starting 18 March 2010, 08:00).

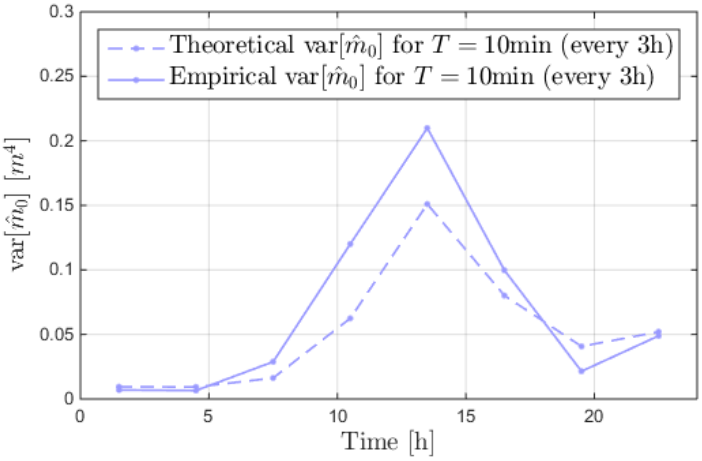

Figure 3.10: Theoretical and empirical variance of $\hat{m}_0$ for an estimation interval $T = 10$ minutes (Belmullet, starting 18 March 2010, 08:00).

2010 dataset, studied in Figs. 3.5 through 3.7. For example, if 10-min time series are generated repeatedly, the variance of each realisation should present variability with respect to m_0, such as the recorded 10-min samples in Fig. 3.9. However, for some applications, it may be preferable to use simulation methods which produce second-order statistics with less variability, in order to obtain accurate estimates using relatively few, or short, simulations. This option is reflected in the alternative between the *random amplitude* and the *deterministic amplitude* harmonic superposition methods, which are the subject of the next section.

3.3 Harmonic superposition methods

Harmonic superposition is a widely used method to generate random signals from a specified SDF. Define the cut-off frequency f_c, beyond which the spectrum $S_{\eta\eta}$ is assumed to be zero (possibly, f_c is related to the time step of the generated signal *via* the Nyquist relation, so that $f_c = 1/2\Delta t$, but alternatively, the signal may be generated with a time step more refined than $1/2f_c$, in which case FFTs cannot be employed). Define a positive integer M and divide the interval $[0; f_c]$ into $M+1$ frequencies $f_k = k\Delta f, \forall k \in \{0...M\}$, with $\Delta f = f_c/M$. Furthermore, define

$$\nu_k = S_{\eta\eta}(f_k)\Delta_f \tag{3.18}$$

The harmonic discretisation of the spectrum is illustrated in Fig. 3.11. Δ_f is the width of each red bar, and the area under the k^{th} bar represents ν_k.

From the discretisation in Fig. 3.11, two methods are usually employed to generate a random time-series. With the Random Amplitude (RA) variant, hereafter denoted HRA, y is generated as:

$$y(t) = \frac{1}{2}\sum_{k=-M}^{M} \upsilon_k e^{-2i\pi f_k t} \tag{3.19}$$

where $\forall k \geq 0$, $\upsilon_k = a_k + ib_k$, where a_k and b_k are chosen as independent, normally distributed random variables with zero-mean and variance ν_k, and $\upsilon_{-k} = \upsilon_k^*$ where * denotes the complex-conjugate [72]. Also note that $\upsilon_0 = 0$, since $\nu_0 = 0$. The HRA realisation can also be formulated as:

$$y(t) = \sum_{k=0}^{M} A_k \cos(2\pi f_k t + \varphi_k) \tag{3.20}$$

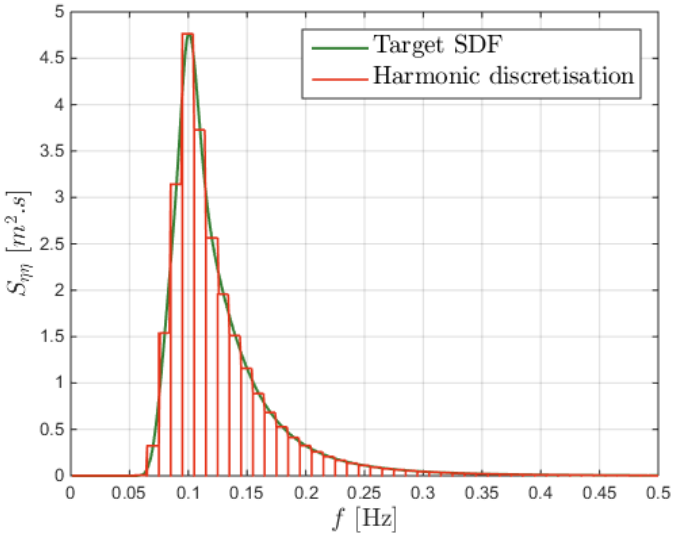

Figure 3.11: Spectrum discretisation for the harmonic superposition method ($M = 50$).

where the φ_k are randomly chosen, following a uniform distribution in $[0;2\pi]$, and the A_k follow a Rayleigh distribution with variance $2\nu_k$. The two RA formulations, in (3.19) and (3.20), are strictly equivalent with, in fact, $A_k^2 = a_k^2 + b_k^2 = |\upsilon_k|^2$.

With the Deterministic Amplitude (DA) variant, hereafter denoted HDA, y is generated as:

$$y(t) = \frac{1}{2} \sum_{k=-M}^{M} \upsilon_k e^{-2i\pi f_k t} \tag{3.21}$$

where $\forall k \geq 0$, $\upsilon_k = \sqrt{2\nu_k} e^{-i\varphi_k}$, and the φ_k are chosen as independent random variables, uniformly-distributed in $[0;2\pi]$. Similarly to Eq. (3.20), the HDA realisation may be formulated as:

$$y(t) = \sum_{k=0}^{M} A_k \cos(2\pi f_k t + \varphi_k) \tag{3.22}$$

where $A_k = \sqrt{2\nu_k}$.

Both HRA and HDA methods produce periodic realisations with period $T_{per} = 1/\Delta f$, and therefore the frequency step limits the length of the simulated signals that can be achieved. The controversy, relative to the use of RA or DA methods, has been briefly mentioned in Section 3.1. In particular, with the HDA method, as detailed hereafter, the generated signals have the very same variance at each realisation. In the following, the HDA and HRA methods are examined, in the light of the analysis carried out in Section 3.2.

3.3.1 HRA

3.3.1.1 Law of the generated process

Let us consider the random process $y(t)$ generated through the HRA method. Let us consider a finite collection of time instants, $t_i, i \in [1;N]$, and $\mathbf{y} = (y(t_1), \ldots y(t_N))^T$. From Eq. (3.19), the components of $\mathbf{y}$ are given as

$$\mathbf{y}_i = y(t_i) = \frac{1}{2} \sum_{k=-M}^{M} \upsilon_k e^{-2i\pi f_k t_i} = \sum_{k=0}^{M} a_k \cos(2i\pi f_k t_i) + b_k \sin(2i\pi f_k t_i) \tag{3.23}$$

so that $\mathbf{y}$ is a linear combination of the a_k and b_k, $k \in \{1 \ldots M\}$, which are zero-mean Gaussian. Therefore, $\mathbf{y}$ itself is a Gaussian random vector. Having shown that every discrete set of samples

of the generated random signal $y(t)$ has a multivariate Gaussian distribution, it follows from the definition of a Gaussian process (see for example [23]) that the generated process $y(t)$ is Gaussian.

The ACF of the generated process y can be calculated. From the definition of υ_k, it can be easily verified that $\forall k,l \in \{-M...M\}$, $\langle \upsilon_k \upsilon_l^* \rangle = 2\nu_k \delta(k-l)$. Thus, recalling that y is real-valued, and using the linearity of the expected value, the covariance between $y(t)$ and $y(t+\tau)$ can be calculated as follows:

$$\begin{aligned}
\langle y(t)y(t+\tau)\rangle &= \langle y(t)y^*(t+\tau)\rangle \\
&= \langle \frac{1}{2}\sum_{k=-M}^{M} \upsilon_k e^{-2i\pi f_k t} \times \frac{1}{2}\sum_{l=-M}^{M} \upsilon_l^* e^{2i\pi f_l (t+\tau)} \rangle \\
&= \frac{1}{4}\langle \sum_{k=-M}^{M}\sum_{l=-M}^{M} \upsilon_k e^{-2i\pi f_k t} \upsilon_l^* e^{2i\pi f_l (t+\tau)} \rangle \\
&= \frac{1}{4}\sum_{k=-M}^{M}\sum_{l=-M}^{M} \langle \upsilon_k \upsilon_l^* \rangle e^{-2i\pi f_k t} e^{2i\pi f_l (t+\tau)} \\
&= \frac{1}{4}\sum_{k=-M}^{M} \langle \upsilon_k \upsilon_k^* \rangle e^{2i\pi f_k \tau} \\
&= \sum_{k=0}^{M} \nu_k \cos(2\pi f_k \tau)
\end{aligned} \tag{3.24}$$

The above quantity does not depend on t, so that the generated random process is stationary and, replacing ν_k with its expression in Eq. (3.18), the ACF of the generated process is:

$$R_{yy}(\tau) = \sum_{k=0}^{M} S(k\Delta f)\cos(2\pi k \Delta f \tau)\Delta f \tag{3.25}$$

Finally, the generated process is a stationary Gaussian process, and it is possible to calculate its autocorrelation function, R_{yy}, given in Eq. (3.25). Eq. (3.25) is, in fact, a Riemann approximation of the Wiener-Khinchin relation expressed in Eq. (3.4). Reducing Δf, the accuracy of the approximation can be made arbitrarily good. However, R_{yy} is periodic, which reflects the fact that each generated signal is periodic, with a period $T_{per} = 1/\Delta f$. Fig. 3.12 shows the approximations to the target ACF, obtained for increasing values of M, i.e. decreasing values of Δf.

It can be observed, from Fig. 3.12, that:

- The chosen simulation time T should be lower than, or equal to, $1/\Delta f$ (the self-repetition period of the generated signal). For example in Fig. 3.12b, simulating a signal longer than 100s would be pointless, since no additional information is generated beyond 100s. As a consequence, if Δf is large (Fig. 3.12a), only very short duration signals can be usefully generated.

- If Δf is large (Figs. 3.12a and 3.12b), the ACF is significantly distorted, even for relatively small lag values well inside $[0; 1/\Delta f]$, as illustrated in Fig. 3.12a.

- With a small enough Δf, and with a simulation time $T \ll 1/\Delta f$, the approximation to the target ACF is excellent over the complete duration of the simulated signal. For example, this is the case in Fig. 3.12c up to $T \approx 140$s, or in Fig. 3.12d, up to $T \geq 200$s.

- With small enough Δf, and choosing $T = 1/\Delta f$, the approximation to the target ACF is excellent well inside the simulated signal, but the first and last samples are correlated due to the periodicity issue, for example considering $T = 1/\Delta f = 200$s, in Fig. 3.12c.

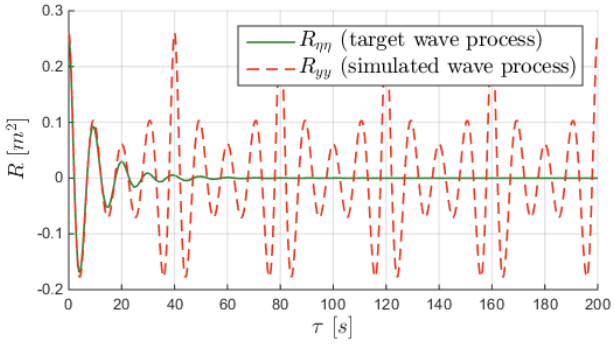

(a) $M = 20$ ($\Delta f = 0.025$)

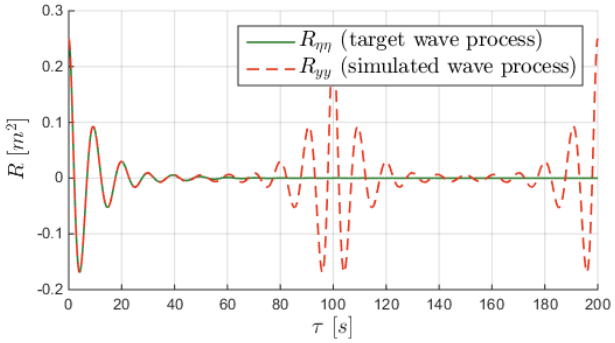

(b) $M = 50$ ($\Delta f = 0.01$)

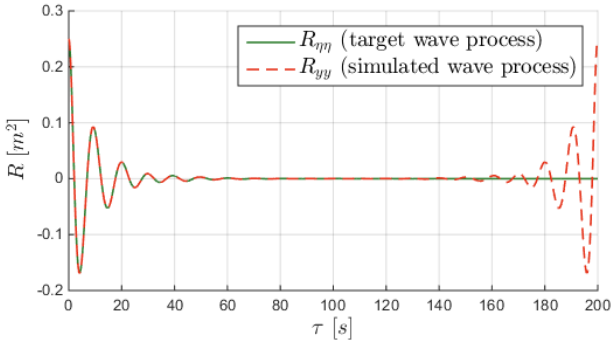

(c) $M = 100$ ($\Delta f = 0.005$)

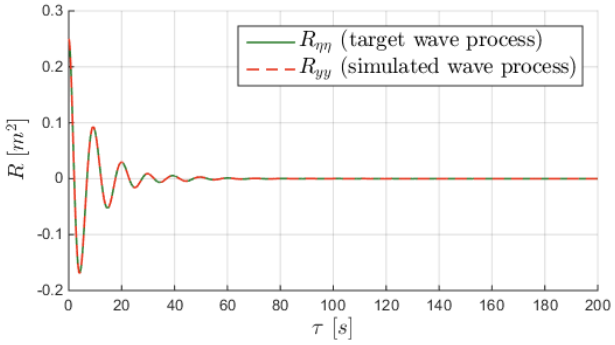

(d) $M = 200$ ($\Delta f = 0.0025$)

Figure 3.12: $R_{\eta\eta}$ *vs* R_{yy}, for the spectrum of Fig. 3.1a, using HRA or HDA methods with various numbers of frequency components.

Furthermore, the generated process is not ergodic. Indeed, it is easy to check that the ACF, estimated from an infinitely-long realisation of the signal, can be calculated as:

$$\lim_{T\to\infty}\frac{1}{2T}\int_{-T}^{T} y(t)y^*(t+\tau)dt = \frac{1}{2}\sum_{0}^{M}|\upsilon_k|^2\cos(2\pi f_k\tau) \tag{3.26}$$

which depends on the specific realisation considered because, as seen in Eq. (3.20), $|\upsilon_k|$ follows a Rayleigh distribution with variance $2\nu_k$. However, as discussed in Section 3.2, ergodicity is not an important property to be reproduced by the generated signal, since only finite-length realisations are considered.

Given the above remarks, based on Fig. 3.12, the following guidelines should apply:

- Δf should be chosen 'small enough'. Based on Fig. 3.12, a rule of thumb could be that $T_{per} = 1/\Delta f$ (the self-repetition period) be larger than twice the correlation length of η. Alternatively, another simple criterion could be that the area under the discretised spectrum, $\sum_{k=0}^{M} S_{\eta\eta}(f_k)\Delta f$, approximates m_0 with a given accuracy.
- For a given, small enough Δf:
  - Choosing $T > 1/\Delta f$ is generally pointless, since the generated signal repeats itself, so that no new information is derived by additional simulation time beyond $1/\Delta f$;
  - Choosing $T = 1/\Delta f$, the generated signal is periodic, resulting in correlation between the first and last generated samples. Depending on the intended use of the simulation, periodicity may or may not be an issue, as will be further detailed in the remainder of this section;
  - Choosing $T \ll 1/\Delta f$, the ACF of the generated signal accurately matches the target wave process for all lags within the simulation period.

In summary, the HRA method accurately reproduces the Gaussian properties and the ACF of the target process, provided that Δf is chosen small enough, and that the simulation time T is chosen less than $1/\Delta f$.

3.3.1.2 Variance estimator

The HRA method meets the two conditions, C1 and C2, defined in Section 3.2.1, if Δf is small enough, and for $T < 1/\Delta f$. For $T = 1/\Delta f$, the generated signal is periodic, therefore resulting in statistical correlation between the first and the last generated samples. In this subsection, the statistical properties of the finite-length variance estimator $\hat{m}_0$, obtained from simulated time series, are examined and compared to those expected from a true wave signal, as previously detailed in Section 3.2.2. It is verified that, using the HRA method, $\hat{m}_0$ presents realistic variability around m_0, even when $T = 1/\Delta f$.

Assume that Δf is chosen small enough to allow for an accurate SDF discretisation. Assume that m_0 is estimated based on the generated signal, y, with $T \leq 1/\Delta f$:

$$\hat{m}_0 = \frac{1}{T}\int_{-T/2}^{T/2} y(t)^2 dt \tag{3.27}$$

where, to simplify further calculations, the estimation interval is chosen symmetric with respect to the origin.

Noting that $y(t) = y^*(t)$, and replacing $y(t)$ with its expression in Eq. (3.19) yields:

$$\hat{m}_0 = \frac{1}{T}\int_{t=-T/2}^{T/2}\frac{1}{4}\sum_{k=-M}^{M}\sum_{l=-M}^{M}\upsilon_k\upsilon_l^* e^{-2i\pi(f_k-f_l)t}dt. \tag{3.28}$$

It is easy to verify that

$$\frac{1}{T}\int_{t=-T/2}^{T/2} e^{-2i\pi(f_k-f_l)t} = \Lambda[\pi(f_k-f_l)T] \tag{3.29}$$

so that

$$\hat{m}_0 = \frac{1}{4}\sum_{k=-M}^{M}\sum_{l=-M}^{M} \upsilon_k \upsilon_l^* \Lambda[\pi(f_k-f_l)T] \tag{3.30}$$

Taking the expected value, and using the fact that $\langle \upsilon_k \upsilon_l^* \rangle = 2\delta(k-l)\nu_k$, the following is obtained:

$$\langle \hat{m}_0 \rangle = \sum_{k=0}^{M} \nu_k \tag{3.31}$$

which, replacing ν_k with its expression $S_{\eta\eta}(f_k)\Delta f$ given by the harmonic discretisation, yields

$$\langle \hat{m}_0 \rangle = \sum_{k=0}^{M} S_{\eta\eta}(f_k)\Delta f \tag{3.32}$$

Therefore $\langle \hat{m}_0 \rangle$, obtained from the HRA method, is an accurate approximation of the m_0 value of the target spectrum, provided that Δf is small enough. It is now examined how $\hat{m}_0$ fluctuates around its average, i.e. the variance $\mathrm{var}[\hat{m}_0] = \langle \hat{m}_0^2 \rangle - \langle \hat{m}_0 \rangle^2$ is calculated.

$$\begin{aligned} \hat{m}_0^2 &= \Big(\frac{1}{4}\sum_{k=-M}^{M}\sum_{l=-M}^{M} \upsilon_k \upsilon_l^* \Lambda[\pi(f_k-f_l)T]\Big)^2 \\ &= \frac{1}{16}\sum_{k,l,m,n=-M}^{M} \upsilon_k \upsilon_l^* \upsilon_m \upsilon_n^* \Lambda[\pi(f_k-f_l)T]\Lambda[\pi(f_m-f_n)T] \end{aligned} \tag{3.33}$$

In the expression above, the terms $\Lambda[\pi(f_k-f_l)T]\Lambda[\pi(f_m-f_n)T]$ are deterministic quantities, while the terms $\upsilon_k \upsilon_l^* \upsilon_m \upsilon_n^*$ are random. Using the linearity of the expected value:

$$\langle \hat{m}_0^2 \rangle = \frac{1}{16}\sum_{k,l,m,n=-M}^{M} \langle \upsilon_k \upsilon_l^* \upsilon_m \upsilon_n^* \rangle \Lambda[\pi(f_k-f_l)T]\Lambda[\pi(f_m-f_n)T] \tag{3.34}$$

To simplify the terms $\langle \upsilon_k \upsilon_l^* \upsilon_m \upsilon_n^* \rangle$ in the quadruple sum, several cases must be distinguished, depending on whether the variables υ_i are independent, or not, from each other. In fact, $\forall i, j$, υ_i and υ_j are independent random variables iff $|i| \neq |j|$. Also note that $\forall i$, $\langle \upsilon_i \rangle = 0$, $\langle \upsilon_i^2 \rangle = 0$ and $\langle \upsilon_i \upsilon_i^* \rangle = 2\nu_i$.

Case 1

Amongst $|k|, |l|, |m|, |n|$, the absolute value of one of the indices is different from the three others - say $|k|$, without loss of generality. Then, $\langle \upsilon_k \upsilon_l^* \upsilon_m \upsilon_n^* \rangle = \langle \upsilon_k \rangle \langle \upsilon_l^* \upsilon_m \upsilon_n^* \rangle$. Since $\langle \upsilon_k \rangle = 0$,

$$\langle \upsilon_k \upsilon_l^* \upsilon_m \upsilon_n^* \rangle = 0 \tag{3.35}$$

Case 2

$|k| = |l|$, $|m| = |n|$ and $|k| \neq |m|$. Then,

$$\langle \upsilon_k \upsilon_l^* \upsilon_m \upsilon_n^* \rangle = \langle \upsilon_k \upsilon_l^* \rangle \langle \upsilon_m \upsilon_n^* \rangle \tag{3.36}$$

If $l = -k$, $\langle \upsilon_k \upsilon_l^* \rangle = \langle \upsilon_k^2 \rangle = 0$; similarly, if $n = -m$, $\langle \upsilon_m \upsilon_n^* \rangle = 0$. Therefore, within Case 2, $\langle \upsilon_k \upsilon_l^* \upsilon_m \upsilon_n^* \rangle$ is non-zero only when $k = l$ and $m = n$, yielding

$$\langle \upsilon_k \upsilon_k^* \rangle \langle \upsilon_m \upsilon_m^* \rangle = 4\nu_k \nu_m \tag{3.37}$$

In addition, with $k = l$ and $m = n$,

$$\Lambda[\pi(f_k-f_l)T]\Lambda[\pi(f_m-f_n)T] = \Lambda[\pi(f_k-f_k)T]\Lambda[\pi(f_m-f_m)T] = \Lambda[0]\Lambda[0] = 1 \tag{3.38}$$

Case 3

$|k| = |m|$, $|l| = |n|$ and $|k| \neq |l|$. Then,

$$\langle \upsilon_k \upsilon_l^* \upsilon_m \upsilon_n^* \rangle = \langle \upsilon_k \upsilon_m \rangle \langle \upsilon_l^* \upsilon_n^* \rangle \tag{3.39}$$

For Case 3, the above product is non-zero only if $m = -k$ and $n = -l$:

$$\langle \upsilon_k \upsilon_{-k} \rangle \langle \upsilon_l^* \upsilon_{-l}^* \rangle = \langle \upsilon_k \upsilon_k^* \rangle \langle \upsilon_l^* \upsilon_l \rangle = 4\nu_k \nu_l \tag{3.40}$$

In addition, with $m = -k$ and $n = -l$,

$$\begin{aligned} \Lambda[\pi(f_k - f_l)T]\Lambda[\pi(f_m - f_n)T] &= \Lambda[\pi(f_k - f_l)T]\Lambda[\pi(f_{-k} - f_{-l})T] \\ &= \Lambda[\pi(f_k - f_l)T]\Lambda[\pi(-f_k + f_l)T] \\ &= \Lambda[\pi(f_k - f_l)T]^2 \end{aligned} \tag{3.41}$$

Case 4

$|k| = |n|$, $|l| = |m|$ and $|k| \neq |l|$. Then, similarly to Case 3, $\langle \upsilon_k \upsilon_l^* \upsilon_m \upsilon_n^* \rangle = \langle \upsilon_k \upsilon_n^* \rangle \langle \upsilon_l^* \upsilon_m \rangle$ is non-zero only if $n = k$ and $m = l$:

$$\langle \upsilon_k \upsilon_k^* \rangle \langle \upsilon_l^* \upsilon_l \rangle = 4\nu_k \nu_l \tag{3.42}$$

In addition, with $m = -k$ and $n = -l$,

$$\Lambda[\pi(f_k - f_l)T]\Lambda[\pi(f_m - f_n)T] = \Lambda[\pi(f_k - f_l)T]\Lambda[\pi(f_l - f_k)T] = \Lambda[\pi(f_k - f_l)T]^2 \tag{3.43}$$

Case 5

$|k| = |l| = |m| = |n|$.

Sub-case 5a

Three indices (say k, l, m) are equal, while the fourth index (say n) is equal to $-k$. Then writing, in polar form, $\upsilon_k = A_k e^{i\varphi_k}$, with A_k Rayleigh distributed and φ_k independent of A_k, uniformly distributed in $[0; 2\pi]$:

$$\begin{aligned} \langle \upsilon_k \upsilon_l^* \upsilon_m \upsilon_n^* \rangle &= \langle \upsilon_k \upsilon_k^* \upsilon_k \upsilon_k \rangle \\ &= \langle A_k^4 e^{2i\varphi_k} \rangle \\ &= \langle A_k^4 \rangle \langle e^{2i\varphi_k} \rangle \\ &= 0 \end{aligned} \tag{3.44}$$

since $\langle e^{2i\varphi_k} \rangle = 0$.

Sub-case 5b

$k = m$, $l = n = -k$: Then, using the fact that, for a zero-mean Gaussian random variable x with variance σ^2, $\langle x^4 \rangle = 3\sigma^4$:

$$\begin{aligned} \langle \upsilon_k \upsilon_{-k}^* \upsilon_k \upsilon_{-k}^* \rangle &= \langle (\upsilon_k \upsilon_k^*)^2 \rangle \\ &= \langle (a_k^2 + b_k^2)^2 \rangle \\ &= \langle a_k^4 \rangle 2 \langle a_k^2 \rangle \langle b_k^2 \rangle \langle b_k^4 \rangle \\ &= 3\nu_k^2 + 2\nu_k^2 + 3\nu_k^2 \\ &= 8\nu_k^2 \end{aligned} \tag{3.45}$$

In addition,

$$\Lambda[\pi(f_k - f_l)T]\Lambda[\pi(f_m - f_n)T] = \Lambda[\pi(f_k - f_{-k})T]\Lambda[\pi(f_k - f_{-k})T] = \Lambda[2\pi f_k T]^2 \tag{3.46}$$

Sub-case 5c

$k = l$ and $m = n = -k$, or $k = l = m = n$. Then, as for Sub-case 5b:

$$\begin{aligned}\langle \upsilon_k \upsilon_k^* \upsilon_k \upsilon_k^* \rangle &= \langle (\upsilon_k \upsilon_k^*)^2 \rangle \\ &= 8\nu_k^2\end{aligned} \tag{3.47}$$

In addition,

$$\Lambda[\pi(f_k - f_l)T]\Lambda[\pi(f_m - f_n)T] = \Lambda[\pi(f_k - f_k)T]\Lambda[\pi(f_k - f_k)T] = 1 \tag{3.48}$$

The sum in Eq. (3.34) can now be split into the cases and sub-cases detailed above:

$$\begin{aligned}\langle \hat{m}_0^2 \rangle = 0 \\ &+ \frac{1}{16} \sum_{k=-M}^{M} \sum_{\substack{m=-M \\ |m| \neq k}}^{M} 4\nu_k \nu_m \\ &+ \frac{1}{16} \sum_{k=-M}^{M} \sum_{\substack{l=-M \\ |l| \neq k}}^{M} 4\nu_k \nu_l \Lambda[\pi(f_k - f_l)T]^2 \\ &+ \frac{1}{16} \sum_{k=-M}^{M} \sum_{\substack{l=-M \\ |l| \neq k}}^{M} 4\nu_k \nu_l \Lambda[\pi(f_k - f_l)T]^2 \\ &+ 0 \\ &+ \frac{1}{16} \sum_{k=-M}^{M} 8\nu_k^2 \Lambda[2\pi f_k T]^2 \\ &+ \frac{1}{16} \sum_{k=-M}^{M} 8\nu_k^2 + \frac{1}{16} \sum_{k=-M}^{M} 8\nu_k^2\end{aligned} \tag{3.49}$$

The latter expression can be developed so as to avoid inequality conditions in the double sums:

$$\begin{aligned}\langle \hat{m}_0^2 \rangle = &\frac{1}{16} \sum_{k=-M}^{M} \sum_{m=-M}^{M} 4\nu_k \nu_m - \frac{1}{16} \sum_{k=-M}^{M} 4\nu_k \nu_{-k} - \frac{1}{16} \sum_{k=-M}^{M} 4\nu_k \nu_k \\ &+ \frac{1}{16} \sum_{k=-M}^{M} \sum_{l=-M}^{M} 4\nu_k \nu_l \Lambda[\pi(f_k - f_l)T]^2 - \frac{1}{16} \sum_{k=-M}^{M} 4\nu_k \nu_{-k} \Lambda[2\pi f_k T]^2 - \frac{1}{16} \sum_{k=-M}^{M} 4\nu_k \nu_k \\ &+ \frac{1}{16} \sum_{k=-M}^{M} \sum_{l=-M}^{M} 4\nu_k \nu_l \Lambda[\pi(f_k - f_l)T]^2 - \frac{1}{16} \sum_{k=-M}^{M} 4\nu_k \nu_{-k} \Lambda[2\pi f_k T]^2 - \frac{1}{16} \sum_{k=-M}^{M} 4\nu_k \nu_k \\ &+ \frac{1}{16} \sum_{k=-M}^{M} 8\nu_k^2 \Lambda[2\pi f_k T]^2 \\ &+ \frac{1}{16} \sum_{k=-M}^{M} 8\nu_k^2 + \frac{1}{16} \sum_{k=-M}^{M} 8\nu_k^2\end{aligned} \tag{3.50}$$

Using $\nu_{-k} = \nu_k$, and simplifying redundant terms:

$$\langle \hat{m}_0^2 \rangle = \frac{1}{4} \sum_{k=-M}^{M} \sum_{m=-M}^{M} \nu_k \nu_m + \frac{1}{2} \sum_{k=-M}^{M} \sum_{l=-M}^{M} \nu_k \nu_l \Lambda[\pi(f_k - f_l)T]^2 \tag{3.51}$$

The first term is, in fact, equal to $(\sum_{k=0}^{M} \nu_k)^2 = \langle \hat{m}_0 \rangle^2$, so that the variance of the m_0 estimator is:

$$\mathrm{var}[\hat{m}_0] = \langle \hat{m}_0^2 \rangle - \langle \hat{m}_0 \rangle^2 = \frac{1}{2} \sum_{k=-M}^{M} \sum_{l=-M}^{M} \nu_k \nu_l \Lambda[\pi(f_k - f_l)T]^2 \tag{3.52}$$

Replacing ν_k with $S_{\eta\eta}(f_k)\Delta f$ yields:

$$\text{var}[\hat{m}_0] = \langle \hat{m}_0^2 \rangle - \langle \hat{m}_0 \rangle^2 = \frac{1}{2} \sum_{k=-M}^{M} \sum_{l=-M}^{M} S_{\eta\eta}(f_k) S_{\eta\eta}(f_l) \Lambda[\pi(f_k - f_l)T]^2 \Delta f \Delta f \tag{3.53}$$

which is a Riemann approximation of the double integral in Eq. (3.14).

The above calculations may seem cumbersome and tedious. However, it will be seen in further subsections that calculating $\text{var}[\hat{m}_0]$ for all other WS methods can be carried out using the very same steps, so that it is valuable to develop them here in detail.

In the specific case of the HRA method, calculations could be made, in fact, considerably simpler. Because the generated process y is Gaussian, it is possible to use Isserlis' theorem [85], and to derive the very same calculations as in Eqs. (3.9) through (3.12), this time applied to the simulated signal (as opposed to the real wave signal), so that:

$$\text{var}[\hat{m}_0] = \frac{4}{T} \int_0^T (1 - \frac{t}{T}) R_{yy}(t)^2 dt \tag{3.54}$$

Replacing R_{yy} in Eq. (3.54) with (3.24), and integrating, yields Eq. (3.53). However, as will be seen in the following subsections, Isserlis' theorem [85] only applies when the generated process follows a Gaussian law, which is not the case for all WS methods.

Assuming small enough Δf, the ACF is accurately reproduced for lag values $\tau \ll 1/\Delta f$, as seen in Fig. 3.12. Therefore, given Eq. (3.54), if $T \ll 1/\Delta f$ the variance of the m_0 estimator matches the variance that should be obtained from the target process, given by Eq. (3.12). In addition, it is interesting to examine how $\text{var}[\hat{m}_0]$ is affected when T approaches $1/\Delta f$ or, in other words, when m_0 is estimated from a *periodic* generated signal with period $1/\Delta f$. To that end, it can be seen immediately that, for $T = 1/\Delta f$, all terms of the double sum in (3.53) are zero, except for $k = l$. Therefore, with $T = 1/\Delta f$, Eq. (3.53) becomes

$$\begin{aligned} \text{var}[\hat{m}_0] &= \sum_{k=1}^{M} S_{\eta\eta}^2(f_k) \Delta f \Delta f \\ &= \frac{1}{T} \sum_{k=1}^{M} S_{\eta\eta}^2(f_k) \Delta f \end{aligned} \tag{3.55}$$

which approximates Eq. (3.13). Therefore, even though for T values close to $1/\Delta f$, the variance of $\hat{m}_0$ obtained from the HRA-generated signal may not exactly be equal to the variance of $\hat{m}_0$ obtained from a true wave signal, it is shown that, for $T = 1/\Delta f$, the variance of $\hat{m}_0$ follows the asymptotic law of the true $\text{var}[\hat{m}_0]$. Thus, the self-repetition issue, at the end of the simulation window $[0; 1/\Delta f]$, does not have a significant impact on the variance of the m_0 estimator, which remains realistic even for T close to $1/\Delta f$.

The latter result is numerically confirmed in Fig. 3.13 where, for the same frequency discretisation variants as in Fig. 3.12, the variance of $\hat{m}_0$ is plotted for both the actual signal using Eq. (3.11), and for the HRA-generated signal using Eq. (3.54), for estimates over intervals of length T ranging from 0 to $1/\Delta f$. For $M = 20$, due to the insufficiently accurate spectrum discretisation, the variance of $\hat{m}_0$ tends to be overestimated using the HRA method. In other words, repeatedly generating a signal using the HRA method with $M = 20$, and computing, for each realisation, $\hat{m}_0$ using Eq. (3.27) with any T chosen within $]0; 1/\Delta f]$, the fluctuations of the m_0 estimate around its mean value are slightly larger than if $\hat{m}_0$ was repeatedly estimated, from a record of length T, in a real sea with the target spectrum. In contrast, for $M = 50$, $M = 100$ and $M = 200$, the variance of $\hat{m}_0$, obtained from the simulated signal, is realistic for all T values within $[0; 1/\Delta f]$, in spite of the self-repetition of the generated signal illustrated in Fig. 3.12.

In summary, the foregoing means that, choosing Δf small enough to allow for an accurate discretisation of the SDF, and using the HRA method to simulate signals of length $T \leq 1/\Delta f$,

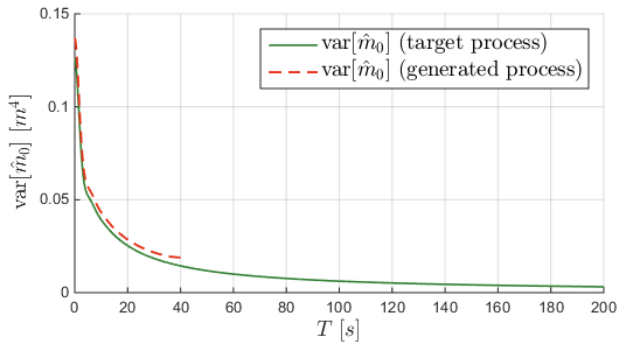

(a) $M = 20$ ($\Delta f = 0.025$)

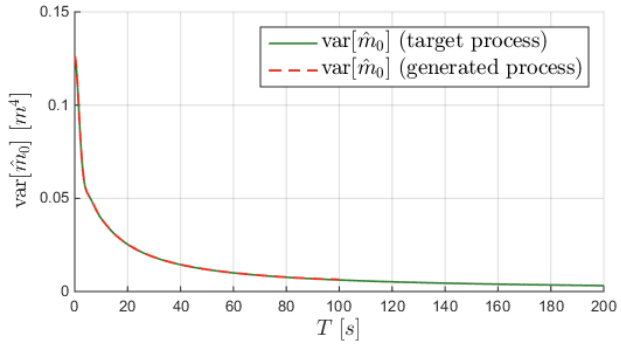

(b) $M = 50$ ($\Delta f = 0.01$)

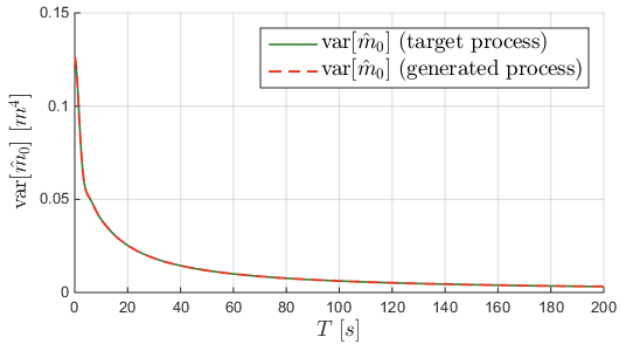

(c) $M = 100$ ($\Delta f = 0.005$)

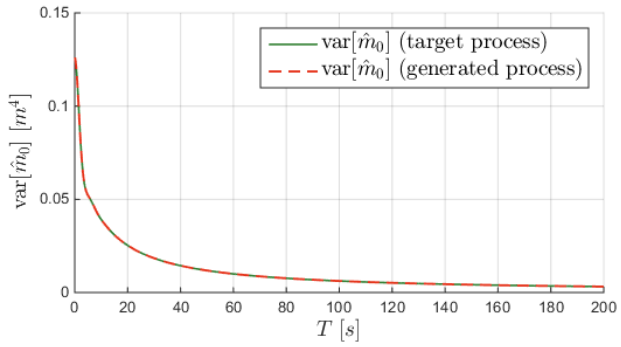

(d) $M = 200$ ($\Delta f = 0.0025$)

Figure 3.13: var[$\hat{m}_0$], for different estimation intervals T, for the target wave process *vs* the process generated through the HRA method (using the same M values as in Fig. 3.12). For the generated process, var[$\hat{m}_0$] is only shown for relevant values of T, i.e. for $T \leq 1/\Delta f$. The target spectrum is the one of Fig. 3.1a.

the finite-length variance estimator, calculated over a part or the totality of the generated signal, presents variations with respect to m_0, which are representative of the variations which would be observed using actual wave records.

3.3.2 HDA

3.3.2.1 Law of the generated process

Unlike the HRA method, the signal generated through the HDA method is not Gaussian, or, more precisely, only tends to a Gaussian process as Δf tends to zero (or equivalently as M tends to infinity), see [87], cited in [65]. Based on Eq. (3.22), the simplest way to verify the non-Gaussianity of the distribution is to note that y is bounded by the sum of $A_k, k \in \{1...M\}$: in other words, the probability that

$$y > \sum_{k=0}^{M} \sqrt{2\nu_k} \tag{3.56}$$

is zero while, in theory, a non-degenerate Gaussian random variable is not bounded.

Although the signal generated using the HDA method is non-Gaussian, its ACF can be calculated as in Eq. (3.24), yielding the very same result as Eq. (3.25):

$$R_{yy}(\tau) = \sum_{k=0}^{M} S_{\eta\eta}(k\Delta f)\cos(2\pi k\Delta f\tau)\Delta f \tag{3.57}$$

Therefore, the process generated through the HDA method is non-Gaussian, wide-sense stationary, and its ACF is an accurate approximation of the target ACF, when Δf is sufficiently small. Like HRA-simulated signals, the HDA method generates periodic signals, with period $1/\Delta f$.

In fact, the HDA method corresponds to a very specific subset of possible HRA realisations, in which for all k in $\{1...M\}$, $a_k^2 + b_k^2 = 2\nu_k$. Then, some of the *inter-simulation* variability is lost, a noteworthy manifestation of which is the fact that the sample signal variance, $\hat{m}_0$, of a signal generated through the HDA method, fluctuates less around m_0 than it should in the actual target sea state. In particular, when $T = 1/\Delta f$, the estimator $\hat{m}_0$ is equal to its average *at each realisation*:

$$\hat{m}_0 = \langle \hat{m}_0 \rangle = \sum_{k=0}^{M} S_{\eta\eta}(k\Delta f)\Delta f \tag{3.58}$$

which would, of course, not be the case if the signal were recorded from an actual sea state.

However, for some applications, the latter property can give the HDA method significant benefits over the HRA method. Consider, for example, a linear or non-linear system, driven by the wave elevation η. Assume that some variable x of the system is of particular interest, and that the variance of the process x must be estimated through numerical simulations. If the HRA method is used, the estimate of $\mathrm{var}[x]$ may differ considerably for each simulation (unless the simulation time is set to a large value), thus reflecting the realistic randomness of the underlying simulated wave process. Therefore, using the HRA method, a long simulation, or alternatively, a large number of short simulations, must be carried out to obtain an estimate of $\mathrm{var}[x]$ with a reasonably small confidence interval. In contrast, using the HDA method, the sample variance of each simulated signal x may present significantly less variability. Thus, a smaller number of simulations (or equivalently, a shorter simulation) may be necessary to obtain an estimate of $\mathrm{var}[x]$ with a small confidence interval. This property will be put to good use in Chapters 6 and 7 of this thesis.

Finally, it is easy to check that the generated HDA signal is ergodic, in the sense that the ACF, as evaluated through integration of $y(t)y(t+\tau)$ over $t \in [-\infty; +\infty]$ for a specific realisation, is equal to its sample-domain average given in Eq. (3.57)[1]. Nevertheless, as discussed earlier in Section 3.2, the interest of verifying the ergodicity property is more theoretical than practical.

[1] In fact, this also holds when $y(t)y(t+\tau)$ is integrated over any time interval of width multiple of $1/\Delta f$.

3.3.2.2 Variance estimator

As mentioned above below Eq. (3.58), with $T = 1/\Delta f$, the sample variance $\hat{m}_0$ of each HDA-generated signal is equal to its average $\langle \hat{m}_0 \rangle$. In this subsection, it is investigated how the variability of $\hat{m}_0$ is affected in the more general case where $T \leq 1/\Delta f$.

Assume that Δf is chosen small enough to allow for an accurate SDF discretisation. Assume that m_0 is estimated based on the generated signal, y:

$$\hat{m}_0 = \frac{1}{T}\int_0^T y(t)^2 dt \tag{3.59}$$

Identically to the case of the HRA method, Eq. (3.34) can be written, and the same five cases described for the quadruple sum can be analysed separately. Cases 1 through 4 (whereby $|k|, |l|, |m|, |n|$ are not all identical) yield the very same results as for the HRA case. However, due to the variables υ_k being non-Gaussian, Case 5 ($|k| = |l| = |m| = |n|$) must be revisited as follows:

Case 5

$|k| = |l| = |m| = |n|$.

Sub-case 5a

Three indices (say k, l, m) are equal, while the fourth index (say n) is equal to $-k$. Then, writing υ_k in polar form as $\upsilon_k = A_k e^{i\varphi_k}$, with $A_k = \sqrt{2\nu_k}$ and φ_k uniformly distributed in $[0; 2\pi]$:

$$\begin{aligned} \langle \upsilon_k \upsilon_l^* \upsilon_m \upsilon_n^* \rangle &= \langle \upsilon_k \upsilon_k^* \upsilon_k \upsilon_k \rangle \\ &= A_k^4 \langle e^{2i\varphi_k} \rangle \\ &= 0 \end{aligned} \tag{3.60}$$

since $\langle e^{2i\varphi_k} \rangle = 0$.

Sub-case 5b

$k = m$, $l = n = -k$:

$$\begin{aligned} \langle \upsilon_k \upsilon_{-k}^* \upsilon_k \upsilon_{-k}^* \rangle &= \langle (\upsilon_k \upsilon_k^*)^2 \rangle \\ &= A_k^4 \\ &= 4\nu_k^2 \end{aligned} \tag{3.61}$$

In addition,

$$\Lambda[\pi(f_k - f_l)T]\Lambda[\pi(f_m - f_n)T] = \Lambda[\pi(f_k - f_{-k})T]\Lambda[\pi(f_k - f_{-k})T] = \Lambda[2\pi f_k T]^2 \tag{3.62}$$

Sub-case 5c

$k = l$ and $m = n = -k$, or $k = l = m = n$. Then, as for Sub-case 5b:

$$\begin{aligned} \langle \upsilon_k \upsilon_k^* \upsilon_k \upsilon_k^* \rangle &= A_k^4 \\ &= 4\nu_k^2 \end{aligned} \tag{3.63}$$

In addition,

$$\Lambda[\pi(f_k - f_l)T]\Lambda[\pi(f_m - f_n)T] = \Lambda[\pi(f_k - f_k)T]\Lambda[\pi(f_k - f_k)T] = 1 \tag{3.64}$$

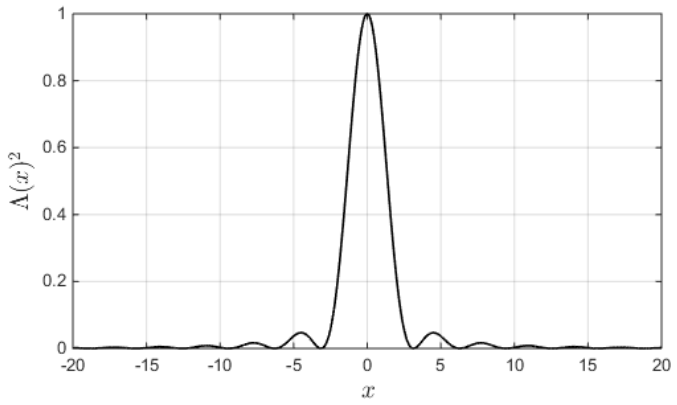

Figure 3.14: Function $\Lambda(x)^2$

Finally, splitting the sum in Eq. (3.34) in terms of all cases and sub-cases yields:

$$\mathrm{var}[\hat{m}_0] = \frac{1}{2}\sum_{k=-M}^{M}\sum_{l=-M}^{M} \nu_k \nu_l \Lambda[\pi(f_k - f_l)T]^2 - \frac{1}{4}\sum_{k=-M}^{M} \nu_k^2 \Lambda[2\pi f_k T]^2 - \frac{1}{2}\sum_{k=-M}^{M} \nu_k^2 \tag{3.65}$$

which differs from Eq. (3.53) by the subtraction of positive terms. The double sum represents the 'correct' variability (which would be obtained using the HRA method), while the two other sums represent the 'missing' variability.

Thus, as expected, the m_0 estimator presents less variance with the HDA method, than with the HRA method: from one realisation to the next, $\hat{m}_0$ varies less than it should around $\langle \hat{m}_0 \rangle$. In particular, when $T = 1/\Delta f$, $\Lambda[\pi(f_k - f_l)T]^2 = \delta(k-l)$, so that Eq. (3.65) yields $\mathrm{var}[\hat{m}_0] = 0$, which shows that, as mentioned earlier in this section, the estimator $\hat{m}_0$ calculated over a periodic realisation of length $1/\Delta f$ is the same at each instance of the generated signal, and equal to

$$\langle \hat{m}_0 \rangle = \sum_{k=0}^{M} S_{\eta\eta}(f_k)\Delta f \tag{3.66}$$

Furthermore, the function $\Lambda^2[x]$ is represented in Fig. 3.14. For any x, such that $|x| \geq 5$, $\Lambda(x) \ll 1$. In addition, for the target spectrum in Fig. 3.11, and more generally for common wave spectra, the SDF, and thus ν_k, are approximately zero below some frequency in the region of 0.025-0.05 Hz. Therefore, in the second sum of Eq. (3.65), those terms corresponding to $f_k \leq 0.15$ are zero, while those for larger f_k are negligible if $2\pi f_k T \geq 5$, which is always true for $T \geq 5/(2\pi \times 0.025) \approx 30$s. Thus, for $T \geq 30$s, Eq. (3.65) can be simplified to

$$\mathrm{var}[\hat{m}_0] = \frac{1}{2}\sum_{k=-M}^{M}\sum_{l=-M}^{M} \nu_k \nu_l \Lambda[\pi(f_k - f_l)T]^2 - \frac{1}{2}\sum_{k=-M}^{M} \nu_k^2 \tag{3.67}$$

where the double sum in (3.67) is equal to $\mathrm{var}[\hat{m}_0]$ in the HRA case, and the second term represents the 'missing' variability.

With the same discretisation settings as in Figs. 3.12 and 3.13, Fig. 3.15 shows the variance of $\hat{m}_0$, for both the actual signal, calculated using (3.12), and for the signal generated through the HDA method, calculated using (3.65), with T ranging from 0 to $1/\Delta f$. It can be observed how, using the HDA method, the variability of the energy content across realisations of the signal, is significantly underestimated, going to zero for $T = 1/\Delta f$. In other words, repeatedly generating a finite-length wave signal using the HDA method, the sample variance calculated in each signal tends to be unrealistically close to m_0, even for $T < 1/\Delta f$. Estimated over $T = 1/\Delta f$, the sample variance is always identically equal to its average.

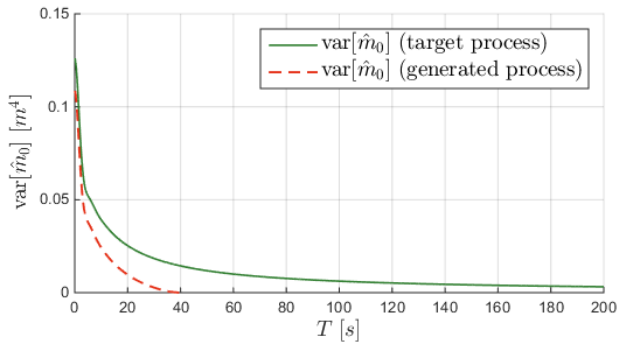

(a) $M = 20$ ($\Delta f = 0.025$)

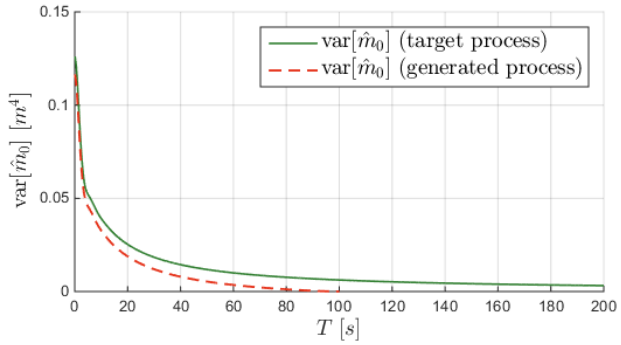

(b) $M = 50$ ($\Delta f = 0.01$)

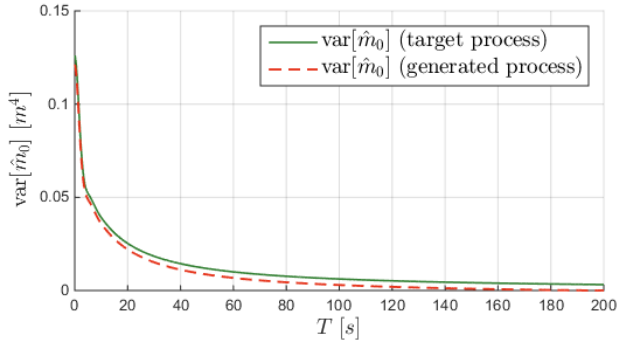

(c) $M = 100$ ($\Delta f = 0.005$)

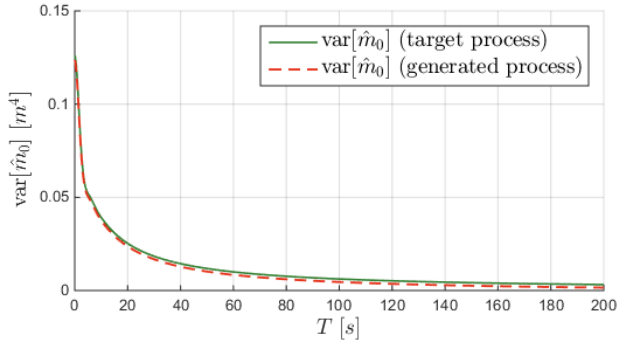

(d) $M = 200$ ($\Delta f = 0.0025$)

Figure 3.15: var[$\hat{m}_0$], for different estimation intervals T, for the target wave process *vs* the process generated through the HDA method (using the same M values as in Fig. 3.12). For the generated process, var[$\hat{m}_0$] is only shown for relevant values of T, i.e. for $T \leq 1/\Delta f$. The target spectrum is the one of Fig. 3.1a.

3.4 Non-harmonic superposition methods

It follows from the preceding section that the HRA method realistically reproduces the statistical properties of a finite-length wave signal recorded in the target wave spectrum, except for the periodicity issue, which arises only when the simulated duration T approaches $1/\Delta f$. However, even with $T = 1/\Delta f$, the properties of the (arguably) most important statistic, $\hat{m}_0$, remain realistic, in as much as $\hat{m}_0$ presents appropriate variability across simulations. In contrast, the HDA method certainly has realistic properties in terms of ACF functions, but does not yield a Gaussian signal. Furthermore, the variability of the HDA signal statistics across simulations is not well represented, with $\hat{m}_0$ presenting unrealistically small variability. However, the latter point can also be an advantage to obtain estimates with a small confidence interval, using only a small number of simulations.

In spite of the above, which supports the fact that harmonic superposition methods are appropriate for simulating a Gaussian sea, some authors have introduced non-harmonic (NH) WS methods, to avoid periodicity in the generated signal. Non-harmonic methods rely on a discretisation of the target spectrum, whereby the frequencies are not evenly spaced. In the so-called equal area (EA) method, the frequency range is discretised into intervals with equal spectral energy - see, for example, [80], Chapter 11 of [83], or more recently [84]. In the random perturbation (RP) method, the frequency range is primarily discretised harmonically, but at each realisation, each frequency is shifted by a small random perturbation, as proposed in [67, 81], of magnitude $d_f \ll \Delta f$. The RP approach supposedly "eliminates" the "deficiency" of self-repetition [65]. Both EA and RP approaches can be generated using a random amplitude variant (EARA, resp. RPRA) or a deterministic amplitude variant (EADA, resp. RPDA), although, for the RP method, deterministic amplitudes are used in [81] and [67].

Non-harmonic methods should, according to their supporters, generate arbitrarily long, non-periodic signals, with a small number of frequency components. The issue pointed out in [65] for NH discretisation is that the FFT algorithm cannot be used to generate sample wave signals (because of the non-harmonic frequency discretisation); however, computation time is unlikely to be an issue with modern computers. This section shows that NH discretisation methods present a more significant drawback, which is that the ACF of the generated signals may differ from the target ACF. The consequences of the mismatch between the NH-generated and the target statistical properties have been experimentally observed, for example in [71], [88] and [82]. The present section provides theoretical insight to support the empirical observations of [71, 82, 88].

3.4.1 The equal-area method

3.4.1.1 Law of the generated process

Let us define the cut-off frequency f_c, such that $S_{\eta\eta}(f)$ is considered to be zero for all $f \geq f_c$. In the equal-area (EA) method, the interval $[0; f_c]$ is divided into M intervals $I_k, k \in [1; M]$, chosen such that all the intervals define the same area ΔE under the spectrum:

$$\forall k \in [1;M], \int_{I_k} S_{\eta\eta}(f)df = \Delta E = \frac{1}{M}\int_0^{f_c} S_{\eta\eta}(f)df \tag{3.68}$$

Fig. 3.16 illustrates the equal-area discretisation of the wave spectrum, for $M = 20$. The area under each yellow bar is equal do ΔE.

For all k, define f_k as the middle point of the interval I_k, and $\nu_k = \Delta E$. Then, similarly to Eqs. (3.19) and (3.21), the signal is generated as

$$y(t) = \frac{1}{2}\sum_{k=-M}^{M} \upsilon_k e^{-2i\pi f_k t} \tag{3.69}$$

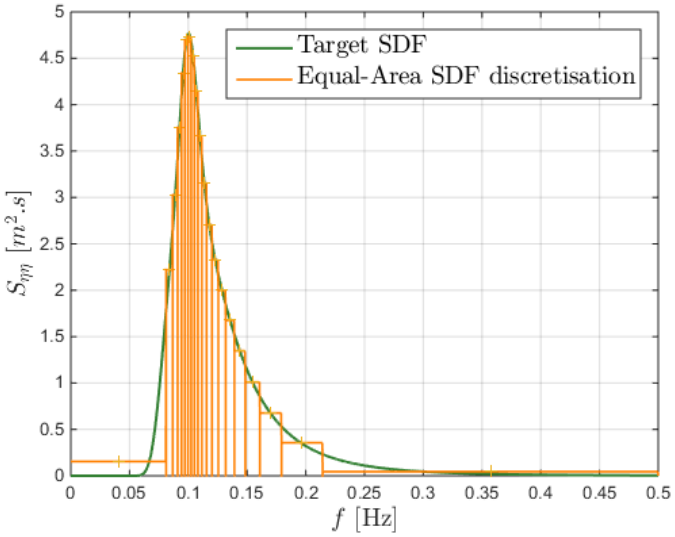

Figure 3.16: Spectrum discretisation for the equal-energy method, with $M = 20$.

Both random-amplitude and deterministic-amplitude methods may be used to generate time series from the equal area discretisation:

- In the EARA variant, for $k \geq 0$, $\upsilon_k = a_k + ib_k$, where a_k and b_k are independent, Gaussian random variables with variance ν_k, and $\upsilon_{-k} = \upsilon_k^*$. Similarly to the HRA case, the resulting process is Gaussian.

- In the EADA variant, for $k \geq 0$, $\upsilon_k = \sqrt{2\nu_k}e^{-i\varphi_k}$ and $\upsilon_{-k} = \upsilon_k^*$, where φ_k is uniformly distributed in $[0; 2\pi]$. Similarly to the HDA case, the resulting process is non-Gaussian.

With both EARA and EADA variants, it is possible to compute the ACF of the generated signal, identically to the calculations in Eq. (3.24):

$$R_{yy}(\tau) = \sum_{k=0}^{M} \nu_k \cos(2\pi f_k \tau) \tag{3.70}$$

Since $\nu_k = \Delta E$,

$$R_{yy}(\tau) = \Delta E \sum_{k=0}^{M} \cos(2\pi f_k \tau) \tag{3.71}$$

which can be reformulated as

$$R_{yy}(\tau) = \sum_{k=0}^{M} S_k \cos(2\pi f_k \tau) \Delta f_k \tag{3.72}$$

where Δf_k is the width of I_k and $S_k = \Delta E / \Delta f_k$ is the average value of the SDF in the interval I_k.

Although, from Eq. (3.72), $R_{yy}(\tau)$ may be seen as a Riemann approximation of Eq. (3.4), from Eq. (3.71) it can be seen that all sinusoidal components have equal amplitude, and thus $R_{yy}(\tau)$ does not fade out to zero as it should if the target ACF were actually matched. As a result, the ACF can be significantly distorted, as shown in Fig. 3.17, if the number of components is not chosen large enough. By increasing M, the amplitude of the unwanted oscillations observed in the ACF is reduced; however, a relatively large M is necessary for the ACF to be 'small enough': in Fig. 3.17, $M = 100$ seems to be an appropriate compromise. However, the main benefit of using the EARA approach, which is the use of fewer frequency components than the HRA method, to

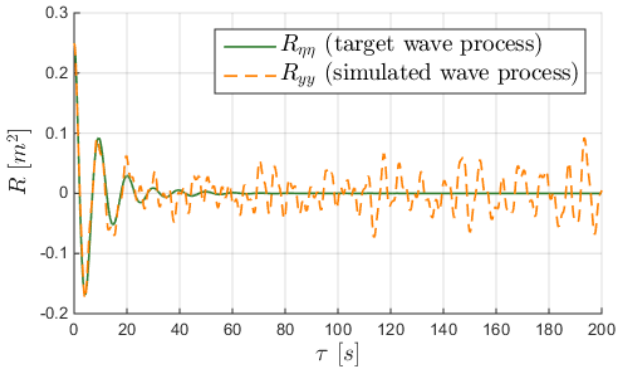

(a) $M = 20$

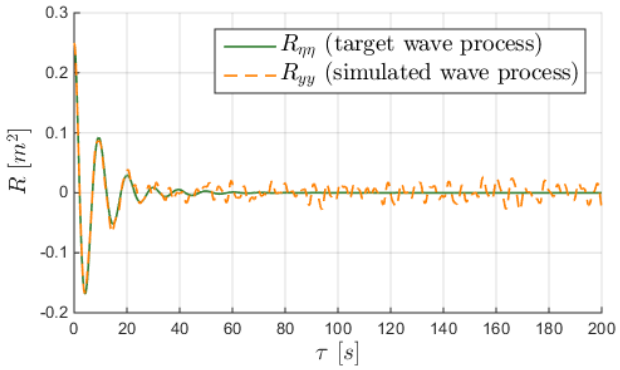

(b) $M = 50$

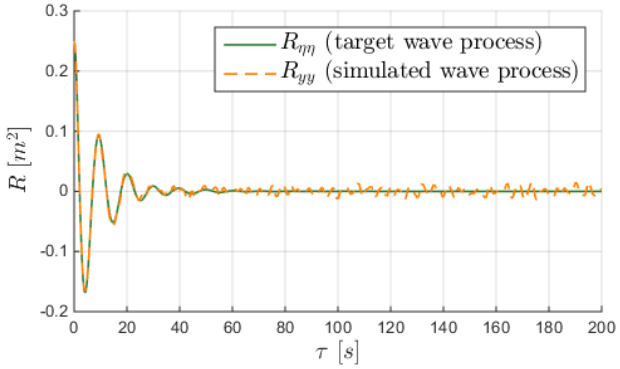

(c) $M = 100$

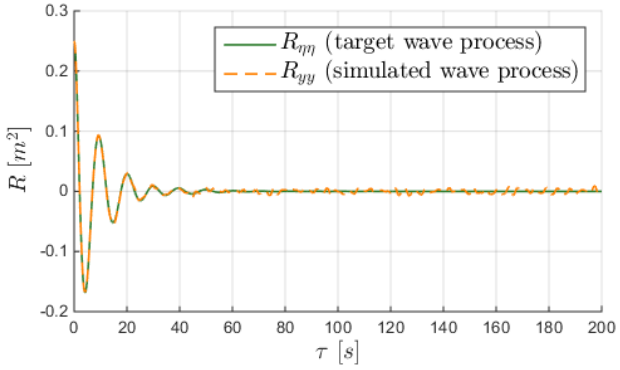

(d) $M = 200$

Figure 3.17: $R_{\eta\eta}$ *vs* R_{yy}, for the spectrum of Fig. 3.1a, using the EARA or EADA methods with various numbers of frequency components.

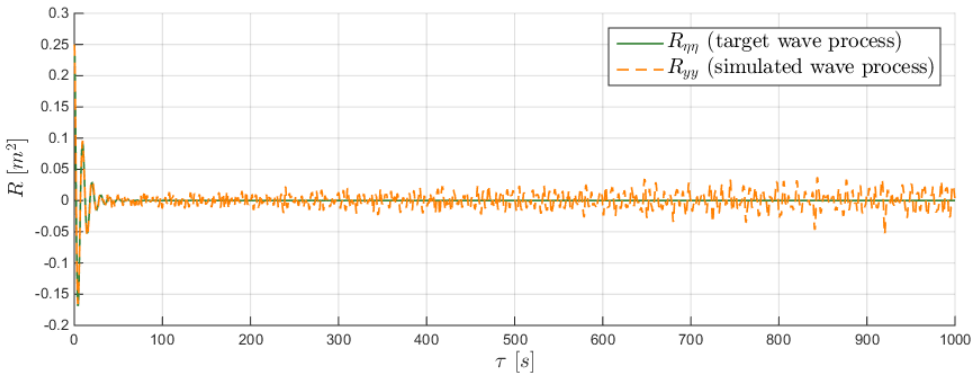

Figure 3.18: $R_{\eta\eta}$ *vs* R_{yy}, for the spectrum of Fig. 3.1a, using the EARA or EADA methods, with $M = 100$ and large simulation time.

generate an arbitrarily long signal, is not evident, since with the HRA method, $M \approx 100$ is also a suitable choice.

Furthermore, the amplitude of the unwanted ACF oscillations tends to grow for larger lag values, as shown in Fig. 3.18 with $M = 100$. Therefore, it is definitely not true to say that the EA discretisation allows the simulation of arbitrarily long signals with the target ACF properties.

Finally, note that the unwanted oscillations of the ACF, observed in Fig. 3.17, and obtained from theoretical calculations, correspond to the ones experimentally pointed out in [82].

3.4.1.2 Variance estimator

In the following calculations, it is examined whether the distortion of the ACF function, observed in Fig. 3.17, affects $\text{var}[\hat{m}_0]$ and makes it different from what it should be in the target wave process.

With the EARA method

The variance of the m_0 estimator, for the EARA method, is obtained using the same calculations as for the HRA case, thus yielding Eq. (3.53). Replacing ν_k in Eq. (3.53), with its expression ΔE, yields:

$$\begin{aligned} \text{var}[\hat{m}_0] &= \frac{1}{2}\Delta E^2 \sum_{k=-M}^{M} \sum_{l=-M}^{M} \Lambda[\pi(f_k - f_l)T]^2 \\ &= \frac{1}{2} \sum_{k=-M}^{M} \sum_{l=-M}^{M} S_{\eta\eta}(f_k) S_{\eta\eta}(f_l) \Lambda[\pi(f_k - f_l)T]^2 \Delta f_k \Delta f_l \end{aligned} \tag{3.73}$$

Again, the above expression is an approximation of Eq. (3.14). For a given number of components M, the approximation (3.73) is more accurate than with equally-spaced frequencies. This can be verified in Fig. 3.19a: even with $M = 20$, $\text{var}[\hat{m}_0]$ almost perfectly matches that, which should be obtained from the target wave process, while with the same M, the HRA method (Fig. 3.13a) yields an inaccurate $\text{var}[\hat{m}_0]$.

However, in Eq. (3.73), all terms tend to zero with $1/T^2$ with T increasing, except for $k = l$. Therefore, $\text{var}[\hat{m}_0]$ tends to $M\Delta E^2 = m_0^2/M$, when T tends to infinity, instead of going to zero following a law in $1/T$. Thus, for large T values, $\text{var}[\hat{m}_0]$ tends to be overestimated, although the influence of this residual value is not visible for the relatively small time durations shown in Fig. 3.19. In other words, repeatedly generating long signals using the EARA method, and calculating

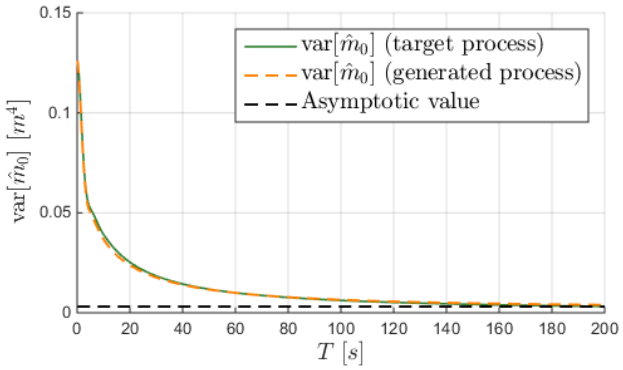

(a) $M = 20$

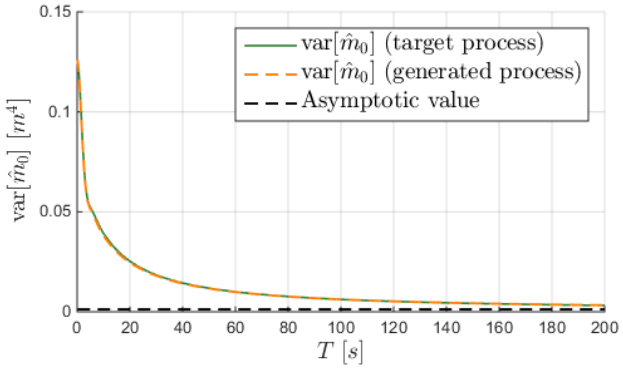

(b) $M = 50$

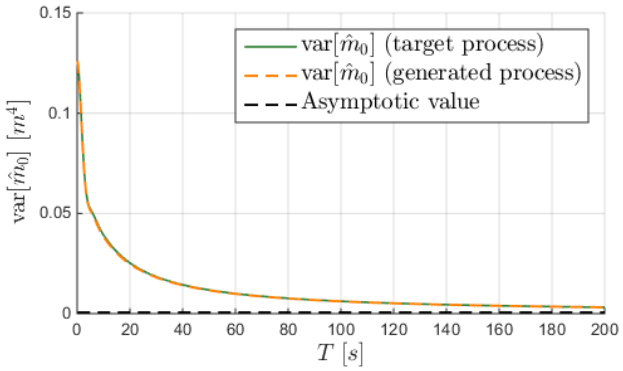

(c) $M = 100$

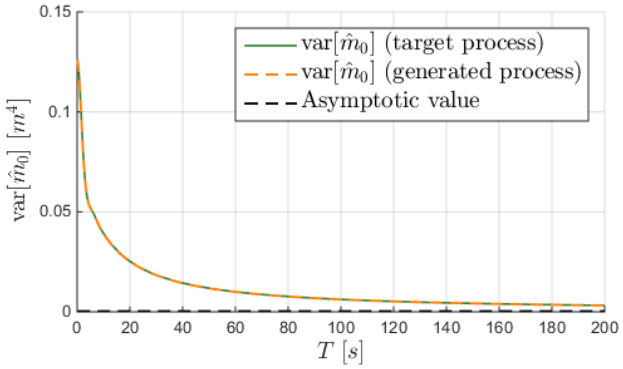

(d) $M = 200$

Figure 3.19: var[$\hat{m}_0$], for different estimation intervals T, for the target wave process *vs* the process generated through the EARA method (using various M values). The target spectrum is the one of Fig. 3.1a.

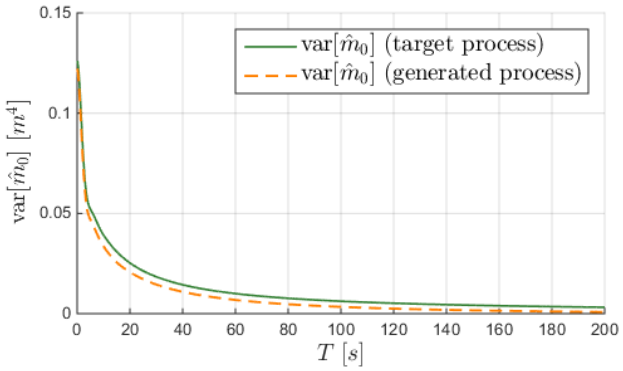

(a) $M = 20$

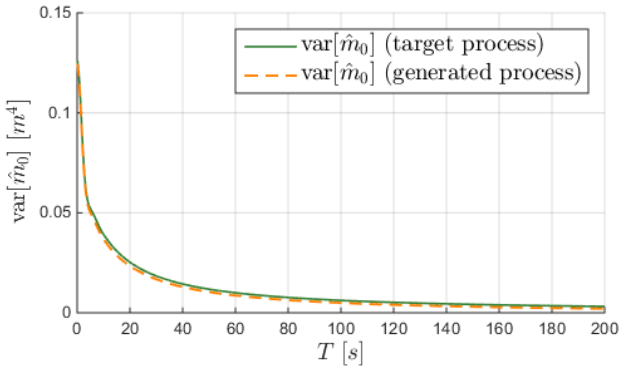

(b) $M = 50$

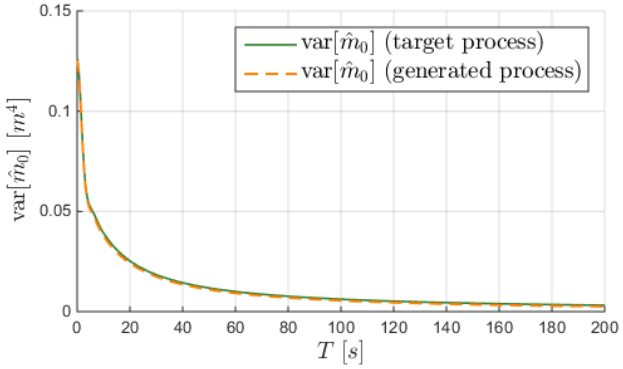

(c) $M = 100$

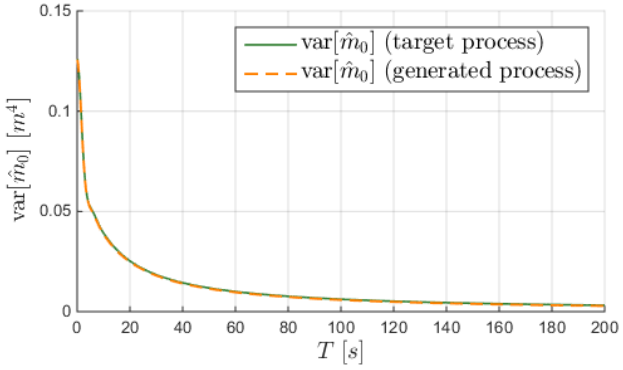

(d) $M = 200$

Figure 3.20: $\mathrm{var}[\hat{m}_0]$, for different estimation intervals T, for the target wave process *vs* the process generated through EADA (using various M values). The target spectrum is that of Fig. 3.1a.

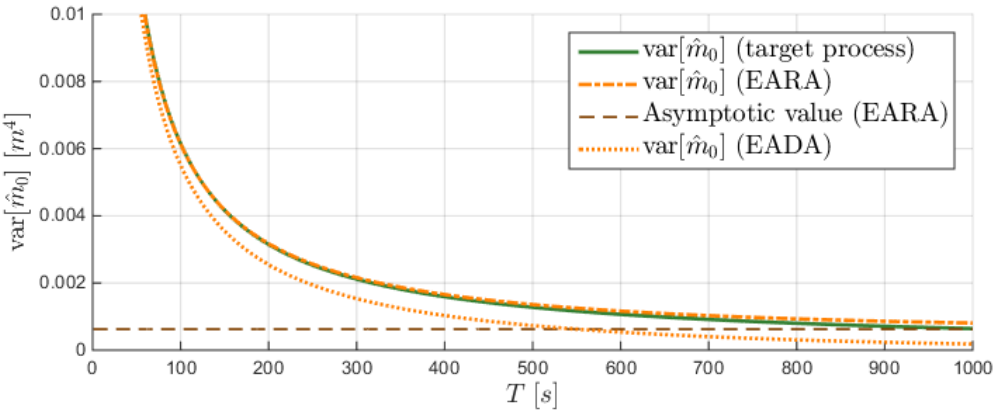

Figure 3.21: var[$\hat{m}_0$], for long estimation intervals T, for the target wave process *vs* the process generated through EARA and EADA methods, with $M = 100$. The target spectrum is that of Fig. 3.1a.

$\hat{m}_0$ in each of them, the observed fluctuations of $\hat{m}_0$ around $\langle \hat{m}_0 \rangle$ would tend to be unrealistically large. The magnitude of the overestimation decreases with $1/M$.

With the EADA method

The variance of the m_0 estimator, for the EADA method, is obtained using the same calculations as for the HDA case, thus yielding Eq. (3.65). Using $\nu_k = \Delta E$ yields:

$$\text{var}[\hat{m}_0] = \frac{1}{2}\Delta E^2 \sum_{k=-M}^{M} \sum_{l=-M}^{M} \Lambda[\pi(f_k - f_l)T]^2 - \frac{1}{4}\Delta E^2 \sum_{k=-M}^{M} \Lambda[2\pi f_k T]^2 - M\Delta E^2 \tag{3.74}$$

Similarly to Eq. (3.67), for $T \geq 30$s, and using $\Delta E = m_0/M$, Eq. (3.74) can be further simplified into

$$\text{var}[\hat{m}_0] = \Delta E^2 \sum_{k=-M}^{M} \sum_{l=-M}^{M} \Lambda[\pi(f_k - f_l)T]^2 - \frac{m_0^2}{M} \tag{3.75}$$

In Eq. (3.75), the first sum represents var[$\hat{m}_0$] as obtained with the EARA method. For large T, the double sum tends to m_0^2/M with $1/T^2$, so that var[$\hat{m}_0$] tends to zero with $1/T^2$. The law in $1/T^2$ (instead of $1/T$) implies that, for large T values, var[$\hat{m}_0$] is necessarily underestimated with respect to the correct value. However, as can be appreciated in Fig. 3.20, the inaccurate asymptotic behaviour does not have any visible effect for $T \leq 200$s. In fact, for $T \leq 200$s, var[$\hat{m}_0$] is clearly more realistic with the EADA method, than it is with the HDA method (Fig. 3.15): for an identical number of components M, the m_0 estimator from EADA signals presents more realistic variations than that from HDA signals.

The asymptotic behaviour of var[$\hat{m}_0$] is examined in more detail in Fig. 3.21, for $M = 100$ components. With the EARA method, the estimator variance var[$\hat{m}_0$] becomes more and more distinct from the target estimator variance as T approaches 1000s, because, with the EARA method, var[$\hat{m}_0$] tends to the asymptotic value, m_0^2/M, while the correct var[$\hat{m}_0$] continues to decrease to 0 with $1/T$. However, it is only for large T ($T \approx 1000$s) that var[$\hat{m}_0$] from EARA simulations becomes incorrect. With the EADA method, var[$\hat{m}_0$] tends to 0 as $1/T^2$, resulting in visible underestimation of var[$\hat{m}_0$] with respect to the target value.

Overall, the benefits of using the EA discretisation method, over harmonic discretisation, are not clear. Certainly, the signals generated through the EARA or EADA methods are not periodic, which avoids the strict limitation of $T \leq 1/\Delta f$ on the signal duration, resulting from the HRA and HDA approaches. However, the ACF of the generated EARA or EADA signals is distorted

with respect to the target ACF, over the complete span of the generated signal. This contrasts with the HRA and HDA methods, whereby choosing T small enough with respect to $1/\Delta f$ guarantees that the target ACF is accurately approximated over the whole length of the simulation. The spurious correlation, observed in the generated EARA and EADA signals, may induce errors into the statistical analysis of simulation results.

Using either EARA or EADA methods, with a relatively small number of components M, the variability of the finite-duration m_0 estimator is realistically reproduced for relatively small T - which is not the case for the HDA method. However, as discussed in Section 3.3, the possibility of generating signals which all have the same variance can also be seen as a benefit of the HDA method. Furthermore, as shown by the incorrect asymptotic behaviour of $\mathrm{var}[\hat{m}_0]$, it is certainly not true to say that EARA or EADA methods allow for the simulation of arbitrarily long wave signals, using a small number of frequency components, without inducing statistical inaccuracies.

Even if a relatively small number of components could be used to generate long wave signals using EA methods, it should also be noted that, for each wave spectrum, the EA discretisation involves accurate integration of the spectrum in order to build equal-area frequency intervals. Furthermore, EA implies that the set of frequencies differs for each spectrum, which may complicate the frequency-domain analysis of wave-driven dynamical systems.

In summary, especially in applications where simulations must be carried out from a variety of wave spectra, the apparent benefits of the EA discretisation method are probably more than offset by the possible inaccuracies in the ACF function, and by the time-consuming spectrum discretisation procedure.

3.4.2 The random-perturbation method

3.4.2.1 Law of the generated signal

Define $f_k = k\Delta f$, with $\Delta f = f_c/M$, as for the harmonic superposition methods presented in Section 3.3. With the RP method, the signal y is generated as

$$y(t) = \frac{1}{2}\sum_{k=-M}^{M} \upsilon_k e^{-2i\pi f'_k t} \tag{3.76}$$

where $\upsilon_k = a_k + ib_k$ have either random or deterministic amplitude, and f'_k is randomly generated as $f'_k = f_k + \varepsilon_k$, where the ε_k are independently generated random perturbations, following a uniform distribution in $[-d_f, d_f]$, where d_f is a parameter chosen by the user. The authors who introduced the RP method [81] recommend choosing $d_f \ll \Delta f$.

$y(t)$ may be reformulated as

$$y(t) = \frac{1}{2}\sum_{k=-M}^{M} \tilde{\alpha}_k(t) e^{2i\pi f_k t} \tag{3.77}$$

where $\tilde{\alpha}_k(t) = \upsilon_k e^{-2i\pi\varepsilon_k t}$. This time, even if the coefficients υ_k have random amplitudes, $y(t)$ cannot be proven to be Gaussian, because terms of the form $\cos(\varepsilon_k t)$ or $\sin(\varepsilon_k t)$ are not Gaussian. However, the ACF of the generated signal can be computed:

$$\langle y(t)y^*(t+\tau)\rangle = \frac{1}{4}\sum_{k=-M}^{M}\sum_{l=-M}^{M} \langle \tilde{\alpha}_k(t)\tilde{\alpha}_l^*(t+\tau)\rangle e^{-2i\pi f_k t} e^{2i\pi f_l (t+\tau)} \tag{3.78}$$

The above sum can be examined under three cases:

1. For $|k| \neq |l|$, $\tilde{\alpha}_k(t)$ and $\tilde{\alpha}_l(t+\tau)$ are independent, so that

$$\langle \tilde{\alpha}_k(t)\tilde{\alpha}_l^*(t+\tau)\rangle = \langle \tilde{\alpha}_k(t)\rangle \langle \tilde{\alpha}_l^*(t+\tau)\rangle = 0 \tag{3.79}$$

2. For $k = -l$, using independence of υ_k and $e^{-2i\pi\varepsilon_k t}$ and $\langle\alpha_k^2\rangle = 0$:

$$\langle\tilde{\alpha}_k(t)\tilde{\alpha}_l^*(t+\tau)\rangle = \langle\tilde{\alpha}_k(t)\tilde{\alpha}_k(t+\tau)\rangle = \langle\alpha_k^2\rangle\langle e^{-2i\pi\varepsilon_k t}e^{-2i\pi\varepsilon_k(t+\tau)}\rangle = 0 \tag{3.80}$$

3. For $k = l$, using independence of υ_k and $e^{-2i\pi\varepsilon_k t}$ and $\langle\upsilon_k\upsilon_k^*\rangle = 2\nu_k$:

$$\langle\tilde{\alpha}_k(t)\tilde{\alpha}_l^*(t+\tau)\rangle = 2\nu_k\langle e^{2i\pi\varepsilon_k\tau}\rangle \tag{3.81}$$

Recalling that ε_k is uniformly distributed in $[-d_f; d_f]$, it can be easily calculated that

$$\langle e^{2i\pi\varepsilon_k\tau}\rangle = \frac{\sin(2\pi d_f\tau)}{2\pi d_f\tau} \tag{3.82}$$

Finally,

$$\langle y(t)y^*(t+\tau)\rangle = \frac{1}{2}\sum_{k=-M}^{M}\nu_k\frac{\sin(2\pi d_f\tau)}{2\pi d_f\tau}e^{2i\pi f_k\tau} \tag{3.83}$$

which only depends on τ. Therefore y is wide-sense stationary, and its ACF is

$$R_{yy}(\tau) = \frac{\sin(2\pi d_f\tau)}{2\pi d_f\tau}\sum_{k=0}^{M}S_{\eta\eta}(f_k)\cos(2\pi f_k\tau)\Delta f \tag{3.84}$$

Eq. (3.84) is equal to the ACF of Eq. (3.25), obtained through harmonic superposition, modulated by the function $\Lambda(2\pi d_f\tau)$. Three cases may be considered:

- If, as advocated in [81], $d_f \ll \Delta f$, then $\Lambda(2\pi d_f\tau) \approx 1$ for $\tau \leq 1/\Delta f$, and therefore $R_{yy}(\tau)$ remains the same as for the case of harmonic superposition, as seen in Fig. 3.22b. Thus, it is illusory to think that RP circumvents the issue of self-repetition.
- If $d_f \gg \Delta f$, then $R_{yy}(\tau)$ is significantly affected for τ well within $[0; 1/\Delta f]$, as seen in Fig. 3.22d.
- More interesting is the case where d_f is set to a reasonable compromise, such that $\Lambda(2\pi d_f\tau) \approx 1$ over the correlation length of the target signal, but $\Lambda(2\pi d_f\tau)$ is sufficiently close to zero for $\tau \geq 1/\Delta f$, as in Fig. 3.22c.

3.4.2.2 Variance estimator

As for HRA or HDA methods, the variance estimator can be calculated as:

$$\hat{m}_0 = \frac{1}{4}\sum_{k=-M}^{M}\sum_{l=-M}^{M}\upsilon_k\upsilon_l^*\Lambda[\pi(f_k' - f_l')T] \tag{3.85}$$

However, this time, $(f_k' - f_l') = (f_k - f_l) + (\varepsilon_k - \varepsilon_l)$ is, in fact, a random variable, so that $\Lambda[\pi(f_k' - f_l')T]$ is a random variable as well, rather than a deterministic quantity.

With the RPRA method

With the RPRA method, the same calculations as for the HRA method can be derived, with the exception that the deterministic terms $\Lambda(\pi(f_k - f_l))$ are replaced with random variables $\Lambda(\pi(f_k' - f_l'))$. The following expression is obtained:

$$\mathrm{var}[\hat{m}_0] = \frac{1}{2}\sum_{k=-M}^{M}\sum_{l=-M}^{M}\nu_k\nu_l\langle\Lambda[\pi(f_k' - f_l')T]^2\rangle \tag{3.86}$$

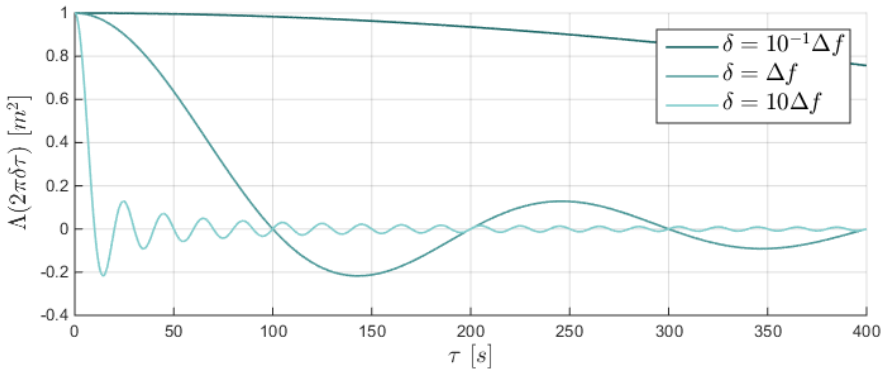

(a) $\Lambda(2\pi d_f \tau)$

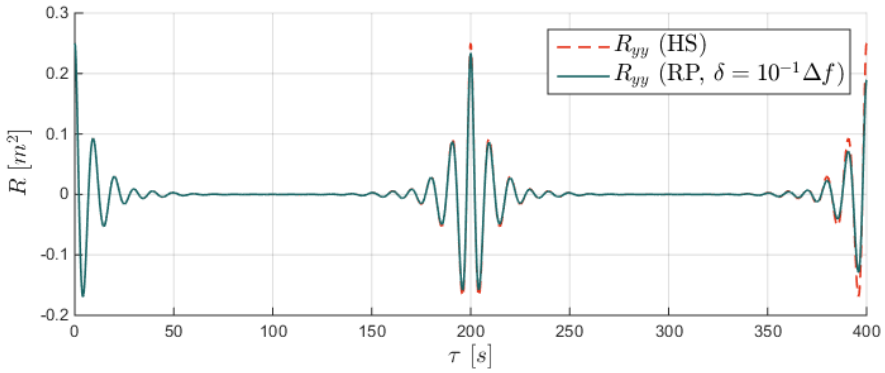

(b) $d_f = 0.1\Delta f$

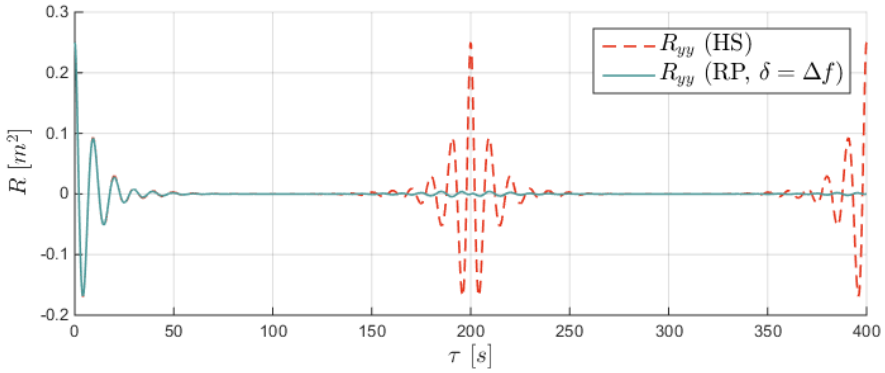

(c) $d_f = \Delta f$

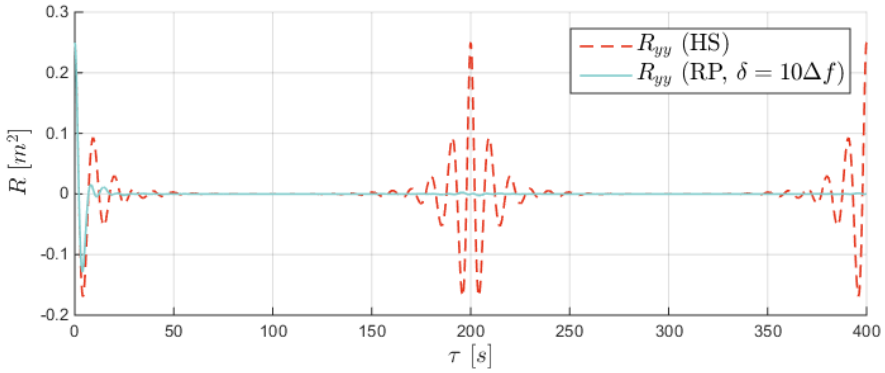

(d) $d_f = 10\Delta f$

Figure 3.22: $R_{\eta\eta}$ *vs* R_{yy}, for the spectrum of Fig. 3.1a, using RPRA or RPDA methods, with $M = 100$ and three different values for d_f.

Eq. (3.86), because of the terms in $\langle\Lambda[\pi(f'_k - f'_l)T]^2\rangle$, cannot be calculated analytically, and is thus less straightforward to analyse than Eqs. (3.53) and (3.73). However, for all $k \neq l$, $\langle\Lambda[\pi(f'_k - f'_l)T]^2\rangle$ is bounded above as follows:

$$0 \leq \langle\Lambda[\pi(f'_k - f'_l)T]^2\rangle \leq \langle\frac{1}{(\pi(f'_k - f'_l)T)^2}\rangle \tag{3.87}$$

Therefore, $\mathrm{var}[\hat{m}_0]$ can be bounded as follows:

$$\frac{1}{2}\sum_{k=-M}^{M}\nu_k^2 \leq \mathrm{var}[\hat{m}_0] \leq \frac{1}{2}\sum_{k=-M}^{M}\nu_k^2 + \frac{1}{T^2}\frac{1}{2}\sum_{k=-M}^{M}\sum_{\substack{l=-M \\ l\neq k}}^{M}\nu_k\nu_l\langle\frac{1}{(\pi(f'_k - f'_l))^2}\rangle \tag{3.88}$$

Replacing ν_k with $S_{\eta\eta}(f_k)\Delta f$ shows that $\mathrm{var}[\hat{m}_0]$ tends to $\sum_{k=0}^{M} S_{\eta\eta}(f_k)^2\Delta f^2$ as at least $1/T^2$. Therefore, similarly to the EARA method, $\mathrm{var}[\hat{m}_0]$ is overestimated for large T values.

With the RPDA method

With the RPDA method, the same calculations as for the HDA case can be derived, with the exception that the deterministic terms $\Lambda(\pi(f_k - f_l))$ are replaced with random variables $\Lambda(\pi(f'_k - f'_l))$. The following expression is obtained:

$$\mathrm{var}[\hat{m}_0] = \frac{1}{2}\sum_{k=-M}^{M}\sum_{l=-M}^{M}\nu_k\nu_l\langle\Lambda[\pi(f'_k - f'_l)T]^2\rangle - \frac{1}{4}\sum_{k=-M}^{M}\nu_k^2\langle\Lambda[2\pi f'_k T]^2\rangle - \frac{1}{2}\sum_{k=-M}^{M}\nu_k^2 \tag{3.89}$$

Using the same bounds as for the RPRA case, it is found that

$$0 \leq \mathrm{var}[\hat{m}_0] \leq \frac{1}{T^2}\frac{1}{2}\sum_{k=-M}^{M}\sum_{\substack{l=-M \\ l\neq k}}^{M}\nu_k\nu_l\langle\frac{1}{(\pi(f'_k - f'_l))^2}\rangle \tag{3.90}$$

so that $\mathrm{var}[\hat{m}_0]$ tends to zero in at least $1/T^2$. Therefore, similarly to the EADA method, $\mathrm{var}[\hat{m}_0]$ tends to be underestimated for large T values.

Given the fact that, for both RPRA and RPDA methods, $\mathrm{var}[\hat{m}_0]$ cannot be obtained analytically, numerical RPRA and RPDA simulations are run to obtain empirical estimates of $\mathrm{var}[\hat{m}_0]$ for various estimation intervals, with $M = 100$s and $d_f = \Delta f$. The results are shown in Fig. 3.23, and confirm that, with the RPRA method, $\mathrm{var}[\hat{m}_0]$ tends to the predicted asymptotic value with $1/T^2$ while, with the RPDA method, $\mathrm{var}[\hat{m}_0]$ tends to zero with $1/T^2$, i.e. faster than $\mathrm{var}[\hat{m}_0]$ from the correct signal. Therefore, the qualitative behaviour is the same for the EARA and RPRA methods (resp. the EADA and RPDA methods), but the magnitude of the inaccuracies is greater for the RP method than for the EA method, in spite of an identical number of components $M = 100$.

Overall, using RP methods, it is possible to avoid the generation of periodic signals, and to make the ACF of the generated signal fade out to zero, without increasing the number of frequency components. To obtain such a result, and in contrast to the commonly advocated procedure, the parameter d_f, which governs the magnitude of the random frequency perturbation, should not be set to a value smaller than Δf, but instead equal to or larger than Δf. However, d_f should not be chosen so large so as to distort the ACF over the correlation length of the target process.

In fact, RPRA and RPDA methods can be seen as variants of the harmonic superposition techniques, whereby the initial choice of complex amplitudes (υ_k, in the formalism of this chapter) is slowly phase-modulated with $e^{-2i\pi\varepsilon_k t}$, at a speed which is different, and randomly chosen, for each component k. The modulation speed, limited by the parameter d_f, must not be too slow (in which case periodicity still occurs), or too fast (in which case the short-term ACF properties of the signal are distorted).

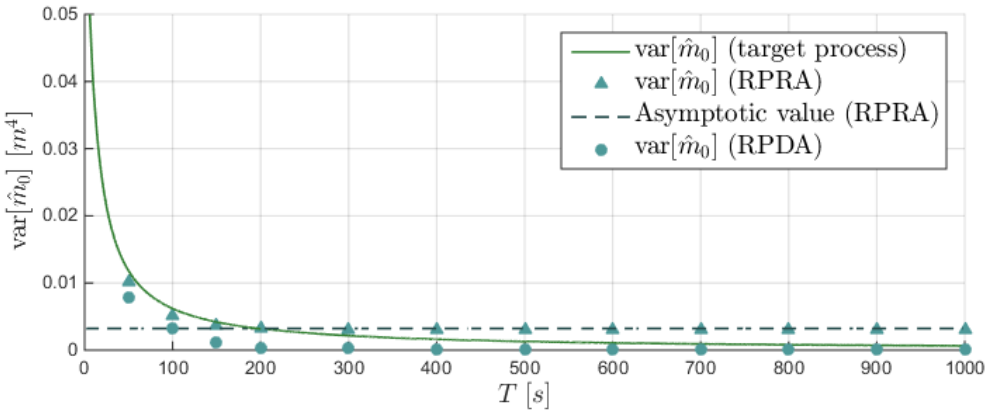

Figure 3.23: $\mathrm{var}[\hat{m}_0]$, for long estimation intervals T, for the target wave process *vs* the process generated through RPRA and RPDA methods, with $M = 100$ and $d_f = \Delta f$. For RPRA and RPDA methods, $\mathrm{var}[\hat{m}_0]$ is obtained empirically using 500 simulations. The target spectrum is that of Fig. 3.1a.

Nevertheless, for both RPRA and RPDA methods, the generated process is not Gaussian, so that a correct ACF function does not ensure that the generated signal has all the desired statistical characteristics of the target wave process. In particular, it is shown that, for time series generated with the RPRA method, the m_0 estimator presents more variability than it should as the estimation interval grows. In contrast, with the RPDA method, the variability of the m_0 estimator is under-represented. This is a particular manifestation of the generated signals not being statistically accurate simulations of the target signal. Similarly to the EADA and EARA methods, it is certainly not true to say that RPRA or RPDA methods allow for the simulation of arbitrarily long wave signals, using a small number of frequency components, without introducing statistical inaccuracy.

Furthermore, like EA, RP implies that the set of frequencies differs for each random realisation, which may both complicate the frequency-domain analysis of wave-driven dynamical systems, and constitute a significant computational burden if a large number of wave signals must be generated.

In summary, the apparent benefits of the RP discretisation method are probably more than offset by possible statistical inaccuracies, and by the time-consuming signal generation procedure.

3.5 Discussion

3.5.1 Extension to other simulated variables

This chapter is primarily focused on simulating the wave elevation η. However, the results extend, at least qualitatively, far beyond this sole variable. Consider a linear system, which is driven by the wave elevation process, and consider any output x of such a process. Define $H_{\eta x}(f)$, the complex frequency-domain transfer function which relates the wave elevation to the output of interest. Then, under the Gaussian random excitation η, x is also a Gaussian random process, with SDF given by $S_{xx}(f) = |H_{\eta x}(f)|^2 S_{\eta\eta}(f)$ [25]. Therefore, the simulation techniques applicable to any other variable related to η *via* a linear transfer function can be analysed in the same way as developed in Sections 3.2 through 3.4.

Previous work, carried out within the scope of this thesis [89], considered the specific case of a WEC, modelled as a linear system, and driven by random waves. For a linear WEC model, it is easy to show [89] that the following two procedures are statistically equivalent:

- Procedure 1: a) Generate a time series of η using any of the WS methods described above;

b) Obtain the steady-state output x using a time-domain simulation method in the generated η.

- Procedure 2: Apply the same WS method as in Procedure 1, using $S_{xx}(f)$ instead of $S_{\eta\eta}(f)$, to generate a random time series of the output x.

The only difference between the two procedures is that, in Procedure 2, the phase relationship between a specific instance of η and the corresponding x is not modelled (because η is not explicitly simulated). For a linear WEC system, the equivalence between Procedures 1 and 2 has important consequences: as explained in [89], using the HDA method and calculating the steady-state WEC response over a period $T = 1/\Delta f$, the average absorbed power in the target sea state, $\langle P \rangle$, can be calculated using only one random simulation.

For non-linear WEC models, although $\langle P \rangle$ estimated over $T = 1/\Delta f$ may vary from run to run, the variability of $\langle P \rangle$ remains significantly smaller than it would be using the HRA method [79], thus requiring fewer simulations for a given confidence level. However, for a non-linear system, it cannot be proven, to the best of the author's knowledge, that using the HDA method produces unbiased estimates with respect to HRA. Therefore, if possible, some preliminary simulations should be carried out, to ascertain whether the HDA and HRA methods yield the same results, as further exemplified in Chapter 6 of this thesis.

3.5.2 Extension to other statistics

In general, the primary goal of running statistically accurate simulations of random processes is to estimate one or several statistical quantities. Throughout this chapter, the quantity taken as an example was the variance, m_0. It has been shown that for a given spectrum discretisation method, DA and RA variants yield the same average value $\langle \hat{m}_0 \rangle$, which is a good approximation to m_0 if the spectrum is discretised with sufficient accuracy. DA, however, yields estimates $\hat{m}_0$ which present less variability around $\langle \hat{m}_0 \rangle$ than using RA. In short, as far as m_0 is concerned, DA yields unbiased estimates, with less variability than RA.

As briefly mentioned in Section 3.1, the latter observation seems to hold for a number of other statistical quantities, such as peak frequency, groupiness factor, maximum wave height, steepness, etc. as suggested in experiments carried out by a number of authors [74, 75, 76], including the work reported in [89], carried out within the scope of this thesis.

Nevertheless, it must be stressed that DA yielding unbiased estimates may not necessarily be true for any statistical quantity.

3.5.3 Comparison between simulation methods

As shown in Section 3.3, harmonic WS methods satisfy conditions C1 and C2, and thus are suitable for random wave simulation, under the condition that the spectrum discretisation is accurate enough (in the examples of this chapter, $\Delta f \approx f_c/100$), and that the simulation time T is less than, or equal to $1/\Delta f$. Given the capabilities of modern computers, it is extremely unlikely that such requirements would represent significant limitations.

In contrast, there seems to be no strong rationale for using any of the non-harmonic WS methods. In particular, using EARA or EADA methods, it seems difficult to determine a clear limit for the simulation time beyond which the ACF becomes distorted (while using HRA or HDA methods, $1/\Delta f$ is a simple choice). With RPRA or RPDA methods, the setting of d_f may be delicate, but with the example spectrum studied in this chapter, self-repetition can be avoided for $d_f \approx \Delta f$, while preserving a satisfactory ACF. However, with RP more so than with EA, the variability of the m_0 estimate is not accurately reproduced, when T is large. In addition, for both EA and RP, the generation process is significantly more complicated and time consuming than with harmonic discretisation.

Therefore, choosing between the HRA and HDA methods seems to be the most reasonable alternative.

Table 3.1: Summary table of wave superposition methods - assuming $M \geq 100$

	HRA	**HDA**
Gaussian?	Yes	No
ACF	Accurate up to $T \approx 1/\Delta f$	Accurate up to $T \approx 1/\Delta f$
var$[\hat{m}_0]$ $(T \leq 1/\Delta f)$	Realistic	Underestimated; 0 for $T = 1/\Delta f$
var$[\hat{m}_0]$ $(T > 1/\Delta f)$	——— *not relevant* ———	——— *not relevant* ———
	EARA	**EADA**
Gaussian?	Yes	No
ACF	Gradually distorted as T increases	Gradually distorted as T increases
var$[\hat{m}_0]$ $(T \leq M/f_c)$	Realistic	Realistic
var$[\hat{m}_0]$ $(T > M/f_c)$	Overestimated for $T \gg M/f_c$	Underestimated for $T \gg M/f_c$
	RPRA (with $d_f \approx \Delta f$)	**RPDA (with $d_f \approx \Delta f$)**
Gaussian?	No	No
ACF	Accurate for all T	Accurate for all T
var$[\hat{m}_0]$ $(T \leq 1/\Delta f)$	Realistic	Underestimated
var$[\hat{m}_0]$ $(T > 1/\Delta f)$	Overestimated	Underestimated

3.6 Summary

It has been shown that two conditions are necessary and sufficient for the simulated wave process to be statistically representative of the target sea state: (C1) the generated process should be Gaussian, and (C2) its ACF should satisfy the Wiener-Khinchine relation with the target spectrum, for all lag values within the intended simulation length. In particular, the Gaussian distribution followed by the target process introduces significant variability in the wave statistics estimated over finite-length time intervals. This variability is more particularly exemplified for the finite-length estimator of the signal variance m_0, using real wave time series and theoretical analysis.

Harmonic and non-harmonic wave superposition methods have been thoroughly analysed and compared, using conditions C1 and C2 as guidelines. The corresponding findings are summarised in Table 3.1.

Harmonic WS methods constitute a simple and clear alternative. For applications where it is essential that the short-term variability of natural ocean waves be accurately simulated, the HRA method is appropriate. In such a case, and if periodicity must absolutely be avoided, Δf can simply be chosen such that $1/\Delta f$ exceeds T by more than the correlation length of the wave process. With such settings, the HRA method satisfies C1 and C2. Alternatively, if accurate statistics must be estimated from relatively few and short simulations, the HDA method may be considered a more suitable option. However, for the system under study (linear or non-linear) and the statistics of interest (variance or other), it should be ascertained that the HDA method produces unbiased estimates with respect to the HRA method.

Non-harmonic discretisation methods, in contrast, introduce statistical distortion. With EA, the ACF of the generated process may be significantly impacted, which can only be mitigated by increasing the number of frequency components. Furthermore, for large estimation intervals, the variance of the m_0 estimator is either overestimated (with the EARA method) or underestimated (with the EADA method). As far as RP is concerned, unlike the commonly advocated procedure [81] whereby $d_f \ll \Delta f$, the parameter d_f should be chosen at least equal to Δf, but not so large as to affect the generated process ACF for small lag values. The resulting process, however, is non-Gaussian, and for estimation intervals $T \geq 1/\Delta f$, the variance of the m_0 estimator is either overestimated (with the RPRA method), or underestimated (with the RPDA method).

Thus, it is not true to say that non-harmonic WS methods allow the simulation time to be arbitrarily extended, without increasing the number of frequency components. Clearly, the potential benefits of non-harmonic discretisation schemes are offset by hidden statistical distortion, and by the additional complexity introduced by the simulation procedures.

Finally, if the intended simulation length is so large that WS methods constitute a significant

computational burden, white-noise filtering techniques may be considered. However, it must be stressed that, providing requirements C1 and C2 are met, there should be no difference between simulating one extremely long time series, or many shorter time series with the same total simulated length. Therefore, it seems unlikely that any practical case may be found, where harmonic WS methods would not be relevant as a realisation technique.

Part II

A harmonic balance technique for the numerical simulation of non-linear wave energy converter models

Chapter 4

Wave energy converter models

4.1 Introduction

Numerical WEC simulation

Given the high cost of physical experiments (both in wave tanks and at sea), the development of wave energy concepts relies, to a large extent, on numerical simulations [3]. Gradual improvement in available computational power, and scientific progress in WEC modelling, have jointly contributed to making increasingly realistic simulations achievable.

The modelling and numerical simulation of WECs significantly differ from that of ships or other marine structures [3], both in its aim and in the associated challenges:

- The aim of WEC simulation is, most of the time, oriented towards power production assessment, while for other marine applications, the focus is mostly on structural design. Nevertheless, it may be reasonably argued that, if wave energy technologies are to converge and be developed to an industrial scale, the aims of WEC simulations should also include structural design - see, for example, Chapter 14 of [3].

- In traditional marine applications, waves are seen as a disturbance of which the effects should be minimised. Therefore ships and marine structure are designed *not* to resonate in ocean waves, and to keep their oscillatory motion relatively small, which is, most of the time, consistent with the use of linear hydrodynamic theory. In contrast, wave energy converters may be designed to undergo large amplitude motions in order to maximise power capture, which makes linear theory inadequate [11, 90].

The numerical simulation of WECs or WEC systems involves a suitable *model*, and a suitable *solution technique*. At this stage, the terms *simulation*, *model* and *solution technique* (or *method*), as employed in this thesis, deserve proper definitions:

1. **Model, or mathematical model:** A differential equation, or a set of differential equations, which describe the dynamical behaviour of a wave energy system.

2. **Solution method, or numerical solution method:** A numerical technique, or a combination of numerical techniques, which may be used to compute the solution for the differential equations of a wave energy device model.

3. Accordingly, the **simulation** of a WEC consists of calculating, using an appropriate numerical method, the solution for the differential equation of a WEC model.

The above definitions differ from the terminology employed in other works, such as [3], where the term “model” is interchangeably used for what is referred to, in this thesis, as model, solution method, or simulation. The author of this thesis believes that the distinction is important. For

example, a linear differential equation (the *model*) may be solved by means of various *solution methods*, such as time-domain numerical integration, or frequency-domain calculations.

As mentioned in the introduction, the focus of this thesis is on applications where the speed of numerical calculations is of primary importance. Computational efficiency is crucial, in particular, when extensive simulation is required, e.g. for power assessment, whereby the WEC outcome must be calculated in a large number of sea states (see Chapter 2), or for WEC optimisation, whereby a wide range of design parameters have to be quickly evaluated. Real-time control of WECs [9] is another application where models must lend themselves to efficient calculations. As a consequence, the main objective of this chapter is to define a reasonably general formulation for WEC models, which can offer an appropriate degree of realism, while being amenable to efficient solution methods as required in the applications identified. This elementary formulation is a prerequisite for introducing the harmonic balance method in Chapter 5.

The variety of WEC modelling approaches

There exists a variety of WEC models for numerical simulation, with various strengths depending on the intended use and on the specific device considered. For a review of numerical modelling approaches, the reader is referred to the book of Folley [3]. As far as hydrodynamic modelling is concerned, the range of existing approaches extends from linear, time-invariant models, some of which are not significantly more complicated than a mass-spring-damper system, to computational fluid dynamics (CFD), which solves the full hydrodynamic interaction governed by the Navier-Stokes equations. Nevertheless, even the simplest WEC models, entirely described by linear theory, lend themselves to a wealth of theoretical analysis [7] which has kept its relevance until nowadays, well into the era of CFD.

Linear models can be solved efficiently, significantly faster than real-time[1], using frequency-domain calculations. In contrast, CFD runs much slower than real-time and, as such, is only suitable for specific applications, such as the study of extreme events or particular physical phenomena. Between those two extremes, there exists a range of approaches where a lesser or greater amount of realism is added, through the addition or removal of assumptions.

In recent years, renewed interest in non-linear hydrodynamic WEC modelling has emerged in relation to control. Indeed, power-maximising control of wave energy devices, mentioned in the introduction, is known to have the potential to help reducing the levelised cost of energy (LCOE) for wave energy technologies, by maximising the amount of power absorbed, at a given capital cost [9]. Power-maximising control strategies tend to magnify the amplitude of the motions undergone by the WECs, which invalidates the assumption of small motion [11], essential for the validity of linear hydrodynamics. Therefore, there is a need for more realistic WEC models, which are not only computationally tractable, but also present themselves in a mathematical form amenable to the theoretical tools of model-based control. The development of such models has been under investigation at COER (see for example the work of Giorgi [91]), where this thesis has been carried out.

Although hydrodynamic interaction has been the focus of the discussion in the previous paragraphs, it is only a part of a complete WEC model. In particular, in comparison to hydrodynamic modelling, the conversion of mechanical energy into electrical energy through the power take-off (PTO) system has received far less interest in academic publications. *Wave-to-wire* modelling approaches for WEC systems, i.e. including PTO components, are reviewed in [92]. Mooring systems, which have also been relatively overlooked, may play an equally important role in the dynamics of WEC systems [93].

[1] i.e. the run time for one second of simulation is $\ll$ 1s.

Solution methods

Of course, models and solution methods are not independent from each other, some solution methods being more appropriate than others for specific types of models. Thus, the challenge of numerical simulation consists of finding an appropriate mathematical model *and* a compatible numerical solution technique. In fact, more often than not, models are designed, or modified, so as to be amenable to certain solution techniques: for example, the linearisation of a non-linear system around an equilibrium point is commonplace procedure, which allows frequency-domain calculations to be employed.

Adding more realism into a model often comes at the price of increasing the computational cost associated with its simulation: the solution method may have to be changed to a more sophisticated one in order to accommodate a new type of differential equation; the dimension of the model may increase, etc. For example, when non-linear effects are taken into account, the usual frequency-domain analysis is typically replaced with time-domain integration [3] to solve the dynamical equations. Furthermore, as will be further discussed throughout the remainder of this section, a clear-cut gap exists between those models which are "distributed in space", and thus expressed as a set of partial differential equations (PDE), such as the Navier-Stokes equations [94], and those which can be expressed as integro-differential equations (IDEs), such as Cummins' equation [95] (see Section 4.3.3), or ordinary differential equations (ODEs), for example when the convolution term of Cummins' equation is approximated by means of a state-space representation [96]. ODEs and IDEs usually have low dimension (typically less than 10 for a single device), and thus can be solved relatively easily and efficiently. In addition, ODE models lend themselves to analysis tools and control methods from the theory of non-linear dynamical systems [97]. IDE and ODE descriptions thus form a suitable category of models for computationally-efficient solution methods and control calculations.

More specifically, in the remainder of this thesis, **IDE models** refer to differential equations combining:

- *linear or non-linear* terms which 'statically' depend on the state variables, as in ODEs;
- *linear* memory terms represented in integral form.

In general, IDE WEC models are written in a mathematical form similar to the following:

$$\dot{\mathbf{x}}(t) = \mathbf{f}(\mathbf{x}(t),t) + \int_0^\infty \mathbf{K}(\tau)\mathbf{x}(t-\tau)d\tau \tag{4.1}$$

If the convolution kernel $\mathbf{K}$ is zero, Eq. (4.1) reduces to an ODE. For simplicity, and since ODEs form a special case of IDEs, both ODEs and 'strict' IDEs (containing an integral term) will be referred to as IDE models. Eq. (4.1) will be given a more specific mathematical form throughout the rest of this chapter, with an emphasis on non-linear terms and memory terms, which present the most challenge from the point of view of numerical simulation.

The focus of this chapter is on clarifying what types of physical WEC models can be described by an IDE, and on identifying more specific formulations than Eq. (4.1), in the context of WEC modelling.

Chapter organisation

The rest of this chapter is organised as follows:

- Section 4.2 introduces the basic principles of WEC modelling, involving three main subsystems: the coupled fluid-structure system, the PTO system and the mooring system.

- Models for WEC hydrodynamic interaction problems are briefly reviewed in Section 4.3. A generic formulation for hydrodynamic interaction models is proposed, with clearly understood limitations, and with a specific emphasis on the most computationally challenging modelling terms: non-linear terms and linear memory terms.

- Models for PTO systems are briefly discussed in Section 4.4, with an emphasis on their mathematical formulation.

- Models for mooring systems are briefly discussed in Section 4.5, with an emphasis on their mathematical formulation.

- Based on the preceding sections, a generic IDE formulation for WEC models is proposed and discussed in Section 4.6.

- The main contributions and salient points of this chapter are summarised in Section 4.7.

4.2 WEC modelling: general principles

The variety of WEC operating principles and concepts makes it difficult to propose a general formulation for WEC models. However, it can safely be asserted that any WEC system comprises one or several moving components which are activated by the surrounding fluid. The term "moving component" may be understood in a broad sense: for example, in oscillating water columns, the air column may be modelled as a rigid piston (see, for example, [98] and other work carried out at Instituto Superior Tecnico in Lisbon University), and therefore may be seen as a "moving component", although it is not strictly speaking part of the WEC itself[2].

Therefore, the basis of WEC hydrodynamic modelling is Newton's second law, which relates the motion of moving parts to the forces exerted onto the WEC system. As articulated in Chapter 2 of [3], forces can be split into external forces, due to the hydrodynamic interaction between the WEC and the surrounding fluid, and reaction forces, which are due to the mechanical effect of the power take-off (PTO) system, or to the mooring arrangement. Also taking into account the gravity force, Newton's second law then reads:

$$\mathbf{M}_b \ddot{\boldsymbol{\xi}} = \mathbf{f}_g + \mathbf{f}_f + \mathbf{f}_{pto} + \mathbf{f}_m \tag{4.2}$$

where:

- ξ represents the generalised coordinates describing the dynamics of those WEC moving parts, which are directly activated under the mechanical action of the waves, and dots represent time derivatives;

- $\mathbf{M}_b$ denotes the inertia matrix of the moving parts, which are directly activated under the mechanical action of the wave;

- $\mathbf{f}_g$ is the force due to gravity;

- $\mathbf{f}_f$ is the force exerted by the fluid onto the moving parts;

- $\mathbf{f}_{pto}$ represents the forces exerted by the PTO system;

- $\mathbf{f}_m$ represents the forces exerted by the mooring system.

[2]This is but one instance where it is useful to employ the term *WEC system*, as opposed to *WEC*: the model of the WEC system may also include the description of physical elements or phenomena which are not physically part of the WEC (as a manufactured device), but which participate in the WEC operation.

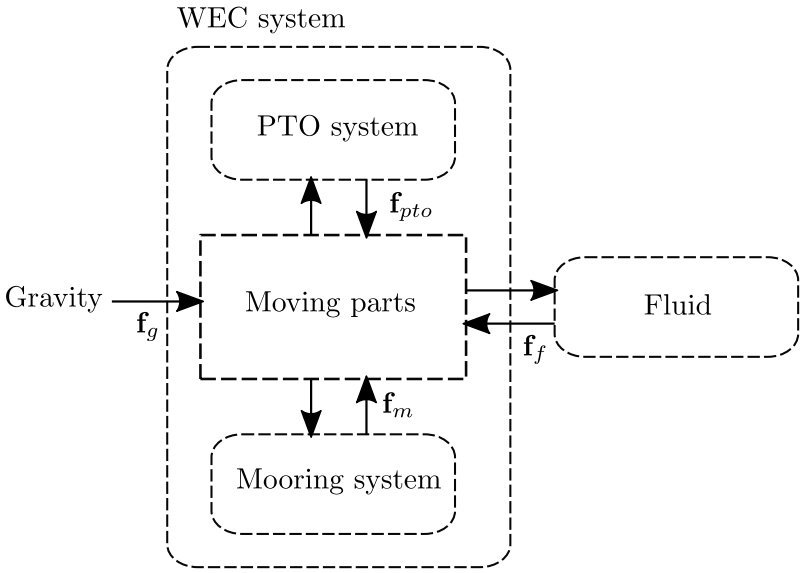

Figure 4.1: Schematic diagram of a WEC model

Eq. (4.2) does *not* imply that the forces are independent from each other.

In the following, the bold letter **f** represents a generalised force, composed of a force, a torque, or both. When forces, or torques, need to be expressed separately, they are denoted **F** and **T**. For example, the mooring (generalised) force is defined as:

$$\mathbf{f}_m = \begin{pmatrix} \mathbf{F}_m \\ \mathbf{T}_m \end{pmatrix} \tag{4.3}$$

Apart from the gravity force, which is straightforwardly calculated, the calculation of the three other forces, $\mathbf{f}_f$, $\mathbf{f}_{pto}$ and $\mathbf{f}_m$, requires that the corresponding systems - hydrodynamic interaction, PTO system, mooring system - are modelled with sufficient accuracy. In fact, in a realistic model, moorings, PTO and hydrodynamic interaction would all have their own internal dynamics. Thus, a WEC model can be said to describe the interaction of the wave-activated moving parts with three subsystems: the surrounding fluid (*hydrodynamic interaction*), the mooring system, and the PTO system. Those three essential components are schematically represented in the diagram of Fig. 4.1, and are discussed in the next subsections, with a more detailed focus on hydrodynamic interaction which has been, by far, the subject of most academic work related to WECs.

4.3 Models for hydrodynamic interaction

The motion of the surrounding fluid, and its interaction with the moving WEC, are governed by the laws of fluid mechanics. The set of partial differential equations which govern fluid mechanics, in the most general case, are called the Navier-Stokes equations, and have been well established since the middle of the XIX$^{\text{th}}$ century [94]. The model defined by the Navier-Stokes equation has proved able to describe the motion of any known fluid with excellent accuracy. However, given the highly complicated and non-linear nature of the Navier-Stokes equations, analytical solutions are only available under very restrictive sets of assumptions, and even the *numerical* solution of specific problems in physics or engineering is carried out under various simplifying assumptions, so that, as formulated by Katz [94], *"the science of fluid mechanics has focused on simplifying this complex mathematical model and on providing partial solutions for more restricted conditions."*

Accordingly, the typology of hydrodynamic models for WEC systems mostly reflects the choices made in terms of simplifying assumptions. The brief overview which follows browses

from the less restrictive to the most restrictive modelling approaches. The resulting order of presentation for the various modelling approaches does not follow any chronological progression - quite the contrary in fact, since the most complete models for describing the fluid dynamics only became computationally tractable in relatively recent years, using CFD, while the most restrictive models, such as Cummins' equation [95], have been analysed and have led to exploitable results for more than 50 years. The books from Folley [3] and Molin [99] are a valuable companion to the following subsections.

4.3.1 The Navier-Stokes equations and CFD simulations

For applications of any practical significance in hydrodynamic engineering, including the modelling of wave energy systems, the Navier-Stokes equations reduce to the mass and momentum conservation equations, to which relevant boundary conditions are added, typically at the vertical and horizontal boundaries of the domain considered, and on the surface of the device. Note that, for WEC modelling, the fluids of interest are both water and air, since the WEC system may be in contact with both.

Modelling the fluid compressibility is, in most WEC-related applications, unnecessary (Chapter 6 of [3]), but may be useful to study extreme events such as wave slamming. In the following, only the more usual case of the *incompressible* Navier-Stokes equations is considered. For an incompressible fluid, the mass conservation equation (or continuity equation), in its differential form, reads as follows:

$$\nabla.\mathbf{u} = 0 \tag{4.4}$$

where $\mathbf{u}$ is the velocity vector field. The momentum conservation equation, again for an incompressible fluid, can be given as:

$$\rho(\frac{\partial \mathbf{u}}{\partial t} + \mathbf{u}.\nabla\mathbf{u}) = \rho\mathbf{F}_{\text{dist}} - \nabla p + \mu\nabla^2\mathbf{u} \tag{4.5}$$

where ρ is the fluid density, p is the pressure, μ is the fluid viscosity coefficient, and $\mathbf{F}_{\text{dist}}$ represents a distributed force per unit mass (e.g. gravity).

Eqs. (4.4) and (4.5), together with boundary conditions, form the model which describes the dynamics of the fluid surrounding the WECs. The boundary conditions at the contact surface with the WEC and, conversely, the pressure force exerted by the fluid onto the WEC, together make the hydrodynamic interaction a *coupled* model.

The solution of Eqs. (4.4) and (4.5) can be carried out numerically using CFD techniques, which include both "traditional" CFD (relying on a spatial discretisation of the fluid domain), and the more recent technique of smooth particle hydrodynamics (SPH), which represents the fluid as a mass of interacting particles. Details on the available numerical software, and existing CFD studies applied to WEC systems, may be found in Chapter 6 of [3], or [100]. The most common CFD method in the wave energy field is termed *Reynolds-averaged Navier-Stokes* (RANS) [101] and solves for Eqs. (4.4) and (4.5).

CFD can also be used to solve simplified versions of Eqs. (4.4) and (4.5). In particular, the *Euler* equation corresponds to the case where the fluid viscosity coefficient, μ, is assumed equal to zero. In [101], both RANS and Euler simulations are compared for a cylindrical heaving point-absorber (HPA) wave energy device[3]. While RANS simulations can account for dissipative effects due to both viscosity and vorticity, with the Euler formulation, dissipative terms are solely due to vorticity. Results from [101] suggest that, for a full-scale heaving point-absorber, the dominant dissipative effects are due to vortex shedding, while viscosity only plays a minor role. In such a case, the Euler equations may be an appropriate model.

Modelling the WEC dynamics using the full Navier-Stokes or Euler equation is vital, for applications involving the detailed study of extreme events, specific physical phenomena or to

[3]Heaving point-absorbers are a category of wave energy devices, operating in the vertical (heave) mode of motion, and of small dimension relative to the typical incident wavelength.

validate simplified modelling approaches. Nevertheless, the heavy computational requirements associated with CFD make the approach, as yet, inadequate for quick and extensive calculations. Thus, more tractable modelling approaches for WEC hydrodynamics are essential.

Finally, note that "CFD", in its common acceptance, refers to numerical tools for the solution of the Navier-Stokes equations with relatively few simplifying assumptions, such as Eqs. (4.4) and (4.5). However, strictly speaking, the term "CFD" could also apply to the numerical solution of simpler versions of the Navier-Stokes equations, such as potential flow models discussed in the next subsection.

4.3.2 Non-linear potential flow models

In the non-linear potential flow approach, starting from Eqs. (4.4) and (4.5), two additional assumptions are made, which greatly simplify the incompressible Navier-Stokes equations:

- The fluid is inviscid, i.e. viscous effects are neglected (as for the Euler equation);
- The fluid is irrotational.

Such assumptions are generally acceptable far from the boundary layer [94], but they may be unrealistic in the vicinity of the interface between the device and the fluid. Assuming inviscid and irrotational flow, it can be shown that the velocity field $\mathbf{u}$ can be expressed as the gradient of a so-called (scalar) *velocity potential* ϕ, so that $\mathbf{u} = \nabla\phi$. The continuity and momentum conservation equations then take the form of the Laplace equation (here expressed in Cartesian coordinates):

$$\nabla^2\phi = \frac{\partial^2\phi}{\partial x^2} + \frac{\partial^2\phi}{\partial y^2} + \frac{\partial^2\phi}{\partial z^2} = 0 \tag{4.6}$$

and Bernoulli's equation:

$$gz + \frac{p - p_a}{\rho} + \frac{1}{2}\nabla\phi.\nabla\phi + \frac{\partial\phi}{\partial t} = 0 \tag{4.7}$$

where p_a denotes the atmospheric pressure.

At the free-surface, the **dynamic boundary condition**, obtained by applying Bernoulli's equation at the free-surface, reads:

$$g\eta + \left[\frac{1}{2}\nabla\phi.\nabla\phi + \frac{\partial\phi}{\partial t}\right]_{z=\eta} = 0 \tag{4.8}$$

The free-surface **kinematic boundary conditions** states that a fluid particle at the free surface stays at the free surface (or cannot cross the free surface); in other words, the velocity of the fluid normal to the free surface must be equal to the free-surface velocity. In mathematical terms, the kinematic boundary condition requires that, in $z = \eta(x,y,t)$,

$$\frac{\partial\eta}{\partial t} + \frac{\partial\eta}{\partial x}\frac{\partial\phi}{\partial x} + \frac{\partial\eta}{\partial y}\frac{\partial\phi}{\partial y} = \frac{\partial\phi}{\partial z} \tag{4.9}$$

At the contact surface between a solid body and the fluid, a **no-flow condition** through the solid surface applies, which is mathematically expressed, at all points P of the contact surface, as:

$$\mathbf{n}_P.\mathbf{u} = \mathbf{n}_P.\nabla\phi \tag{4.10}$$

where $\mathbf{u}$ is the velocity of the point P belonging to the solid, and $\mathbf{n}$ is the unit vector, normal to the contact surface at P, and pointing towards the fluid domain. In particular, at the sea bottom:

$$\mathbf{n}_P.\nabla\phi|_{z=-h} = 0 \tag{4.11}$$

Condition (4.10), applied to a floating body, is a normal velocity condition, and makes the fluid motion dependent on the body velocity while, conversely, the body motion is influenced by the

pressure force exerted by the fluid onto the body surface, which can be calculated from Bernoulli's equation if ϕ is known. Therefore, the hydrodynamic interaction is, again, a coupled problem.

Finally, the conditions at the horizontal boundaries of the fluid domain depend on the problem considered - regarding, for example, whether the simulated domain corresponds to a wave tank or to open sea. In particular, for open-sea simulations, far-field conditions may apply [7], expressing the fact that, far from the solid body interacting with the fluid, the influence of the solid body on the flow must tend to zero. The various boundary conditions will receive further attention in Section 4.3.3.

Different approaches exist for the solution of a non-linear potential flow model, which can be broadly classified into *Mixed Eulerian-Lagrangian* (MEL) schemes and *high-order spectral* (HOS) methods[4] - see Chapter 5 of [3]. HOS methods are relatively efficient compared to MEL schemes, and therefore are particularly suitable for simulations of a wave field within a large domain and over long periods. However, unlike MEL methods, HOS cannot model overturning waves.

By definition, a significant limitation of potential flow models is their inability to capture drag effects due to viscosity and vortex shedding, which can be important for appropriately modelling the fluid close to a wave energy device. A possible solution could be the coupling of a HOS solver (for the far-field) with CFD (in the vicinity of the device) - see Chapter 5 of [3].

Both the incompressible Navier-Stokes equations (4.4) and (4.5), which are usually solved using CFD, and the more restrictive non-linear potential flow model (4.6) and (4.7), share a significant drawback, from the point of view of computational tractability, and ease of theoretical analysis of the WEC dynamics: the formulation of both categories of models is primarily continuous in space and, as such, expressed as a set of partial differential equations. Therefore, the dimension of the problem to solve is, in theory, infinite, although the numerical solution eventually relies on some discretisation of the modelling equations.

The next two sections deal with categories of models, which take the form of IDEs, as defined in the introduction to this chapter.

4.3.3 Linear hydrodynamic models and Cummins' equation

IDE hydrodynamic models typically have a relatively small dimension (corresponding, roughly, to the number of hydrodynamic degrees of freedom). Even though the study of wave energy arrays can make the dimension of the model significantly larger, the dimension of IDE models is by no means comparable with the large number of variables involved in the numerical solution of the Navier-Stokes, Euler or Laplace equations, in the models of Sections 4.3.1 and 4.3.2.

As yet, IDE WEC models are mainly based on the theory of *linear potential flow*, whereby the kinematic and dynamic free-surface boundary conditions, and the no-flow condition (on the body hull), are linearised, assuming that the wave height is small compared to the wave length, and that the body motion is small enough for the wetted surface to remain approximately constant.

While this section focuses on linear models, stemming from the linear potential flow theory, the next section (4.3.4) presents non-linear extensions of the linear potential flow model, and discusses alternative ways by which new IDE models might be developed, able to capture the realistic features of the Navier-Stokes equations of (4.4) and (4.5).

4.3.3.1 Dynamical equations for a freely-floating body

In this subsection, the motions of a freely-floating body, with six degrees of freedom, is considered. The following developments also extend, with relatively few changes, to structures with constrained motions (e.g. a bottom-mounted flap-type device), or structures with multiple bodies (interconnected or not).

[4]HOS methods are an example of spectral methods [102], applied to a problem in fluid mechanics: the spatial distribution of the potential flow is expressed as a series expansion, which is integrated forward in time. Spectral methods, of which the harmonic balance technique forms a special case, will be introduced in the next chapter.

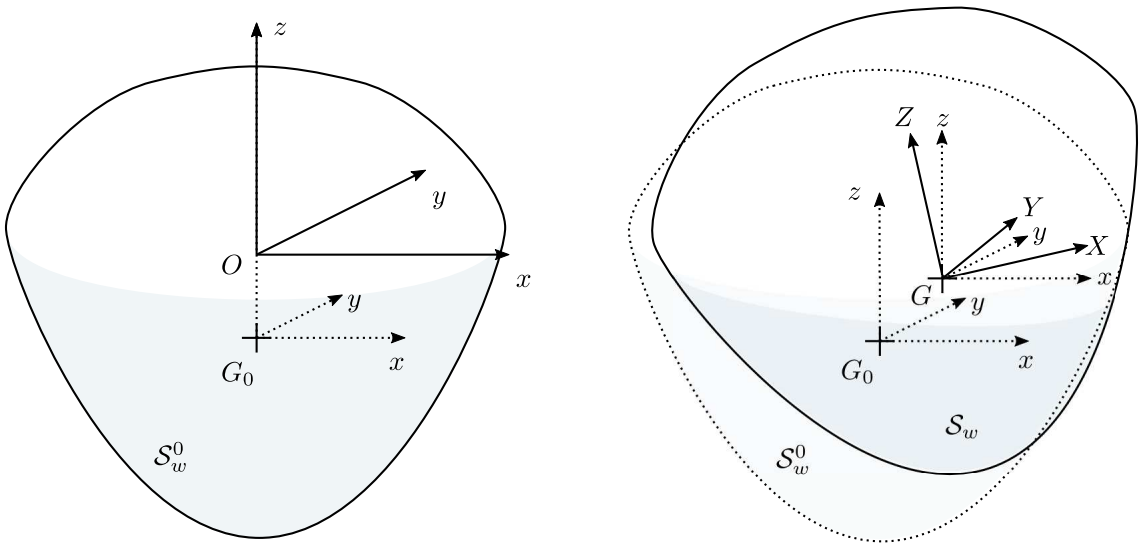

Figure 4.2: Reference frame definition for a freely-floating body

Table 4.1: Conventional names of the six fundamental hydrodynamic degrees of freedom

Notation	Name
x_G	Surge
y_G	Sway
z_G	Heave
r_x	Roll
r_y	Pitch
r_z	Yaw

Let us define $Oxyz$ the reference frame in which the fluid motion is described. At rest, the gravity centre of the floating body, G, occupies a position G_0 which is assumed, without loss of generality, to be vertically aligned with O, as shown in the left-hand-side of Fig. 4.2. Define a reference frame $GXYZ$, attached to the body and such that, at rest, $GXYZ$ coincides with G_0xyz. As sketched in Fig. 4.2, the body motion is entirely described by the position of G relative to G_0, noted (x_G, y_G, z_G), and by the rotation of $GXYZ$ with respect to $Gxyz$, noted (r_x, r_y, r_z).

Assuming small rotation angles, the coordinates in G_0xyz of any point P belonging to the solid body, with coordinates (X_P, Y_P, Z_P) relative to G, can be obtained as:

$$\mathbf{x}_P := \begin{pmatrix} x_P \\ y_P \\ z_P \end{pmatrix} = \begin{pmatrix} x_G \\ y_G \\ z_G \end{pmatrix} + \begin{pmatrix} X_P \\ Y_P \\ Z_P \end{pmatrix} + \begin{pmatrix} r_x \\ r_y \\ r_z \end{pmatrix} \times \begin{pmatrix} X_P \\ Y_P \\ Z_P \end{pmatrix} \tag{4.12}$$

and the velocity of the point P is obtained as:

$$\mathbf{u}_P := \begin{pmatrix} \dot{x}_P \\ \dot{y}_P \\ \dot{z}_P \end{pmatrix} = \begin{pmatrix} \dot{x}_G \\ \dot{y}_G \\ \dot{z}_G \end{pmatrix} + \begin{pmatrix} \dot{r}_x \\ \dot{r}_y \\ \dot{r}_z \end{pmatrix} \times \begin{pmatrix} X_P \\ Y_P \\ Z_P \end{pmatrix} \tag{4.13}$$

The terminology for the six fundamental hydrodynamic degrees of freedom, inherited from the naval tradition and summarised in Table 4.1, is employed to describe the motions of wave energy converters. By convention, in the wave energy field, the x axis is usually chosen aligned with the main wave direction.

Define ξ as the generalised body coordinates:

$$\xi = \begin{pmatrix} x_G \\ y_G \\ z_G \\ r_x \\ r_y \\ r_z \end{pmatrix} \tag{4.14}$$

and $\mathbf{M}_b$ the inertia matrix of the body:

$$\mathbf{M}_b = \begin{pmatrix} M & 0 & 0 & 0 & 0 & 0 \\ 0 & M & 0 & 0 & 0 & 0 \\ 0 & 0 & M & 0 & 0 & 0 \\ 0 & 0 & 0 & I_{XX} & I_{XY} & I_{XZ} \\ 0 & 0 & 0 & I_{YX} & I_{YY} & I_{YZ} \\ 0 & 0 & 0 & I_{ZX} & I_{ZY} & I_{ZZ} \end{pmatrix} \tag{4.15}$$

Assuming that the only external forces acting on the body are the gravity force and the pressure forces from the fluid (viscosity is neglected), Newton's second law is written as follows:

$$\mathbf{M}_b \ddot{\xi} = \begin{pmatrix} \mathbf{F}_p + \mathbf{F}_g \\ \mathbf{T}_p \end{pmatrix} \tag{4.16}$$

where $\mathbf{F}_p \in \mathbb{R}^3$ is the resultant of the pressure forces, $\mathbf{F}_g$ is the gravity force, and $\mathbf{T}_p \in \mathbb{R}^3$ is the moment of the pressure forces about the gravity centre G. $\mathbf{F}_p$ and $\mathbf{T}_p$ are expressed as:

$$\mathbf{F}_p = -\iint\limits_{P \in \mathcal{S}_w} p\, \mathbf{n}_P \, dS - \iint\limits_{P \in \overline{\mathcal{S}}_w} p_a \mathbf{n}_P \, dS \tag{4.17}$$

and

$$\mathbf{T}_p = -\iint\limits_{P \in \mathcal{S}_w} p\, \overrightarrow{GP} \times \mathbf{n}_P \, dS - \iint\limits_{P \in \overline{\mathcal{S}}_w} p_a \overrightarrow{GP} \times \mathbf{n}_P \, dS \tag{4.18}$$

where $\mathcal{S}_w$ denotes the (instantaneous) wetted surface of the floating body, as illustrated in Fig. 4.2, and $\mathbf{n}_P$ is the unit vector normal to the body surface in point P, pointing outwards.

In Eqs. (4.17) and (4.18), the pressure must be deduced from Bernoulli's equation which, in turn, implies that the fluid motion is known.

4.3.3.2 Linearised fluid equations

Assuming that potential flow theory is valid, i.e. that the fluid is inviscid and irrotational, the **Laplace equation** remains identical to (4.6):

$$\nabla^2 \phi = \frac{\partial^2 \phi}{\partial x^2} + \frac{\partial^2 \phi}{\partial y^2} + \frac{\partial^2 \phi}{\partial z^2} = 0 \tag{4.19}$$

Neglecting quadratic contributions, **Bernoulli's equation** (4.7) may be linearised as:

$$gz + \frac{p - p_a}{\rho} + \frac{\partial \phi}{\partial t} = 0 \tag{4.20}$$

Bernoulli's equation can be used to express the pressure in the fluid domain as a function of the potential ϕ:

$$p = p_a + \rho\left(\frac{\partial \phi}{\partial t} - gz\right) \tag{4.21}$$

Outside the fluid domain, $p = p_a$. Assuming a constant and uniform atmospheric pressure p_a, it is easy to see that the contribution of p_a to the overall pressure force (4.17) and torque (4.18), when integrated over the total surface of the body $\mathcal{S}_w \cup \overline{\mathcal{S}}_w$, amounts to zero. Therefore, in Eqs. (4.17) and (4.18), only the term $\rho(\frac{\partial \phi}{\partial t} - gz)$ needs to be explicitly integrated over $\mathcal{S}_w$:

$$\mathbf{F}_p = -\iint_{P \in \mathcal{S}_w} \rho(\frac{\partial \phi}{\partial t} - gz)\, \mathbf{n}_P \, dS \tag{4.22}$$

and

$$\mathbf{T}_p = -\iint_{P \in \mathcal{S}_w} \rho(\frac{\partial \phi}{\partial t} - gz)\overrightarrow{GP} \times \mathbf{n}_P \, dS \tag{4.23}$$

The various boundary conditions are also linearised. The non-linear **dynamic boundary condition** (4.8) is linearised, assuming that variations of η are small, and that ϕ and its derivatives are small, which allows the quadratic terms to be neglected:

$$g\eta + \left.\frac{\partial \phi}{\partial t}\right|_{z=0} = 0 \tag{4.24}$$

Neglecting quadratic terms again, the **kinematic boundary condition** (4.9) is linearised as:

$$\frac{\partial \eta}{\partial t} = \frac{\partial \phi}{\partial z} \tag{4.25}$$

Using the dynamic boundary condition, expressing the constraint at $z = 0$ instead of η (because η is assumed small), the kinematic boundary condition becomes:

$$\left[\frac{\partial^2 \phi}{\partial t^2} + g\frac{\partial \phi}{\partial z}\right]_{z=0} = 0 \tag{4.26}$$

The **no-flow condition** (4.10) is responsible for the coupling between the fluid and the body motion. It reads:

$$\mathbf{n}_P.\mathbf{u}_P = \mathbf{n}_P.\nabla\phi \quad \text{for } P \in \mathcal{S}_w \tag{4.27}$$

where $\mathbf{u}_P$ is the velocity of the point P belonging to the solid, and $\mathbf{n}_P$ is the unit vector, normal to the body surface at P, and pointing towards the fluid domain. For motions of small amplitude, the linearisation of the no-flow condition (4.27) consists of expressing it over the mean wetted surface $\mathcal{S}_w^0$, as opposed to the instantaneous wetted surface $\mathcal{S}_w$:

$$\mathbf{n}_P.\mathbf{u}_P = \mathbf{n}_P.\nabla\phi \quad \text{for } P \in \mathcal{S}_w^0 \tag{4.28}$$

Furthermore, the no-flow condition also applies on the sea bottom $z = -H$, which yields:

$$\frac{\partial \phi}{\partial z}|_{z=-H} = 0 \tag{4.29}$$

Finally, depending on the problem considered, **far-field conditions** apply [7, 99], and will be given more detail when appropriate.

4.3.3.3 Hydrostatic terms

A first step towards the solution of the dynamical equations (4.16) consists of combining the static pressure term $-\rho gz$ of Bernoulli's equation (4.21), together with gravity, into a hydrostatic restoring force and torque, which represents the balance between gravity and Archimedes force and torque.

More specifically, integrating the hydrostatic pressure $-\rho gz$ over the wetted surface $\mathcal{S}_w$ yields the hydrostatic (or Archimedes) force and torque:

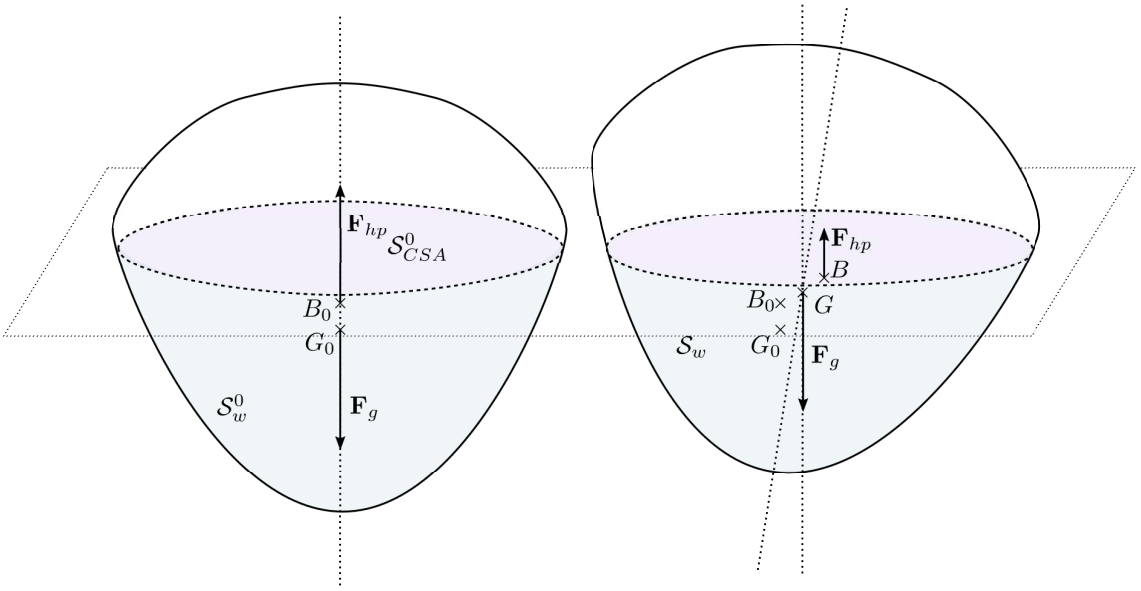

Figure 4.3: Schematic diagram of hydrostatic force and torque exerted onto a freely-floating body. *In the right-hand-side diagram, the smaller modulus of* $\mathbf{F}_{hp}$*, with respect to that of* $\mathbf{F}_g$*, results in a restoring force directed downwards. The misalignment of* $\vec{GB}$ *with the vertical axis results in a torque which tends to restore the body to its inclination at rest.*

- The hydrostatic force

$$\mathbf{F}_{hp}(\xi) = \iint_{P \in \mathcal{S}_w(\xi)} \rho g z \, \mathbf{n}_P \, dS \tag{4.30}$$

  is vertically-oriented, pointing upwards, with modulus $\rho V_d(\xi)$, where $V_d(\xi)$ is the displaced volume of fluid, when the body is in position ξ;

- The hydrostatic torque

$$\mathbf{T}_{hp}(\xi) = \iint_{P \in \mathcal{S}_w(\xi)} \rho g z \, \overrightarrow{GP} \times \mathbf{n}_P \, dS = \overrightarrow{GB}(\xi) \times \mathbf{F}_{hp}(\xi) \tag{4.31}$$

  where B is called the *buoyancy centre* and is equal to the centroid of the displaced volume of fluid, when the body is in position ξ. The subscript hp stands for 'hydrostatic pressure'. Note that, because $\mathbf{F}_{hp}$ is always vertically oriented, the third component of $\mathbf{T}_{hp}(\xi)$, corresponding to the torque in yaw (axis Oz), is always zero.

When the floating body is in hydrostatic equilibrium (which, given the chosen convention for the frame G_0xyz, corresponds to $\xi = \mathbf{0}$), the following conditions hold:

- The force $\mathbf{F}_{hp}$ cancels gravity $\mathbf{F}_g$; therefore, the weight ρV_0 of the displaced volume of fluid at rest, V_0, is equal to the body mass;

- The torque $\mathbf{T}_{hp}$ is zero, therefore, the buoyancy centre B_0 (in equilibrium) is vertically aligned with the centre of gravity.

The hydrostatic equilibrium position is represented in the left-hand-side diagram of Fig. 4.3.

Consider a displacement ξ with respect to the equilibrium position, illustrated in the right-hand-side diagram of Fig. 4.3. The geometry of the submerged volume is modified, thus resulting in a non-zero vertical force $\mathbf{F}_{hp} + \mathbf{F}_g$, and a non-zero torque $\mathbf{T}_{hp}$ about the pitch and roll axis, since the buoyancy centre is no longer vertically aligned with G. Note that surge, sway and yaw

motion does not modify the geometry of the immersed volume, so that it has no impact on the total hydrostatic force and torque.

Define $\mathbf{F}_s = \mathbf{F}_{hp} + \mathbf{F}_g$ and $\mathbf{T}_s = \mathbf{T}_{hp}$. Assuming that the displacement ξ is small, $\mathbf{F}_s$ and $\mathbf{T}_s$ can be expressed linearly as a function of the displacement ξ, as follows (see Appendix A of [99]):

$$\mathbf{f}_s = \begin{pmatrix} \mathbf{F}_s \\ \mathbf{T}_s \end{pmatrix} = -\mathbf{S}_{hs}\xi \tag{4.32}$$

where

$$\mathbf{S}_{hs} = \begin{pmatrix} 0 & 0 & 0 & 0 & 0 & 0 \\ 0 & 0 & 0 & 0 & 0 & 0 \\ 0 & 0 & S_{zz} & S_{zr_x} & S_{zr_y} & 0 \\ 0 & 0 & S_{r_xz} & S_{r_xr_x} & S_{r_xr_y} & 0 \\ 0 & 0 & S_{r_yz} & S_{r_yr_x} & S_{r_yr_y} & 0 \\ 0 & 0 & 0 & 0 & 0 & 0 \end{pmatrix} \tag{4.33}$$

is called the *hydrostatic stiffness matrix*. The components of $\mathbf{S}_{hs}$ are calculated from the geometry of the floating body in hydrostatic equilibrium, as follows:

$$\begin{cases} S_{zz} = \rho g \iint\limits_{\mathcal{S}^0_{CSA}} dS \\ S_{r_xz} = S_{zr_x} = \rho g \iint\limits_{\mathcal{S}^0_{CSA}} Y dS \\ S_{r_yz} = S_{zr_y} = -\rho g \iint\limits_{\mathcal{S}^0_{CSA}} X dS \\ S_{r_xr_x} = \rho g (V_0 \|\overrightarrow{GB_0}\| + \iint\limits_{\mathcal{S}^0_{CSA}} Y^2 dS) \\ S_{r_yr_y} = \rho g (V_0 \|\overrightarrow{GB_0}\| + \iint\limits_{\mathcal{S}^0_{CSA}} X^2 dS) \\ S_{r_xr_y} = S_{r_yr_x} = -\rho g \iint\limits_{\mathcal{S}^0_{CSA}} XY dS \end{cases} \tag{4.34}$$

where $\mathcal{S}^0_{CSA}$ is the cross-sectional area formed by the intersection of the body in equilibrium with the fluid surface at rest (see Fig. 4.3).

The floating body is *hydrostatically stable* if $\mathbf{f}_s$, when the body is displaced, tends to restore it to its hydrostatic equilibrium position. In general, floating structures, including WECs, are designed to ensure hydrostatic stability. In such a case, $\mathbf{F}_s$ (resp. $\mathbf{T}_s$) is called *hydrostatic restoring force* (resp. *torque*).

4.3.3.4 Wave-body interaction

Define the vector $\mathbf{N}_P$, for each point P of $\mathcal{S}_w$, as:

$$\mathbf{N}_P = \begin{pmatrix} \mathbf{n}_P \\ \overrightarrow{GP} \times \mathbf{n}_P \end{pmatrix} \tag{4.35}$$

Having expressed the hydrostatic restoring force and torque as in Eq. (4.32), and using the notation $\mathbf{N}_P$ of Eq. (4.35), Newton's second law (4.16) is now written as:

$$\mathbf{M}_b\ddot{\xi} + \mathbf{S}_{hs}\xi = -\iint\limits_{P\in\mathcal{S}_w} \rho \frac{\partial \phi}{\partial t} \mathbf{N}_P \, dS \tag{4.36}$$

Considering that variations in the wetted surface are small, the integration over $\mathcal{S}_w$ is approximated by integration over the wetted surface at rest, $\mathcal{S}^0_w$:

$$\mathbf{M}_b\ddot{\xi} + \mathbf{S}_{hs}\xi = -\iint\limits_{P\in\mathcal{S}^0_w} \rho \frac{\partial \phi}{\partial t} \mathbf{N}_P \, dS \tag{4.37}$$

To proceed further with the solution, given the problem linearity, it is useful to assume that the fluid follows a sinusoidal motion at a single frequency ω, and to consider the forced, steady-state, response of the floating body (at the same frequency). Thus parametrised, the fluid and body motions can be written as follows:

$$\begin{cases} \phi(x,y,z,t) = \Re\{\hat{\phi}(x,y,z)e^{-i\omega t}\} \\ \xi = \Re\{\hat{\xi}e^{-i\omega t}\} \end{cases} \tag{4.38}$$

and the problem amounts to finding the complex function $\hat{\phi}(x,y,z)$ and vector $\hat{\xi}$. Furthermore, the total complex potential $\hat{\phi}$ can be written as the sum of three contributions:

- The **incident potential**, $\hat{\phi}_I$, corresponds to the undisturbed wave field in the absence of the floating body.
- The **diffracted potential**, $\hat{\phi}_D$, corresponds to the modification of the incident wave field because of the presence of the body (considered at rest). Together, the incident and diffracted potentials must satisfy the no-flow condition (4.28) on the hull surface at rest $\mathcal{S}_w^0$:

$$\mathbf{n}_P.\nabla(\hat{\phi}_D + \hat{\phi}_I) = 0 \text{ for } P \in \mathcal{S}_w^0 \tag{4.39}$$

- The **radiated potential**, $\hat{\phi}_R$, is due to the motion of the body in its six degrees of freedom, and therefore can be written as the sum of six contributions:

$$\hat{\phi}_R = \sum_{d=1}^{6} -i\omega\hat{\xi}_d\hat{\phi}_{R_d} \tag{4.40}$$

  where $\hat{\phi}_{R_d}$ is the radiated potential generated by the body when it is forced to oscillate in the mode d with unit amplitude.

The total potential is given as:

$$\hat{\phi} = \hat{\phi}_I + \hat{\phi}_D + \hat{\phi}_R \tag{4.41}$$

The incident potential $\hat{\phi}_I$ is given by Airy's wave theory (see Chapter 2). For a wave with amplitude A propagating along the direction θ, and defining $\hat{\eta}(\omega,\theta) = Ae^{-i\varphi}$ the wave elevation is given as follows:

$$\eta(t) = \Re\{Ae^{i\tilde{k}(\omega)(x\cos\theta+y\sin\theta)-i(\omega t+\varphi)}\} = \Re\{\hat{\eta}(\omega,\theta)e^{i\tilde{k}(\omega)(x\cos\theta+y\sin\theta)}e^{-i\omega t}\} \tag{4.42}$$

and the incident potential is written as:

$$\begin{aligned} \hat{\phi}_I(x,y,z) &= -A\frac{ig}{\omega}\frac{\cosh(\tilde{k}(\omega)(z+H))}{\cosh(\tilde{k}(\omega)H)}e^{i\tilde{k}(\omega)(x\cos\theta+y\sin\theta)-i\varphi} \\ &= -\hat{\eta}\frac{ig}{\omega}\frac{\cosh(\tilde{k}(\omega)(z+H))}{\cosh(\tilde{k}(\omega)H)}e^{i\tilde{k}(\omega)(x\cos\theta+y\sin\theta)} \end{aligned} \tag{4.43}$$

where ω and the wave number $\tilde{k}(\omega)$ satisfy the dispersion relation (2.10).

The linearised fluid equations, introduced in Section 4.3.3.2, and satisfied by the diffracted potential $\hat{\phi}_D$, are summarised as follows:

$$\begin{cases} \nabla^2\hat{\phi}_D = \frac{\partial^2\hat{\phi}_D}{\partial x^2} + \frac{\partial^2\hat{\phi}_D}{\partial y^2} + \frac{\partial^2\hat{\phi}_D}{\partial z^2} = 0 \text{ in the fluid domain} & \textit{Laplace equation} \\ [-\omega^2\hat{\phi}_D + g\frac{\partial\hat{\phi}_D}{\partial z}]_{z=0} = 0 & \textit{Kinematic boundary condition} \\ \frac{\partial\hat{\phi}_D}{\partial z}|_{z=-H} = 0 & \textit{No-flow condition at the sea bottom} \\ \mathbf{n}_P.\nabla\hat{\phi}_D = -\mathbf{n}_P.\nabla\hat{\phi}_I \quad \text{for } P \in \mathcal{S}_w^0 & \textit{No-flow condition on the body hull} \\ \lim_{r\to\infty}\sqrt{r}(\frac{\partial\hat{\phi}_D}{\partial r} - i\tilde{k}(\omega)\hat{\phi}_D) = 0 \text{ where } r = \sqrt{x^2+y^2} & \textit{Far-field condition} \end{cases} \tag{4.44}$$

The far-field condition is valid for waves diffracted by a body in the two directions of the horizontal plane. It expresses the fact that, in the distance, diffracted waves propagate radially, have a wave number $\tilde{k}(\omega)$, and an amplitude decreasing in $1/\sqrt{r}$ (for energy conservation) [99].

The radiated potential satisfies the same equations as the diffracted potential, except for the no-flow condition on the body hull. For each of the six potentials $\hat{\phi}_{R_d}$, from Eqs. (4.13) and (4.40), it is easy to find that the no-flow condition (4.28) takes the following form:

$$\mathbf{n}_P.\nabla\hat{\phi}_{R_d} = \mathbf{N}_{Pd} \quad \text{for } P \in \mathcal{S}_w^0 \tag{4.45}$$

where $\mathbf{N}_{Pd}$ represents the d^{th} component of $\mathbf{N}_P$.

Therefore, the equations, introduced in Section 4.3.3.2, and satisfied by the radiated potential $\hat{\phi}_R$, are summarised as follows:

$$\begin{cases} \nabla^2\hat{\phi}_{R_d} = \frac{\partial^2\hat{\phi}_{R_d}}{\partial x^2} + \frac{\partial^2\hat{\phi}_{R_d}}{\partial y^2} + \frac{\partial^2\hat{\phi}_{R_d}}{\partial z^2} = 0 \text{ in the fluid domain} & \textit{Laplace equation} \\ [-\omega^2\hat{\phi}_{R_d} + g\frac{\partial\hat{\phi}_{R_d}}{\partial z}]_{z=0} = 0 & \textit{Kinematic boundary condition} \\ \frac{\partial\hat{\phi}_{R_d}}{\partial z}|_{z=-H} = 0 & \textit{No-flow condition at the sea bottom} \\ \mathbf{n}_P.\nabla\hat{\phi}_{R_d} = \mathbf{N}_{Pd} \quad \text{for } P \in \mathcal{S}_w^0 & \textit{No-flow condition on the body hull} \\ \lim_{r\to\infty}\sqrt{r}(\frac{\partial\hat{\phi}_{R_d}}{\partial r} - ik\hat{\phi}_{R_d}) = 0 \text{ where } r = \sqrt{x^2+y^2} & \textit{Far-field condition} \end{cases} \tag{4.46}$$

Although analytical solutions for the radiation-diffraction problem can be found in some cases, such as vertical cylinders [99], for more general structures the problem is solved numerically using boundary element methods (BEMs), with a discretisation of the body hull geometry. In the wave energy community, the most common BEM solvers are WAMIT[5] and NEMOH[6], both of which have been employed in the case studies presented in Part III of this thesis.

Integrating the pressure due to the incident and diffracted potentials over $\mathcal{S}_w^0$ yields:

$$\begin{aligned} \mathbf{f}_D + \mathbf{f}_I &= -\iint_{P\in\mathcal{S}_w^0} \rho(\frac{\partial\phi_I}{\partial t} + \frac{\partial\phi_D}{\partial t})\mathbf{N}_P\, dS \\ &= \Re\{[i\omega \iint_{P\in\mathcal{S}_w^0} \rho(\hat{\phi}_I + \hat{\phi}_D)\mathbf{N}_P\, dS]Ae^{-i(\omega t+\varphi)}\} \\ &= \Re\{[i\omega \iint_{P\in\mathcal{S}_w^0} \rho(\hat{\phi}_I + \hat{\phi}_D)\mathbf{N}_P\, dS]\hat{\eta}e^{-i\omega t}\} \end{aligned} \tag{4.47}$$

The force $\mathbf{F}_e := \mathbf{F}_D + \mathbf{F}_I$ and the torque $\mathbf{T}_e := \mathbf{T}_D + \mathbf{T}_I$ are called **excitation force** and **excitation torque**, respectively. Assuming that the incident and diffracted potentials have been computed for a wide range of frequencies and directions of the incoming wave, it is now possible to define a complex transfer function $\mathbf{H}_{\eta e}(\omega,\theta)$ which relates the incoming wave elevation in complex form, $\hat{\eta}(\omega,\theta)$, to the resulting excitation force and torque. $\mathbf{H}_{\eta e}(\omega,\theta)$ is given as:

$$\mathbf{H}_{\eta e}(\omega,\theta) = i\omega \iint_{P\in\mathcal{S}_w^0} \rho(\hat{\phi}_I(\omega,\theta) + \hat{\phi}_D(\omega,\theta))\mathbf{N}_P\, dS \tag{4.48}$$

Assuming that the incident wave field consists of a superposition of wave trains $\hat{\eta}(\omega,\theta)$ of different frequencies and travelling along different directions, the total excitation force and torque are given as:

$$\mathbf{f}_e(t) = \sum_\omega \sum_\theta \Re\{\hat{\mathbf{f}}_e(\omega,\theta)e^{-i\omega t}\} \tag{4.49}$$

where

$$\hat{\mathbf{f}}_e(\omega,\theta) = \mathbf{H}_{\eta e}(\omega,\theta)\hat{\eta}(\omega,\theta) \tag{4.50}$$

[5] http://www.wamit.com/

[6] https://lheea.ec-nantes.fr/logiciels-et-brevets/nemoh-toolbox-192933.kjsp

If the effects of incident and diffracted waves must be examined individually, it is also possible to separately express the force (resp. torque) due to the incident potential ϕ_I - called the **dynamic Froude-Krylov force (resp. torque)** - and the force (resp. torque) due to the diffracted waves:

$$\begin{cases} \hat{\mathbf{f}}_{FK,d}(\omega,\theta) = \mathbf{H}_{\eta I}(\omega,\theta)\hat{\eta}(\omega,\theta) \\ \hat{\mathbf{f}}_{D}(\omega,\theta) = \mathbf{H}_{\eta D}(\omega,\theta)\hat{\eta}(\omega,\theta) \end{cases} \tag{4.51}$$

where

$$\begin{cases} \mathbf{H}_{\eta I}(\omega,\theta) = i\omega \iint\limits_{P\in\mathcal{S}_w^0} \rho\hat{\phi}_I(\omega,\theta)\mathbf{N}_P \, dS \\ \mathbf{H}_{\eta D}(\omega,\theta) = i\omega \iint\limits_{P\in\mathcal{S}_w^0} \rho\hat{\phi}_D(\omega,\theta)\mathbf{N}_P \, dS \end{cases} \tag{4.52}$$

Now consider the radiation force, due to the body motion in the mode d:

$$\begin{aligned} \mathbf{f}_{R_d}(t) &= -\iint\limits_{P\in\mathcal{S}_w^0} \rho\frac{\partial\phi_R}{\partial t}\mathbf{N}_P \, dS \\ &= \Re\{[\iint\limits_{P\in\mathcal{S}_w^0} \omega^2\rho\hat{\phi}_{R_d}\mathbf{N}_P \, dS]\hat{\xi}_d e^{-i\omega t}\} \end{aligned} \tag{4.53}$$

Define the following (column) vectors:

$$\begin{cases} \mathbf{A}_{R_d} = -\Re\{\iint\limits_{P\in\mathcal{S}_w^0} \rho\hat{\phi}_{R_d}\mathbf{N}_P \, dS\} \\ \mathbf{B}_{R_d} = -\omega\Im\{\iint\limits_{P\in\mathcal{S}_w^0} \rho\hat{\phi}_{R_d}\mathbf{N}_P \, dS\} \end{cases} \tag{4.54}$$

$\mathbf{f}_{R_d}(t)$ can be written as

$$\mathbf{f}_{R_d}(t) = \Re\{(-\omega^2\mathbf{A}_{R_d} - i\omega\mathbf{B}_{R_d})\hat{\xi}_d e^{-i\omega t}\} \tag{4.55}$$

For general oscillations, involving the six modes simultaneously, the six corresponding contributions are summed:

$$\mathbf{f}_R(t) = \Re\{\sum_{d=1}^{6}(-\omega^2\mathbf{A}_{R_d} - i\omega\mathbf{B}_{R_d})\hat{\xi}_d e^{-i\omega t}\} \tag{4.56}$$

which is more conveniently written in matrix form as:

$$\mathbf{f}_R(t) = \Re\{(-\omega^2\mathbf{A}_R - i\omega\mathbf{B}_R)\hat{\xi}e^{-i\omega t}\} \tag{4.57}$$

where

$$\begin{cases} \mathbf{A}_R = \begin{bmatrix} \mathbf{A}_{R_1} & \cdots \mathbf{A}_{R_6} \end{bmatrix} \\ \mathbf{B}_R = \begin{bmatrix} \mathbf{B}_{R_1} & \cdots \mathbf{B}_{R_6} \end{bmatrix} \end{cases} \tag{4.58}$$

Finally, for oscillations combining different frequencies, the total radiation force reads:

$$\mathbf{f}_R(t) = \Re\{\sum_{\omega}(-\omega^2\mathbf{A}_R(\omega) - i\omega\mathbf{B}_R(\omega))\hat{\xi}(\omega)e^{-i\omega t}\} \tag{4.59}$$

The frequency-dependent matrices $\mathbf{A}_R(\omega)$ and $\mathbf{B}_R(\omega)$ are called the **radiation added mass matrix** and the **radiation damping matrix**, respectively.

The transfer functions $\mathbf{H}_{\eta I}(\omega,\theta)$, $\mathbf{H}_{\eta D}(\omega,\theta)$, the radiation matrices $\mathbf{A}_R(\omega)$ and $\mathbf{B}_R(\omega)$, as well as $\mathbf{S}_{hs}$, are the typical outputs provided by hydrodynamic BEM solvers. Once the BEM solver has been run, solving the linear dynamical equations is straightforward, provided that the other forces (PTO and mooring system) are also modelled linearly. For example, assume that there is no PTO force, i.e. $\mathbf{f}_{pto} = \mathbf{0}$. Assume that the mooring system (see Section 4.5) exerts a linear

restoring force in the surge and sway direction (to prevent the floating body from drifting away) and a restoring moment in yaw (to maintain the body aligned with a prescribed direction of the *Oxy* plane):

$$\mathbf{f}_m = -\mathbf{S}_m \xi \tag{4.60}$$

with

$$\mathbf{S}_m = \begin{pmatrix} S_{m_{XX}} & 0 & 0 & 0 & 0 & 0 \\ 0 & S_{m_{YY}} & 0 & 0 & 0 & 0 \\ 0 & 0 & 0 & 0 & 0 & 0 \\ 0 & 0 & 0 & 0 & 0 & 0 \\ 0 & 0 & 0 & 0 & 0 & 0 \\ 0 & 0 & 0 & 0 & 0 & S_{m_{r_z r_z}} \end{pmatrix} \tag{4.61}$$

Now, for any combination of incoming waves with different frequencies and directions, and described in complex form $\hat{\eta}(\omega,\theta)$, the WEC motion can be calculated as follows:

$$\xi(t) = \Re\{\sum_{\omega}\sum_{\theta} \hat{\xi}(\omega,\theta) e^{-i\omega t}\} \tag{4.62}$$

where for each frequency ω and direction θ, $\hat{\xi}(\omega,\theta)$ is the solution of the following linear system:

$$[-\omega^2(\mathbf{M}_b + \mathbf{A}_R(\omega)) - i\omega\mathbf{B}_R(\omega) + \mathbf{S}_m + \mathbf{S}_{hs}]\hat{\xi}(\omega,\theta) = \hat{\mathbf{f}}_e(\omega,\theta) \tag{4.63}$$

and $\hat{\mathbf{f}}_e(\omega,\theta)$ is calculated as in Eq. (4.50).

Eq. (4.63) computes the steady-state WEC response to a variety of wave inputs. It is possible to define WEC transfer functions, which relate the solution $\hat{\xi}(\omega,\theta)$ to the wave input:

- If the wave input is considered to be the *excitation force*, then the transfer function $\mathbf{H}_{e\xi}(\omega)$ is calculated as

$$\mathbf{H}_{e\xi}(\omega) = [-\omega^2(\mathbf{M}_b + \mathbf{A}_R(\omega)) - i\omega\mathbf{B}_R(\omega) + \mathbf{S}_m + \mathbf{S}_{hs}]^{-1} \tag{4.64}$$

- If the wave input is considered to be the *wave elevation,* for a wave propagating along a given direction θ, then the transfer function $\mathbf{H}_{\eta\xi}(\omega,\theta)$ is calculated as

$$\mathbf{H}_{\eta\xi}(\omega,\theta) = \mathbf{H}_{e\xi}(\omega)\mathbf{H}_{\eta e}(\omega,\theta) \tag{4.65}$$

4.3.3.5 Cummins' equation

Assuming that linear potential flow theory is valid to describe hydrodynamic interactions, Eq. (4.63) is not yet entirely satisfactory. Firstly, no transient is modelled when solving Eq. (4.63); therefore, it is not possible to use Eq. (4.63) to know how the WEC reaches its steady-state motion in the incoming waves. Furthermore, some terms, other than those involved in Eq. (4.63), may need to be modelled in a non-linear way. For example, the PTO or mooring systems may be modelled in a non-linear fashion. Besides, as detailed in the subsection 4.3.4.1, some non-linear correction terms may be added to Eq. (4.63) in order to account for appropriate non-linear hydrodynamical effects.

Therefore, Eq. (4.63) needs an equivalent representation in the time domain. If the wave excitation occurs at a single frequency ω, the time-domain equivalent for Eq. (4.63) is a simple second-order linear system written as:

$$[\mathbf{M}_b + \mathbf{A}_R(\omega)]\ddot{\xi} + \mathbf{B}_R(\omega)\dot{\xi} + [\mathbf{S}_m + \mathbf{S}_{hs}]\xi = \mathbf{f}_e(t) \tag{4.66}$$

where

$$\mathbf{f}_e(t) = \sum_{\theta} \Re\{\mathbf{H}_{\eta e}(\omega,\theta)\hat{\eta}(\omega,\theta)e^{-i\omega t}\} \tag{4.67}$$

Difficulties arise when the wave input is polychromatic, i.e. contains more than one frequency. Indeed, the radiation force coefficients in Eq. (4.63) are frequency-dependent, which makes it impossible to use a classical linear second-order equation as a time-domain equivalent representation. Instead, Cummins [95] proposed to use the theory of integro-differential equations to model a ship's motion in an arbitrary wave field. Starting from the assumptions underlying linear hydrodynamic theory, the notion of *response superposition* - which usually means that a system's response is the sum of its responses to each individual *sinusoidal input* - is generalised by stating that the ship's and fluid's responses to infinitesimal *impulses* may be summed. Such an approach yields the well-known *Cummins' equation* [95]:

$$[\mathbf{M}_b + \mathbf{A}_\infty]\ddot{\xi} + \int_{\tau=0}^{\infty} \mathbf{K}_R(\tau)\dot{\xi}(t-\tau)d\tau + [\mathbf{S}_m + \mathbf{S}_{hs}]\xi = \mathbf{f}_e(t) \tag{4.68}$$

where the radiation *impulse response kernel*, $\mathbf{K}_R(\tau)$, and the radiation *infinite-frequency added mass*, $\mathbf{A}_\infty$, are related to the radiation frequency-dependent damping and added mass matrices, $\mathbf{B}_R(\omega)$ and $\mathbf{A}_R(\omega)$, through *Ogilvie's relations* [103]:

$$\begin{cases} \mathbf{B}_R(\omega) = \int_{\tau=0}^{\infty} \mathbf{K}_R(\tau)\cos(\omega\tau)d\tau \\ \mathbf{A}_R(\omega) = \mathbf{A}_\infty - \frac{1}{\omega}\int_{\tau=0}^{\infty} \mathbf{K}_R(\tau)\sin(\omega\tau)d\tau \end{cases} \tag{4.69}$$

and

$$\begin{cases} \mathbf{K}_R(\tau) = \frac{2}{\pi}\int_{\tau=0}^{\infty} \mathbf{B}_R(\omega)\cos(\omega\tau)d\omega \\ \mathbf{A}_\infty = \lim_{\omega\to\infty} \mathbf{A}_R(\omega) \end{cases} \tag{4.70}$$

Cummins' equation (4.68) was extensively validated in real seas for the response of ship motion, including in severe seas [103]. Eq. (4.68), and its frequency-domain equivalent (4.63), also form the basis for the vast majority of hydrodynamic WEC models [8], and have been studied extensively [7].

4.3.3.6 Approximation methods for the radiation memory terms

The convolution term in Cummins' equation represents a significant computational burden in time-marching numerical integration procedures. A direct computation of the convolution integral makes it preferable to use numerical schemes with a fixed time step (see Chapter 3 of [3]). Alternatively, to circumvent the need for the direct computation of the integral, various methods have been proposed in the literature [104], which approximate the radiation memory terms, using a *state-space approximation* or *Pronys method* [96]. Both approaches result in the system dynamical equations being expressed as an ODE, where the number of states depends on the order of the radiation approximation.

In particular, with state-space approximation approaches, Eq. (4.68) is augmented as follows:

$$\begin{cases} [\mathbf{M}_b + \mathbf{A}_\infty]\ddot{\xi} + + \mathbf{C}_R^{ss}\mathbf{x}_R^{ss} + [\mathbf{S}_m + \mathbf{S}_{hs}]\xi = \mathbf{f}_e(t) \\ \dot{\mathbf{x}}_R^{ss} = \mathbf{A}_R^{ss}\mathbf{x}_R^{ss} + \mathbf{B}_R^{ss}\dot{\xi} \end{cases} \tag{4.71}$$

where $\mathbf{x}_R^{ss}$ is a 'non-physical' state-vector, of which the size depends on the order chosen for the state-space approximation, and $\mathbf{A}_R^{ss}$, $\mathbf{B}_R^{ss}$ and $\mathbf{C}_R^{ss}$ are matrices of appropriate dimensions, determined so that the transfer function of the following state-space system:

$$\begin{cases} \dot{\mathbf{x}}_R^{ss} = \mathbf{A}_R^{ss}\mathbf{x}_R^{ss} + \mathbf{B}_R^{ss}\dot{\xi} \\ \mathbf{f}_R^{ss} = \mathbf{C}_R^{ss}\mathbf{x}_R^{ss} \end{cases} \tag{4.72}$$

is a satisfactory approximation to the transfer function $\mathbf{H}_{\dot{\xi}R}(\omega) := i\omega\mathbf{A}_R(\omega) + \mathbf{B}_R(\omega)$ which, from Eq. (4.57), relates the body velocity to the resulting radiation force.

A dynamical equation in the form of Eq. (4.71) can be easily recast in a state-space form (as a 1st-order ODE), for which more elaborate integration schemes, with adaptive time steps, can be employed. An example of such an integration scheme, widespread in the context of WEC simulation [3], is the Dormand-Prince solver, which is the default method in the Matlab/Simulink[7] simulation environment. It is estimated in [96] that state-space or Pronys methods allow for a reduction in the computational time by a factor between 8 and 80, with respect to the direct convolution approach. Nevertheless, the overall modelling accuracy is sensitive to the quality of the radiation approximation [96] while, with direct convolution and a constant integration time step method (such as a Runge-Kutta method), the accuracy of the radiation force calculation is guaranteed, when the time step tends to zero [104]. One of the case studies of Chapter 6 will provide the opportunity to examine these aspects in practice.

4.3.4 Bridging the gap between non-linear hydrodynamic modelling and IDE WEC models

Cummins' equation (4.68), and its frequency-domain equivalent (4.63), rely on linear hydrodynamic theory, and thus may become inaccurate when some of the assumptions of linear hydrodynamics are violated. In particular, as stressed in the introduction to this chapter, WECs may be designed to resonate in incident waves, thus violating the assumption of small motions [11]. Furthermore, neglecting drag forces due to the fluid viscosity and vortex shedding may result in overestimated WEC motion [101] and power absorption [57]. However, given the high computation cost associated with the PDE non-linear models of Sections 4.3.1 and 4.3.2, it is tempting to preserve Cummins' equation as the basis for the model formulation, improved through the addition of appropriate non-linear correction terms, as discussed in Section 4.3.4.1.

Such approaches are theoretically inconsistent, because they violate the linearity assumptions, while preserving an equation structure which was initially justified based on those very assumptions. Nevertheless, they deserve to be detailed here, because they may improve the realism of the hydrodynamic model results, at a relatively modest computational cost compared to that of CFD and the non-linear potential flow solvers of Sections 4.3.1 and 4.3.2. However, it must be stressed that there is, as yet, no published validation study to confirm the empirical validity of such approaches. Therefore, Section 4.3.4.2 also briefly discusses alternative ways in which new IDE models might be developed, in order to capture the realistic features of the Navier-Stokes equations (4.4) and (4.5), while remaining of small dimension, and avoiding the theoretical pitfall associated with the models of Section 4.3.4.1.

4.3.4.1 Non-linear extensions to Cummins' equation

To account for vorticity- or viscosity-induced dissipative forces, the most common method consists of adding the so-called Morison drag formula [105] to Eq. (4.68) which, in the context of WECs, expresses the dissipative drag term as a quadratic function of the relative velocity between the undisturbed oscillatory flow and the moving body [38]:

$$\mathbf{f}_{dis} = -\frac{1}{2}\rho\mathcal{A}_{dis}\mathbf{C}_{dis}|\dot{\xi} - \mathbf{u}_I|(\dot{\xi} - \mathbf{u}_I) \tag{4.73}$$

where $\mathbf{u}_I$ is the velocity of the undisturbed incident flow ϕ_I, $\mathcal{A}_{dis}$ is a matrix of characteristic areas and $\mathbf{C}_{dis}$ is a matrix of drag coefficients, which must be identified empirically. Assuming that the body velocity is significantly larger than the fluid velocity, a simplified form for Eq. (4.73) is often found in the literature - see for example [8, 106, 107] and Chapter 4 of [3]:

$$\mathbf{f}_{dis} = -\frac{1}{2}\rho\mathcal{A}_{dis}\mathbf{C}_{dis}|\dot{\xi}|\dot{\xi} \tag{4.74}$$

[7] www.mathworks.com

Sometimes, a linear dissipative term $-\mathbf{C}_{dis,l}\dot{\xi}$ is also added to Eq. (4.74) [106, 107] so that, defining $\mathbf{C}_{dis,q} := \frac{1}{2}\rho\mathcal{A}_{dis}\mathbf{C}_{dis}$ as the quadratic drag coefficient of Eq. (4.74), the total drag force is expressed as follows:

$$\mathbf{f}_{dis} = -\mathbf{C}_{dis,l}\dot{\xi} - \mathbf{C}_{dis,q}|\dot{\xi}|\dot{\xi} \tag{4.75}$$

The identification of drag coefficients is not a simple task, and is subject to significant uncertainty [101]. Therefore, a sensitivity analysis can be carried out, to assess the impact of the accuracy of the identified coefficients upon the simulation results. In [38], which assesses the performance of a selection of WEC concepts, it is found that varying $\mathbf{C}_{dis}$, from 1 to 4 times its nominal value, does not change the calculated power production by more than 30%. However, results in [38] do not assume that the WECs considered are operating under resonant-type control, which would likely enhance viscous dissipation effects. In [101], it is suggested to compare results from physical experiments or from a RANS solver (which include both fluid viscosity and vorticity effects) with those of an Euler solver (which only models vorticity effects), in order to discriminate the viscous effects (which do not scale through Froude scaling) from vorticity effects (which do scale through Froude scaling). Such a procedure could make the scaling of identified drag coefficients more robust. Although the results of [101] do not consider resonant-type control, they are based on monochromatic waves which match the WEC resonant frequency.

In addition to enhancing drag forces, amplifying the device motion may result in geometric non-linearities, due to the fact that the wetted surface $\mathcal{S}_w$ cannot be considered constant and equal to $\mathcal{S}_w^0$ any more: in particular, the simplified expression of Eq. (4.32) for the static pressure terms is no longer acceptable, and the dynamic pressure $\rho\partial\phi/\partial t$ cannot be integrated over $\mathcal{S}_w^0$ as in Eq. (4.37). A possible remedy consists of integrating the static and incident dynamic pressure over the exact instantaneous wetted surface, as opposed to the wetted surface at rest, while radiation and diffraction terms remain modelled linearly [8, 11, 90, 108]. The integration of the static pressure over $\mathcal{S}_w$ yields the so-called *non-linear static Froude-Krylov force*, while the integration of the dynamic incident pressure term $\rho\partial\phi_I/\partial t$ yields the so called *non-linear dynamic Froude-Krylov force*. The sum of static and dynamic non-linear Froude-Krylov forces is simply referred to as the *non-linear Froude-Krylov force*. The Froude-Krylov forces are thus given by the following equations:

$$\begin{cases} \mathbf{f}_{FK}^{st}(\xi,t) = \iint\limits_{P\in\mathcal{S}_w(\xi,t)} \rho g z \mathbf{N}_P dS \\ \mathbf{f}_{FK}^{dyn}(\xi,t) = -\iint\limits_{P\in\mathcal{S}_w(\xi,t)} \rho\frac{\partial\phi_I}{\partial t}\mathbf{N}_P dS \\ \mathbf{f}_{FK}(\xi,t) = \mathbf{f}_{FK}^{st}(\xi,t) + \mathbf{f}_{FK}^{dyn}(\xi,t) = -\iint\limits_{P\in\mathcal{S}_w(\xi,t)} \rho[\frac{\partial\phi_I}{\partial t} - gz]\mathbf{N}_P dS \end{cases} \tag{4.76}$$

where $\phi_I = \hat{\phi}_I(x,y,z)e^{-i\omega t}$ is given by combining Eqs. (4.38) and (4.43). The integration domain $\mathcal{S}_w(\xi,t)$ is calculated from the instantaneous body position ξ and from the free-surface η *corresponding to the undisturbed incident wave*. It is also possible to include, in Eq. (4.76), the 'incident' quadratic terms $\frac{\rho}{2}\nabla\phi_I.\nabla\phi_I$ of the Bernoulli equation (4.7), see for example [90, 108] but, for the sake of simplicity, such an option is not considered in this discussion.

Whether or not the quadratic terms are included, it is easily verified that the sum of the static and incident dynamic pressure fields, taken at the free surface η, are not zero which, when calculating the integrals in (4.76), is physically unrealistic. Therefore, the incident potential flow can be modified using a change of variables called *Wheeler stretching* [109]:

$$\hat{\phi}_I^W(x,y,z) = \hat{\phi}_I(x,y,\zeta) \tag{4.77}$$

where

$$\zeta := \frac{H(z-\eta)}{H+\eta} \tag{4.78}$$

Alternatively, and somewhat more rigorously, the incident potential can be calculated from non-linear wave theory, for example by running a HOS solver with no device (if polychromatic waves

are considered) [110], or by using semi-analytical formulations such as Stokes waves [111] (for monochromatic, deep-water waves), cnoidal waves [111] (for monochromatic, shallow-water waves), or Rienecker-Fenton waves [112] (whereby, for monochromatic, deep- or shallow-water waves, the incident potential flow is numerically approximated using a truncated Fourier expansion so as to satisfy the non-linear boundary conditions of Section 4.3.2). Preserving Airy's formulation for the incident potential is compared with Rienecker-Fenton's waves in [11], while Airy's formulation, the Wheeler stretching approach, Rienecker-Fenton's waves (for monochromatic waves) and HOS (for polychromatic waves) are compared in [113].

In practice, integrating the incident pressure can be carried out numerically through a discretisation of the hull. A remeshing routine may be used [90, 108] to discretise at best the instantaneous wetted surface $\mathcal{S}_w$; alternatively, a fine mesh can be used for the hull discretisation, so that integration over $\mathcal{S}_w$ only requires selecting those panels which are immersed [114]. In some cases, such as axisymmetric heaving point absorbers, analytical formulations can be used, which circumvent the need for a discretisation of the hull, and thus greatly reduce the computation time of non-linear Froude-Krylov force calculations [115].

Non-linear extensions to Cummins's equation can doubtlessly provide valuable qualitative insight into the importance of different non-linear dynamical effects. To that end, idealised, archetypal WEC models can be used as valuable case studies, as investigated at COER in recent years [11, 90, 113]. In particular, comparing cylindrical and spherical heaving point absorbers, [11] shows the major effect of non-linear static Froude-Krylov forces, when the device is made to resonate in incoming waves.

There are, at least, two major theoretical inconsistencies in non-linear Froude-Krylov approaches:

- The flow decomposition into its incident, diffracted and radiated components, in Eq. (4.41), stems from the linearity of the whole fluid-structure coupled problem, while the aim of non-linear Froude-Krylov approaches is *precisely* to model non-linear effects;
- Even if the flow decomposition is assumed true, keeping diffraction and radiation forces modelled linearly is questionable, especially if the device undergoes large vertical excursions.

The rationale behind such an abuse of the linear potential flow theory is that, for a body which is small compared to the wave length, such as a heaving point absorber, radiation and diffraction forces are small compared to Froude-Krylov forces. Note, however, that under controlled conditions, the control force acting onto the WEC tends to cancel static terms (such as the static Froude-Krylov force) [116], which might enhance the relative importance of modelling dissipative terms (such as radiation and drag forces). Therefore, non-linear Froude-Krylov extensions would need empirical validation under controlled conditions which, to the best of the author's knowledge, is still missing in the literature.

Non-linear extensions to Cummins' equation are included, for example, in the open-source WEC simulation software WECSIM [8], which offers the possibility of calculating Froude-Krylov forces non-linearly [117], and adding a viscous drag term in the simplified quadratic form of Eq. (4.74) [107].

Without giving any additional detail about viscous drag or non-linear Froude-Krylov force calculations, it can be reasonably claimed that the non-linear effects associated with such extensions of Cummins' equation will be written in a mathematical form such as:

$$\mathbf{f}_{nl} = \mathbf{f}_{nl}(\xi(t), \dot{\xi}(t), \tilde{e}_1(t), \tilde{e}_2(t), ..., \tilde{e}_{N_{F.T.}}(t)) \tag{4.79}$$

where $\tilde{e}_1(t), \tilde{e}_2(t), ..., \tilde{e}_{N_{F.T.}}(t)$ are a set of $N_{F.T.}$ forcing terms, which depend on the incident waves. For example, considering the Morrison formula of Eq. (4.73), $\mathbf{f}_{nl}$ depends on the WEC velocity

[8] https://wec-sim.github.io/WEC-Sim/

$\dot{\xi}$ and on the incident flow velocity $\mathbf{u}_I$. Similarly, the non-linear Froude-Krylov integrals of Eq. (4.76) depend on the WEC position (ξ) and on wave-dependent forcing terms (the incident pressure terms which enter into account in the integrals).

4.3.4.2 Towards new types of IDE models?

Under the restrictive assumptions of linear hydrodynamics, the fluid-structure interaction problem can be expressed as a function of the body dynamics only, as seen in Section 4.3.3. However, Section 4.3.4.1 suggests that preserving such an advantageous formulation, while introducing non-linear corrections, unavoidably leads to encountering theoretical inconsistencies and, as far as non-linear Froude-Krylov forces are concerned, has not been demonstrated empirically. However, removing assumptions brings back to equations which are distributed in space, as in Sections 4.3.1 and 4.3.2.

In addition, it should be stressed that, even if non-linear extensions to Cummins' equation were shown to have a wide range of empirical validity, such approaches rely on linear hydrodynamic BEM solvers, which usually take a significant amount of time to compute the hydrodynamic coefficients corresponding to the hull geometry of the WEC under study. Within the scope of hydrodynamic optimisation, even if Eq. (4.68) (possibly with some non-linear correction term) could be solved efficiently, calculating linear hydrodynamic coefficients at each cost function evaluation could turn out to be computationally prohibitive.

A possible solution could be the development of black-box or grey-box parametric models, identified from experiments, as proposed in [91]. However, such models rely heavily on the specific experiments chosen for the identification, and therefore may not be suitable for applications such as control and optimisation, where the operational space of the system is difficult to know (or guarantee) *a priori* (in terms of wave input, but also in terms of parameter values in the case of optimisation).

A possible way to avoid such shortcomings could consist of going back to the Navier-Stokes, Euler or non-linear potential flow equations, and to apply model order reduction techniques. Typically, in the field of fluid dynamics, model order reduction schemes first consider the Navier-Stokes equation, discretised in space [118]:

$$\frac{d\mathbf{x}_{NS}}{dt} = \mathbf{f}(\mathbf{x}_{NS}, t) \tag{4.80}$$

where $\mathbf{x}$ often has dimension N_{NS} larger than 10^6. The state vector is projected onto a set of basis functions, via a matrix Φ, as well as the discretised Navier-Stokes equation (4.80), via a matrix Ψ. If the two sets of basis functions are bi-orthonormal (see [118]), the resulting reduced-order model takes the following form:

$$\frac{d\mathbf{a}_{NS}}{dt} = \Psi^T \mathbf{f}(\Phi \mathbf{a}_{NS}, t) \tag{4.81}$$

where $\mathbf{a}_{NS}$, of dimension $N_a \ll N_x$, is the projection of $\mathbf{x}_{NS}$ and constitutes the reduced-order state vector. Therefore, the model to simulate is that of Eq. (4.81), formulated in terms of $\mathbf{a}_{NS}$, instead of that of Eq. (4.80). In the case of the incompressible Navier-Stokes equations, which are pertinent for wave energy applications, such an approach can be particularly advantageous, thanks to the quadratic form of the non-linearities, which makes the evaluation of $\mathbf{f}$ in Eq. (4.81) very efficient.

There are various possibilities to determine appropriate projections. Many popular methods are based on the state vector trajectory $\mathbf{x}_{NS}$ obtained from specific experiments [118, 119], which can be problematic in control and optimisation, for the same reason as the black-box or grey-box parametric models discussed above: the operational space of the system is not known *a priori*. For such applications, moment-matching model-order reduction techniques [119], which focus on reproducing the input-output behaviour of the system (as opposed to accurately reconstructing the whole state $\mathbf{x}_{NS}$), could make the reduced-order model less dependent on specific experiments.

To the author's knowledge, model order reduction of the Navier-Stokes, Euler or non-linear potential flow equations has not yet been investigated for the hydrodynamic modelling of WECs,

and could be an interesting path to investigate towards realistic and tractable models, suitable in particular for efficient simulation, optimisation and control.

4.3.5 Summary

In summary, from Sections 4.3.3 and 4.3.4, provided that a suitable IDE model can be determined, the hydrodynamic interaction component of the WEC dynamics in Eq. (4.2) may be written in the following form:

$$\mathcal{L}_f\{\xi\} - \mathbf{n}_f\{\xi,t\} - \mathbf{e}_f(t) - \mathbf{f}_m - \mathbf{f}_{pto} = \mathbf{0} \tag{4.82}$$

with

$$\begin{cases} \mathcal{L}_f\{\xi\} = [\mathbf{M}_b + \mathbf{A}_\infty]\ddot{\xi} + \mathbf{C}_f\dot{\xi} + \mathbf{S}_f\xi + \int_{\tau=0}^{\infty} \mathbf{K}_R(\tau)\dot{\xi}(t-\tau)d\tau \\ \mathbf{n}_f\{\xi,t\} := \mathbf{n}_f(\xi,\dot{\xi},t), \end{cases} \tag{4.83}$$

where, depending on the modelling option:

- $\mathbf{e}_f(t)$ may be the excitation force, the diffraction force, or any other additive forcing term derived from the incident wave;
- $\mathbf{C}_f$ represents a linear damping term (such as a linear viscous drag term) and $\mathbf{S}_f$ represents a linear restoring coefficient (typically the hydrostatic stiffness);
- $\mathbf{n}_f\{\xi,t\}$ represents some non-linear modelling terms dependent on ξ, its time-derivative, and the time-dependence represents possible forcing inputs derived from the incident wave, as in Eq. (4.79).

From the discussion of Section 4.3.4.2, in alternative formulations, more state variables may be included in addition to ξ, in order to describe more realistically the fluid-structure interaction dynamics.

Although, throughout this section, the case of a single floating body was considered, the modelling of a more complex system (for example involving several interconnected moving parts, or arrays or interacting WECs) would not fundamentally modify the form of Eq. (4.82).

Finally, note that the forcing terms ($\mathbf{e}_f(t)$, as well as the possible forcing terms in $\mathbf{n}$) are said, above, to be 'derived from the incident wave'. In practice, this means that those signals can be derived from some independent wave input, typically the wave elevation at some reference point in the horizontal plane. From Chapters 2 and 3, such a wave input can be considered a Gaussian process, and thus may be generated using harmonic superposition, as discussed thoroughly in Chapter 3.

4.4 Models for the PTO system

4.4.1 PTO components

The PTO system is responsible for converting the motion of the moving parts into exploitable energy. The conversion stages can be detailed as described in Fig. 4.4, adapted from [92] and [120]:

- The transmission stage converts the reciprocating motion of the moving parts into a rotary motion, exploitable by a rotary generator. The transmission system may consist of a hydraulic system, a mechanical gearbox or, more rarely, a pneumatic or magnetic transmission system. If a linear generator is employed instead of a rotary generator, the transmission stage is not necessary, which is described in the lower part of Fig. 4.4.
- In the generation stage, the rotary generator converts the rotation mechanical energy into electricity. With a linear generator, the motion of the generator is, instead, reciprocating.

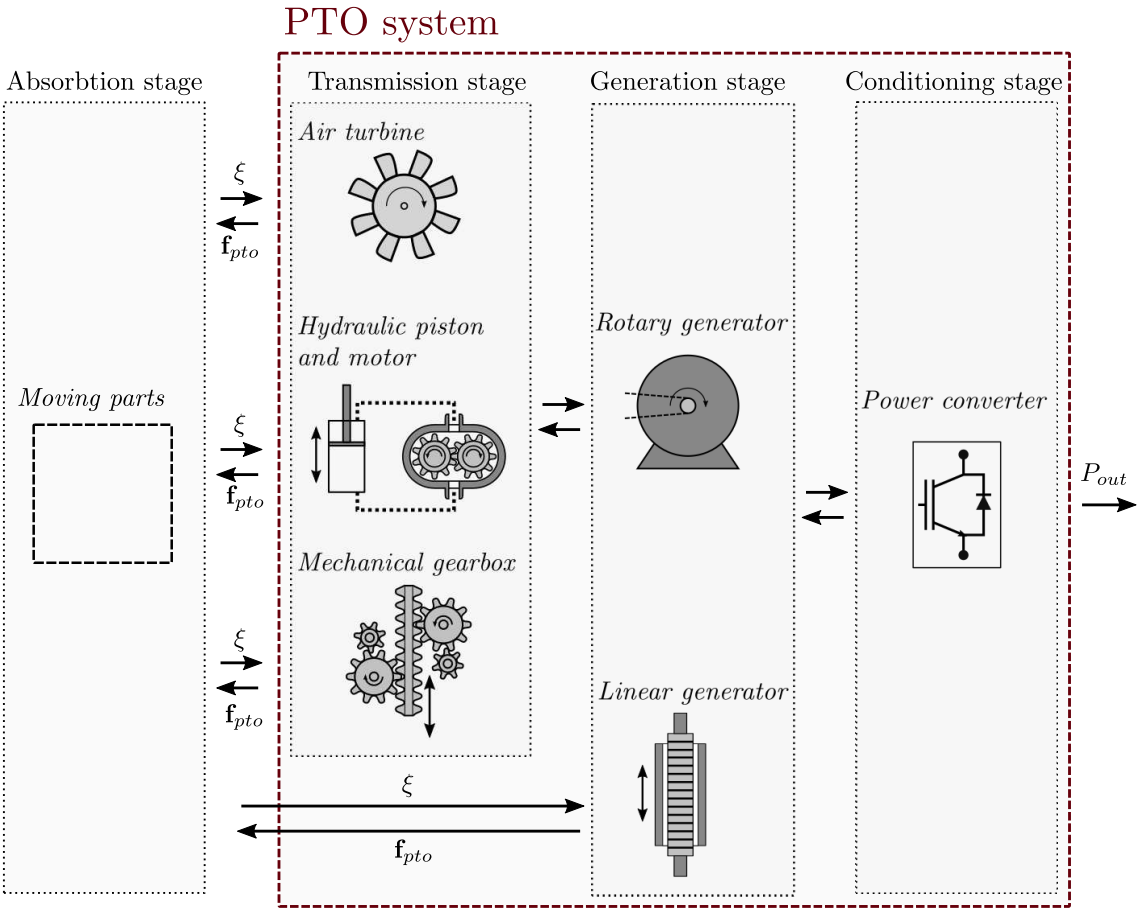

Figure 4.4: Schematic diagram of the most common PTO system components for WECs, adapted from [92] and [120]

- Finally, in order to comply with grid requirements, a power converter may be used to ensure prescribed quality of the output power delivered to the grid.

4.4.2 Towards parsimonious PTO models

WEC models which, in addition to representing the hydrodynamic interaction, include all conversion stages of the PTO systems, are referred to as *wave-to-wire* models. Given the scope of this chapter, it is important to determine the mathematical forms, which wave-to-wire models can take. From this perspective, it is useful to examine a particular example of a wave-to-wire WEC model, recently developed and validated at COER [121, 122, 123], and which certainly articulates all the main issues associated with the incorporation of the PTO dynamics in a WEC system model. The PTO model introduced and validated in [121, 122] comprises:

- a hydraulic circuit, activated under the effect of a piston rigidly connected to the WEC moving component;
- a rotary generator, activated by a hydraulic motor driven by the hydraulic circuit;
- a back-to-back power converter.

From [121, 122], it appears clearly that the three conversion stages can be modelled in state-space form, i.e. without requiring distributed variables, or without the use of memory terms as in

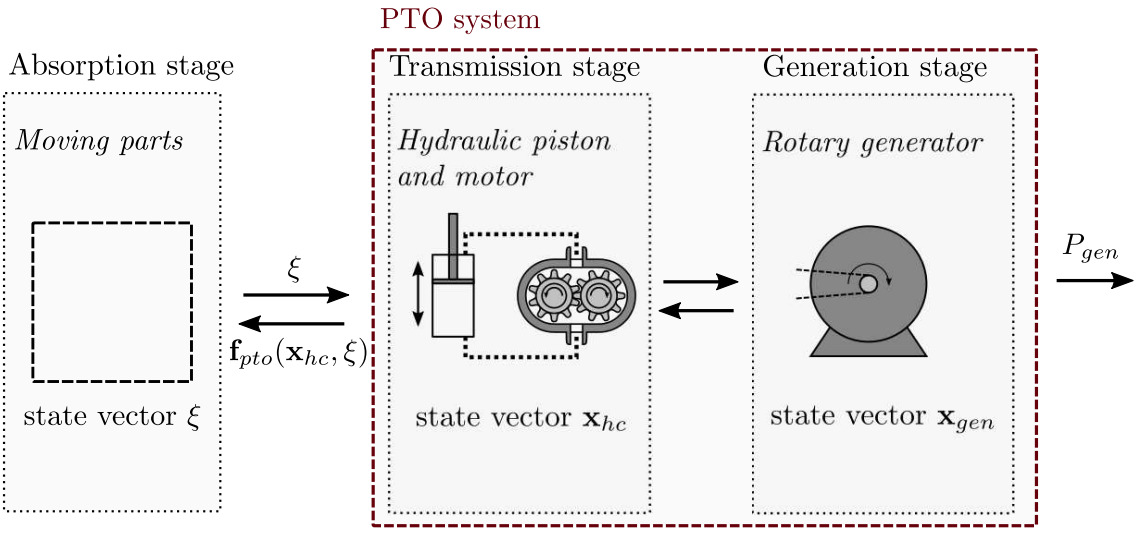

Figure 4.5: Simplified diagram of a WEC PTO system components, adapted from [125], with a hydraulic circuit for the transmission stage, and a rotary generator for the generation stage. The conversion stage is not modelled.

Cummins' equation (4.68). The more accurate the model, the more state variables must be added to account for specific physical effects. The number of additional variables necessary to describe the PTO system dynamics seems relatively reasonable - of the order of 6 for the PTO system in the complete model, without taking into account the conditioning stage. An issue, more important than the number of variables, is in fact that the time scales of the dynamics, corresponding to the different subcomponents, presents significant diversity: As studied in [124], the hydraulic system is a stiff system if compressibility effects are modelled, with dynamics orders of magnitude faster than those of the WEC motion. Furthermore, the electrical components of the generator are also subject to fast dynamics. Those high-frequency dynamics represent a major computational burden, since they imply that a very fine time step should be used, when numerically solving the corresponding differential equations.

A possible remedy consists of designing PTO models, which capture the essential dynamics of the WEC-PTO interaction, and provide realistic results in terms of power generation, without necessarily representing in detail the totality of the internal dynamics of the PTO system. Such a pragmatic approach is studied in [123] and [124], where the possibility of simplifying different parts of the PTO system description is investigated. A first step consists of excluding the power conditioning stage from the model, as illustrated in Fig. 4.5. Indeed, while the generator dynamics indeed have an influence on the power converter, the power converter has little or no influence onto the generator dynamics, so that the generator model can be decoupled from that of the converter. One is then left with variables to describe the hydraulic circuit dynamics ($\mathbf{x}_{hc}$), and variables to describe the generator dynamics ($\mathbf{x}_{gen}$).

Furthermore, it is found in [123] and [124] that, by neglecting compressibility effects in the hydraulic circuit, as well as transient electrical dynamics in the generator, the number of variables for the whole PTO system is reduced to only one (the generator rotational speed), while maintaining excellent agreement with the results of the complete wave-to-wire model, in terms of PTO force, pressure and power production, both on average and considering time-histories, and including experiments where the WEC is under reactive control. Note that, in this simplified model, it is found essential to preserve a realistic description of the various loss terms, which occur in the hydraulic piston and in the hydraulic motor, and which, fortunately, do not necessitate the addition of more state variables. The fast dynamics in the hydraulic and electrical subsystems, which were of negligible magnitude compared to the wave input dynamics, are eliminated by the model sim-

plifications. This permits all dynamics considered in the model to have similar time scales, from the wave input to the power output.

4.4.3 Summary

In summary, if the internal dynamics of the PTO system do not need to be modelled accurately, the PTO force may be written as a linear or non-linear function $\mathbf{h}_{pto}$ of the moving component dynamics, as follows:

$$\mathbf{f}_{pto} = \mathbf{h}_{pto}(\xi, \dot{\xi}) \tag{4.84}$$

Alternatively, if some internal dynamics of the PTO system must be explicitly modelled, as in [123, 124] and Fig. 4.5, Eq. (4.84) may be augmented with appropriate variables $\mathbf{x}_{pto}$ as follows:

$$\begin{cases} \dot{\mathbf{x}}_{pto} = \mathbf{g}_{pto}(\mathbf{x}_{pto}, \xi, \dot{\xi}, t) \\ \mathbf{f}_{pto} = \mathbf{h}_{pto}(\xi, \dot{\xi}, \mathbf{x}_{pto}) \end{cases} \tag{4.85}$$

where the first equation represents the internal PTO dynamics.

The results discussed in Section 4.4.2 suggest that $\mathbf{x}_{pto}$ need not be of large dimension, and that its dynamics described by Eq. (4.85) can have the same time scale as those of the moving parts, described in Eq. (4.82).

4.5 Models for mooring dynamics

4.5.1 Basic principles

Modelling the interaction of the moving parts with the mooring system can be important for many WECs, with the exception of devices which are directly mounted on the seabed or on some fixed structure. The following discussion is primarily based on [93], which reviews mathematical models for mooring systems in the context of wave energy. Mooring systems comprise a combination of the following components: anchors, buoys, weights and lines, which are schematically represented in Fig. 4.6. Those elements can be arranged following a variety of mooring configurations [93] including one or several mooring lines.

The basis of mooring system modelling is, like for the WEC moving parts, Newton's equation, applied to the different components of the mooring system. The most challenging components to model are, by far, the mooring lines, which in essence constitute distributed systems because the modelling variables depend on the curvilinear distance s along the line. The complete description of a mooring line may involve a significant number of variables, some of which are illustrated in Fig. 4.6:

- *Input variables:* the forcing terms for the mooring line dynamical equations include, at least, the position of the connection point between the line and the WEC moving part. This, with the force exerted by the mooring line onto the WEC, creates the coupling between the mooring and WEC dynamics. Some external forcing terms may be added, such as wave forces and currents acting directly onto the mooring components.

- *Distributed variables:* some of the unknown variables in the mooring dynamical equations are distributed across the curvilinear distance s along the line, such as the line position $\mathbf{r}_l(s)$ and its derivatives, as well as the tension $\mathbf{T}_l(s)$ along the mooring line.

- *Scalar variables:* some important variables, entering into account in the mooring line dynamical equations, are not distributed, such as the length of the mooring line or the coordinates of the touchdown point.

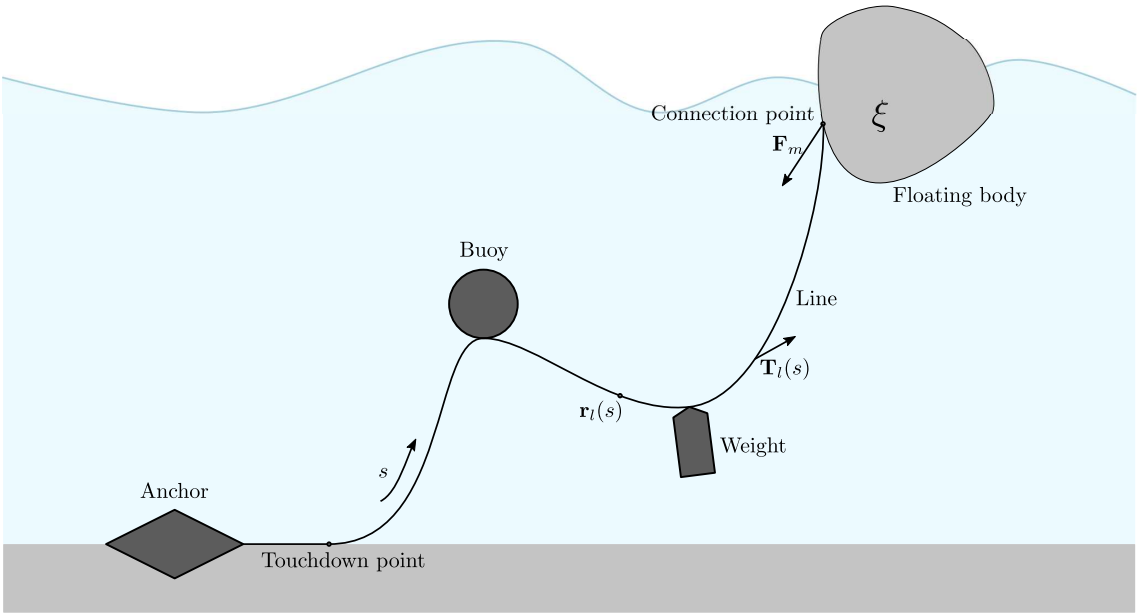

Figure 4.6: Schematic diagram of typical mooring components - adapted from [93]

Because of the distributed variables, the mooring line dynamical models usually take the form of partial differential equations, where the two integration variables are t and s.

In addition to coupling with the WEC motion, the physical effects which can be taken into account include the buoyancy and weight of the mooring line components, the inertial and damping effects due to hydrodynamic interaction of the mooring components with the surrounding fluid, and possible interactions with the sea bottom. Specific dynamics such as snap loads can also be given particular attention. Finally, note that the mooring line may, in fact, connect the floating body to the PTO system. In such a case, the interaction between the mooring line and the PTO system must also be considered.

The mathematical models can be classified into two broad categories: static and quasi-static models on the one hand, and dynamic models on the other hand.

4.5.2 Static and quasi-static models

Assuming constant environmental load, the focus of static models is to determine the equilibrium position of the WEC-mooring coupled system. Typically, by forcing the WEC to remain at a prescribed position away from its equilibrium position, the static mooring line position (described by the *catenary equation* [93]) is solved, and the static restoring force exerted by the mooring system onto the WEC can be determined. Applying such a procedure across a range of WEC positions provides curves of static restoring forces, illustrated in Fig. 4.7 (adapted from [126]).

In a quasi-static approach, although the WEC is modelled dynamically, the mooring system is assumed to be, at each instant, in static equilibrium. As a result, the mooring force onto the WEC can be modelled as a static restoring force (linear or non-linear), such as the one illustrated in Fig. 4.7, in the form:

$$\mathbf{f}_m = \tilde{\mathbf{f}}_m(\xi) \tag{4.86}$$

4.5.3 Dynamic models

Dynamic models represent the WEC and mooring system dynamics in a coupled way (similarly to the PTO dynamics being described using additional variables). In general, dynamic models

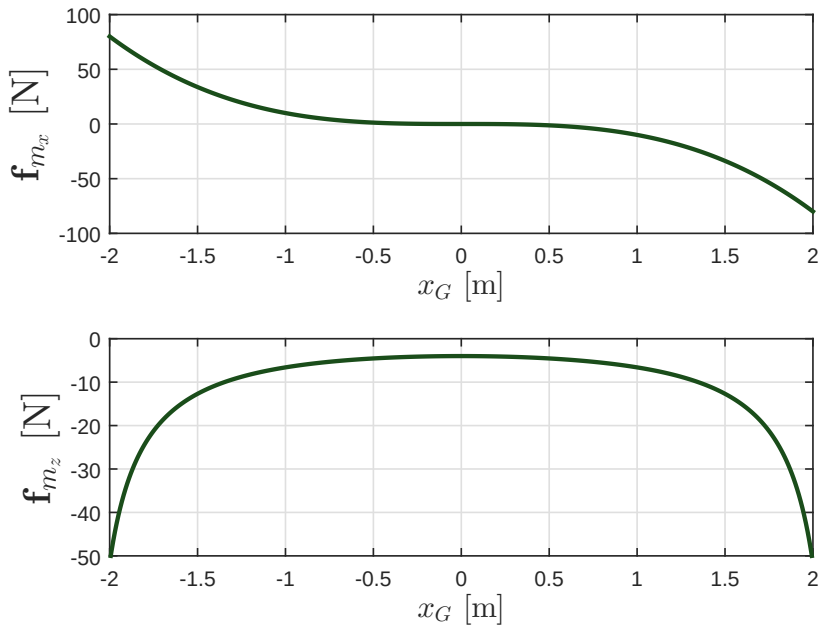

Figure 4.7: An example of static mooring restoring forces - adapted from [126]

require a spatial discretisation of the mooring lines, in order to transform the corresponding PDEs into a set of ODEs. Three main approaches are identified for mooring line discretisation:

- the lumped mass approach, which represents the mooring line as a chain of interconnected mass-spring-damper systems;
- finite-differences, which describe the mooring line by means of infinitesimal differential elements;
- finite element methods, whereby within each small 'segment' (or *element*) of the mooring line, the variables are described by means of basis functions (typically, Legendre polynomials). Compared to the lumped mass approach, finite element methods can provide more accurate results using a smaller number of discretised variables [93].

Solving for the discretised PDEs is essential to accurately model the mooring dynamics, but may result in the addition of a large number of variables in the overall WEC system model. Within the context of computationally-efficient WEC simulations, e.g. for power assessment, more concise representations may be desirable. In particular, some researchers have focused on how to describe the mooring force $\mathbf{f}_m$ directly as a function of the WEC coordinates ξ and their time-derivatives [93, 127, 128]. Typically, high-fidelity simulations or physical experiments are run choosing appropriate conditions, and the results are used to identify a concise model in a pertinent mathematical form $\mathbf{f}_m = \tilde{\mathbf{f}}_m(\xi, \dot{\xi}, \ddot{\xi})$:

- A possible approach consists of linearising the mooring system model, either by linearising the governing equations directly, or by finding linear transfer functions from the results of high-fidelity simulations or physical experiments. In such a case, it is easy to define a transfer function $\mathbf{H}_{\xi_m}$ such that, in complex form, the WEC position and the mooring force are related as follows:

$$\hat{\mathbf{f}}_m(\omega) = \mathbf{H}_{\xi_m}(\omega)\hat{\xi}(\omega) \tag{4.87}$$

  However, a linear description can be highly inaccurate [93].

- Based on high-fidelity simulations, physical experiments, or directly from the governing equations, another approach is to identify the parameters of some non-linear function, typically a polynomial (although Volterra models and artificial neural networks have also been reported [93]). For example, in [128] and other works by the same authors, including [127] in a wave energy context, the mooring force is expressed as a Taylor expansion up to cubic order, involving position, velocity and acceleration of the floating body.

The main difficulty associated with system identification procedures is that they must be based on experiments or simulations, which span a broad enough range of conditions, representative of those which the WEC will experience.

Similarly to the fluid-structure interaction problem, discussed in Section 4.3.4.2, model-order reduction techniques may be used, based on the mooring equations directly.

4.5.4 Summary

In summary, if a static or quasi-static model is suitable, or if an accurate system identification is successfully carried out, a concise representation can be formulated, whereby the mooring system is not explicitly modelled, and the mooring force is directly provided as some linear or non-linear function of ξ and its derivatives:

$$\mathbf{f}_m = \tilde{\mathbf{f}}_m(\xi, \dot{\xi}, \ddot{\xi}) \tag{4.88}$$

With consideration to the following chapter, the case where $\tilde{\mathbf{f}}_m$ is given in a polynomial form is of particular interest, because polynomial functions are infinitely smooth in their arguments.

Alternatively, it may be necessary to retain an explicit representation of the mooring system internal variables. In such a case, denoting $\mathbf{x}_m$ as the state variables associated with the mooring system components, the interaction between the WEC and the mooring system can be given in the following (linear or non-linear) state-space form:

$$\begin{cases} \dot{\mathbf{x}}_m = \mathbf{g}_m(\mathbf{x}_m, \xi, \dot{\xi}, \ddot{\xi}, t) \\ \mathbf{f}_m = \mathbf{h}_m(\mathbf{x}_m, \xi, \dot{\xi}, \ddot{\xi}, t) \end{cases} \tag{4.89}$$

where the dependence on t of $\mathbf{g}_m$ and $\mathbf{h}_m$ expresses the fact that environmental variables, such as waves or current, may also directly act on the mooring components.

4.6 A generic formulation for IDE WEC models

Finally, from Sections 4.2, 4.3, 4.4 and 4.5, it is now possible to give a little more substance to Eq. (4.1). Assuming that each of the three subsystems (hydrodynamic interaction, PTO system and mooring system) are modelled with explicitly-represented internal dynamics ξ, $\mathbf{x}_{pto}$ and $\mathbf{x}_m$, Eqs. (4.2), (4.82), (4.89) and (4.85) can be combined to yield a model of the form:

$$\mathcal{L}\{\mathbf{x}\} - \mathbf{n}\{\mathbf{x}, t\} - \mathbf{e}(t) = \mathbf{0} \tag{4.90}$$

where:

- The vector $\mathbf{x}$ comprises the variables modelling the three subsystems:

$$\mathbf{x} = \begin{pmatrix} \xi \\ \mathbf{x}_{pto} \\ \mathbf{x}_m \end{pmatrix} \tag{4.91}$$

- The linear terms $\mathcal{L}$ take the following form:

$$\mathcal{L}\{\mathbf{x}\} = (\mathbf{M} + \mathbf{M}_\infty)\ddot{\mathbf{x}} + \mathbf{C}\dot{\mathbf{x}} + \mathbf{S}\mathbf{x} + \int_{\tau=0}^{\infty} \mathbf{K}(\tau)\dot{\mathbf{x}}(t-\tau)d\tau \tag{4.92}$$

- The non-linear terms $\mathbf{n}\{\mathbf{x},t\}$ can be detailed as:

$$\mathbf{n}\{\mathbf{x},t\} := \mathbf{n}(\mathbf{x},\dot{\mathbf{x}},\ddot{\mathbf{x}},t) \tag{4.93}$$

  where the time-dependence represents forcing inputs derived from the incident waves, as discussed in Section 4.3.5. To represent the forcing terms more explicitly, Eq. (4.93) can be further detailed as:

$$\mathbf{n}(\mathbf{x},\dot{\mathbf{x}},\ddot{\mathbf{x}},t) = \mathbf{n}(\mathbf{x},\dot{\mathbf{x}},\ddot{\mathbf{x}},\tilde{e}_1(t),\tilde{e}_2(t),...,\tilde{e}_{N_{F.T.}}(t)) \tag{4.94}$$

  where $\tilde{e}_1(t),\tilde{e}_2(t),...,\tilde{e}_{N_{F.T.}}(t)$ are forcing terms, all derived from one or more independent wave inputs;

- $\mathbf{e}(t)$ represents an additive forcing input, derived from the incident waves.

The inertia, damping and stiffness matrices $\mathbf{M}$, $\mathbf{C}$ and $\mathbf{S}$, in Eq. (4.92), as well as the non-linear function $\mathbf{n}$ in Eq. (4.76), can involve contributions from the three subsystems. In contrast, it is more likely that the convolution and added mass terms, $\mathbf{K}$ and $\mathbf{M}_\infty$, only describe the radiation effects in that part of the model, describing the hydrodynamic interaction, and therefore can be further specified as:

$$\begin{cases} \mathbf{K}(\tau) = \begin{pmatrix} \mathbf{K}_R(\tau) & \mathbf{0} & \mathbf{0} \\ \mathbf{0} & \mathbf{0} & \mathbf{0} \\ \mathbf{0} & \mathbf{0} & \mathbf{0} \end{pmatrix} \\ \mathbf{M}_\infty = \begin{pmatrix} \mathbf{A}_\infty & \mathbf{0} & \mathbf{0} \\ \mathbf{0} & \mathbf{0} & \mathbf{0} \\ \mathbf{0} & \mathbf{0} & \mathbf{0} \end{pmatrix} \end{cases} \tag{4.95}$$

At this stage, consistently with Eq. (4.95), it is convenient to define the frequency-dependent added mass and damping matrices $\mathbf{A}(\omega)$ and $\mathbf{B}(\omega)$, defined as:

$$\begin{cases} \mathbf{A}(\omega) = \begin{pmatrix} \mathbf{A}_R(\omega) & \mathbf{0} & \mathbf{0} \\ \mathbf{0} & \mathbf{0} & \mathbf{0} \\ \mathbf{0} & \mathbf{0} & \mathbf{0} \end{pmatrix} \\ \mathbf{B}(\omega) = \begin{pmatrix} \mathbf{B}_R(\omega) & \mathbf{0} & \mathbf{0} \\ \mathbf{0} & \mathbf{0} & \mathbf{0} \\ \mathbf{0} & \mathbf{0} & \mathbf{0} \end{pmatrix} \end{cases} \tag{4.96}$$

where $[\mathbf{A}(\omega),\mathbf{B}(\omega)]$ on the one hand, and $[\mathbf{K}_R(\tau),\mathbf{A}_\infty]$ on the other hand, are related through Ogilvie's formula (4.69) and (4.70). $\mathbf{A}(\omega)$ and $\mathbf{B}(\omega)$ will be useful in Chapter 5.

The formulation of Eq. (4.90) has the merit of articulating, in a generic way, two components, namely memory terms and non-linear effects, which are often present in WEC models, and which are computationally challenging: the former because they tend to slow down time-domain numerical simulations, and the latter because they make linear frequency-domain calculations (which would circumvent the issue of memory terms) impossible.

The forcing terms of the model represented by Eq. (4.90), which consist of $\mathbf{e}(t)$ and $\tilde{e}_1(t),\tilde{e}_2(t)$,..., $\tilde{e}_{N_{F.T.}}(t)$ inside the expression for $\mathbf{n}$, deserve a detailed discussion. Throughout the rest of this thesis, the forcing,terms will be assumed to derive from one or more external *incident wave signals* (such as the wave elevation at some reference location), which are assumed Gaussian, following Chapter 2, and constitute the true forcing input to the system represented by Eq. (4.90). As seen in Chapter 3, such incident wave signals can be numerically simulated using harmonic superposition (either HRA or HDA). In such a case, the incident wave signal is periodic with period noted T, and it can be realistically assumed that all the forcing terms, $\mathbf{e}(t)$ and $\tilde{e}_1(t),\tilde{e}_2(t)$,..., $\tilde{e}_{N_{F.T.}}(t)$, are also periodic with period T.

In fact, in all the WEC model examples considered throughout the rest of this thesis (see Chapters 5 and 6):

- The incident wave signal is considered to be the free-surface elevation $\eta(t)$, measured at some reference point of the horizontal plane, assuming that the incident waves are unidirectional;
- All the forcing terms are *linearly* derived from $\eta(t)$.

As a consequence, if η is simulated using harmonic superposition, every forcing term involved in Eq. (4.90) can be easily derived, by multiplying the frequency-domain coefficients of η with appropriate transfer functions. This will be most clearly illustrated through the example of a spherical heaving point-absorber, developed in Chapter 6.

However, for the harmonic balance method to apply, as introduced in the next chapter, it is enough to know that each of the forcing terms $\mathbf{e}(t)$ and $\tilde{e}_1(t), \tilde{e}_2(t)$,..., $\tilde{e}_{N_{F.T.}}(t)$ is periodic with the same period T, without necessarily assuming that the relationship between the incident wave signals (say, η) and every forcing term is *linear*.

4.7 Summary

Current modelling approaches for WECs have been briefly reviewed, concerning the three main subsystems composing a WEC model: the hydrodynamic interaction coupled system, the PTO system and the mooring system. For each of the three subsystems, the chosen perspective was to understand which models lend themselves to a mathematical representation as a set of ODEs or IDEs, and what degree of realism can be reasonably expected from such models, which have the significant benefit of avoiding spatially-distributed variables. Finally, a generic IDE formulation for WEC models is proposed in Eq. (4.90), which encompasses as many WEC models as possible without resorting to spatially-distributed variables, and explicitly articulates both non-linear terms and memory terms, which are a salient and challenging feature of numerous IDE WEC models.

The chosen mathematical representation is a non-autonomous IDE, i.e. forcing terms are present. Those forcing terms can be referred to as the "wave inputs" to the model, and they derive from one or more external incident wave signals (such as the wave elevation at some reference location), which are modelled as Gaussian processes, following Chapters 2 and 3. When the incident wave signal is generated using harmonic superposition, all the forcing terms in Eq. (4.90) can be assumed to be periodic.

Admittedly, this chapter does not bring any new piece of knowledge in the field of wave energy. Therefore it may seem that its main outcome - Eq. (4.90) - is not worth the somewhat lengthy discussion which precedes it. However, since Eq. (4.90) and its variations will be the basis, upon which the harmonic balance technique is applied to the WEC simulation problem in Chapter 5, it is preferable to ensure that the reader is convinced, beforehand, that such a formulation is reasonably broad *and* realistic. While Eq. (4.1) is somewhat imprecise, it is now clear where Eq. (4.90) stands within the broader panorama of WEC modelling: it can safely be said that the formulation of Eq. (4.90) is capable of including mooring and PTO systems, modelled with a satisfactory degree of realism, and that its range of applicability, concerning hydrodynamic interaction, has been defined.

Furthermore, the basic aspects of WEC modelling detailed throughout this chapter will prove useful when introducing practical case studies, at the end of Chapter 5 and in Part III of this thesis. Finally, concerning hydrodynamic interaction, the author believes that the discussion of Section 4.3.4 can help in bridging the gap between 'traditional' WEC hydrodynamic modelling on the one hand, and the field of system dynamics and control on the other hand.

Chapter 5

The harmonic balance method for the numerical simulation of wave energy converters

5.1 Introduction

Numerical simulation approaches for IDE WEC models

Chapter 4 has given an overview of WEC modelling approaches, and has defined a class of WEC models described by equations in the form of Eq. (4.90). In the wave energy community, for WEC models such as (4.90), two main types of simulation methods are traditionally employed: frequency-domain calculations (when the non-linear terms $\mathbf{n}$ reduce to zero), and time-domain numerical integration schemes, already briefly discussed in Section 4.3.3.6 (when non-linear effects must be considered, or when transient dynamics are under investigation). Time-domain integration is orders of magnitude slower than frequency-domain calculations, in particular due to the computational cost of evaluating the radiation memory terms at each integration step. Techniques which approximate radiation memory terms (in a state-space form, or using Prony's method) circumvent the use of a convolution integral, at the cost of increasing the dimension of the system, while introducing approximation errors.

A third possibility consists of using statistical linearisation (termed "spectral models" by Folley [3]), which has been applied for a statistical characterisation of the WEC model outputs with specific types of non-linear effects. Statistical linearisation, in its current implementation for WEC simulation, operates under the assumption that both inputs and outputs can be modelled as stationary Gaussian processes, and consists of an iterative procedure in order to find the SDF for the output of interest. As per the procedure detailed in Chapter 4 of [3], only velocity-dependent non-linear terms can be handled, as investigated in [129], because the method linearly approximates the mechanical work of the non-linear forces, which is always zero for static forces. However, more recent work [130] shows that the method can be extended to static non-linear terms, by considering the average reactive energy associated with the non-linear forces, instead of their mechanical work. In its domain of application, statistical linearisation is orders of magnitude more efficient than time-domain integration, for providing estimates of the WEC output power or the SDF of any variable of interest. However, by definition, it eventually results in some input-dependent linear approximation for the non-linear dynamical terms, which can affect the results accuracy. In particular, the method is not suitable for calculating the solution *trajectory* of the WEC dynamical equation [129]. Furthermore, statistical linearisation implies that the wave input is Gaussian, and therefore cannot handle individual sinusoids as inputs.

Given the limitations of existing simulation methods for WEC IDE models, the author of

this thesis is convinced that there is scope for investigating other numerical techniques, which accommodate realistic IDE models, and remain more computationally attractive than time-domain integration. This could facilitate the development of wave energy technology, via efficient and accurate power assessment, and via the possibility of carrying out advanced design optimisation that go beyond linear hydrodynamics.

The harmonic balance method

Commonly used in several engineering applications, such as non-linear electric circuit analysis, vibration analysis of large-scale mechanical systems and fluid dynamics, the harmonic balance (HB) method is a special case of spectral methods[1], whereby the steady-state solution of a differential equation with periodic forcing terms is parametrised in terms of Fourier series. As will be further detailed throughout this chapter, the HB method efficiently and accurately deals with the two challenging features of Eq. (4.90), namely the convolution terms and the non-linear modelling terms.

The HB method results in the numerical solution being parametrised using a relatively small number of parameters (the Fourier expansion coefficients of the approximate solution), in contrast to time-domain integration procedures, where the solution must be calculated at a potentially large number of time steps. The method avoids the need for simulating transient dynamics, which is beneficial when only the steady-state WEC behaviour is of interest. Under conditions which will be specified throughout this chapter, the HB method also has appealing properties in terms of accuracy, since a small increase in the number of basis functions can decrease the error norm by several orders of magnitude.

Concerning computational time, the efficiency of the HB method largely depends on the quality of its practical implementation. More specifically, the HB method results in a non-linear algebraic equation of the following form:

$$\mathbf{r}(\hat{\mathbf{x}}) = \mathbf{0} \tag{5.1}$$

where $\hat{\mathbf{x}}$ is a vector representing the coefficients of the Fourier expansion of the unknown solution, and $\mathbf{r}$ is a *residual* vector. Eq. (5.1) is usually solved for $\hat{\mathbf{x}}$, using Newton's method or other related gradient-based algorithms. The explicit computation of the Jacobian of $\mathbf{r}$ in Eq. (5.1) is instrumental in improving the computational efficiency of the solution. Therefore, in this chapter, the practical details of the residual Jacobian computation are given appropriate care.

Finally, given the associated solution parametrisation, HB provides an interesting framework to explore the solution space, when some parameters of the WEC model or forcing terms vary. In particular, the *sensitivity equation* [97], which expresses how the solution changes for a small change in specific model parameters, can be solved at little computation cost using HB. This can be used to obtain an advantageous starting guess for the solution of Eq. (5.1), when the HB equation has already been solved for a closely-related WEC model or forcing signal, as will be detailed in Chapter 6. The sensitivity equation can also be used within the scope of gradient-based WEC optimisation, as will be shown in Chapter 7. Therefore, this chapter also presents how the sensitivity equation can be solved within the HB framework.

Chapter organisation

The rest of this chapter is organised as follows:

- The HB method is introduced in Section 5.2, within the broader framework of spectral methods;
- Section 5.3 presents the HB formulation for WEC models described by Eq. (4.90);

[1] *not* to be confused with the terminology "spectral models" in [3]

- Section 5.4 gives additional detail on the numerical method employed for the solution of the WEC HB equation;
- Based on an introductory example of a WEC model, Section 5.5 discusses further some of the fundamental properties of the HB method, in terms of practical implementation, accuracy, and comparison with time-domain numerical integration schemes;
- Considering a WEC model depending continuously on, and differentiable with respect to some design parameters, Section 5.6 shows how the sensitivity equation is efficiently solved in the HB framework;
- Section 5.7, based on the preceding sections, outlines a methodology for efficient WEC simulation employing HB;
- Finally, the main contributions of this chapter are summarised and discussed in Chapter 5.8.

5.2 The harmonic balance method: theoretical background

5.2.1 Spectral methods

Consider an integro-differential equation of the form:

$$\mathcal{H}\{y,s\} = e(s) \tag{5.2}$$

where e is a forcing term, s is the integration variable (space or time), $\mathcal{H}\{.\}$ is an integro-differential operator, which may be either linear or non-linear, and $y(s)$ is the unknown solution. Eq. (5.2) may also be subject to boundary conditions.

Define a suitable family of basis functions, $\Phi_n(s)$, for $n \in \mathbb{N}$. Spectral methods consist of searching for an approximation of y by a combination of a finite number of basis functions:

$$y(s) \approx y_N(s) := \sum_{n=0}^{N} \hat{y}_n \Phi_n(s) \tag{5.3}$$

Define

$$\hat{\mathbf{y}}_N = \begin{pmatrix} \hat{y}_0 \\ \hat{y}_1 \\ \vdots \\ \hat{y}_N \end{pmatrix} \tag{5.4}$$

and define the residual function

$$r(\hat{\mathbf{y}}_N, s) := \mathcal{H}\{y_N, s\} - e(s) \tag{5.5}$$

Then, the spectral method consists of finding a vector of coefficients $\hat{\mathbf{y}}_N$, which makes $r(\hat{\mathbf{y}}_N, s)$ as small as possible. The basic idea of spectral methods, as presented here, does not specify whether the differential equation is scalar- or vector-valued. In the latter case, $y(s)$, $e(s)$ and $\Phi_n(s)$ must be thought of as vector-valued functions of the variable s. The dimension of the integration variable s has not been specified either, but the presentation of spectral methods would remain the same for a multi-variate problem, i.e. if s were vector- rather than scalar-valued.

Many variants of spectral methods exist, which are defined by the choice of the functional basis, and the way the residuals are minimised. Concerning the functional basis, the most widespread family of functions are Chebyshev polynomials, which should be used as a default method [102]. However, with periodic boundary conditions, i.e. when the solution is assumed periodic in the integration domain, Fourier series are more appealing [102] (although Chebyshev polynomials

can work too). As discussed in Section 4.7, the steady-state WEC simulation problem is typically formulated as an IDE with periodic forcing terms, and thus lends itself particularly well to a parametrisation in terms of harmonic sinusoids.

Using Fourier or Chebyshev polynomials, and assuming that the actual solution is infinitely smooth[2], spectral methods are said to have an *exponential convergence rate* [102], which means that, when increasing the order N of the approximation, the error decreases faster than any law of the form $N^{-\beta}$, $\beta \in \mathbb{R}^+$. In applications, the convergence rate is ultimately governed by the presence or not, and nature of singularities, i.e. by the possible presence of discontinuities in the solution or one of its derivatives.

The residuals can be minimised in many different ways; however, as pointed out in [131], cited in Chapter 3 of [102], most methods to minimise r can be analysed in the common framework of "mean weighted residuals". Given the interval of integration $[s_{min}; s_{max}]$, define an inner product between two functions f and g in $L_2([s_{min}; s_{max}])$:

$$(f|g) := \int_{s_{min}}^{s_{max}} f(s)g(s)w(s)ds \tag{5.6}$$

where $w(s) \geq 0$ is a suitable weighting function. Then, the $N+1$ spectral coefficients of $\hat{\mathbf{y}}_N$ are found by solving for $N+1$ "mean weighted residual" equations

$$\big(\psi_i(s)|r(\hat{\mathbf{y}}_N, s)\big) = 0, \quad i \in \{0, 1, ...N\} \tag{5.7}$$

where the ψ_i are appropriately-chosen "test functions". Concerning the choice of test functions ψ_i, the two most interesting cases are *pseudo-spectral* (PS) and *Galerkin* methods.

Pseudo-spectral, or collocation methods

In PS methods, the test functions are chosen as

$$\psi_i(s) = \delta(s - s_i) \tag{5.8}$$

where the s_i form a grid of "collocation points" and $\delta(s)$ is the Dirac delta function. In essence, $\hat{\mathbf{y}}_N$ is determined by solving the following system of $N+1$ equations:

$$r(\hat{\mathbf{y}}_N, s_i) = 0, \quad i \in \{0, 1, ...N\} \tag{5.9}$$

The appropriate choice of collocation points depends on the problem considered and on the choice of basis functions ϕ_i. With a Fourier basis and periodic boundary conditions, a uniform grid is typically used [132].

Galerkin method

In the Galerkin method, the test functions are chosen to be identical to the basis functions:

$$\psi_i(s) = \phi_i(s) \tag{5.10}$$

so that the residuals are, in fact, projected onto the chosen functional basis, and $\hat{\mathbf{y}}_N$ is found by setting the spectral coefficients of the residuals to zero.

Note that, given the inner product specified in Eq. (5.6), basis functions are typically chosen orthogonal with respect to each other. Indeed, for an orthogonal set of basis functions (which is

[2] i.e. its derivatives of any order exist, and are continuous

the case for both Fourier and Chebyshev polynomials), the coefficients of the expansion of any function

$$f(s) = \sum_{n=0}^{\infty} \hat{f}_n \Phi_n(s) \tag{5.11}$$

can be computed using the inner product as:

$$\hat{f}_n = \frac{(\Phi_n | f)}{(\Phi_n | \Phi_n)} \tag{5.12}$$

5.2.2 The Harmonic Balance method

In the remainder of this thesis, the integration variable will be time, so that s is replaced with t. This deserves a brief discussion, because time-domain integration ($s = t$) is not the most usual application of spectral methods [102]. Instead, the integration variables are more often spatial. In fact, for differential equations involving both space and time derivatives, the solution is more usually expanded in space only, while integration in time is solved through a time-marching procedure [102, 133]. More specifically, given a spatial coordinate x and the time coordinate t, the solution is searched amongst expansions of the form

$$y_N(x,t) = \sum_{n=0}^{N} \hat{y}_n(t) \phi_n(x) \tag{5.13}$$

In other words, the expansion is *spatial*, and its coefficients are time varying. An example application for the three-dimensional simulation of ocean waves may be found in [134], and in HOS methods to solve the non-linear potential flow equations, as discussed in Section 4.3.2.

However, in some applications, spectral methods can be used successfully for the solution of differential equations *in the time domain*. In particular, problems which are time-periodic or quasi-periodic [135] lend themselves to a Fourier spectral approach, which approximates the steady-state solution of the non-linear differential equation considered. In such a context, the Fourier spectral (or Fourier-Galerkin) approach, is usually referred to as the *harmonic balance* (HB) method.

A brief review of the diverse applications and variants of the HB method can be found in the introduction of [135]. Engineering applications include, in particular, analysis and simulation of non-linear electric circuits, aeroelastic systems, periodic flows in fluid dynamics, and vibration in mechanical engineering (especially for large-scale mechanical problems). The HB framework also provides tools for the theoretical study of non-linear dynamical systems, in particular, bifurcation and stability analysis.

The mathematical foundations, upon which the HB method can be justified, are studied in [136], [137], and more recently, in [138]. Specifically, given a non-autonomous, non-linear, periodic differential equation, for which an *approximate* solution has been found (regardless of *how* it has been found), conditions are given for the existence of an *exact* solution in the vicinity of the approximate solution, and bounds on the approximation error are provided. However, those results are generally not used when the HB method is applied in practice [138].

5.2.3 Relevance of the HB method to the problem of WEC simulation

This subsection examines why HB can be identified as a relevant framework for the solution of the WEC differential equation, by highlighting similarities between the WEC simulation problem, and other types of problems which have been successfully solved using the HB approach.

In HB applications, the forcing term in the dynamical equation, $e(t)$, is assumed periodic in time. Typically, the forcing term is even assumed harmonic at a single frequency [135]. However, the forcing term is sometimes assumed to be multi-harmonic. In particular, the HB method has been used by some authors to determine the power spectrum of non-linear mechanical systems under random excitation [139]. As seen in Chapter 3 of this thesis, for the specific case

of Gaussian waves, a stationary random process may be approximated using a Fourier expansion covering the process spectrum [23]. Therefore, both the random excitation and the solution may be approximated using Fourier series, thus resulting in a HB problem, where the forcing term is multi-harmonic. By generating several samples of the excitation process, and solving for the Fourier approximation of the system response for each sample, the power spectrum of the response process can be estimated [139, 140, 141]. Likewise, the input to the WEC model, in a given wave spectrum, is also random, and can be modelled as a multi-harmonic, periodic signal, as thoroughly examined in Chapter 3. Therefore, from the point of view of the forcing terms, the WEC simulation problem is similar to the non-linear vibration analysis problems successfully treated in [139, 140, 141].

When large-scale, non-linear mechanical systems are considered, the application of Newton's second law typically yields second-order differential equations of the form [135]:

$$\mathbf{M}\ddot{\mathbf{x}} + \mathbf{C}\dot{\mathbf{x}} + \mathbf{S}\mathbf{x} - \mathbf{n}(\mathbf{x}, \dot{\mathbf{x}}) = \mathbf{e}(t) \tag{5.14}$$

where $\mathbf{x}$ represents the unknown displacement solution, $\mathbf{M}$ is the inertia matrix, $\mathbf{C}$ the damping matrix, $\mathbf{S}$ the stiffness matrix, $\mathbf{n}$ is a non-linear function of the system variables, and $\mathbf{e}(t)$ is the forcing term. WEC models, because they contain a mechanical part, as discussed in Chapter 4, can also be written in the form of second-order differential equations, with a combination of linear and non-linear terms, articulated in Eq. (4.90). Large-scale problems in structural dynamics, with formulations of the form (5.14), can be accurately solved using the HB method, reportedly orders of magnitude faster than time-marching schemes [142]. Although IDE models of single WEC systems typically have small dimension (of the same order of magnitude as the hydrodynamic degrees of freedom), WEC array models may be seen as large-scale mechanical systems. Therefore, the benefits of the HB method, as observed in [135] or [142], may extend to the simulation of WEC systems, and WEC arrays in particular.

In non-linear circuit analysis [132, 143, 144], a slightly different type of equation is usually solved using the HB method:

$$\int_0^\infty \mathbf{K}(\tau)\mathbf{v}(t-\tau)d\tau + \mathbf{n}(\mathbf{v}, \dot{\mathbf{v}}) + \mathbf{i}_s(t) = 0 \tag{5.15}$$

where $\mathbf{v}$ is the vector of (unknown) voltages at the circuit nodes and $\dot{\mathbf{v}}$ their time derivatives; the source current $\mathbf{i}_s(t)$ represents the forcing term, assumed periodic; $\mathbf{n}$ is a non-linear current function; finally, $\mathbf{K}(\tau)$ is the impulse-response kernel associated with the linear part of the circuit.

Eq. (5.15) is a first-order IDE. As seen, for example, in [143, 144], when the solution is parametrised in terms of Fourier basis functions, the linear memory (or convolution) term can be easily calculated, using the frequency-domain transfer function corresponding to the impulse-response kernel $\mathbf{K}(\tau)$. Thus, using the HB method, the computational cost of calculating the convolution integral is avoided. As seen in Chapter 4, IDE WEC models derived from a non-linear extension of Cummins' equation also typically contain a convolution integral, due to the radiation memory effect. As will be further detailed in Section 5.3, the treatment of the convolution integral in the HB framework also proves highly beneficial for WEC simulation.

Note that the electrical analogue has been used for a long time in the analysis of *linear* WEC models [7], as a means to assist in the theoretical understanding of WEC dynamics, and to apply well-known electrical engineering methods to the modelling, analysis and control [9] of WEC systems. Interestingly, the analogy can be extended to *non-linear* electrical circuit and WEC system models. In [145], and other works by the same authors, a systematic representation of WEC systems through equivalent electrical circuits is examined, including non-linear effects associated with the mooring line and the PTO system. The application of the HB technique to WEC simulation, as examined in the next sections and chapters, suggests that, beyond the simple analogy between non-linear WEC and electric circuit models, powerful numerical tools for non-linear circuit simulation can be successfully transposed to non-linear WEC model simulation.

5.3 Application of the harmonic balance method for the simulation of wave energy converters

As discussed in Chapter 4, Eq. (4.90) describes the WEC system dynamics in residual form. In Eq. (4.90), the non-linear term $\mathbf{n}\{\mathbf{x},t\}$ denotes a non-linear function $\mathbf{n}(\mathbf{x},\dot{\mathbf{x}},\ddot{\mathbf{x}},t)$. For simplicity and ease of notation, throughout the rest of this chapter, it will be assumed that $\mathbf{n}$ depends on $\mathbf{x}$ up to the first-order derivative only, i.e. $\mathbf{n}\{\mathbf{x},t\} := \mathbf{n}(\mathbf{x},\dot{\mathbf{x}},t)$. However, all the developments presented easily extend to the more general case of second-order derivatives.

5.3.1 Projection of the variables onto the Fourier basis

The Fourier spectral method (i.e. the HB method) is applied for the numerical solution of Eq. (4.90). Define $\Delta\omega = 2\pi/T$, the period of the forcing terms (and presumably of the solution), an integer N_ω, and for $n = 1...N_\omega$, $\omega_n = n\Delta\omega$. Each component of the unknown solution $\mathbf{x}(t)$ is expressed as a Fourier series:

$$\forall d \in \{1...D\},\ x_d(t) = \frac{1}{\sqrt{2}}\hat{x}_{d,0} + \sum_{n=1}^{N_\omega} \hat{x}_{d,2n-1}\cos(\omega_n t) + \hat{x}_{d,2n}\sin(\omega_n t) \tag{5.16}$$

where D is the dimension of $\mathbf{x}$.

The expansion (5.16) is the application, for the special case of a Fourier functional basis, of the generic expansion of Eq. (5.3). In Eq. (5.16), there are $2N_\omega + 1$ basis functions involved, with

$$\phi_0(t) = \frac{1}{\sqrt{2}} \quad \text{and} \quad \begin{cases} \phi_{2n-1}(t) = \cos(\omega_n t) \\ \phi_{2n}(t) = \sin(\omega_n t) \end{cases} \quad \text{for } n = 1...N_\omega \tag{5.17}$$

If the very same formalism as in Eq. (5.3) were rigorously adopted, the expansion of Eq. (5.16) should be described as being of order $2N_\omega$. However, throughout the rest of this thesis, the expansion of Eq. (5.16) will be referred to as being of order N_ω, to more clearly convey the idea of a Fourier expansion up to the N_ω^{th} harmonic.

Define the following inner product $(.|.)$, for any functions f and g in $L_2([0;T])$:

$$(f|g) := \frac{2}{T}\int_0^T f(t)g(t)\,dt \tag{5.18}$$

The chosen Fourier basis is obviously orthonormal with respect to the inner product $(.|.)$. Accordingly, the Fourier coefficients of any function f in $L_2([0;T])$ can be recovered as:

$$\begin{cases} \hat{f}_0 = \frac{1}{T}\int_{t=0}^{T} f(t)\,dt \\ \hat{f}_{2n-1} = \frac{2}{T}\int_{t=0}^{T} \cos(\omega_n t)f(t)\,dt \\ \hat{f}_{2n} = \frac{2}{T}\int_{t=0}^{T} \sin(\omega_n t)f(t)\,dt \end{cases} \tag{5.19}$$

After those preliminary remarks on the Fourier basis, the expansion of the vector-valued $\mathbf{x}(t)$ is constructed. For $i = 0...2N_\omega$, note

$$\hat{\mathbf{x}}_i = \begin{pmatrix} \hat{x}_{1,i} \\ \vdots \\ \hat{x}_{D,i} \end{pmatrix} \tag{5.20}$$

which corresponds to the i^{th} (vector-valued) coefficient in the expansion of $\mathbf{x}(t)$. In other words,

$$\mathbf{x}(t) = \frac{1}{\sqrt{2}}\hat{\mathbf{x}}_0 + \sum_{n=1}^{N_\omega} \cos(\omega_n t)\hat{\mathbf{x}}_{2n-1} + \sin(\omega_n t)\hat{\mathbf{x}}_{2n} \tag{5.21}$$

Concatenating the $\hat{\mathbf{x}}_i$ together, the solution $\mathbf{x}(t)$ is entirely characterised by the vector $\hat{\mathbf{x}} \in \mathbb{R}^{D(2N_\omega+1)}$ defined as:

$$\hat{\mathbf{x}} = \begin{pmatrix} \hat{\mathbf{x}}_0 \\ \vdots \\ \hat{\mathbf{x}}_{2N_\omega} \end{pmatrix} \tag{5.22}$$

From the trigonometric functional basis, define $2N_\omega + 1$ diagonal matrix-valued functions $\varphi_i(t) \in \mathbb{R}^{D\times D}$:

$$\begin{cases} \varphi_0(t) = \frac{1}{\sqrt{2}}\mathbb{I}_D \\ \varphi_{2n-1}(t) = \cos(\omega_n t)\mathbb{I}_D \\ \varphi_{2n}(t) = \sin(\omega_n t)\mathbb{I}_D \end{cases} \tag{5.23}$$

and concatenate them into a matrix $\Phi(t) \in \mathbb{R}^{D\times(2N_\omega+1)D}$, defined as:

$$\Phi(t) = \begin{pmatrix} \varphi_0(t) & \varphi_1(t) & \cdots & \varphi_{2N_\omega}(t) \end{pmatrix} \tag{5.24}$$

Accordingly, given the parametrisation $\hat{\mathbf{x}}$, $\mathbf{x}(t)$ is conveniently expressed as:

$$\mathbf{x}(t) = \sum_{i=0}^{2N_\omega} \varphi_i(t)\hat{\mathbf{x}}_i = \Phi(t)\hat{\mathbf{x}} \tag{5.25}$$

The derivatives of $\mathbf{x}(t)$ can be readily expanded in terms of the coefficients of $\mathbf{x}(t)$:

$$\dot{\mathbf{x}}(t) = \sum_{n=1}^{N_\omega} -\omega_n \sin(\omega_n t)\hat{\mathbf{x}}_{2n-1} + \omega_n \cos(\omega_n t)\hat{\mathbf{x}}_{2n} \tag{5.26}$$

so that

$$\begin{cases} \hat{\dot{\mathbf{x}}}_0 = \mathbf{0}_{\mathbb{R}^D} \\ \hat{\dot{\mathbf{x}}}_{2n-1} = \omega_n \hat{\mathbf{x}}_{2n} \\ \hat{\dot{\mathbf{x}}}_{2n} = -\omega_n \hat{\mathbf{x}}_{2n-1} \end{cases} \tag{5.27}$$

Define a block-diagonal matrix $\Omega \in \mathbb{R}^{D(2N_\omega+1)\times D(2N_\omega+1)}$ as:

$$\Omega = \begin{pmatrix} \Omega_0 & \mathbf{0} & \cdots & \mathbf{0} \\ \mathbf{0} & \Omega_1 & \cdots & \mathbf{0} \\ \vdots & \vdots & \ddots & \vdots \\ \mathbf{0} & \mathbf{0} & \cdots & \Omega_{N_\omega} \end{pmatrix} \tag{5.28}$$

where the matrices on the diagonal are given as:

$$\begin{cases} \Omega_0 = \mathbf{0}_D \\ \Omega_n = \begin{pmatrix} \mathbf{0}_D & \omega_n \mathbb{I}_D \\ -\omega_n \mathbb{I}_D & \mathbf{0}_D \end{pmatrix} \quad \text{for } n = 1 \ldots N_\omega \end{cases} \tag{5.29}$$

Then, the expansion of the first-order derivative, $\hat{\dot{\mathbf{x}}}$, is given as

$$\hat{\dot{\mathbf{x}}} = \Omega\hat{\mathbf{x}} \tag{5.30}$$

Similarly, the expansion of the second-order derivative, $\hat{\ddot{\mathbf{x}}}$, is given as:

$$\hat{\ddot{\mathbf{x}}} = \Omega^2\hat{\mathbf{x}} \tag{5.31}$$

Note that Eq. (4.90) may also be expressed as a first-order IDE, by considering a different state vector $\bar{\mathbf{x}}$ defined as:

$$\begin{cases} \bar{\mathbf{x}}_1 := \mathbf{x} \\ \bar{\mathbf{x}}_2 := \dot{\mathbf{x}} \end{cases} \quad \text{and} \quad \bar{\mathbf{x}} := \begin{pmatrix} \bar{\mathbf{x}}_1 \\ \bar{\mathbf{x}}_2 \end{pmatrix} \tag{5.32}$$

so that Eq. (4.90) may be recast in terms of $\bar{\mathbf{x}}$ and its first-order derivative alone. However, such a formulation requires a two-fold increase in the number of variables: instead of being of size D like $\mathbf{x}$, the state vector $\bar{\mathbf{x}}$ is of size $2D$, thus resulting in a residual equation of size $2D$. In the spectral formulation, first- and second-order derivatives (and, in fact, derivatives of any order) are straightforwardly expressed, without any approximation, as a function of the expansion of $\mathbf{x}$, as seen in Eqs. (5.30) and (5.31). Therefore, from a practical point of view, there is no strong rationale for adopting a "first-order" formulation. Instead, it is better to preserve the "second-order" formulation of Eq. (4.90), which is treated in an easy way using a spectral method, and maintains the problem size as small as possible.

The linear terms in Eq. (4.90) deserve special attention. Assume that $\mathbf{x}$ is expanded as

$$\mathbf{x}(t) = \frac{1}{\sqrt{2}}\hat{\mathbf{x}}_0 + \sum_{n=1}^{N_\omega} \cos(\omega_n t)\hat{\mathbf{x}}_{2n-1} + \sin(\omega_n t)\hat{\mathbf{x}}_{2n} \tag{5.33}$$

Replacing $\mathbf{x}$ with its expansion in the linear part of Eq. (4.90), detailed in Eq. (4.92), $\mathcal{L}\{\mathbf{x}\}$ yields:

$$\begin{aligned}
\mathcal{L}\{\mathbf{x},t\} = &\sum_{n=1}^{N_\omega} -\omega_n^2[\mathbf{M}+\mathbf{M}_\infty]\hat{\mathbf{x}}_{2n-1}\cos(\omega_n t) - \omega_n^2[\mathbf{M}+\mathbf{M}_\infty]\hat{\mathbf{x}}_{2n}\sin(\omega_n t) \\
&+ \sum_{n=1}^{N_\omega} \omega_n \mathbf{C}\hat{\mathbf{x}}_{2n}\cos(\omega_n t) - \omega_n \mathbf{C}\hat{\mathbf{x}}_{2n-1}\sin(\omega_n t) \\
&+ \frac{1}{\sqrt{2}}\mathbf{S}\hat{\mathbf{x}}_0 + \sum_{n=1}^{N_\omega} \mathbf{S}\hat{\mathbf{x}}_{2n-1}\cos(\omega_n t) + \mathbf{S}\hat{\mathbf{x}}_{2n}\sin(\omega_n t) \\
&+ \sum_{n=1}^{N_\omega} \Big[\int_{\tau=0}^{\infty} \mathbf{K}(\tau)\omega_n \cos(\omega_n(t-\tau))\, d\tau\Big]\, \hat{\mathbf{x}}_{2n} - \Big[\int_{\tau=0}^{\infty} \mathbf{K}(\tau)\omega_n \sin(\omega_n(t-\tau))\, d\tau\Big]\, \hat{\mathbf{x}}_{2n-1}
\end{aligned} \tag{5.34}$$

Recalling that, as defined in Eqs. (4.96) and (4.95), $[\mathbf{K}(\tau), \mathbf{M}_\infty]$ are related to frequency domain equivalent matrices $[\mathbf{A}(\omega), \mathbf{B}(\omega)]$ through Ogilvie's formula (4.69) and (4.70), the convolution terms can be simplified as follows:

$$\begin{aligned}
\int_{\tau=0}^{\infty} \mathbf{K}(\tau)\cos(\omega_n(t-\tau))\, d\tau &= \cos(\omega_n t)\int_{\tau=0}^{\infty} \mathbf{K}(\tau)\cos(\omega_n\tau)\, d\tau + \sin(\omega_n t)\int_{\tau=0}^{\infty} \mathbf{K}(\tau)\sin(\omega_n\tau)\, d\tau \\
&= \cos(\omega_n t)\mathbf{B}(\omega_n) - \omega_n \sin(\omega_n t)[\mathbf{A}(\omega_n) - \mathbf{M}_\infty]
\end{aligned} \tag{5.35}$$

where the second equality is deduced from Ogilvie's relation [103], given in Eqs. (4.69) and (4.70). Similarly:

$$\begin{aligned}
\int_{\tau=0}^{\infty} \mathbf{K}(\tau)\sin(\omega_n(t-\tau))\, d\tau &= -\cos(\omega_n t)\int_{\tau=0}^{\infty} \mathbf{K}(\tau)\sin(\omega_n\tau)\, d\tau + \sin(\omega_n t)\int_{\tau=0}^{\infty} \mathbf{K}(\tau)\cos(\omega_n\tau)\, d\tau \\
&= \omega_n \cos(\omega_n t)[\mathbf{A}(\omega_n) - \mathbf{M}_\infty] + \sin(\omega_n t)\mathbf{B}(\omega_n)
\end{aligned} \tag{5.36}$$

Finally, $\mathcal{L}$ has the following expansion:

$$\begin{aligned}\mathcal{L}\{\mathbf{x},t\} = &\sum_{n=1}^{N_\omega} -\omega_n^2\mathbf{M}\hat{\mathbf{x}}_{2n-1}\cos(\omega_n t) - \omega_n^2\mathbf{M}\hat{\mathbf{x}}_{2n}\sin(\omega_n t)\\ &+\sum_{n=1}^{N_\omega} \omega_n\mathbf{C}\hat{\mathbf{x}}_{2n}\cos(\omega_n t) - \omega_n\mathbf{C}\hat{\mathbf{x}}_{2n-1}\sin(\omega_n t)\\ &+\frac{1}{\sqrt{2}}\mathbf{S}\hat{\mathbf{x}}_0 + \sum_{n=1}^{N_\omega} \mathbf{S}\hat{\mathbf{x}}_{2n-1}\cos(\omega_n t) + \mathbf{S}\hat{\mathbf{x}}_{2n}\sin(\omega_n t)\\ &+\sum_{n=1}^{N_\omega} \omega_n\mathbf{B}(\omega_n)\hat{\mathbf{x}}_{2n}\cos(\omega_n t) - \omega_n\mathbf{B}(\omega_n)\hat{\mathbf{x}}_{2n-1}\sin(\omega_n t)\\ &+\sum_{n=1}^{N_\omega} -\omega_n^2\mathbf{A}(\omega_n)\hat{\mathbf{x}}_{2n-1}\cos(\omega_n t) - \omega_n^2\mathbf{A}(\omega_n)\hat{\mathbf{x}}_{2n}\sin(\omega_n t)\end{aligned} \tag{5.37}$$

Define a block-diagonal matrix $\mathbf{L} \in \mathbb{R}^{D(2N_\omega+1)\times D(2N_\omega+1)}$, as follows:

$$\mathbf{L} = \begin{pmatrix} \mathbf{L}_0 & \mathbf{0} & \cdots & \mathbf{0} \\ \mathbf{0} & \mathbf{L}_1 & \cdots & \mathbf{0} \\ \vdots & \vdots & \ddots & \vdots \\ \mathbf{0} & \mathbf{0} & \cdots & \mathbf{L}_{N_\omega} \end{pmatrix} \tag{5.38}$$

where the matrices on the diagonal are given as:

$$\begin{cases} \mathbf{L}_0 = \mathbf{S} \\ \mathbf{L}_n = \begin{pmatrix} \mathbf{S} - \omega_n^2[\mathbf{M}+\mathbf{A}(\omega_n)] & \omega_n[\mathbf{C}+\mathbf{B}(\omega_n)] \\ -\omega_n[\mathbf{C}+\mathbf{B}(\omega_n)] & \mathbf{S} - \omega_n^2[\mathbf{M}+\mathbf{A}(\omega_n)] \end{pmatrix} & \text{for } n = 1...N_\omega \end{cases} \tag{5.39}$$

Then, if $\hat{\mathbf{x}}$ represents the coefficients of the Fourier expansion of $\mathbf{x}$, the linear terms $\mathcal{L}\{\mathbf{x}\}$ are readily expanded as

$$\hat{\mathcal{L}} = \mathbf{L}\hat{\mathbf{x}} \tag{5.40}$$

Accordingly, for a given solution $\hat{\mathbf{x}}$, the inertial and linear terms can be expressed in time as:

$$\mathcal{L}\{\Phi(t)\hat{\mathbf{x}},t\} = \Phi(t)\mathbf{L}\hat{\mathbf{x}} \tag{5.41}$$

Eqs. (5.40) and (5.41) are important, because they show that the linear terms can be treated easily using a Fourier spectral approach: while the original formulation (4.90) involved a convolution product, if a solution parametrised in terms of Fourier series is considered, the linear terms can be calculated in a particularly simple way. Also note that the matrix $\mathbf{L}$ has relatively few non-zero entries, so that operations involving $\mathbf{L}$ are computationally cheap.

An additional remark is appropriate with respect to the additive input $\mathbf{e}(t)$. If the WEC system is simulated in regular, linear waves, then the additive input will take the form of a single sinusoidal function, with period T_w. The fundamental frequency $\Delta\omega$ in the Fourier expansion may thus be chosen as $\Delta\omega = 2\pi/T_w$, and $\mathbf{e}(t)$ is *exactly* expressed as

$$\mathbf{e}(t) = \Phi(t)\hat{\mathbf{e}} \tag{5.42}$$

where

$$\hat{\mathbf{e}} = \begin{pmatrix} \mathbf{0}_{\mathbb{R}^D} \\ \hat{\mathbf{e}}_1 \\ \hat{\mathbf{e}}_2 \\ \mathbf{0}_{\mathbb{R}^D} \\ \vdots \\ \mathbf{0}_{\mathbb{R}^D} \end{pmatrix} \in \mathbb{R}^{D(2N_\omega+1)} \tag{5.43}$$

If, instead, irregular, linear Gaussian waves are simulated, it has been seen in Chapter 3 that a wave signal can be correctly generated as a sum of harmonic sinusoids (HRA or HDA methods). Then, if $\Delta\omega$ is the fundamental frequency which allows for an accurate discretisation of the target spectrum, $\mathbf{e}(t)$ is expressed as

$$\mathbf{e}(t) = \Phi(t)\hat{\mathbf{e}} \tag{5.44}$$

where

$$\hat{\mathbf{e}} = \begin{pmatrix} \hat{\mathbf{e}}_0 \\ \hat{\mathbf{e}}_1 \\ \hat{\mathbf{e}}_2 \\ \vdots \\ \vdots \\ \hat{\mathbf{e}}_{N_\omega} \end{pmatrix} \in \mathbb{R}^{D(2N_\omega+1)} \tag{5.45}$$

and the components $\hat{\mathbf{e}}_i$ are randomly derived from the wave spectrum, following either HRA or HDA. Of course, if some of the dimensions $d = 1...D$ do not represent hydrodynamic degrees of freedom, the corresponding entries of each term $\hat{\mathbf{e}}_i = \begin{pmatrix} \hat{e}_{1,i} & \cdots & \hat{e}_{D,i} \end{pmatrix}^T$ should be chosen equal to zero.

Finally, given a parametrisation of $\mathbf{x}$ as a trigonometric series specified by the vector $\hat{\mathbf{x}}$, and using Eqs. (5.25), (5.30), (5.31), (5.41) and (5.42), the residual equation of Eq. (4.90) can be written as follows:

$$\forall t \in [0;T], \quad \Phi(t)\mathbf{L}\hat{\mathbf{x}} - \mathbf{n}\big(\Phi(t)\hat{\mathbf{x}}, \Phi(t)\Omega\hat{\mathbf{x}}, t\big) - \Phi(t)\hat{\mathbf{e}} = 0 \tag{5.46}$$

In summary, this subsection explains how the variable $\mathbf{x}$ and its derivatives are projected onto the chosen functional basis (in this case, a Fourier basis), which is the essence of spectral methods. It also shows how the linear terms in the dynamical equations are readily expanded as a function of the expansion of $\mathbf{x}$. Finally, the additive excitation term can also be specified in terms of Fourier series. As a result, the residual equation (4.90), expressed as a function of the chosen parametrisation $\hat{\mathbf{x}}$, takes the form of Eq. (5.46). The latter equation may be solved using different "mean-weighted residual" approaches, as discussed previously in Section 5.2.1. In the following subsections, the Galerkin and the PS approaches are considered in detail.

5.3.2 Galerkin formulation

In the Galerkin approach, the residuals are projected onto the chosen functional basis, i.e. the trigonometric functions for the case of the HB method. Given that the linear and excitation terms are readily projected as $\mathbf{L}\hat{\mathbf{x}}$ and $\hat{\mathbf{e}}$, respectively, Eq. (5.46) results in the following set of $D(2N_\omega+1)$ equations :

$$\mathbf{L}\hat{\mathbf{x}} - \hat{\mathbf{n}}(\hat{\mathbf{x}}) - \hat{\mathbf{e}} = \mathbf{0}_{\mathbb{R}^{D(2N_\omega+1)}} \tag{5.47}$$

where

$$\begin{cases} \hat{\mathbf{n}}_0(\hat{\mathbf{x}}) = \frac{1}{T}\int\limits_{t=0}^{T} \mathbf{n}\big(\Phi(t)\hat{\mathbf{x}}, \Phi(t)\Omega\hat{\mathbf{x}}, t\big)\, dt \\ \hat{\mathbf{n}}_{2n-1}(\hat{\mathbf{x}}) = \frac{2}{T}\int\limits_{t=0}^{T} \cos(\omega_n t)\mathbf{n}\big(\Phi(t)\hat{\mathbf{x}}, \Phi(t)\Omega\hat{\mathbf{x}}, t\big)\, dt \\ \hat{\mathbf{n}}_{2n}(\hat{\mathbf{x}}) = \frac{2}{T}\int\limits_{t=0}^{T} \sin(\omega_n t)\mathbf{n}\big(\Phi(t)\hat{\mathbf{x}}, \Phi(t)\Omega\hat{\mathbf{x}}, t\big)\, dt \end{cases} \tag{5.48}$$

Eq. (5.47) corresponds to a proper *harmonic balance* equation, because it states that the Fourier coefficients, associated with the linear, non-linear and forcing terms in the dynamical equation, must cancel each other, for every order of the Fourier expansion up to N_ω.

The HB equation is typically solved using an iterative root-finding method, such as the Newton-Raphson procedure [146], which will be described in more detail in Section 5.4. At each iteration

of the solution procedure, the residuals given by the left-hand side of Eq. (5.47), as well as their Jacobian, must be evaluated, which can be a challenging task for the non-linear terms $\hat{\mathbf{n}}(\hat{\mathbf{x}})$.

In specific cases, the Fourier coefficients $\hat{\mathbf{n}}$ may be obtained analytically, as a non-linear function of the coefficients $\hat{\mathbf{x}}$. In particular, this task is relatively straightforward when non-linearities are in quadratic or cubic form, see for example [141]. With such non-linearities, the Newton-Raphson procedure is made considerably more simple and efficient. In [140, 141], it is suggested to carry out a cubic approximation of the non-linear terms at each iteration of the Newton-Raphson algorithm. Other researchers [147, 148] propose a methodology to recast the dynamical equations (4.90) in a way which only involves quadratic non-linear terms, even if the original non-linear terms are not in a polynomial form [148]. This latter possibility, although it may be an interesting path for future work, has not been investigated within the scope of this thesis.

Instead, no further assumption is made on the nature of the non-linearities, apart from their being differentiable. In such a case, the baseline method consists of evaluating the Fourier coefficients $\hat{\mathbf{n}}$ (and their derivatives for the Jacobian computation) by means of numerical integration. To that end, $\mathbf{n}\big(\Phi(t)\hat{\mathbf{x}}, \Phi(t)\Omega\hat{\mathbf{x}}, t\big)$ and its derivatives with respect to the components of $\hat{\mathbf{x}}$ must be calculated at a discrete number of points in $[0;T]$, before the integrals can be evaluated through finite differences.

Discretise the interval $[0;T]$ into N_t points $t_j = j\Delta t$, $j = 1...N_t$, with $\Delta t = T/N_t$. Define

$$\Phi_{N_t} := \begin{pmatrix} \Phi(t_1) \\ \Phi(t_2) \\ \vdots \\ \Phi(t_{N_t}) \end{pmatrix} \tag{5.49}$$

For a reasonably accurate calculation of the Fourier coefficients, N_t must be greater than, or equal to $2N_\omega + 1$. Furthermore, it is easily found that

$$\frac{2}{N_t}\Phi_{N_t}^T\Phi_{N_t} = \mathbb{I}_{N_\omega} \tag{5.50}$$

The non-linear terms are discretised in time in the form of a vector $\mathbf{n}_{N_t}(\hat{\mathbf{x}})$ containing the non-linear term, evaluated at each time t_j, for a given solution $\hat{\mathbf{x}}$:

$$\mathbf{n}_{N_t}(\hat{\mathbf{x}}) := \begin{pmatrix} \mathbf{n}\big(\Phi(t_1)\hat{\mathbf{x}}, \Phi(t_1)\Omega\hat{\mathbf{x}}, t_1\big) \\ \vdots \\ \mathbf{n}\big(\Phi(t_{N_t})\hat{\mathbf{x}}, \Phi(t_{N_t})\Omega\hat{\mathbf{x}}, t_{N_t}\big) \end{pmatrix} \in \mathbb{R}^{N_t D} \tag{5.51}$$

From Eq. (5.48), and using a rectangle integration rule, $\hat{\mathbf{n}}$ may be evaluated as follows:

$$\hat{\mathbf{n}}(\hat{\mathbf{x}}) \approx \frac{2}{N_t}\Phi_{N_t}^T\mathbf{n}_{N_t}(\hat{\mathbf{x}}) \tag{5.52}$$

Therefore, in practice, the $2N_\omega + 1$ equations which are solved can be written as follows:

$$\mathbf{L}\hat{\mathbf{x}} - \frac{2}{N_t}\Phi_{N_t}^T\mathbf{n}_{N_t}(\hat{\mathbf{x}}) - \hat{\mathbf{e}} = \mathbf{0}_{\mathbb{R}^{D(2N_\omega+1)}} \tag{5.53}$$

More detail about the solution method through iterative root-finding algorithms is given in Section 5.4, with a particular focus on the explicit computation of the Jacobian of the residuals. The aim of introducing Eq. (5.53) at this stage is merely to better highlight the relationship between the Galerkin and PS formulations, the latter being the subject of Section, 5.3.3.

5.3.3 Pseudo-spectral formulation

With the PS formulation, the residuals are set to zero at $N_t := 2N_\omega + 1$ collocation points. Using a Fourier functional basis, the points can be taken to be uniformly spaced [102]. Define the vector $\mathcal{L}_{N_t} \in \mathbb{R}^{DN_t}$, which represents the linear terms taken at the N_t collocation points, as

$$\mathcal{L}_{N_t} := \begin{pmatrix} \mathcal{L}\{\mathbf{x}, t_1\} \\ \vdots \\ \mathcal{L}\{\mathbf{x}, t_{N_t}\} \end{pmatrix} \tag{5.54}$$

Similarly, define

$$\mathbf{e}_{N_t} := \begin{pmatrix} \mathbf{e}(t_1) \\ \vdots \\ \mathbf{e}(t_{N_t}) \end{pmatrix} \in \mathbb{R}^{DN_t} \tag{5.55}$$

Given the expansion specified by $\hat{\mathbf{x}}$, the linear and forcing terms at the N_t collocation points, $\mathcal{L}_{N_t}$ and $\mathbf{e}_{N_t}$, can be calculated respectively as:

$$\mathcal{L}_{N_t} = \Phi_{N_t} \mathbf{L} \hat{\mathbf{x}} \quad \text{and} \quad \mathbf{e}_{N_t} = \Phi_{N_t} \hat{\mathbf{e}} \tag{5.56}$$

where Φ_{N_t} is defined in Eq. (5.49).

$\mathcal{L}_{N_t}$ depends on the unknown vector $\hat{\mathbf{x}}$, but $\mathbf{e}_{N_t}$ does not, and thus can be pre-computed. Finally, the set of N_t algebraic equations to solve is:

$$\Phi_{N_t} \mathbf{L} \hat{\mathbf{x}} - \mathbf{n}_{N_t}(\hat{\mathbf{x}}) - \Phi_{N_t} \hat{\mathbf{e}} = \mathbf{0}_{\mathbb{R}^{DN_t}} \tag{5.57}$$

Using the rectangle rule for the numerical approximation of the Galerkin harmonic balance equation (5.47), it can be seen from Eqs. (5.53) and (5.57) that the Galerkin and PS formulations are very similar to each other. In particular, choosing $N_t = 2N_\omega + 1$ in the Galerkin formulation, using Eq. (5.50), and multiplying Eq. (5.57) with $\frac{2}{N_t}\Phi_{N_t}^T$ on the left hand-side, the two formulations are strictly equivalent. Increasing N_t of the Galerkin method beyond $2N_\omega + 1$, which is known as *oversampling* [132], may improve the accuracy of the Galerkin technique, for a given order N_ω. In the limit as N_t tends to infinity (and thus the rectangle approximation approaches the exact integrals (5.48)), the solution $\hat{\mathbf{x}}$ obtained corresponds to the first N_ω harmonics of the *exact* solution. However, the gain in accuracy should be balanced against the additional computational burden of a more accurate integral calculation. For more detail, the reader is referred to [132] and [102].

Therefore, the Galerkin and PS formulations are strictly equivalent if, in the Galerkin formulation, the Fourier integrals are approximated with a rectangle rule using $N_t = 2N_\omega + 1$ points. However, the Galerkin formulation offers the flexibility of improving the solution accuracy through oversampling, at some additional computational cost. A brief practical comparison of the two approaches is presented in Section 5.5, where it will be shown that little benefit is obtained from oversampling.

Finally, note that of Eqs. (5.47) and (5.57), only the former is, strictly speaking, a harmonic balance method. With the PS formulation of Eq. (5.57), the residuals are not set to zero through cancellation of harmonics, but through collocation. Yet, the application of the PS formulation, for the solution of mechanical problems with a large number of harmonics, is sometimes termed *high dimensional harmonic balance* [149], although it should be more accurately termed *trigonometric collocation* [150].

5.4 Solving the harmonic balance equation

As mentioned in Section 5.3.2, in this work, the residual equation is solved using an iterative root-finding algorithm. More specifically, gradient-based methods, derived from the Newton-Raphson procedure [146], are used to solve non-linear equations (5.53) and (5.57).

The basic Newton-Raphson algorithm is recalled here. Either Eqs. (5.53) or (5.57) can be formulated as follows:

$$\mathbf{r}(\hat{\mathbf{x}}) = 0_{\mathbb{R}^{D(2N_\omega+1)}} \tag{5.58}$$

where $\mathbf{r}$ represents the residual vector, either in the frequency domain (Eq. (5.53)) or at the collocation points (Eq. (5.57)).

Choose an initial solution, $\hat{\mathbf{x}}^{(0)}$. Then, at each iteration k of the method, with $k \geq 1$, the residuals $\mathbf{r}$ and their Jacobian, denoted $\frac{\partial \mathbf{r}}{\partial \hat{\mathbf{x}}}$, are evaluated at the current solution $\hat{\mathbf{x}}^{(k)}$, and the next iterate $\hat{\mathbf{x}}^{(k+1)}$ is found by solving the following linear system:

$$\mathbf{r}(\hat{\mathbf{x}}^{(k)}) + \left.\frac{\partial \mathbf{r}}{\partial \hat{\mathbf{x}}}\right|_{\hat{\mathbf{x}}^{(k)}} (\hat{\mathbf{x}}^{(k+1)} - \hat{\mathbf{x}}^{(k)}) = 0_{\mathbb{R}^{D(2N_\omega+1)}} \tag{5.59}$$

The algorithm stops when the chosen norm of the residuals $\mathbf{r}$ falls below a predefined threshold ε, where the norm is typically the Euclidean norm. Newton's algorithm is represented in the diagram of Fig. 5.1, assuming that the Galerkin version (5.53) of the HB method is used. In Fig. 5.1, it can be seen that an initial solution is found by solving the linear problem $\mathbf{L}'\hat{\mathbf{x}}^{(0)} = \hat{\mathbf{e}}$, where $\mathbf{L}'$ denotes a matrix, constructed in a way similar to $\mathbf{L}$, obtained for a linearised version of Eq. (4.90). The choice of an appropriate initial solution is further discussed in Section 5.4.2.

A crucial step of Newton's method is the computation of the residual function Jacobian at the current iterate, $\frac{\partial \mathbf{r}}{\partial \hat{\mathbf{x}}}|_{\hat{\mathbf{x}}^{(k)}}$, which is a $D(2N_\omega+1) \times D(2N_\omega+1)$ matrix. For some problems, it is impossible, or cumbersome, to find an exact formulation for the Jacobian. In such cases, the Jacobian is usually numerically estimated through a finite-difference method [146]. However, Jacobian evaluation through finite differences can be computationally costly, and is subject to inaccuracies which may negatively affect the computation time, by increasing the number of Newton iterations. Therefore, it is preferable, when possible, to compute the gradient explicitly. Fortunately, both equations (5.53) and (5.57) lend themselves to explicit Jacobian calculation, which is detailed hereafter.

5.4.1 Explicit Jacobian computation of the residuals

5.4.1.1 The pseudo-spectral case

In the pseudo-spectral case, from Eq. (5.57), the residual function is given as:

$$\mathbf{r}(\hat{\mathbf{x}}) = \Phi_{N_t} \mathbf{L}\hat{\mathbf{x}} - \mathbf{n}_{N_t}(\hat{\mathbf{x}}) - \Phi_{N_t}\hat{\mathbf{e}} \tag{5.60}$$

where $N_t = 2N_\omega + 1$ and $\mathbf{n}_{N_t}$ is defined as in Eq. (5.51).

The Jacobian of the non-linear terms is the only challenging calculation. For a given time t, the Jacobian of the non-linear terms $\mathbf{n}$ at time t, with respect to the time-domain values of $\mathbf{x}(t)$ and $\dot{\mathbf{x}}(t)$, is given as:

$$\frac{\partial \mathbf{n}}{\partial \mathbf{x}}(t) = \begin{pmatrix} \frac{\partial n_1}{\partial x_1} & \cdots & \frac{\partial n_1}{\partial x_D} \\ \vdots & \ddots & \vdots \\ \frac{\partial n_D}{\partial x_1} & \cdots & \frac{\partial n_D}{\partial x_D} \end{pmatrix}_{\mathbf{x}(t),\dot{\mathbf{x}}(t),t} \in \mathbb{R}^{D\times D} \tag{5.61}$$

and

$$\frac{\partial \mathbf{n}}{\partial \dot{\mathbf{x}}}(t) = \begin{pmatrix} \frac{\partial n_1}{\partial \dot{x}_1} & \cdots & \frac{\partial n_1}{\partial \dot{x}_D} \\ \vdots & \ddots & \vdots \\ \frac{\partial n_D}{\partial \dot{x}_1} & \cdots & \frac{\partial n_D}{\partial \dot{x}_D} \end{pmatrix}_{\mathbf{x}(t),\dot{\mathbf{x}}(t),t} \in \mathbb{R}^{D\times D} \tag{5.62}$$

where the subscript $\mathbf{x}(t),\dot{\mathbf{x}}(t),t$ means that each component $\partial n_i/\partial x_j$ (resp.$\partial n_i/\partial \dot{x}_j$) is evaluated at the point $(\mathbf{x}(t),\dot{\mathbf{x}}(t),t)$.

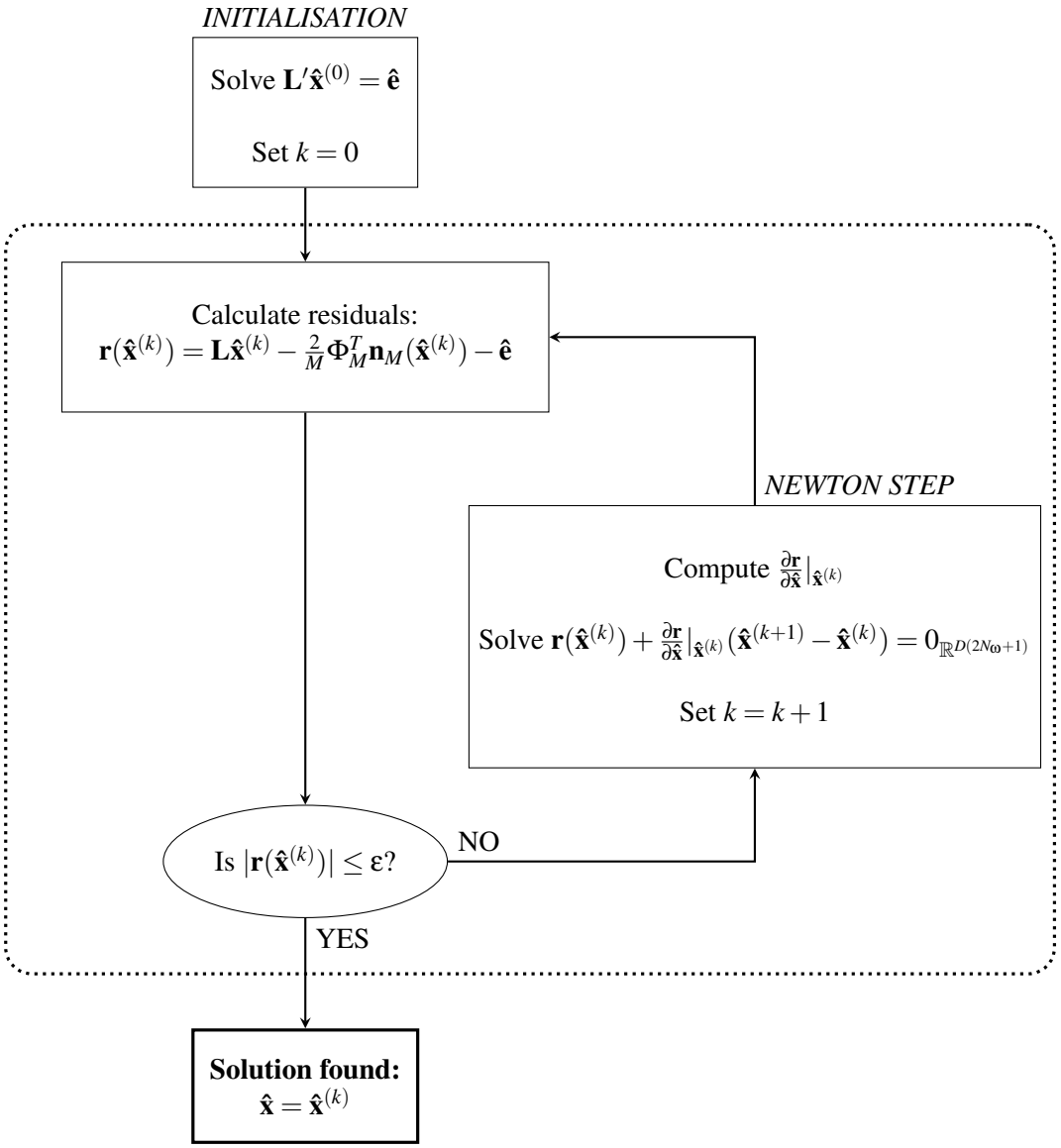

Figure 5.1: Application of Newton's method to solve the HB equation

Recalling that $\mathbf{x}(t)$ and $\dot{\mathbf{x}}(t)$ are obtained from $\hat{\mathbf{x}}$ as $\Phi(t)\hat{\mathbf{x}}$ and $\Phi(t)\Omega\hat{\mathbf{x}}$, respectively, the Jacobian of $\mathbf{n}$ at time t, with respect to the components of $\hat{\mathbf{x}}$, is given as follows:

$$\frac{\partial \mathbf{n}}{\partial \hat{\mathbf{x}}}(t) = \frac{\partial \mathbf{n}}{\partial \mathbf{x}}(t)\Phi(t) + \frac{\partial \mathbf{n}}{\partial \dot{\mathbf{x}}}(t)\Phi(t)\Omega \tag{5.63}$$

Using the fact that $\mathbf{n}_{N_t}(\hat{\mathbf{x}}) = \begin{pmatrix} \mathbf{n}(t_1) \\ \vdots \\ \mathbf{n}(t_{N_t}) \end{pmatrix}$, the Jacobian of $\mathbf{n}_{N_t}(\hat{\mathbf{x}})$ is given as

$$\frac{\partial \mathbf{n}_{N_t}}{\partial \hat{\mathbf{x}}} = \begin{pmatrix} \frac{\partial \mathbf{n}}{\partial \hat{\mathbf{x}}}(t_1) \\ \vdots \\ \frac{\partial \mathbf{n}}{\partial \hat{\mathbf{x}}}(t_{N_t}) \end{pmatrix} \tag{5.64}$$

Define the block-diagonal matrices

$$\mathbf{D}_{\mathbf{x}} = \begin{pmatrix} \frac{\partial \mathbf{n}}{\partial \mathbf{x}}(t_1) & \cdots & \mathbf{0} \\ \vdots & \ddots & \vdots \\ \mathbf{0} & \cdots & \frac{\partial \mathbf{n}}{\partial \mathbf{x}}(t_{N_t}) \end{pmatrix} \in \mathbf{R}^{DN_t \times DN_t} \tag{5.65}$$

and

$$\mathbf{D}_{\dot{\mathbf{x}}} = \begin{pmatrix} \frac{\partial \mathbf{n}}{\partial \dot{\mathbf{x}}}(t_1) & \cdots & \mathbf{0} \\ \vdots & \ddots & \vdots \\ \mathbf{0} & \cdots & \frac{\partial \mathbf{n}}{\partial \dot{\mathbf{x}}}(t_{N_t}) \end{pmatrix} \in \mathbf{R}^{DN_t \times DN_t} \tag{5.66}$$

Now, using Eqs. (5.63) and (5.64), the Jacobian $\partial \mathbf{n}_{N_t} / \partial \hat{\mathbf{x}}$ is concisely specified as:

$$\frac{\partial \mathbf{n}_{N_t}}{\partial \hat{\mathbf{x}}} = \mathbf{D}_{\mathbf{x}} \Phi_{N_t} + \mathbf{D}_{\dot{\mathbf{x}}} \Phi_{N_t} \Omega \tag{5.67}$$

From Eqs. (5.60) and (5.67), the procedure to compute the Jacobian of $\mathbf{r}$, at a given solution $\hat{\mathbf{x}}$, can be detailed as follows:

1. Compute the time-domain solution and its derivative at discrete instants $t_1 \ldots t_{N_t}$, as $\mathbf{x}_{N_t} = \Phi_{N_t} \hat{\mathbf{x}}$ and $\dot{\mathbf{x}}_{N_t} = \Phi_{N_t} \Omega \hat{\mathbf{x}}$;
2. Evaluate the non-linear terms $\mathbf{n}$ and their derivatives, $\frac{\partial \mathbf{n}}{\partial \mathbf{x}}$ and $\frac{\partial \mathbf{n}}{\partial \dot{\mathbf{x}}}$, along the trajectory $\{\mathbf{x}_{N_t}, \dot{\mathbf{x}}_{N_t}\}$; use the derivatives to construct $\mathbf{D}_{\mathbf{x}}$ and $\mathbf{D}_{\dot{\mathbf{x}}}$;
3. Obtain $\frac{\partial \mathbf{n}_{N_t}}{\partial \hat{\mathbf{x}}} = \mathbf{D}_{\mathbf{x}} \Phi_{N_t} + \mathbf{D}_{\dot{\mathbf{x}}} \Phi_{N_t} \Omega$;
4. Finally, the complete Jacobian (including non-linear *and* linear terms) is:

$$\frac{\partial \mathbf{r}}{\partial \hat{\mathbf{x}}} = \Phi_{N_t} \mathbf{L} - \frac{\partial \mathbf{n}_{N_t}}{\partial \hat{\mathbf{x}}} \tag{5.68}$$

5.4.1.2 The Galerkin case

In the Galerkin case, using the rectangle integration rule, from Eq. (5.53) the residuals are given as follows:

$$\mathbf{r}(\hat{\mathbf{x}}) = \mathbf{L}\hat{\mathbf{x}} - \frac{2}{N_t} \Phi_{N_t}^T \mathbf{n}_{N_t}(\hat{\mathbf{x}}) - \hat{\mathbf{e}} \tag{5.69}$$

where N_t may be larger than $2N_\omega + 1$. The Jacobian for the non-linear terms is calculated in a way similar to the PS case, except that $\mathbf{n}$ and its derivatives $\frac{\partial \mathbf{n}}{\partial \mathbf{x}}$ and $\frac{\partial \mathbf{n}}{\partial \dot{\mathbf{x}}}$ are evaluated at N_t points in time, where N_t is equal to, or greater than $2N_\omega + 1$. The procedure can be detailed as follows:

1. Compute the time-domain solution and its derivative at discrete times $t_1 \ldots t_{N_t}$, as $\mathbf{x}_{N_t} = \Phi_{N_t} \hat{\mathbf{x}}$ and $\dot{\mathbf{x}}_{N_t} = \Phi_{N_t} \Omega \hat{\mathbf{x}}$;
2. Evaluate the non-linear terms $\mathbf{n}$ and their derivatives, $\frac{\partial \mathbf{n}}{\partial \mathbf{x}}$ and $\frac{\partial \mathbf{n}}{\partial \dot{\mathbf{x}}}$, along the trajectory $\{\mathbf{x}_{N_t}, \dot{\mathbf{x}}_{N_t}\}$; use the derivatives to construct $\mathbf{D}_{\mathbf{x}}$ and $\mathbf{D}_{\dot{\mathbf{x}}}$;
3. Obtain $\frac{\partial \mathbf{n}_{N_t}}{\partial \hat{\mathbf{x}}} = \mathbf{D}_{\mathbf{x}} \Phi_{N_t} + \mathbf{D}_{\dot{\mathbf{x}}} \Phi_{N_t} \Omega$;
4. Finally, the complete Jacobian (for non-linear *and* linear terms) is:

$$\frac{\partial \mathbf{r}}{\partial \hat{\mathbf{x}}} = \mathbf{L} - \frac{2}{N_t} \Phi_{N_t}^T \frac{\partial \mathbf{n}_{N_t}}{\partial \hat{\mathbf{x}}} \tag{5.70}$$

The computations are then very similar in the PS and Galerkin approaches. However, in the Galerkin case, if $N_t > 2N_\omega + 1$, the computation of the non-linear part of the residuals, and of its Jacobian, may be more accurate, but slower, than in the PS approach.

5.4.2 Initialisation

The iterative solution of the HB equation requires appropriate initialisation, i.e. a relevant choice for $\hat{\mathbf{x}}^{(0)}$. Indeed:

- It should be ensured that $\hat{\mathbf{x}}^{(0)}$ belongs to the "basin of attraction" of the solution, i.e. that starting from $\hat{\mathbf{x}}^{(0)}$, the iterative algorithm (Newton's method or other) converges to the solution [146].
- Assuming that $\hat{\mathbf{x}}^{(0)}$ does belong to the basin of attraction, the computation time associated with the iterative solution linearly depends on the number of iterations. Therefore, a good initial guess reduces the computational time.

A computationally cheap but generally appropriate initial guess is the solution to an associated linear problem, whereby the term $\mathbf{n}$ is either linearised, or set to zero. $\hat{\mathbf{x}}^{(0)}$ is then found by solving

$$\mathbf{L}'\hat{\mathbf{x}}^{(0)} = \hat{\mathbf{e}} \tag{5.71}$$

For particularly strong non-linearities, in cases where it is not easy to find a satisfactory initial guess for the solution, it may be possible to use a *continuation method* [151]. Parametrise the HB equation (5.53) or (5.57) in terms of a scalar parameter $\lambda \in [0;1]$ such that $\mathbf{r}_{\lambda=1}(\hat{\mathbf{x}}) = \mathbf{r}(\hat{\mathbf{x}})$, and such that the equation $\mathbf{r}_{\lambda=0}(\hat{\mathbf{x}}) = \mathbf{0}$ has a trivial solution. For example (using the PS formulation), λ modulates the magnitude of the non-linear effects so that:

$$\mathbf{r}_\lambda(\hat{\mathbf{x}}) := \Phi_{N_t}\mathbf{L}\hat{\mathbf{x}} - \lambda\mathbf{n}_{N_t}(\hat{\mathbf{x}}) - \Phi_{N_t}\hat{\mathbf{e}} \tag{5.72}$$

Starting from the solution of $\mathbf{r}_{\lambda=0}(\hat{\mathbf{x}}) = \mathbf{0}$, the solution $\hat{\mathbf{x}}(\lambda)$ of $\mathbf{r}_\lambda(\hat{\mathbf{x}}) = \mathbf{0}$ is numerically tracked until $\hat{\mathbf{x}}(\lambda = 1)$ is reached. For example, in a simplistic version of the continuation method, the interval $[0;1]$ is subdivided into a number K of "small enough" intervals $[\lambda_k;\lambda_{k+1}]$ with $\lambda_0 = 0 < \lambda_1 < ... < \lambda_k < \lambda_{k+1} < ...\lambda_K = 1$. The solution $\hat{\mathbf{x}}(\lambda_{k+1})$ would be found using Newton's method, starting from $\hat{\mathbf{x}}(\lambda_k)$ as an initial guess.

Continuation methods not only allow the solution of the original non-linear equation; they also provide the solution for the dynamical equations within the chosen parametric space, i.e. when the parameter λ covers $[0;1]$. Thus, if the parameter λ can be chosen to be physically significant, the continuation method provides a comprehensive picture with regards to how the system reacts to changes in the parameter of interest (in HB applications for non-linear vibration analysis, the parameter of interest is typically the excitation frequency ω [135]). Within the scope of WEC design, continuation methods could be a powerful tool for parametric optimisation and stability analysis.

Although they have been briefly discussed in this subsection for the sake of completeness, continuation methods are not covered in the rest of this thesis. However, the sensitivity of the HB solution to the model parameters will be investigated in Section 5.6, for a case more general than a scalar parameter. In addition, other strategies for initialising the HB algorithm will be further explored in Chapter 6.

5.4.3 Practical implementation

In most cases, if non-linearities are not excessively strong, a simple Newton procedure can be appropriate for solving the HB equation. As a consequence, the Newton procedure, implemented by the author in a Matlab[3] environment, and represented in Fig. 5.1, has been used to produce the numerical results in the first works published, within the scope of this thesis, on the application of the HB method to WEC systems [57, 129].

In subsequent work [152], it was shown that more sophisticated, but more robust gradient-based root-finding algorithms, may be necessary for more difficult problems. The trust-region

[3] See https:mathworks.com

dogleg method, available in the readily-implemented Matlab function *fsolve*, has thus been used by the author as a complement to, or a substitute for the simple Newton procedure [152, 153]. The principle of trust-region methods can be found in [146].

The HB simulation results, presented throughout the rest of this thesis, have been obtained using the simple Newton method when convergence was not an issue, while the *fsolve* trust-region dogleg algorithm was employed for more arduous cases (i.e. cases where the Newton method sometimes failed in converging to a solution).

5.4.4 The alternating frequency/time technique

Note that gradient-based techniques are not the only possibility for solving Eq. (5.58). In particular, the alternating frequency/time (AFT) technique [154], deserves a brief discussion. Consider the Galerkin HB equation (5.53). Define the operator $\mathcal{T}$:

$$\mathcal{T} : \hat{\mathbf{x}} \mapsto \mathbf{L}^{-1}[\hat{\mathbf{n}}(\hat{\mathbf{x}}) + \hat{\mathbf{e}}] \tag{5.73}$$

It is easy to see that Eq. (5.53) can be reformulated as:

$$\mathcal{T}(\hat{\mathbf{x}}) = \hat{\mathbf{x}} \tag{5.74}$$

Using the *contraction mapping* theorem [97], if an initial guess $\hat{\mathbf{x}}^{(0)}$ can be found sufficiently close to the actual solution, and under certain conditions on the operator $\mathcal{T}$ [97], successive iterations of the form

$$\hat{\mathbf{x}}^{(k+1)} = \mathcal{T}(\hat{\mathbf{x}}^{(k)}) \tag{5.75}$$

converge to the actual solution $\hat{\mathbf{x}}^*$. Iterations of Eq. (5.75) form the essence of the AFT technique [154].

The AFT technique does not require any Jacobian calculation or matrix inversion (since $\mathbf{L}^{-1}$ need only be calculated once, at the beginning of the AFT iterations), and only requires the evaluation of the non-linear terms at each iteration. The AFT technique was briefly considered by the author during the course of this thesis; however, it was found that, although each AFT iteration is computationally cheap, many more iterations were necessary to converge, compared to Newton's method. Furthermore, the AFT technique appeared to be significantly less robust than Newton's method, the former often failing where Newton's method only took a few iterations to converge. As a consequence, the AFT method was discarded for the rest of this thesis.

5.5 An introductory example: a flap-type WEC in monochromatic waves

Some of the main features of the HB method, as applied to the WEC simulation problem, are illustrated in this section by means of a simple numerical example, namely, a flap-type WEC in a monochromatic wave signal.

5.5.1 WEC model

The WEC model is the same bottom-mounted, pitching flap which is described in Chapter 4 of [106]. The device is pictured in Fig. 5.2. H represents the mean water depth, also equal to the flap height. The flap is $W = 30$ m wide (transverse to the wave direction), and $D = 1$m thick. The flap faces the wave direction x, and rotates about the y axis. The angle of rotation with respect to the vertical is denoted θ.

From Newton's second law, the dynamical equation governing the rotation angle is as follows:

$$I\ddot{\theta}(t) = \tau_f(t) + \tau_{pto}(t) \tag{5.76}$$

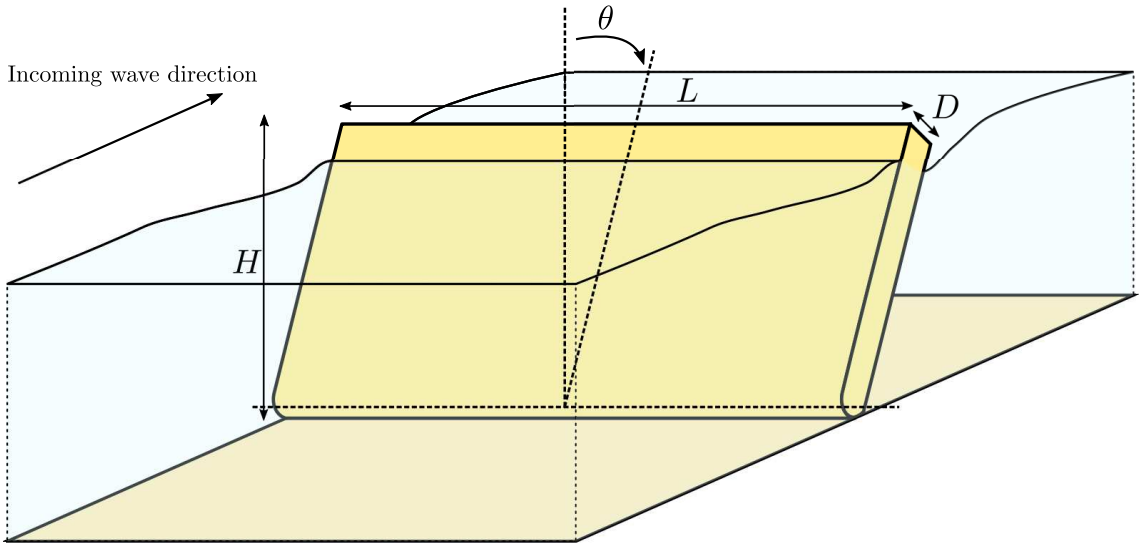

Figure 5.2: Flap-type oscillating wave-surge converter

where I denotes the moment of inertia about the rotation axis, τ_f denotes the hydrodynamic torque, about the y axis, due to the device interaction with the surrounding fluid, and $\tau_{pto}(t)$ the torque exerted by the PTO system. The PTO torque takes the form of a simple linear damping term: $\tau_{pto}(t) = -B_{pto}\dot{\theta}(t)$. The hydrodynamic moments are further detailed as follows:

$$\tau_f(t) = \tau_e(t) + \tau_h(t) + \tau_R(t) + \tau_v(t) \tag{5.77}$$

where

- τ_e is the excitation torque;
- τ_R is the radiation torque, given as $\tau_R(t) = -I_\infty\ddot{\theta}(t) - \int_{\tau=0}^{\infty} K_R(\tau)\dot{\theta}(t-\tau)d\tau$, where I_∞ denotes the radiation infinite-frequency added moment of inertia about the rotation axis, and $K_R(\tau)$ the radiation impulse response kernel;
- τ_h is the hydrostatic restoring torque, calculated as $f_h(t) = -S_h\theta(t)$, where S_h is the hydrostatic stiffness coefficient;
- τ_v is the torque due to non-linear viscous effects, represented through the combination of a linear damping term, $-C_{dis,l}\dot{\theta}(t)$, and a quadratic viscous drag term, $-C_{dis,q}|\dot{\theta}(t)|\dot{\theta}(t)$ (see [106] for more detail).

Finally, the dynamical equation can be written as:

$$(I+I_\infty)\ddot{\theta}(t) + (B_{PTO}+C_{dis,l})\dot{\theta}(t) + \int_{\tau=0}^{\infty} K_R(\tau)\dot{\theta}(t-\tau)d\tau + S_h\theta(t) + C_{dis,q}|\dot{\theta}(t)|\dot{\theta}(t) + S_h\theta(t) = e(t) \tag{5.78}$$

The water density is $\rho = 1025kg.m^{-3}$, and the body density is $\rho_b = \rho/8$. The time domain radiation coefficients, I_∞ and $K_R(\tau)$, are related to their equivalent frequency-domain representation, denoted A_R (for the frequency-dependent added mass) and B_R (for the frequency-dependent damping), through Ogilvie's relations (4.69) and (4.70). The excitation torque transfer function, $H_{\eta e}$, as well as the radiation parameters I_∞, $K_R(\tau)$, A_R and B_R, are all calculated using the hydrodynamic software WAMIT[4].

Parameter	Unit	Num. value
L	[m]	30
D	[m]	1
H	[m]	15
ρ_b	[kg.m^{-3}]	128.125
I	[kg.m^2]	2.44×10^8
S_h	[N.m]	2.97×10^7
$C_{dis,l}$	[N.m.s]	1×10^6
$C_{dis,q}$	[N.m.s^2]	3.7×10^8
I_∞	[kg.m^2]	2.4×10^8

Table 5.1: Main physical parameters of the flap-type device

Table 5.1 summarises the numerical values of the main physical parameters of the flap while, for the sake of illustration, Fig. 5.3 shows the magnitude of the excitation torque transfer function, $|H_{\eta^e}|$, the radiation added mass A_R and damping B_R, and the impulse response kernel K_R.

Eq. (5.78) can be straightforwardly formulated in the general form of Eq. (4.90), as:

$$\mathcal{L}\{\theta\} - n\{\theta, t\} - e(t) = 0 \tag{5.79}$$

with:

- The number of degrees of freedom is only $D = 1$, and the corresponding variable is $x = \theta$;
- The linear operator is given as:

$$\mathcal{L}\{\theta\} := (I + I_\infty)\ddot{\theta}(t) + (B_{pto} + C_{dis,l})\dot{\theta}(t) + \int_{\tau=0}^{\infty} K_R(\tau)\dot{\theta}(t-\tau)d\tau + S_h\theta(t) \tag{5.80}$$

- The non-linear operator is defined as:

$$n\{\theta, t\} = -C_{dis,q}|\dot{\theta}|\dot{\theta} \tag{5.81}$$

- The additive forcing term is $e(t) = \tau_e(t)$.

5.5.2 Implementation of the HB method

In this example, a monochromatic wave excitation signal, with period $T_w = 12$s and amplitude $A_w = 4$m, is considered:

$$\eta(t) = A_w \cos(\omega_w t) \tag{5.82}$$

with $\omega_w = 2\pi/T_w$.

In the HB implementation, the fundamental frequency is set to $\Delta\omega = \omega_w$ and the other frequencies are defined harmonically as $\omega_k = k\Delta\omega$. Following the calculations presented in Section 5.3.1, the block-diagonal matrix $\mathbf{L} \in \mathbb{R}^{(2N_\omega+1)\times(2N_\omega+1)}$ is built as follows:

$$\mathbf{L} = \begin{pmatrix} \mathbf{L}_0 & \mathbf{0} & \cdots & \mathbf{0} \\ \mathbf{0} & \mathbf{L}_1 & \cdots & \mathbf{0} \\ \vdots & \vdots & \ddots & \vdots \\ \mathbf{0} & \mathbf{0} & \cdots & \mathbf{L}_{N_\omega} \end{pmatrix} \tag{5.83}$$

[4] http://www.wamit.com/

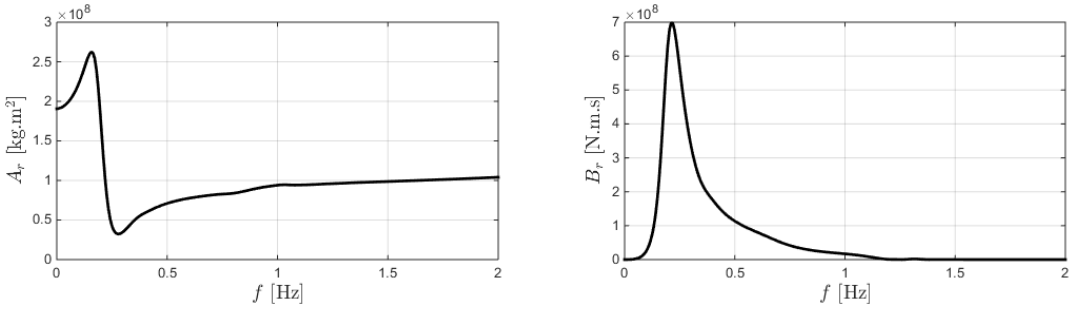

(a) Radiation added mass $A_R(f)$ (b) Radiation damping $B_R(f)$

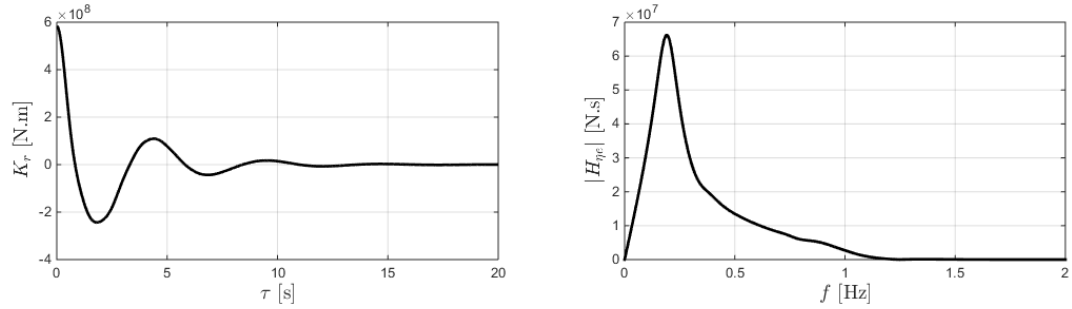

(c) Radiation impulse response kernel $K_R(\tau)$ (d) Magnitude of the excitation torque transfer function $H_{\eta e}$

Figure 5.3: Hydrodynamic characteristics of the flap-type device: time- and frequency-domain radiation coefficients, and frequency-domain excitation torque coefficients

where the matrices on the diagonal are given as:

$$\begin{cases} \mathbf{L}_0 = S_h \\ \mathbf{L}_k = \begin{pmatrix} S_h - \omega_k^2[I + A_R(\omega_k)] & \omega_k[B_{PTO} + C_{dis,l} + B_R(\omega_k)] \\ -\omega_k[B_{PTO} + C_{dis,l} + B_R(\omega_k)] & S_h - \omega_k^2[I + A_R(\omega_k)] \end{pmatrix} \quad \text{for } k = 1 \ldots N_\omega \end{cases} \tag{5.84}$$

The excitation torque is projected onto the Fourier basis as the vector

$$\hat{\mathbf{e}} = \begin{pmatrix} 0 \\ \hat{e}_1 \\ \hat{e}_2 \\ 0 \\ \vdots \\ 0 \end{pmatrix} \tag{5.85}$$

with $\hat{e}_1 = \Re\{H_{\eta e}(\omega_w)\}A_w$ and $\hat{e}_2 = \Im\{H_{\eta e}(\omega_w)\}A_w$.

For the explicit Jacobian computation, detailed in Section 5.4.1, the partial derivatives of the non-linear terms with respect to position and velocity are given as $\partial n/\partial\theta = 0$ and $\partial n/\partial\dot{\theta} = -C_{dis,q}|\dot{\theta}|$.

In the following subsections, to make the reader familiar with the HB framework, these fundamental features of the method are examined:

- How the root-finding algorithm converges to the solution, and how the 'strength' of the non-linear effects can have an impact on the number of iterations;
- How the approximation error of the HB solution (as compared to the exact mathematical solution), decreases with the number of harmonics N_ω;
- How the Galerkin and PS versions of the HB method compare to each other;

- How the HB method compares to a standard time-domain numerical integration scheme, namely the second-order Runge-Kutta method [14].

5.5.3 Root-finding algorithm

As a first introduction to the HB method working principle, Fig. 5.4 illustrates how the root-finding Newton algorithm converges to the solution of the HB equation (starting from the linearised solution, obtained by setting $C_{dis,q}$ to zero and solving $\mathbf{L}\hat{\mathbf{x}}^{(0)} = \hat{\mathbf{e}}$). In addition, the quadratic viscous drag coefficient is set to three different values: $C^*_{dis,q} = 0.5C_{dis,q}$, $C^*_{dis,q} = C_{dis,q}$ and $C^*_{dis,q} = 2C_{dis,q}$, to analyse the impact of higher or lower non-linear effects. In this example, the PS approach ($N_t = 2N_\omega + 1$) is used, and the order of the Fourier approximation is $N_\omega = 10$.

Intuitively, larger non-linear forces imply that the solution is further from the initial (linear) solution $\hat{\mathbf{x}}^{(0)}$. As a consequence, the root-finding algorithm requires more iterations before reaching the solution, as visible in Fig. 5.4a, which shows the residuals decreasing at each iteration of the Newton method, for the three different values of $C^*_{dis,q}$. In the three cases, the residual norm decreases rapidly with the number of iteration, at an exponential rate (i.e. the norm is proportional to ρ^n, where $0 < \rho < 1$). The root-finding algorithm stops when the residuals reach a predefined tolerance value (in this case, $|\mathbf{r}(\hat{\mathbf{x}})| \leq 10^{-6}$).

Fig. 5.4b shows the solutions for $\theta(t)$ corresponding to the three levels of non-linearity, as well as the linear initial solution. As can be expected, a larger level of viscous damping tends to reduce the motion amplitude.

5.5.4 Convergence rate and accuracy

The previous subsection illustrates how the root-finding algorithm converges towards the solution of the HB equation, as the root-finding algorithm iterates, i.e., schematically, as Eq. (5.59) is recursively applied. Choosing a different root-finding algorithm, or computing the Jacobian less accurately, may yield a different, possibly slower, convergence rate [146], but should converge to the same solution.

This subsection examines another crucial aspect of the HB convergence properties, namely, how much accuracy is gained by increasing the number N_ω of harmonics. The convergence of spectral methods to the exact solution, as N_ω increases, is examined in detail in [102], to which the reader is referred to for more insight.

Of course, increasing the order N_ω of the solution expansion yields more accurate results, in the sense that the error between the HB (approximate) solution and the *exact* solution decreases. However, it is typically the case that the exact solution is *not* known (otherwise, why would one need to use the HB method?), so that some indirect estimate of the error should be found. To that end, two facts are of particular interest:

- The rate of convergence to the actual solution is governed by the singularities, induced by the non-linear terms. In particular, if all the functions involved in the differential equation are infinitely smooth, the convergence rate is exponential, which means that, asymptotically, the approximation error is proportional to ρ^{N_ω}, where $0 < \rho < 1$. Therefore, in such a case, increasing N_ω by just one or several units can improve the solution accuracy by one or several orders of magnitude. On the contrary, singularities negatively affect the convergence rate [102]. For example, if the solution has discontinuous first-order derivatives, the convergence rate is only quadratic (i.e. the error decreases in N_ω^{-2}); if the solution has discontinuous second-order derivatives, the convergence rate is only cubic, etc.

- Without knowing the actual solution, the order of magnitude of the approximation error can be evaluated based on the norm of the last coefficient of the solution ($\hat{y}_{N_\omega}$ in the notations of Eq. (5.3)), if the type of convergence rate is known. For example, assuming an exponential

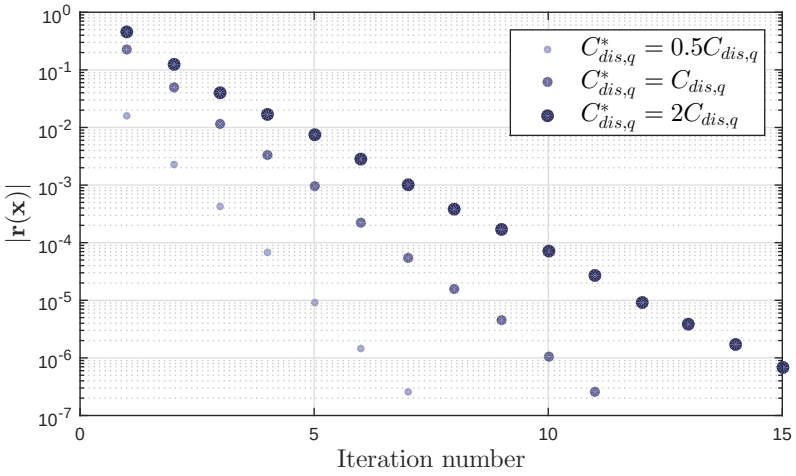

(a) Residual norm $|\mathbf{r}(\hat{\mathbf{x}})|$ *vs* number of iterations

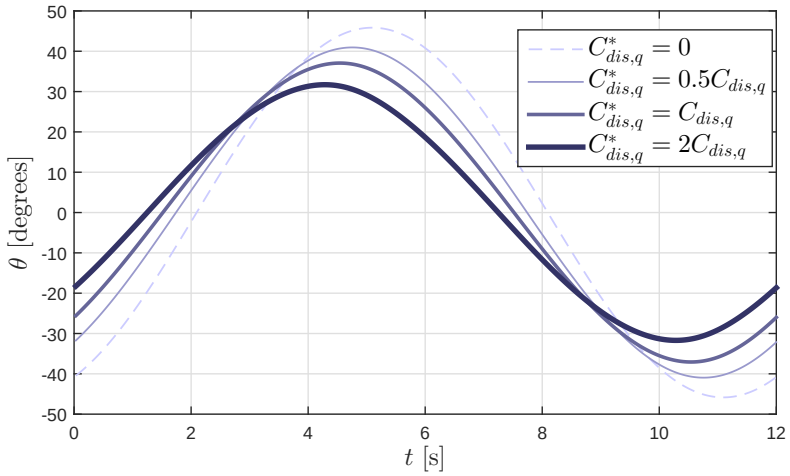

(b) Solution for the angular position of the flap, $\theta(t)$, for the linear problem ($C^*_{dis,q} = 0$) and the three non-linear problems

Figure 5.4: Convergence of the HB algorithm to the non-linear solution with three levels of quadratic viscous damping - flap-type WEC, monochromatic wave excitation with $T_w = 12$s and $A_w = 4$m.

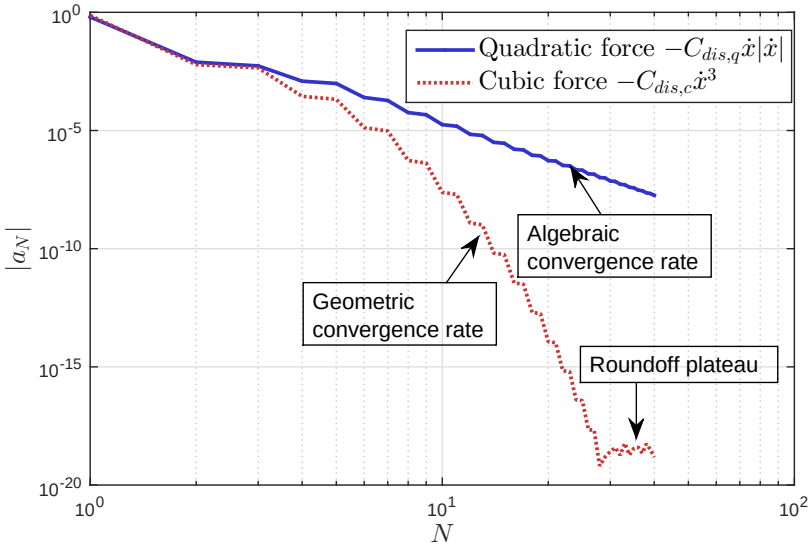

Figure 5.5: Magnitude of the last harmonic of the HB solution as a function of the number of harmonics, with a quadratic viscous drag term (discontinuous second-order derivative) *vs* a cubic viscous drag term (infinitely smooth) - flap-type WEC, monochromatic wave excitation with $T_w = 12$s and $A_w = 4$m.

convergence rate, it is easy to show [102] that the error is of the same order of magnitude as the last coefficient, $\hat{y}_{N_\omega}$, in the solution expansion.

In general, if the non-linearities involved in the dynamical equations have discontinuous i^{th}-order derivatives, it is easy to see that the solution will have discontinuous $(i+1)^{\text{th}}$-order derivatives: indeed, considering a system cast in state-space form $\dot{\mathbf{x}} = \mathbf{f}(\mathbf{x},t)$, the term $\mathbf{f}(\mathbf{x},t)$ has discontinuous i^{th}-order derivatives; therefore the solution

$$\mathbf{x}(t) = \int_{\tau=0}^{t} \mathbf{f}(\mathbf{x}(\tau),\tau)d\tau \tag{5.86}$$

has discontinuous $(i+1)^{\text{th}}$-order derivatives.

In the chosen numerical example, the non-linear term, $n\{\theta,t\} = -C_{dis,q}\dot{\theta}|\dot{\theta}|$, has a discontinuous second-order derivative. Therefore, the solution has discontinuous third-order derivatives which implies that the convergence rate may not be exponential, but rather algebraic in N_ω^{-4} - which is empirically verified in the following paragraphs.

The logarithmic plot of Fig. 5.5 show the magnitude $|a_{N_\omega}|$ of the last harmonic of the HB solution (using the PS formulation) for $N_\omega = 1...40$, where $|a_{N_\omega}| = \sqrt{\hat{x}_{2N_\omega}^2 + \hat{x}_{2N_\omega+1}^2}$. Asymptotically, $|a_{N_\omega}|$ decreases algebraically in N_ω^{-5}.

As explained in [102], the error, encountered by using a PS method of order N_ω, is roughly bounded from above by the sum of the magnitudes of the coefficients $a_{N'_\omega}$, for all $N'_\omega > N_\omega$, which represent the terms of the solution expansion discarded as a result of an approximation of order N_ω. Mathematically, this statement is expressed as follows:

$$|e_{N_\omega}| \leq \sum_{N'_\omega=N_\omega+1}^{\infty} |a_{N'_\omega}| \tag{5.87}$$

Even if the coefficients $a_{N'_\omega}$, for $N'_\omega > N_\omega$, have not been computed, their sum can be estimated if the convergence type (algebraic, exponential, etc.) of the coefficients is known. In the present

case, the sequence $|a_{N_\omega}|$ decreases algebraically, say $|a_{N_\omega}| \approx kN_\omega^{-\beta}$ for some constant k and $\beta > 1$. Using the simple fact that

$$\int_{s=N_\omega+1}^{\infty} ks^{-\beta} ds \leq \sum_{N'_\omega=N_\omega+1}^{\infty} kN'^{-\beta}_\omega \leq \int_{s=N_\omega}^{\infty} ks^{-\beta} ds \tag{5.88}$$

it is not hard to show that, if $|a_{N_\omega}|$ is in the order of $N_\omega^{-\beta}$, the approximation error $|e_{N_\omega}|$ decreases in $N_\omega^{-\beta+1}$. Therefore, in the case considered here, since from Fig. 5.5 the magnitude of the last Fourier coefficient of the solution decreases as N_ω^{-5}, the HB solution error decreases as N_ω^{-4}, which is what was expected.

For the sake of comparison, Fig. 5.5 also presents the results obtained when the non-linear, quadratic viscous drag term is replaced with a cubic damping torque, thus making the non-linearities infinitely smooth. This time, $|a_{N_\omega}|$ (and hence the approximation error) decreases exponentially, thus even more rapidly than with the quadratic formulation. It can also be seen that when N_ω is large enough, the error reaches the machine accuracy, and hence the coefficients obtained by increasing the order of the HB method are not relevant any more, but instead fluctuate randomly, which is termed the "round-off plateau" in [102].

5.5.5 Galerkin *vs* PS formulation

So far, for simplicity, the PS method was chosen for the purpose of numerical illustration, because the PS formulation implies no tuning of the parameter N_t, which otherwise governs the number of points used to approximate the integrals in the Galerkin formulation. It has already been explained in Section 5.3.3 that the PS formulation is strictly equivalent to a Galerkin method with $N_t = 2N_\omega + 1$, assuming a rectangular numerical integration rule. In this subsection, the relative merits of the PS and Galerkin approaches are further investigated. It is shown that there is little rationale in adopting the Galerkin approach with a value for N_t significantly larger than $2N_\omega + 1$.

To that end, Fig. 5.6 shows the magnitude of the last Fourier coefficient of the solution, for $N_\omega = 1...40$, using three variants:

- Galerkin, using $N_t = 2N_\omega + 1$, i.e. the PS approach;
- Galerkin, using $N_t = 100$;
- Galerkin, using $N_t = 400$.

Thus, in the second and third variants, the number of collocation points, which are used to approximate the integrals in the HB equation (5.53), is set to a value larger than $2N_\omega + 1$.

As can be appreciated in Fig. 5.6a, in the two Galerkin methods (with $N_t = 100$ and $N_t = 400$), the coefficients a_{N_ω}, for even N_ω, are zero to machine accuracy. That is because the non-linearity in the dynamical equation is an odd function, and thus, only makes odd harmonics of the fundamental frequency appear in the exact solution. In the PS approach ($N_t = 2N_\omega + 1$), when N_ω is even, the last coefficient of the expansion is found to be non-zero, because the number of integration points, $2N_\omega + 1$, is odd. This, however, does not affect the accuracy of the solution because, as explained in [102], what really governs the solution accuracy is the "envelope" of the coefficients of the last harmonic [102], which can be studied, in the present case, by only considering odd values of N_ω, as shown in Fig. 5.6b.

Examining Fig. 5.6b, it can now be clearly seen that there is almost no difference in accuracy between the three variants considered. In fact, in the Galerkin approach, the effect of increasing N_t, even by a large amount, is insignificant with respect to the gain in accuracy of increasing N_ω, even by only one unit. This result corroborates those of [132]. Since increasing N_t is computationally demanding (because the size of the matrix Φ_{N_t} increases accordingly), there is no rationale for choosing N_t significantly larger than $2N_\omega + 1$. In [132], it is suggested that using N_t between $2N_\omega + 1$ and $3N_\omega$ is sufficient. *Throughout the rest of this thesis, the PS version of the HB method will be employed.*

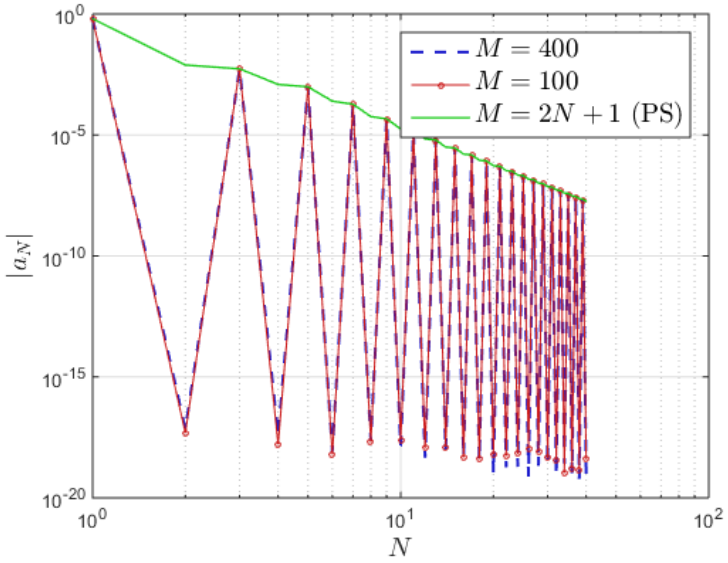

(a) For $N_\omega = 1, 2, ...40$

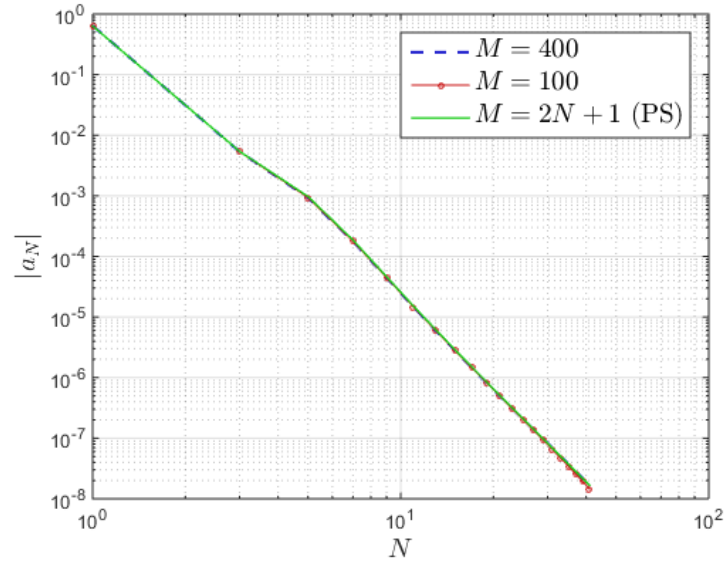

(b) For $N_\omega = 1, 3, 5, ..., 41$

Figure 5.6: $|a_{N_\omega}|$ for three variants of the HB formulation: Galerkin with $N_t = 2N_\omega + 1$ (PS), $N_t = 100$ and $N_t = 400$ - flap-type WEC, monochromatic wave excitation with $T_w = 12$s and $A_w = 4$m.

5.5.6 The HB method *vs* time-domain integration

Finally, this subsection briefly discusses the properties, in terms of convergence, of a standard numerical time-domain integration procedure, namely the 2nd-order Runge-Kutta method [14], abbreviated as RK2. The RK2 scheme is chosen as a point of comparison for the HB method, based on the following grounds:

- The method is simple, in the sense that the integration time step Δt_{RK} is the only parameter, and remains fixed throughout the procedure;
- It is ensured, if the solution is continuous, that the numerical results converge to the exact solution when Δt_{RK} tends to zero [96];
- The computation of the convolution product of Eq. (4.90) cannot be easily carried out if the time step is not constant, as discussed in Chapter 3 of [3]. In contrast, using the RK2 method, the convolution integral can be numerically calculated using, for example, the rectangle integration rule.

Given the three points above, the comparison between HB and RK2 methods can be carried out by computing RK2 results for several time step values Δt_{RK}, and examining how the RK2 accuracy changes with the time step. Note that the HB method directly solves for one, steady-state, period of the solution. In contrast, time-domain integration also models the transient response of the system. Therefore, for a relevant comparison, the RK2 simulations cover several wave periods, in order to ensure that transient effects have the time to fade out. Then, only the very last period of the motion, which can be safely considered to be in steady-state, is compared with HB results.

Furthermore, in order to provide an appropriate point of comparison to assess the RK2 method accuracy, the non-linear terms are removed (by setting $C_{dis,q}$ to zero). By doing so, it is ensured that the HB results (which then coincide with the traditional, linear frequency-domain method) are the *exact* solution, and thus provide an unquestionable baseline.

The root-mean-square error encountered by RK2 integration is computed, over a full wave period T_w (in the steady-state regime), as follows:

$$e_{RMS} = \sqrt{\frac{1}{T_w}\int_{t=0}^{T_w} (\theta_{RK2}(t) - \theta_{HB}(t))^2 dt} \tag{5.89}$$

which is numerically approximated as:

$$e_{RMS} = \sqrt{\frac{1}{N_{tRK}}\sum_{i=1}^{N_{tRK}} (\theta_{RK2}(i\Delta t_{RK}) - \theta_{HB}(i\Delta t_{RK}))^2} \tag{5.90}$$

with $N_{tRK}\Delta t_{RK} = T_w$. The reader may have noticed that the numerical evaluation of the root-mean-square error, in Eq. (5.90), requires the HB solution to be calculated at each (refined) RK2 time step $i\Delta t_{RK}$, where typically $\Delta t_{RK} \ll \Delta t$ (Δt is the time step between the collocation points of the PS HB method). To that end, once the HB solution $\hat{\mathbf{x}}$ has been found, and defining the matrix $\Phi_{N_{tRK}}$ analogously to Φ_{N_t} in (5.49), the solution $\mathbf{x}$ at the RK2 time steps is simply obtained as $\mathbf{x}_{N_{tRK}} = \Phi_{N_{tRK}}\hat{\mathbf{x}}$. The results of Eq. (5.90) are shown in Fig. 5.7, where it can be seen that the solution accuracy improves linearly with $1/\Delta t_{RK}$. This is in contrast to the HB method, for which the accuracy improves more than linearly with N_ω.

For now, given that most of the RK2 simulation time is spent letting the transient effects fade out, and that a monochromatic wave excitation signal is not representative of a wave input for a realistic simulation, any comparison in terms of computational time between the RK2 and HB methods is at best qualitative. Because of the convolution product in Eq. (4.90), the computation time in RK2 increases as $(1/\Delta t_{RK})^2$ (for a *linear* improvement in terms of accuracy). In the HB

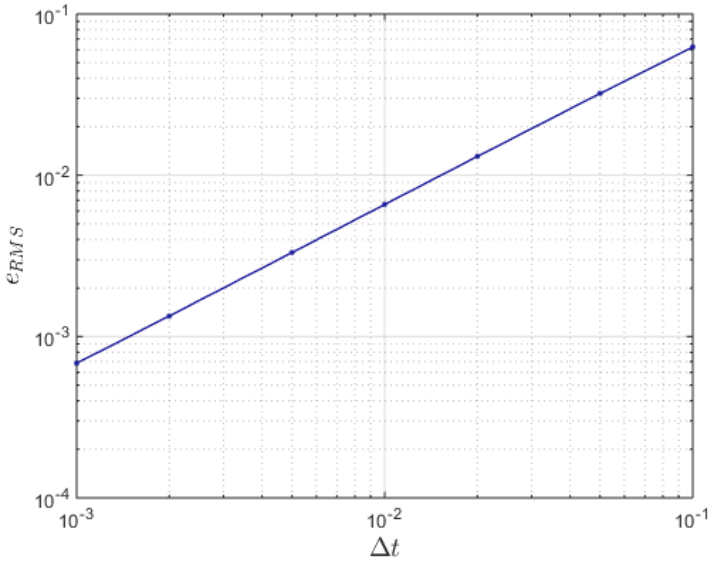

Figure 5.7: Root-mean-square error *vs* integration time step, for the RK2 numerical solution - flap-type WEC, monochromatic wave excitation with $T_w = 12$s and $A_w = 4$m.

method, the computation time is expected to increase as more than N_ω^2 and at most N_ω^3, because of the matrix operations involved in the solution. However, the corresponding improvement in terms of accuracy can be more than linear (in N_ω^{-5} for the example considered in this section). Concerning the relative merits of the HB and RK2 methods, in terms of accuracy and computation time, more will be learnt in Chapter 6, when practical case studies, with realistic wave inputs, will be studied.

5.6 Sensitivity equation within the harmonic balance framework

5.6.1 The sensitivity equation

This section considers models of the type of Eq. (4.90), specified in a parametric form. Define $\alpha \in \mathbb{R}^{N_\alpha}$, as a vector of N_α parameters governing, for example, the geometry of the WEC, or the settings or dimensions of its PTO system. α is assumed to take continuous values in $\mathbb{R}^{N_\alpha}$. Eq. (4.90) is modified in order to represent the fact that the WEC model depends on the parameters α:

$$\mathcal{L}\{\mathbf{x},\alpha\} - \mathbf{n}\{\mathbf{x},t,\alpha\} - \mathbf{e}(t,\alpha) = \mathbf{0} \tag{5.91}$$

where:

- The linear terms $\mathcal{L}$ are now allowed to depend on the parameters α, and thus take the following form:

$$\mathcal{L}\{\mathbf{x},\alpha\} := (\mathbf{M}(\alpha) + \mathbf{M}_\infty(\alpha))\ddot{\mathbf{x}} + \mathbf{C}(\alpha)\dot{\mathbf{x}} + \mathbf{S}(\alpha)\mathbf{x} + \int_{\tau=0}^{\infty} \mathbf{K}(\tau,\alpha)\dot{\mathbf{x}}(t-\tau)d\tau \tag{5.92}$$

- The non-linear terms $\mathbf{n}\{\mathbf{x},t,\alpha\}$ can be detailed as:

$$\mathbf{n}\{\mathbf{x},\alpha,t\} := \mathbf{n}(\mathbf{x},\dot{\mathbf{x}},\ddot{\mathbf{x}},\alpha,t) \tag{5.93}$$

  where the time-dependence represents forcing inputs derived from the incident waves, as discussed in Section 4.3.5, and the parameters α can play a role in the non-linear modelling terms;

- $\mathbf{e}(t,\alpha)$ represents an additive forcing input, derived from the incident waves, and possibly depending on the parameters α.

In some circumstances, it can be interesting to know how the solution $\mathbf{x}$ changes, when the parameters α change, for example when carrying out design optimisation, or if one wants to study the sensitivity of the WEC performance to uncertainties in the modelling parameters. To that end, it is assumed that the terms of $\mathcal{L}$, $\mathbf{n}$ and $\mathbf{e}$ are continuous and differentiable with respect to the parameters α.

In this thesis, as discussed in Section 4.6, the forcing terms in Eq. (5.91) are time-periodic (with period T), because they are essentially derived from a wave input, generated through harmonic superposition. The steady-state solution $\mathbf{x}$, if it exists, is also periodic with period T (which initially justifies the choice of the HB approach). Therefore, when varying the parameter vector α, what is in fact examined is how the *periodic*, steady-state, solution $\mathbf{x}$ varies in the space of periodic solutions with period T.

Denote $\mathbf{x}^*$ as the periodic solution for Eq. (5.91) for a specific value α^* of the parameters. Consider infinitesimal variations in the parameters $\alpha = \alpha^* + \Delta\alpha$. The sensitivity equation expresses the fact that the solution $\mathbf{x} = \mathbf{x}^* + \Delta\mathbf{x}$, for $\alpha = \alpha^* + \Delta\alpha$, must still satisfy the dynamical equation (5.91). The solution to the sensitivity equation should then consist of a periodic, matrix-valued function, $\left.\frac{\partial \mathbf{x}}{\partial \alpha}\right|_{\alpha^*}(t) \in \mathbb{R}^{D\times N_\alpha}$, which specifies how the solution $\mathbf{x}$ at time t changes for infinitesimal variations of α. In other words:

$$\mathbf{x}(t) \approx \mathbf{x}^*(t) + \left.\frac{\partial \mathbf{x}}{\partial \alpha}\right|_{\alpha^*}(t)\Delta\alpha \tag{5.94}$$

First consider a single parameter ($N_\alpha = 1$). For a generic, parametric differential equation $\dot{\mathbf{x}} = \mathbf{f}(\mathbf{x},t,\alpha)$, the sensitivity equation is written [97] as:

$$\frac{\partial \dot{\mathbf{x}}}{\partial \alpha} = \frac{\partial \mathbf{f}}{\partial \alpha} + \frac{\partial \mathbf{f}}{\partial \mathbf{x}}\frac{\partial \mathbf{x}}{\partial \alpha} \tag{5.95}$$

where $\partial\mathbf{f}/\partial\mathbf{x}$ and $\partial\mathbf{f}/\partial\alpha$ are evaluated along the steady-state, periodic, solution $\mathbf{x}(t)$, resulting from a given parameter α. Thus, Eq. (5.95) is, in essence, a linear, time-varying differential equation of the form $\dot{\mathbf{y}} = \mathbf{a}(t)\mathbf{y} + \mathbf{b}(t)$, where the time varying linear coefficients are $\mathbf{a}(t) = \partial\mathbf{f}/\partial\mathbf{x}$ and $\mathbf{b}(t) = \partial\mathbf{f}/\partial\alpha$. The solution of this linear, time-varying differential equation is $\partial\mathbf{x}/\partial\alpha$.

It is not difficult to transpose Eq. (5.95) into the different formalism of Eq. (5.91), which yields the following sensitivity equation:

$$\frac{\partial \mathcal{L}}{\partial \mathbf{x}}\frac{\partial \mathbf{x}}{\partial \alpha} + \left.\frac{\partial \mathcal{L}}{\partial \alpha}\right|_{\mathbf{x}^*} - \left.\frac{\partial \mathbf{n}}{\partial \mathbf{x}}\right|_{\mathbf{x}^*}\frac{\partial \mathbf{x}}{\partial \alpha} - \left.\frac{\partial \mathbf{n}}{\partial \dot{\mathbf{x}}}\right|_{\mathbf{x}^*}\frac{\partial \dot{\mathbf{x}}}{\partial \alpha} - \left.\frac{\partial \mathbf{n}}{\partial \alpha}\right|_{\mathbf{x}^*} - \frac{\partial \mathbf{e}}{\partial \alpha} = \mathbf{0} \tag{5.96}$$

Because of the linearity of the operator $\mathcal{L}$, it can be easily checked that $\frac{\partial \mathcal{L}}{\partial \mathbf{x}}\frac{\partial \mathbf{x}}{\partial \alpha} = \mathcal{L}\{\frac{\partial \mathbf{x}}{\partial \alpha}\}$, so that $\frac{\partial \mathbf{x}}{\partial \alpha}$ may be found by solving the following linear, time-varying differential equation with unknown $\mathbf{s}(t)$:

$$\mathcal{L}\{\mathbf{s}\} - \left.\frac{\partial \mathbf{n}}{\partial \mathbf{x}}\right|_{\mathbf{x}^*}\mathbf{s} - \left.\frac{\partial \mathbf{n}}{\partial \dot{\mathbf{x}}}\right|_{\mathbf{x}^*}\dot{\mathbf{s}} = -\left.\frac{\partial \mathcal{L}}{\partial \alpha}\right|_{\mathbf{x}^*} + \left.\frac{\partial \mathbf{n}}{\partial \alpha}\right|_{\mathbf{x}^*} + \frac{\partial \mathbf{e}}{\partial \alpha} \tag{5.97}$$

Working using time-domain numerical integration, typically $\mathbf{x}^*$ would be determined (using time-domain integration), and Eq. (5.97) would then need to be solved through an additional (time-domain) simulation. In a HB framework, it is shown in the next subsection that the sensitivity equation can be solved using a simple matrix inversion, with little additional computation with respect to the solution of Eq. (5.53) or (5.57).

5.6.2 The sensitivity equation in the HB framework

Since the equation initially considered, Eq. (5.91), is time-periodic, Eq. (5.97) is not only time-varying, but also time-periodic, and can be rewritten in a HB framework. First, assuming that the

PS version of the HB method is employed, define a matrix $\mathbf{L}_s \in \mathbb{R}^{DN_t \times DN_t}$ and a vector $\mathbf{b}_s \in \mathbb{R}^{DN_t}$ as follows:

$$\begin{cases} \mathbf{L}_s := \Phi_{N_t}\mathbf{L} - \mathbf{D}_{\mathbf{x}}\Phi_{N_t} - \mathbf{D}_{\dot{\mathbf{x}}}\Phi_{N_t}\Omega \\ \mathbf{b}_s := -\Phi_{N_t}\frac{\partial \mathbf{L}}{\partial \alpha}\hat{\mathbf{x}}^* + \left.\frac{\partial \mathbf{n}_{N_t}}{\partial \alpha}\right|_{\mathbf{x}^*} + \Phi_{N_t}\frac{\partial \hat{\mathbf{e}}}{\partial \alpha} \end{cases} \tag{5.98}$$

where $\mathbf{L}$, $\mathbf{D}_{\mathbf{x}}$ and $\mathbf{D}_{\dot{\mathbf{x}}}$ are defined as in Eqs. (5.38), (5.65) and (5.66), respectively, Φ_{N_t} is defined in Eq. (5.49) and, similarly to Eqs. (5.51) and (5.64), $\left.\frac{\partial \mathbf{n}_{N_t}}{\partial \alpha}\right|_{\mathbf{x}^*}$ is defined as:

$$\left.\frac{\partial \mathbf{n}_{N_t}}{\partial \alpha}\right|_{\mathbf{x}^*} = \begin{pmatrix} \frac{\partial \mathbf{n}}{\partial \alpha}(t_1) \\ \vdots \\ \frac{\partial \mathbf{n}}{\partial \alpha}(t_{N_t}) \end{pmatrix} \tag{5.99}$$

In Eq. (5.98), it can be recognised that $\mathbf{L}_s$ is identical to the Jacobian of the residuals $\frac{\partial \mathbf{r}}{\partial \hat{\mathbf{x}}}$, computed at each iteration of the HB algorithm. Therefore, $\mathbf{L}_s$ can be seen as a simple by-product of the Newton (or other root-finding) procedure employed to solve the HB equation. The other term, $\mathbf{b}_s$, represents the derivatives, with respect to α, of the linear, additive input and non-linear terms, evaluated at each collocation point along the solution trajectory $\mathbf{x}^* = \Phi_{N_t}\hat{\mathbf{x}}^*$. Once the HB solution $\hat{\mathbf{x}}^*$ has been found, $\mathbf{b}_s$ can be evaluated at little additional cost.

It is now possible to express the sensitivity equation in a HB framework:

$$\mathbf{L}_s \frac{\partial \hat{\mathbf{x}}}{\partial \alpha} = \mathbf{b}_s \tag{5.100}$$

Solving the linear system of Eq. (5.100) provides $\frac{\partial \hat{\mathbf{x}}}{\partial \alpha}$, which specifies how each Fourier coefficient of the HB solution changes with respect to α.

Eq. (5.100) is readily extended to cases where α is not a scalar, but a vector of several (N_α) parameters. Interestingly, the matrix $\mathbf{L}_s$ does not involve any derivative with respect to the parameters. For each component α_i of the parameters, the corresponding vector $\mathbf{b}_{s,i}$ can be evaluated as:

$$\mathbf{b}_{s,i} := -\Phi_{N_t}\frac{\partial \mathbf{L}}{\partial \alpha_i}\hat{\mathbf{x}}^* + \left.\frac{\partial \mathbf{n}_{N_t}}{\partial \alpha_i}\right|_{\mathbf{x}^*} + \Phi_{N_t}\frac{\partial \hat{\mathbf{e}}}{\partial \alpha_i} \tag{5.101}$$

Finally, defining $\mathbf{B}_s = [\mathbf{b}_{s,i}, \cdots \mathbf{b}_{s,N_\alpha}]$, the matrix $\frac{\partial \hat{\mathbf{x}}}{\partial \alpha} \in \mathbf{R}^{DN_t \times N_\alpha}$ (which is the Jacobian of the HB solution with respect to the parameters) is calculated by solving the following linear system:

$$\mathbf{L}_s \frac{\partial \hat{\mathbf{x}}}{\partial \alpha} = \mathbf{B}_s \tag{5.102}$$

In Section 6.4, it will be explained how, when solving problems which have different but close enough parameter values, the HB sensitivity equation can be used to improve the starting guess for the HB algorithm. In Chapter 7, it will be shown how the HB sensitivity equation can be used within a gradient-based algorithm for WEC parametric optimisation, to evaluate the cost function derivative.

5.6.3 Example

The methodology outlined above, in Section 5.6.2, is applied to the flap-type WEC model, considering the viscous drag term $C_{dis,q}$ as the only parameter. Considering a monochromatic input wave with period $T_w = 14$s and amplitude $A_w = 3$m, and taking into account 7 frequencies in the Fourier expansion of the solution, the HB equation is first solved, $\mathbf{b}_s$ and $\mathbf{L}_s$ are then calculated like in Eq. (5.98) and, finally, $\frac{\partial \hat{\mathbf{x}}}{\partial \alpha}$ is obtained by solving Eq. (5.100).

Then, the solution variations for changes in $\alpha = C_{dis,q}$, with respect to a nominal value $C^*_{dis,q}$, can be estimated as follows:

$$\hat{\mathbf{x}} \approx \hat{\mathbf{x}}^* + \frac{\partial \hat{\mathbf{x}}}{\partial \alpha}\Delta\alpha \tag{5.103}$$

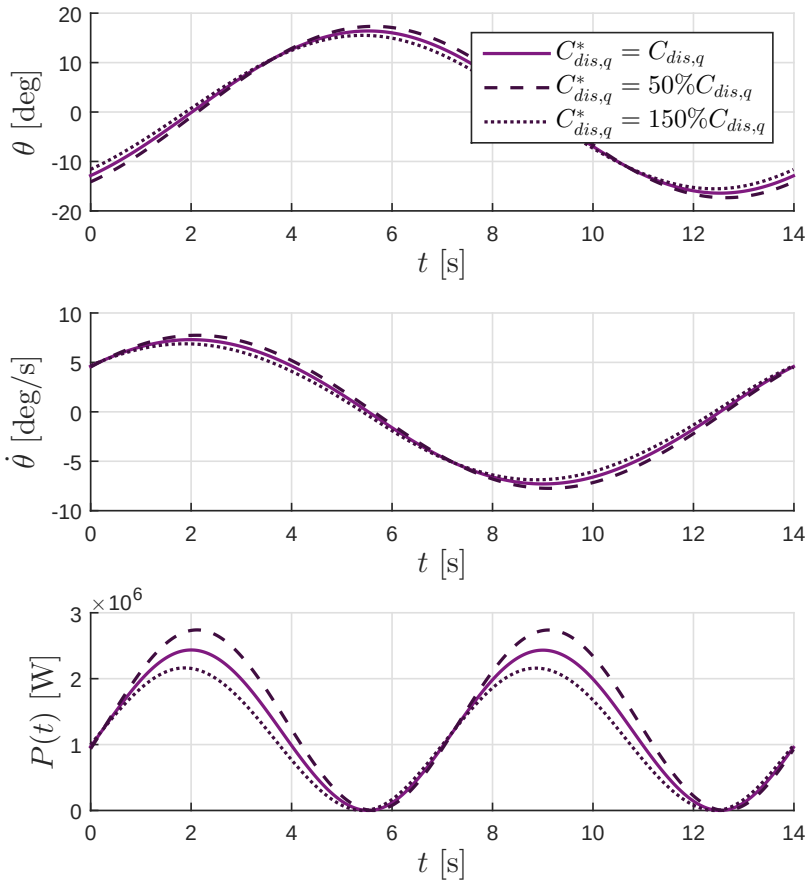

Figure 5.8: Nominal solution and variations with respect to $C_{dis,q}$ - flap-type WEC, monochromatic wave excitation with $A_w = 3$m, $T_w = 14$s

The corresponding results are plotted in Fig. 5.8 for $\Delta\alpha = \pm 50\%\alpha$, in terms of angular position, velocity and absorbed power.

5.7 From the wave spectrum to WEC outputs

5.7.1 From the wave spectrum to time-periodic IDEs

At this stage, by combining the outputs of Parts I and II of this thesis, it is possible to outline a methodology to characterise the WEC outputs in a random sea, based on harmonic superposition for the generation of input wave signals, and on the harmonic balance method to solve for the dynamical equation in any given wave signal.

From Chapter 4, it has been established that a wide range of WEC models, including mooring and PTO systems, can be expressed in a general form:

$$\mathcal{L}\{\mathbf{x}\} - \mathbf{n}\{\mathbf{x}, t\} - \mathbf{e}(t) = 0 \tag{5.104}$$

As discussed in Section 4.6, the forcing terms involved in Eq. (5.104) are all derived from one or more incident wave signals, most typically the free-surface elevation η at some reference location. The incident wave signals can be considered Gaussian, as discussed in Chapter 2. Hence, to obtain a satisfactory characterisation of the WEC response in a given sea state, sample time series of the Gaussian incident wave input must be generated, in a way which is statistically consistent with the Gaussianity assumption and with the target wave spectrum. As seen in Chapter 3, the incident wave input can be usefully generated using harmonic superposition. In particular, choosing the length of the generated signals as $T = 1/\Delta f$, every forcing term involved in Eq. (5.104) is periodic with period T.

Thus, when η (or other incident wave signals) is generated using harmonic superposition, Eq. (5.104) becomes time-periodic, and may be solved efficiently and accurately using the HB method, described previously in this chapter. Two parameters are particularly important in the HB implementation:

- The length of the generated signal, T, determines the frequency step $\Delta f = 1/T = \Delta\omega/2\pi$. As seen in Chapter 3, too coarse a Δf implies that the target spectrum is not well represented - in terms of the generated time-domain signal, this means that significant distortion is introduced in the correlation function.

- The cut-off frequency $f_c = \omega_c/2\pi$ determines the number of harmonics present in the HB solution. Possibly, the cut-off frequency f_{c_η} of the generated wave signal may be chosen to be lower than that of the HB solution, f_c: because of the presence of non-linear terms, the solution may have non-zero components even for those frequencies between f_{c_η} and f_c. While f_{c_η} is primarily chosen so as to capture most of the relevant frequency content of the gravity wave spectrum (which constitutes the forcing input to the system), f_c essentially governs the accuracy of the solution, as illustrated in Section 5.5 for monochromatic waves.

5.7.2 A HB procedure for WEC output characterisation in a given wave spectrum

For a given choice of f_c and T, there are $N_\omega = f_c/\Delta f = f_c \times T$ frequencies, which result in $2N_\omega + 1$ residual equations. If D is the dimension of the system in Eq. (5.104), the size of the problem to solve in the HB technique is thus $N_{HB} = (2N_\omega + 1) \times D$. The computation cost of the solution is governed by:

- The number of iterations, which in turns depends on the algorithm starting point and the strength and nature of the non-linear effects. The computation time depends *linearly* on the number of iterations.

- The problem size N_{HB}: at each Newton iteration, building and inverting the Jacobian matrix - see Section 5.4.1 - requires matrix operations on a N_{HB}-by-N_{HB} matrix, which is, in general, proportional to N_{HB}^{β} - where $3 > \beta > 2$, with a value depending on the efficiency of the Jacobian computation implementation, and on the specific linear solver available. The relationship between problem size and computation time will be empirically investigated in Chapter 6.

Therefore, assuming a given number of iterations, the computation cost of the HB technique primarily depends on the problem size, as more than N_{HB}^2. However, it is more pertinent to consider the computation cost *per second of signal simulated*, i.e. the computation time normalised by T: the computation time to obtain one second of simulated signal, with the HB technique, is thus roughly proportional to $\frac{1}{T}N_{HB}^{\beta} \approx (2Df_c)^{\beta}T^{\beta-1}$. Since D is the (non-tunable) dimension of the model, the actual trade-off which arises is between T and f_c.

Consider the dependence of the computation time on $T^{\beta-1}$: the HB method computation cost *per second of signal simulated* increases *at least* linearly with the simulated duration. This is in contrast with time-marching procedures, briefly discussed at the end of Chapter 4 and with which, for a given time step, the ratio between the computational cost and the simulated duration T remains constant, regardless of T. Hence, two significantly different procedures, depending on whether time-domain integration or the HB method is used, can be identified. Assume that the system output must be calculated over $T_{tot} = 1000$s of wave signal, to ensure that relevant statistical quantities (such as power absorption) are estimated with sufficient confidence:

- With TD integration, the typical procedure consists of generating one incident wave signal of length 1000s, as illustrated in Fig. 5.9a. Some additional time must be allowed at the start of the simulation, to let the transient response fade out.

- With the HB method, it is preferable to run several, shorter simulations with a total length of 1000s, for example five simulations of length $T = 200$s, where T is chosen so as to ensure sufficient spectral discretisation (recalling that $\Delta f = 1/T$). This is illustrated in Fig. 5.9b.

In Fig. 5.9, regardless of the procedure (5.9a or 5.9b), the WEC response is simulated over the same total duration of 1000s, in which average quantities of interest can be estimated, such as power absorption, maximum motion amplitude, etc. Provided that $T = 200$s allows for a sufficiently accurate discretisation of the wave spectrum, and if wave time-series in Figs. 5.9a and 5.9b are generated through HRA (i.e. consistently with the Gaussian representation of ocean waves), the situations in Figs. 5.9a and 5.9b should be statistically identical.

5.7.3 Settings of the HB method

For a given T, f_c determines how accurate the HB solution will be for the generated wave signal with period T. As seen in Section 5.5, increasing f_c by only a small amount may improve the accuracy by several orders of magnitude, but the exact improvement ultimately depends on the specific nature of the non-linearities present in the dynamical model. Therefore, the dependence of the computation time on f_c^{β} involves a trade-off between computation cost and accuracy, which depends on the specific dynamical model under study. How T and f_c can be chosen in practice will be examined in detail in Chapter 6.

Another important aspect to consider is how to choose between deterministic and random amplitudes (HDA or HRA) for wave input generation. Assume that T is chosen sufficiently large to ensure an accurate discretisation of the target spectrum:

- If HRA is adopted, each generated signal of length T has a different variance and, more generally, statistics which differ from their long-term average, as would an actual T-second wave record. Using N_{sim} simulations of length T is then exactly statistically equivalent to

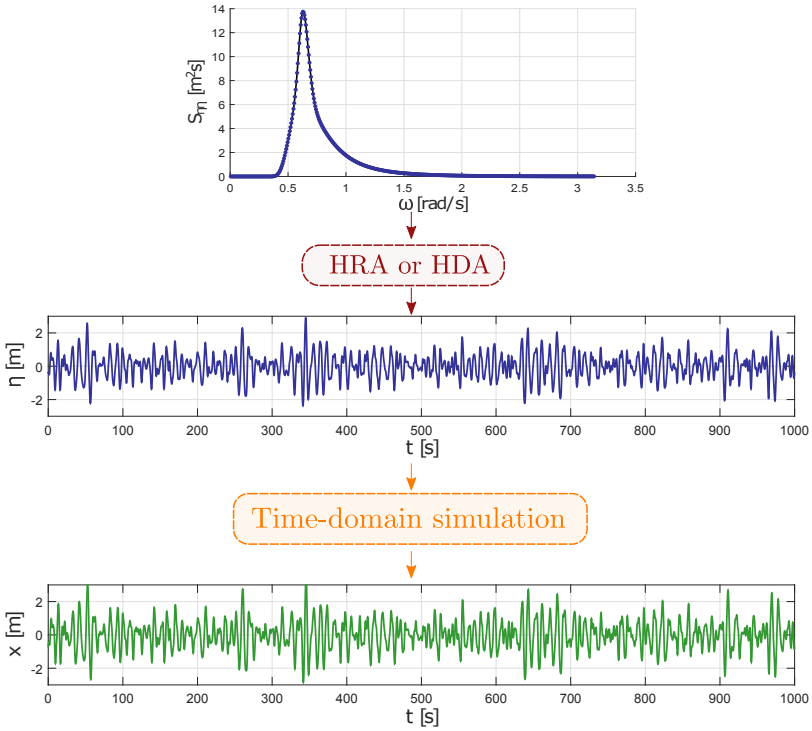

(a) TD simulation procedure

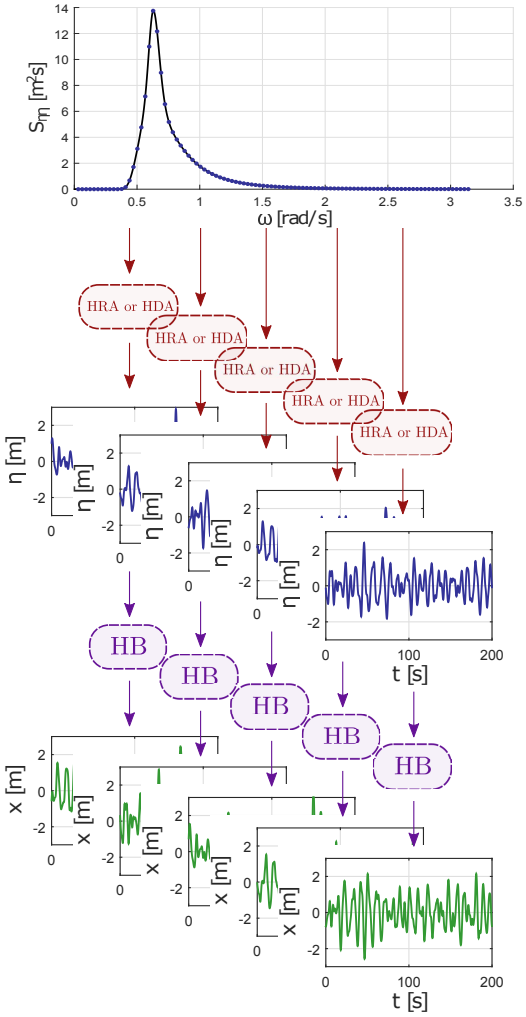

(b) HB simulation procedure

Figure 5.9: Typical WEC simulation procedures using TD integration *vs* the HB method

running one simulation of length $N_{sim} \times T$. However, a relatively large number of simulations may be necessary to obtain statistical estimates, such as power absorption, with sufficient confidence.

- If HDA is adopted, each generated signal of length T has the same variance and, more generally, statistics which are relatively close to their long-term average - which is not what would be observed in actual wave records. However, *if* it can be ensured, as discussed in Chapter 3, that HDA provides unbiased estimates of the statistical quantities of interest, those can be obtained using relatively few simulations.

The choice between HRA and HDA will be empirically studied in Chapter 6, Section 6.6.

5.7.4 Generalisation to multi-directional incident waves

Finally, although the case of multi-directional input waves is not considered in the remainder of this thesis, extending the proposed HB method to multi-directional random waves does not imply strong additional difficulties. The main difference is that, in multi-directional waves, there are multiple incident wave inputs, which can be expressed in the discretised wave number space (k_x, k_y) or in the discretised frequency-direction space (ω, θ): $\mathbf{e}(t)$ is now simply the sum of several, possibly many, independent Gaussian contributions, corresponding to different wave directions (or wave numbers). Similarly, the time-dependent terms in $\mathbf{n}\{\mathbf{x}, t\}$ result from several, possibly many, Gaussian contributions. Generating each of those elementary contributions using harmonic superposition also results in a time-periodic system, which can be solved within the proposed HB framework. However, in contrast to unidirectional waves, it must be ensured that the wave spectrum discretisation, employed for time series generation, allows for a consistent *directional* representation of the spectrum, in addition to an accurate frequency-wise representation. Since such aspects have not been investigated in Part I of this thesis, the case of a multi-directional incident waves will not be considered in the rest of this thesis.

5.8 Summary

In Section 5.2, the HB method is introduced within the broader panorama of spectral methods. The HB method is the name usually given to a *Fourier spectral method* applied to the numerical solution of a *time-periodic differential equation*. The relevance of the HB method, for the numerical simulation of WEC models in the form of Eq. (4.90), is supported by comparison with other engineering domains, where the HB method has been successfully applied.

Section 5.3 shows how Eq. (4.90) is transcribed into a HB residual equation, and offers two variants of the method: the Galerkin version (whereby the solution is found through harmonic cancellation) and the pseudo-spectral version (PS - whereby the residuals are cancelled at a set of collocation points). Section 5.4 provides additional mathematical details, necessary for the efficient solution of the HB equation, with particular emphasis on the explicit calculation of the residual Jacobian.

The fundamental properties of the HB method are further examined throughout Section 5.5 using a relatively simple non-linear WEC model example, simulated for monochromatic incoming wave signals. Of the PS and Galerkin variants of the HB method, in terms of residual minimisation, it is chosen to retain the PS formulation for the remainder of this thesis, given the certain computational overhead, and the meagre accuracy gain, with respect to the PS approach, which can be expected from using an oversampled Galerkin approach. The relationship between the singularities in the non-linear terms of Eq. (4.90), and the convergence rate of the HB solution (i.e. how the integration error decreases with the number of harmonics), is also empirically emphasised.

Section 5.6 considers the situation where the WEC model of Eq. (4.90) depends on modelling parameters. In such a case, solving the so-called *sensitivity equation* indicates how the solution for Eq. (4.90) changes, for infinitesimal changes in the system parameters. Within the HB framework,

the sensitivity equation takes a particularly simple form, since it consists of a linear system, in which the matrix to invert is identical to the HB residual Jacobian.

In Section 5.7, a methodology for the numerical simulation of WECs in random waves using the HB method is outlined, whereby many, relatively short, simulations are favoured over long simulations. The fundamental settings and trade-offs associated with the HB framework primarily concern the length of individual HB-simulated signals, T, and the HB cut-off frequency, f_c.

Nevertheless, this chapter tells little about the possible practical value of the proposed HB simulation framework. In particular, it must be ascertained whether or not the HB method achieves a better trade-off between computational cost and accuracy than standard time-domain numerical integration procedures. Furthermore, appropriate HB method settings, in terms of T and f_c, must be determined for typical WEC models. Chapter 6 will bring answers to such questions.

Part III

Numerical case studies

Chapter 6

Calibration and validation of the harmonic balance method for non-linear WEC model simulation

6.1 Introduction

In this chapter, practical examples for WEC HB numerical simulation in irregular waves are studied in detail, with two main objectives:

- **Calibration:** Discuss how to sensibly choose the parameters of the HB simulation framework, i.e. the cut-off frequency and simulation time, as discussed in Section 5.7, depending on the WEC considered;
- **Validation:** Assess the accuracy and computational performance of the HB technique, using as a baseline the more usual approach of the RK2 time-domain numerical integration procedure.

For a meaningful validation, a set of four WEC systems is chosen, presenting a variety of challenges and non-linear effects, further detailed throughout this chapter: the flap-type WEC already introduced in Chapter 5; a spherical heaving point absorber (HPA) considering non-linear Froude-Krylov forces; an array of four cylindrical HPAs; and a model of the ISWEC device [12, 13], a pitching WEC developed at Politecnico di Torino.

It may be difficult to identify, at first glance, in what operational space the HB method should be validated. In particular, by amplifying the WEC motion, power-maximising control strategies [7, 9] may significantly broaden its operational range [113], and enhance the impact of non-linear effects [11]. Therefore, when validating the HB method, it should be ensured that increased levels of non-linear effects can be handled.

Throughout this chapter, it is assumed that all the WECs considered can be 'controlled' by means of a two-parameter control law in the form $f_{PTO} = -k_{pto}x_{d_{pto}} - b_{pto}\dot{x}_{d_{pto}}$, where d_{pto} denotes the degrees of freedom through which power is transferred to the PTO system. The two PTO parameters can be tuned for a given sea state, to improve power absorption by ensuring that the device resonates in the incoming waves. By exploring a wide range of (k_{pto}, b_{pto}) settings, it is ensured that resonance conditions will be met, and hence it can be ascertained whether or not the proposed HB simulation method is robust to enhanced levels of non-linear effects. The methodology employed in this chapter, for the HB method calibration and validation, consists of the following:

- **Step 1:** For each WEC, a 'design' sea state is chosen, depending on the device characteristics. In the design sea state, the HB settings f_c and T are calibrated, using 'reasonable' PTO parameters;

- **Step 2:** Once f_c and T have been chosen, the HB method is run over a wide range of (k_{pto}, b_{pto}) PTO parameters. The HB method performance can thus be studied both off-resonance and in resonant conditions, in terms of computation time and accuracy, through comparison with the results of RK2 numerical integration. Examining the results at resonance, or close to resonance, allows the HB method accuracy to be assessed when non-linear effects are emphasized.

- **Step 3:** The relevance of the f_c and T values initially chosen is verified in resonant conditions and, if necessary, f_c and T can be adjusted.

Chapter organisation

The remainder of this chapter is organised as follows:

- The WEC models corresponding to each case study are presented in Section 6.2;

- Section 6.3 examines how the parameters of the HB simulation method can be calibrated (Step 1 above);

- A detailed comparison between the HB method and TD integration results is provided in Section 6.4 (Step 2 above), both at resonance and off-resonance;

- The initial f_c, T settings are validated *ex-post*, in resonant conditions (Step 3 above), in Section 6.5;

- The relative merits of the HRA and HDA approaches are discussed in Section 6.6;

- The main outcomes of this chapter are summarised and discussed in Section 6.7.

6.2 Case studies

Different WEC models are considered, presenting a reasonable variety of challenges. For each case, the connection with the mathematical formalism outlined in Chapter 4 is explicitly formulated, and the main characteristics of each model are highlighted in relation to the HB method, in particular:

- **Number and nature of degrees of freedom:** how many DoFs are there, and do they correspond to moving parts in contact with the waves, or do they model the dynamics of the mooring or PTO system?

- **Typical dynamics:** a small device, with relatively fast dynamics, is likely to be deployed in a location with relatively small, high-frequency waves ($T_p < 10$s), while larger devices are likely to be deployed in more energetic locations, with wave energy concentrated in the lower part of the spectrum. Furthermore, faster dynamics are likely to require the inclusion of more frequencies into the HB solution;

- **Nature of the non-linear effects** considered in the WEC model.

For each WEC considered, a linearised version of the model is also determined. The linearised model, in addition to providing a possible starting point for the HB algorithm, is used to give an approximate idea of the typical speed of the WEC dynamics, as shown in Section 6.2.6.

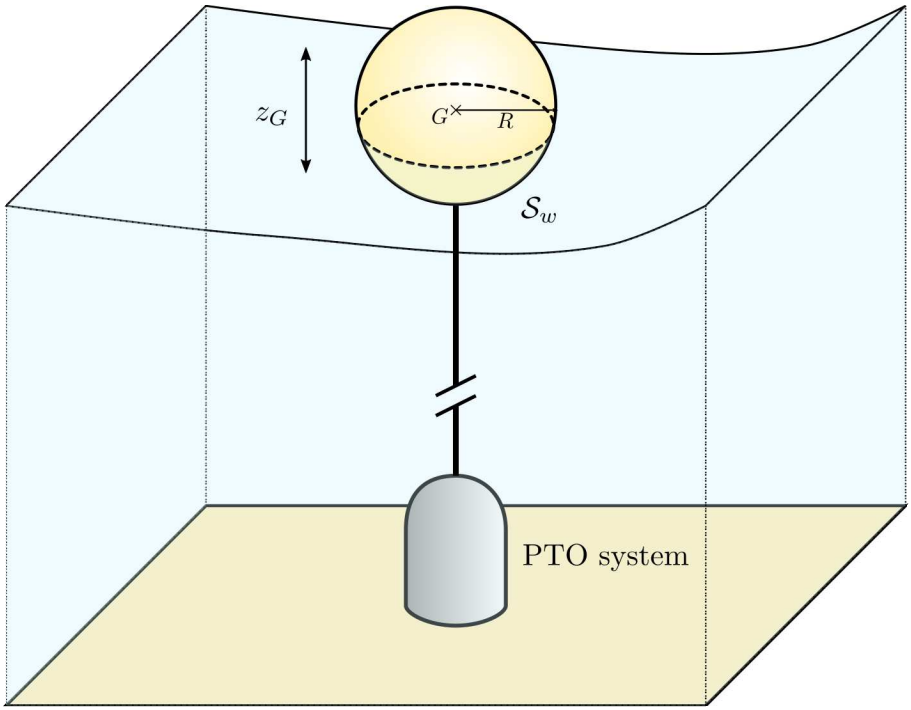

Figure 6.1: Schematic view of a spherical heaving point-absorber

6.2.1 Flap-type oscillating wave surge converter

The first WEC model considered is the flap-type WEC already described in Section 5.5 as an introductory example. It has only one DoF, and the non-linear dynamical effect included in the model consists of a quadratic viscous drag term. The flap natural dynamics are relatively slow, with a resonant period in the order of 25s. Similarly to the other WEC models considered, the PTO control torque is modelled parametrically in the form $\tau_{pto} = -k_{pto}\theta - b_{pto}\dot{\theta}$. The linearised version of the flap model is simply obtained by suppressing the quadratic drag term.

6.2.2 Spherical heaving point-absorber

Non-linear model

The second case study consists of a spherical heaving point-absorber. The buoy, a sphere with a radius of 2.5m, is assumed to be rigidly connected to the sea bottom through the PTO system, as illustrated in Fig. 6.1. Thus, the only degree of freedom considered is the heaving motion of the floating buoy. The buoy density is chosen to be half that of sea water so that, at rest, the position of the gravity centre is $z_G = 0$. Without loss of generality, the buoy gravity centre is assumed to be located at $(x,y) = (0,0)$.

The hydrodynamic model used for the sphere considers a non-linear calculation of static and dynamic Froude-Krylov forces, in the spirit of [108], as discussed in Section 4.3.4.1. Indeed, the device has a non-constant cross-sectional area; as a consequence, if it undergoes large motions, for example under the effect of reactive control, geometric non-linear effects may become significant. Additionally, a viscous damping coefficient is employed, in order to represent possible viscous dissipative effects. The radiation force and diffraction force remain modelled linearly. The radiation frequency-domain coefficients $A_R(\omega)$ and $B_R(\omega)$ are computed using the hydrodynamic software NEMOH[1], as well as their time-domain counterparts $K_R(\tau)$ (the radiation impulse-response kernel) and m_∞ (the radiation added mass), and the diffraction and excitation force transfer functions

[1] https://lheea.ec-nantes.fr/logiciels-et-brevets/nemoh-toolbox-192933.kjsp

$H_{\eta d}(\omega)$ and $H_{\eta e}(\omega)$. The non-linear terms (viscous drag and non-linear Froude-Krylov forces) are detailed in the following.

The heaving sphere device is subject to a quadratic viscous drag force, which depends on the relative velocity of the device with respect to the free surface, as follows:

$$f_{dis}(z,\eta) = -C_{dis,q}(\dot{z}_G - \dot{\eta})|\dot{z}_G - \dot{\eta}| \tag{6.1}$$

Based on [155], $C_{dis,q}$ can be roughly calibrated as:

$$C_{dis,q} = \frac{1}{2}\rho\pi R^2 \tag{6.2}$$

where ρ denotes the density of sea water.

The non-linear computation of Froude-Krylov forces is carried out by taking into account the instantaneous position of the device with respect to the free surface. Since the device is relatively small with respect to typical wave lengths:

- The free surface is approximated by a plane $z = \eta(t)$, where $\eta(t)$ is the undisturbed free-surface elevation at $(x,y) = (0,0)$, as represented in Fig. 6.2.
- Over the sphere wetted surface, the dependence of the pressure field on the horizontal coordinates (x,y) is neglected.

Furthermore, the dynamic pressure field is modified following the Wheeler stretching [109] change of variable, so that the total static and incident pressure, measured at the free surface, is exactly zero. The integration of the pressure over the instantaneous wetted surface is carried out analytically, similarly to the approach presented in [115], and in contrast to the method in [108] which is based on a numerical discretisation of the wetted surface. With the above assumptions, the approach of [108] can be efficiently incorporated into the HB framework. The static pressure force can be expressed as

$$p_s(z) = -\rho g z \tag{6.3}$$

For a monochromatic wave in infinite water depth, the dynamic incident pressure (see Section 4.3) is written as follows:

$$p_{dyn}(z,t,\omega) = \Re\{\rho g\hat{\eta}(\omega)e^{-j\omega t + k(\omega)z}\} \tag{6.4}$$

where $k(\omega) = \frac{\omega^2}{g}$ is the wave number, and $\hat{\eta}(\omega)$ denotes the complex wave amplitude. With the Wheeler stretching approach in infinite water depth, the dynamic pressure is modified, by replacing z with $\zeta = z - \eta$, the horizontal coordinate relative to the free surface:

$$p_{dyn}(\zeta,t,\omega) = \Re\{\rho g\hat{\eta}(\omega)\, e^{-j\omega t + k(\omega)\zeta}\}. \tag{6.5}$$

The total incident dynamic pressure, due to the superposition of waves of different frequencies and complex amplitudes, is then:

$$p_{dyn}(\zeta,t) = \rho g \int_{\omega=0}^{\infty} \Re\{\hat{\eta}(\omega)\, e^{-j\omega t}\} e^{k(\omega)\zeta} d\omega \tag{6.6}$$

It can be easily verified that, taken at the free surface ($\zeta = 0$), the static pressure (6.3) equals $p_s = -\rho g\eta$, and the dynamic pressure (6.6) reduces to $p_{dyn} = \rho g\eta$, so that the sum of the incident and static pressures is zero at the free surface, as per the Wheeler stretching approach. The total

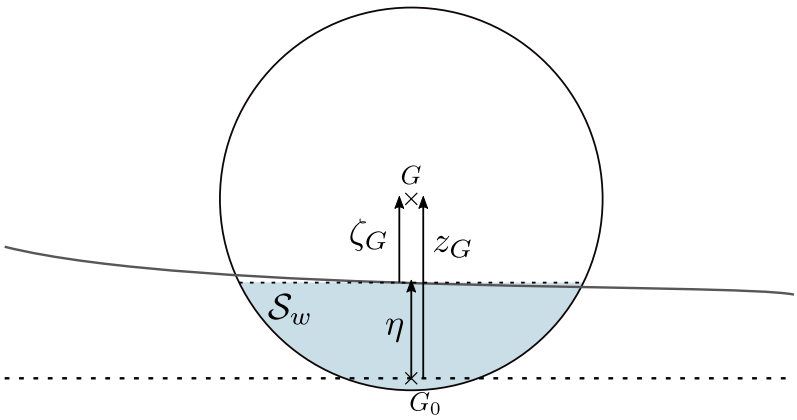

Figure 6.2: Schematic view of a spherical heaving point-absorber

vertical force due to the static pressure over the immersed surface $\mathcal{S}_w$ of the body can be calculated as follows:

$$\begin{aligned} f_s(t) &= \big[- \int\limits_{\mathrm{P}\in\mathcal{S}_w} -\rho g z_P \mathbf{n}_P \, dS \big].\mathbf{u}_z \\ &= \big[\int\limits_{\mathrm{P}\in\mathcal{S}_w} \rho g \zeta_P \mathbf{n}_P \, dS + \int\limits_{\mathrm{P}\in\mathcal{S}_w} \rho g \eta(t) \mathbf{n}_P \, dS \big].\mathbf{u}_z \\ &= \rho g \mathcal{V}_{im}(t) - \rho g \eta(t) \mathcal{S}_{int}(t) \end{aligned} \tag{6.7}$$

where $\mathcal{V}_{im}$ denotes the immersed volume of the body, and $\mathcal{S}_{int}$ denotes the area of the intersection between the body and the free surface (considered to be horizontal).

For a sphere in heave, with radius R and density $\rho/2$, denoting ζ_G as the position of the sphere gravity center relatively to the free surface, (6.7) can be analytically derived as follows:

$$f_s(\zeta_G, t) = \rho g \pi \big[\frac{2}{3} R^3 - R^2 \zeta_G + \frac{1}{3} \zeta_G^3 - \eta(t)(R^2 - \zeta_G^2) \big] \tag{6.8}$$

The total vertical incident pressure force over the body can be written as follows:

$$\begin{aligned} f_{dyn} &= \big[- \int\limits_{\mathrm{P}\in\mathcal{S}_w} p_{dyn}(z_P) \, \mathbf{n}_P \, dS \big].\mathbf{u}_z \\ &= \big[- \int\limits_{\mathrm{P}\in\mathcal{S}_w} \rho g \int\limits_{\omega=0}^{\infty} \Re\{\hat{\eta}(\omega) \mathrm{e}^{j\omega t}\} \mathrm{e}^{k(\omega)\zeta_P} d\omega \, \mathbf{n}_P \, dS \big].\mathbf{u}_z \\ &= \big[- \rho g \int\limits_{\omega=0}^{\infty} \Re\{\hat{\eta}(\omega) \mathrm{e}^{j\omega t}\} \big(\int\limits_{\mathrm{P}\in\mathcal{S}_w} \mathrm{e}^{k(\omega)\zeta_P} \, \mathbf{n}_P \, dS \big) d\omega \big].\mathbf{u}_z \end{aligned} \tag{6.9}$$

For a sphere, the integral of $\mathrm{e}^{k(\omega)\zeta_P}$ over the immersed surface $\mathcal{S}_w$ can be analytically derived, yielding:

$$\begin{aligned} \int\limits_{\mathrm{P}\in\mathcal{S}_w} \mathrm{e}^{k(\omega)\zeta} \mathbf{n}_P \, dS = 2\pi \big[&- \frac{\zeta_G}{k(\omega)} - \frac{1}{k(\omega)^2} \\ &+ \big(\frac{R}{k(\omega)} + \frac{1}{k(\omega)^2} \big) \mathrm{e}^{-k(\omega)R} \mathrm{e}^{k(\omega)\zeta_G} \big] \mathbf{u}_z \end{aligned} \tag{6.10}$$

Define the following integral:

$$J(\zeta_G,t) = 2\pi\rho g \int_0^\infty \Re\{\hat{\eta}(\omega)\mathrm{e}^{-j\omega t}\} \times (\frac{R}{k(\omega)} + \frac{1}{k(\omega)^2})\mathrm{e}^{-k(\omega)R}\mathrm{e}^{k(\omega)\zeta_G} d\omega \tag{6.11}$$

and, for any integer $n \in \mathbb{Z}$:

$$I_n(t) = 2\pi\rho g \int_0^\infty \Re\{\hat{\eta}(\omega)\mathrm{e}^{-j\omega t}\} k(\omega)^n d\omega \tag{6.12}$$

Using expressions (6.11) and (6.12), Eq. (6.9) can be expressed as

$$f_{dyn}(\zeta_G,t) = I_{-1}(t)\zeta_G + I_{-2}(t) - J(\zeta_G,t) \tag{6.13}$$

Because of the term J, using the expression (6.13) directly as a non-linear modelling term would lead to a relatively inefficient integration over ω to evaluate the non-linear term at each time step (or HB root-finding iteration), which would slow down any simulation technique (either the HB method, or time-domain integration). Thus, it is more interesting to carry out a development of $J(\zeta_G,t)$, using a polynomial expansion of the exponential term, e^{ζ_G}. Define the following integral:

$$J_n(t) = \frac{2\pi\rho g}{n!} \int_0^\infty \Re\{\hat{\eta}(\omega)\mathrm{e}^{-j\omega t}\} (\frac{R}{k(\omega)} + \frac{1}{k(\omega)^2})\mathrm{e}^{-k(\omega)R} k(\omega)^n d\omega, \tag{6.14}$$

Eq. (6.13) can now be formulated as

$$f_{dyn}(\zeta_G,t) = I_{-1}(t)\zeta_G + I_{-2}(t) - \sum_{n=0}^{\infty} J_n(t)\zeta_G^n \tag{6.15}$$

so that the dynamic pressure force can be expanded to any arbitrary order n_{max} to reach a target degree of accuracy. Fig. 6.3 shows the first three terms of the sum in (6.15), taken in the limit case $\zeta_G = R$, for a periodic wave signal derived from a typical JONSWAP spectrum ($H_{m_0} = 2$, $T_p = 10$, $\gamma = 3.3$). As can be seen in Fig. 6.3, the magnitude of the functions $J_n(t)$ decreases rapidly with the order n, so that, in practice, there is no noticeable difference between the results obtained with $n_{max} = 2$ or $n_{max} = 3$. In this case study, $n_{max} = 3$ is chosen.

The PTO force, similarly to the flap-type WEC, consists of two terms, a linear damping term $-b_{pto}\dot{z}_G$, and a restoring term $-k_{pto}z_G$. The device natural resonance period is of the order of 3.3s, which is below typical sea wave periods. Therefore, k_{pto} will play the role of a negative stiffness term, with the goal of shifting the resonance of the device towards the incoming wave period. Note that choosing k_{pto} negative, with magnitude larger than the WEC's linear hydrostatic stiffness s_h, yields a system with an overall negative stiffness $k_{pto} + s_h$, which cannot be considered realistic since such a system would be unstable at the equilibrium point $z_G = 0$. In fact, as will be seen in Section 6.4.2, unstable motion can even be observed for a small but positive total stiffness $k_{pto} + s_h$.

Finally, the dynamical equation describing the WEC model can be written as:

$$\mathcal{L}\{z_G\} - n\{z_G,t\} - e(t) = 0 \tag{6.16}$$

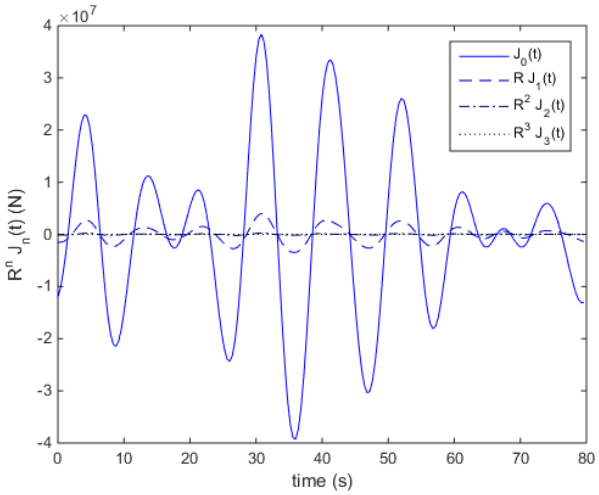

Figure 6.3: Terms $J_n(t)\zeta_G^n$ of expansion (6.15), taken at $\zeta_G = R$, for a typical JONSWAP spectrum ($H_{m_0} = 2m$, $T_p = 10s$) (reproduced from [57])

where

$$\begin{cases} \mathcal{L}\{z_G\} = (m+m_\infty)\ddot{z}_G + b_{pto}\dot{z}_G + k_{pto}z_G + \int_{\tau=0}^{\infty} K_R(\tau)\dot{z}_G(t-\tau)d\tau \\ n\{z_G,t\} = -C_{dis,q}(\dot{z}_G - \dot{\eta})|\dot{z}_G - \dot{\eta}| + I_{-1}(t)(z_G - \eta(t)) + I_{-2}(t) - \sum_{n=0}^{3} J_n(t)(z_G - \eta(t))^n \\ e(t) = f_d(t) \end{cases} \tag{6.17}$$

where $f_d(t)$ represents the diffraction forces, linearly derived from the incoming wave elevation η. In Eq. (6.16), all the forcing inputs present in the non-linear terms $n\{z_G,t\}$ are derived from the wave elevation η, which constitutes, as discussed in Section 4.6, the only independent incident wave signal. Therefore, to simulate a specific wave realisation using either HB or TD methods, the complex coefficients $\hat{\eta}$ of η are first randomly generated for a discrete set of harmonic frequencies (using HRA or HDA, as discussed in Chapter 3), and the complex coefficients of $\dot{\eta}$, I_{-1}, I_{-2} and $J_{i=0\cdots3}$ are calculated according to their definition: for example, from Eq. (6.14), the complex amplitude $\hat{J}_n(\omega_i)$ is calculated as:

$$\hat{J}_n(\omega_i) = \left[\frac{2\pi\rho g}{n!}\left(\frac{R}{k(\omega_i)} + \frac{1}{k(\omega_i)^2}\right)e^{-k(\omega_i)R}k(\omega_i)^n\right]\hat{\eta}(\omega_i) \tag{6.18}$$

Then, to run a simulation, all forcing signals η, $\dot{\eta}$, etc. can be generated through Fourier transforms. In the HB method, those signals are generated at the collocation points where the non-linear terms are evaluated (given that the PS version of the HB method is used, as seen in Section 5.3). For RK2 integration, the forcing terms are generated for each time step of the integration scheme.

Linearised model

The linearised model of the sphere is obtained by suppressing the quadratic drag term, and by replacing the non-linear calculation of Froude-Krylov forces with its linear counterpart. More specifically:

- The sum of the diffraction force and the dynamic pressure force of Eq. (6.15) are together replaced with the excitation force $f_e(t)$, linearly derived from η using the wave elevation-to-excitation force transfer function;

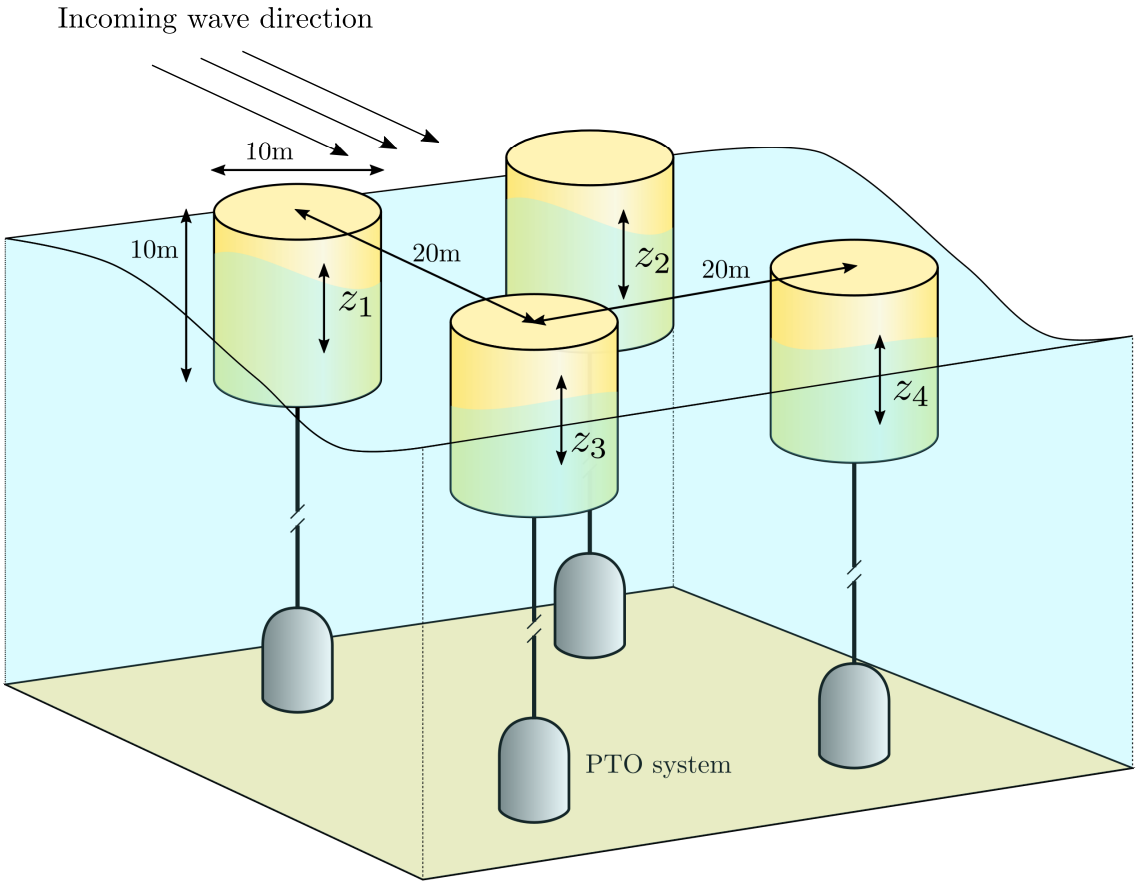

Figure 6.4: Schematic view of an array of four cylindrical heaving point-absorbers

- The non-linear static pressure force of Eq. (6.8) is replaced with the linear hydrostatic restoring term $f_s = -s_h z_G$, where $s_h = \rho g \pi R^2$.

6.2.3 An array of four cylindrical heaving point-absorbers

Non-linear model

The modelling of wave energy converter arrays can be a challenging task, as studied in detail in Part II of [3]. In particular, diffracted waves from each device modify the wave excitation force experienced by every other device, while waves radiated by the motion of each device exert forces onto every other device.

In this specific case study, an array of four identical, cylindrical heaving point absorbers is investigated. Each device is assumed to be rigidly connected to the sea bottom through its PTO system. The devices are arranged in a 20-by-20m square, as pictured schematically in Fig. 6.4. The overall system considered thus has four degrees of freedom and is described by the vector

$$\mathbf{z} = \begin{pmatrix} z_1 \\ z_2 \\ z_3 \\ z_4 \end{pmatrix} \tag{6.19}$$

where z_i corresponds to the vertical displacement of the gravity centre of the i^{th} device with respect to its equilibrium position (assumed to be at the still water level).

Because of the constant cross-sectional area of the four hulls in the heaving mode of motion, it can be reasonably expected that geometric non-linearities are negligible. Therefore, the excitation

and hydrostatic restoring forces are calculated within the framework of linear hydrodynamic wave theory. The incoming waves are assumed to be unidirectional, propagating in the direction of the axis formed by bodies 1 and 3 (or equivalently bodies 2 and 4), as shown in Fig. 6.4. The excitation forces are:

$$\mathbf{e}(t) = \begin{pmatrix} e_1(t) \\ e_2(t) \\ e_3(t) \\ e_4(t) \end{pmatrix} \tag{6.20}$$

where e_i is the excitation force acting onto the i^{th} device, and includes the diffraction effects induced by the presence of surrounding devices. The frequency-domain coefficients of $\mathbf{e}$ are obtained as $\hat{\mathbf{e}}(\omega) = \mathbf{H}_{\eta e}(\omega)\hat{\eta}(\omega)$, where $\mathbf{H}_{\eta e}(\omega)$ is the 4-by-1 free surface-to-excitation force transfer function, and $\hat{\eta}(\omega)$ denotes the frequency components of the free surface, considered at the origin of the vertical plane. The hydrostatic restoring term is linearly expressed as:

$$\mathbf{f}_s = -\mathbf{S}_h \mathbf{z} \tag{6.21}$$

where $\mathbf{S}_h = s_h \mathbb{I}_4$ and $s_h = \rho\pi R^2$.

The devices interact with each other dynamically through the radiation forces, which are also calculated linearly. The radiation forces involve 16 interaction terms, corresponding to the effect of the motion of the i^{th} body onto the j^{th} for all pairs $(i, j) \in \{1 \cdots 4\} \times \{1 \cdots 4\}$, and which are expressed as follows:

$$\mathbf{f}_R = -\mathbf{M}_\infty \ddot{\mathbf{z}} - \int_{\tau=0}^{\infty} \mathbf{K}_R(\tau)\dot{\mathbf{z}}(t-\tau)d\tau \tag{6.22}$$

where $\mathbf{M}_\infty$ is the 4-by-4 radiation added mass matrix and $\mathbf{K}_R(\tau)$ is the 4-by-4 radiation impulse response kernel.

Similarly to the other case studies, the PTO force is expressed as

$$\mathbf{f}_{pto} = -\mathbf{B}_{pto}\dot{\mathbf{z}} - \mathbf{K}_{pto}\mathbf{z} \tag{6.23}$$

where $\mathbf{B}_{pto} = b_{pto}\mathbb{I}_4$ and $\mathbf{K}_{pto} = k_{pto}\mathbb{I}_4$, which implies that the coefficients b_{pto} and k_{pto} are chosen identically for the four devices.

A Morrison quadratic drag term is added to the model, to account for possible viscous and vortex shedding effects. For each device, the viscous force takes the following form:

$$f_{dis,i} = -C_{dis,q}(\dot{z}_i - \dot{\eta}_i)|\dot{z}_i - \dot{\eta}_i| \tag{6.24}$$

where η_i denotes the incident free surface elevation at the centre of the i^{th} device. Based on [155], $C_{dis,q}$ can be roughly calibrated as:

$$C_{dis,q} = \frac{1}{2}\rho\pi R^2 \tag{6.25}$$

where $R = 5m$ is the radius of each device.

The dynamical equation finally reads:

$$\mathcal{L}\{\mathbf{z}\} - \mathbf{n}\{\mathbf{z}, t\} - \mathbf{e}(t) = \mathbf{0}_{\mathbb{R}^4} \tag{6.26}$$

with

$$\begin{cases} \mathcal{L}\{\mathbf{z}\} = (\mathbf{M} + \mathbf{M}_\infty)\ddot{\mathbf{z}} + \mathbf{B}_{pto}\dot{\mathbf{z}} + (\mathbf{K}_{pto} + \mathbf{S}_h)\mathbf{z} + \int_{\tau=0}^{\infty} \mathbf{K}_R(\tau)\dot{\mathbf{z}}(t-\tau)d\tau \\ \mathbf{n}\{\mathbf{z}, t\} = -C_{dis,q}(\dot{\mathbf{z}} - \dot{\eta})|\dot{\mathbf{z}} - \dot{\eta}| \end{cases} \tag{6.27}$$

where $\eta = \begin{pmatrix} \eta_1 ... \eta_4 \end{pmatrix}^T$ is the vector of the wave elevation at the centre of each device, and $\mathbf{M} = m_b \mathbb{I}_4$ where m_b is the mass of each body. The hydrodynamic parameters for the excitation force vector, $\mathbf{H}_{\eta e}(\omega)$, time-domain radiation force vectors, $\mathbf{K}_R$ and $\mathbf{M}_\infty$, as well as their frequency-domain counterparts $\mathbf{B}_R(\omega)$ and $\mathbf{A}_R(\omega)$, have been calculated using the WAMIT[2] hydrodynamic software.

[2] http://www.wamit.com/

State-space approximation of the radiation memory terms

In time-domain simulations, the computation of the radiation convolution integral can represent the main computational burden [3, 96]. This is particularly the case with multiple hydrodynamic degrees of freedom: in this 4-device array, the convolution product in fact represents 16 integrals. As discussed in Section 4.3.3.6, the radiation convolution terms can be approximated using a state-space representation. In order to ensure a fairer comparison between HB and TD methods in general, the possibility is investigated of approximating the convolution terms by means of a state-space representation. To that end, each of the 16 interaction terms (of body i onto body j) is approximated in the following state-space form, of dimension D_R:

$$\begin{cases} \dot{\mathbf{x}}_{R_{ij}}^{ss} = \mathbf{A}_{R_{ij}}^{ss}\mathbf{x}_{R_{ij}} + \mathbf{B}_{R_{ij}}^{ss}\dot{z}_i \\ f_{R_{ij}} = \mathbf{C}_{R_{ij}}^{ss}\mathbf{x}_{R_{ij}}^{ss} \end{cases} \tag{6.28}$$

where $\mathbf{A}_{R_{ij}}^{ss} \in \mathbb{R}^{D_R \times D_R}$, $\mathbf{B}_{R_{ij}}^{ss} \in \mathbb{R}^{D_R \times 1}$, $\mathbf{C}_{R_{ij}}^{ss} \in \mathbb{R}^{1 \times D_R}$, and $\mathbf{x}_{R_{ij}}^{ss}$ is a non-physical state vector representing the 'internal dynamics' of the radiation memory terms.

Note

$$\begin{cases} \mathbf{A}_R^{ss} := \begin{pmatrix} \mathbf{A}_{R_1}^{ss} & \mathbf{0} & \mathbf{0} \\ \mathbf{0} & \ddots & \mathbf{0} \\ \mathbf{0} & \mathbf{0} & \mathbf{A}_{R_4}^{ss} \end{pmatrix} \in \mathbb{R}^{(16D_R)\times(16D_R)} \\ \mathbf{B}_R^{ss} := \begin{pmatrix} \mathbf{B}_{R_1}^{ss} \\ \vdots \\ \mathbf{B}_{R_4}^{ss} \end{pmatrix} \in \mathbb{R}^{(16D_R)\times 4} \\ \mathbf{C}_R^{ss} := \begin{pmatrix} \mathbf{C}_{R_1}^{ss} & \mathbf{0} & \mathbf{0} \\ \mathbf{0} & \ddots & \mathbf{0} \\ \mathbf{0} & \mathbf{0} & \mathbf{C}_{R_4}^{ss} \end{pmatrix} \in \mathbb{R}^{4\times(16D_R)} \end{cases} \tag{6.29}$$

where

$$\begin{cases} \mathbf{A}_{R_j}^{ss} := \begin{pmatrix} \mathbf{A}_{R_{1j}}^{ss} & \mathbf{0} & \mathbf{0} \\ \mathbf{0} & \ddots & \mathbf{0} \\ \mathbf{0} & \mathbf{0} & \mathbf{A}_{R_{4j}}^{ss} \end{pmatrix} \in \mathbb{R}^{(4D_R)\times(4D_R)} \\ \mathbf{B}_{R_j}^{ss} := \begin{pmatrix} \mathbf{B}_{R_{1j}}^{ss} & \mathbf{0} & \mathbf{0} \\ \mathbf{0} & \ddots & \mathbf{0} \\ \mathbf{0} & \mathbf{0} & \mathbf{B}_{R_{4j}}^{ss} \end{pmatrix} \in \mathbb{R}^{(4D_R)\times 4} \\ \mathbf{C}_{R_j}^{ss} := \begin{pmatrix} \mathbf{C}_{R_{1j}}^{ss} & \cdots & \mathbf{C}_{R_{4j}}^{ss} \end{pmatrix} \in \mathbb{R}^{1\times(4D_R)} \end{cases} \tag{6.30}$$

and $\mathbf{0}$ denotes matrices with zero elements of appropriate dimensions. The dynamical equation of Eq. (6.26), augmented with the radiation state variables, is now written as follows:

$$\begin{cases} (\mathbf{M}+\mathbf{M}_\infty)\ddot{\mathbf{z}} + \mathbf{B}_{pto}\dot{\mathbf{z}} + (\mathbf{K}_{pto}+\mathbf{S}_h)\mathbf{z} + \mathbf{C}_R^{ss}\mathbf{x}_R^{ss} - \mathbf{n}\{\mathbf{z},t\} = \mathbf{e}(t) \\ \dot{\mathbf{x}}_R^{ss} = \mathbf{A}_R^{ss}\mathbf{x}_R^{ss} + \mathbf{B}_R^{ss}\dot{\mathbf{z}} \end{cases} \tag{6.31}$$

The state-space approximation $(\mathbf{A}_{R_{ij}}, \mathbf{B}_{R_{ij}}, \mathbf{C}_{R_{ij}})$ is determined, for each interaction ij, based on the recently-proposed moment-matching technique [156], using the FOAMM software toolbox[3] developed at COER. Note that, given the symmetry of the problem, there are in fact only 3 types of interactions: from a given body onto itself, from a given body onto its nearest neighbours, and from a given body onto that located at the opposite corner of the square formed by the four bodies (see Fig. 6.4). Therefore, the FOAMM application needs only to be run three times, which is sufficient

[3] http://www.eeng.nuim.ie/coer/downloads/

to provide each entry of the matrices $\mathbf{A}_R^{ss}$, $\mathbf{B}_R^{ss}$ and $\mathbf{C}_R^{ss}$. With the moment-based approach, the approximation is carried out by choosing key *interpolating frequencies*, at which it is ensured that the approximating system exactly matches the behaviour of the target system. The size D_R of the resulting state-space system is twice the number of interpolating frequencies. In this work, two approximations are employed: one obtained by using only one interpolating frequency ($D_R = 2$), and one by using two interpolating frequencies ($D_R = 4$).

Linearised model

The linearised model corresponding to Eq. (6.26) is obtained by simply suppressing **n**, i.e. the quadratic terms (the first-order derivative of the quadratic terms, at the origin, is zero)[4].

6.2.4 The ISWEC device

Non-linear model

Developed at Politecnico di Torino, the ISWEC (Inertial Sea Wave Energy Converter) is a device which produces energy from ocean waves, by exploiting the gyroscopic effect, generated by the combination of the hull pitching motion with the rotation of a flywheel, in a gyroscope system enclosed within the hull. The ISWEC working principle is described in more detail in [126]. Fig. 6.5 illustrates the main system components of the ISWEC device: the hull, the gyroscope (rotating in its frame), and the PTO system which exploits the back-and-forth rotation ε of the gyroscope frame about the PTO axis.

The hull is entirely sealed, thus isolating all the internal mechanical components from the sea. Sea waves induce a pitch motion r_y onto the hull. The flywheel rotates about its axis with a regulated angular speed $\dot{\varphi}_{pto}$ which, combined with the hull pitching motion, generates a gyroscopic torque acting onto the gyroscope frame, about the PTO axis OX. As a result, the entire gyroscope frame rotates back and forth about the PTO axis (*precession* motion), with an angle ε.

Although the ISWEC primarily captures energy from the pitch hydrodynamic degree of freedom, in practice the hull also moves in the other hydrodynamic DoFs, in particular heave and surge. However, for the sake of simplicity, the ISWEC heave and surge motion is omitted in the remainder of this thesis, which effectively neglects the mooring dynamics. Therefore, the system has two DoFs only: one for the hull (pitch, denoted r_y), and one for the gyroscopic system (precession about the PTO axis, denoted ε).

The hydrodynamic interaction of the pitching hull with the incoming waves is described through Cummins' equation, with the addition of a quadratic viscous damping term:

$$(I+I_\infty)\ddot{r}_y + \int_{\tau=0}^{\infty} K_R(\tau)\dot{r}_y(t-\tau)d\tau + s_h r_y + C_{dis,q}|\dot{r}_y|\dot{r}_y - J_g\dot{\varphi}_{pto}\dot{\varepsilon}\cos\varepsilon = \tau_w \tag{6.32}$$

where I is the system inertia about the pitching axis, the radiation forces in the pitching mode are represented through the added inertia I_∞ and impulse response kernel K_R, s_h is the hydrostatic stiffness in pitch, $C_{dis,q}$ is a quadratic viscous drag coefficient, and τ_y represents the incoming wave torque, calculated from the free surface using a transfer function $H_{\eta e}(\omega)$. All hydrodynamic coefficients, in the frequency domain ($H_{\eta e}(\omega)$, $A_R(\omega)$, $B_R(\omega)$) and in the time domain (I_∞, K_R) have been computed using the WAMIT hydrodynamic software[5]. $C_{dis,q}$ has been primarily calibrated using 1:20 scale prototype wave tank tests, and subsequently scaled via Froude relationships - see

[4]Note that, in the spirit of statistical linearisation, as presented in Chapter 4 of [3], an alternative approach consists of determining a linear approximation to the quadratic viscous drag. Such an approximation, however, requires an iterative procedure, which must be carried out for each specific wave input considered, and for every change in the other system parameters. In other words, a linear approximation for the quadratic terms would be simulation-dependent. Such a possibility is not investigated here.

[5]http://www.wamit.com/

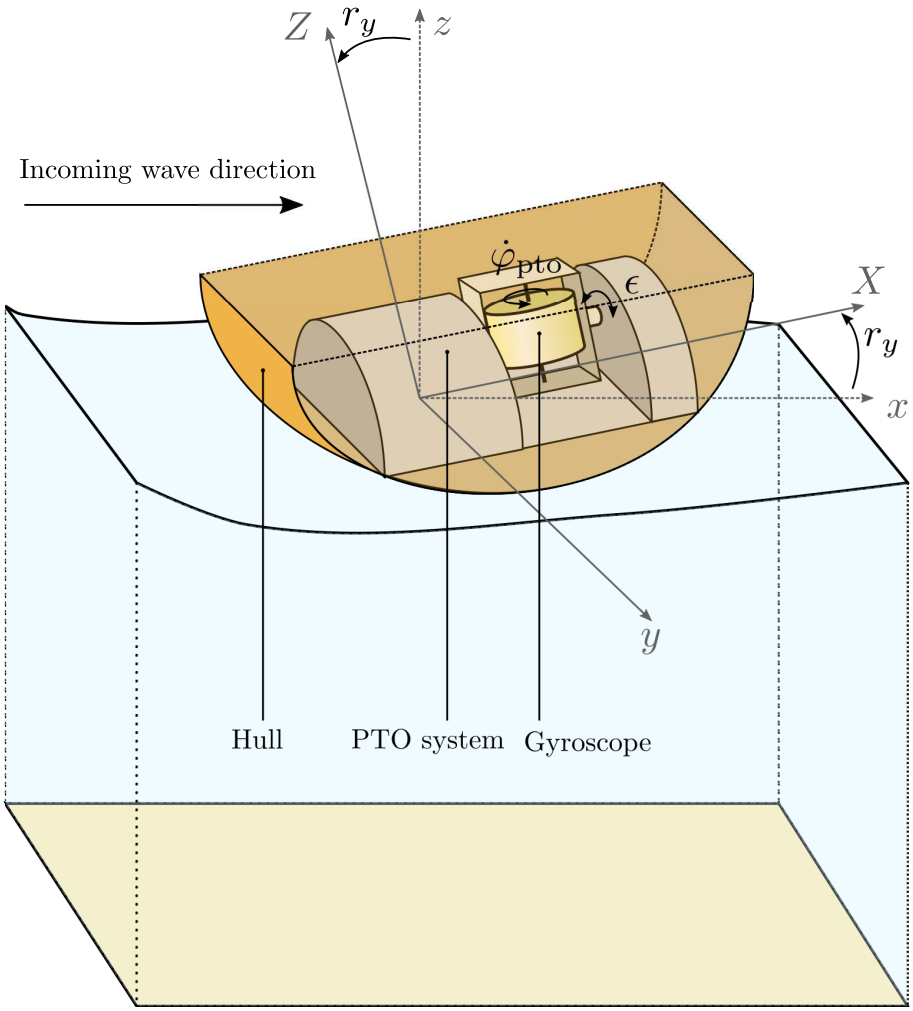

Figure 6.5: Schematic view of an ISWEC-like pitching device. The length, width and height of the hull are 15m, 8m and 5m, respectively.

Chapter 2 of [157]. Finally, the term $J_g\dot{\varphi}_{pto}\dot{\varepsilon}\cos\varepsilon$, where J_g is the flywheel moment of inertia about its rotation axis, represents a non-linear coupling under the effect of the gyroscope system.

The ISWEC PTO dynamics are determined by expressing the motion of the gyroscope system about the PTO axis:

$$I_g\ddot{\varepsilon} + J_g\dot{\varphi}_{pto}\dot{r}_y\cos\varepsilon = \tau_{pto} \tag{6.33}$$

where I_g is the inertia of the whole gyroscope system (flywheel and frame) about the precession axis, and τ_{pto} is the torque exerted by the PTO system onto the gyroscope system. Similarly to the other WECs studied in this chapter, a two-parameter PTO control force is introduced, in the form $\tau_{pto} = -b_{pto}\dot{\varepsilon} - k_{pto}\varepsilon$. Note that energy is transmitted between the pitching motion and the gyroscope system through the non-linear coupling term $J_g\dot{\varphi}_{pto}\dot{r}_y\cos\varepsilon$.

Finally, the dynamical equation for the ISWEC model takes the following form:

$$\mathcal{L}\{\mathbf{x}\} - \mathbf{n}\{\mathbf{x}\} - \mathbf{e}(t) = \mathbf{0}_{\mathbb{R}^2} \tag{6.34}$$

where

$$\begin{cases} \mathbf{x} = \begin{pmatrix} r_y \\ \varepsilon \end{pmatrix} \\ \mathcal{L}\{\mathbf{x}\} = (\mathbf{M}+\mathbf{M}_\infty)\ddot{\mathbf{x}} + \mathbf{C}\dot{\mathbf{x}} + \mathbf{S}\mathbf{x} + \int_{\tau=0}^{\infty} \mathbf{K}_R(\tau)\dot{\mathbf{x}}(t-\tau)d\tau \\ \mathbf{n}(\mathbf{x}) = \begin{pmatrix} -C_{dis,q}|\dot{r}_y|\dot{r}_y + J_g\dot{\varphi}_{pto}\dot{\varepsilon}\cos\varepsilon \\ -J_g\dot{\varphi}_{pto}\dot{r}_y\cos\varepsilon \end{pmatrix} \\ \mathbf{e}(t) = \begin{pmatrix} \tau_w(t) \\ 0 \end{pmatrix} \end{cases} \tag{6.35}$$

and

$$\begin{cases} \mathbf{M} = \begin{pmatrix} I+I_\infty & 0 \\ 0 & I_g \end{pmatrix} \\ \mathbf{C} = \begin{pmatrix} 0 & 0 \\ 0 & c_{pto} \end{pmatrix} \\ \mathbf{S} = \begin{pmatrix} s_h & 0 \\ 0 & k_{pto} \end{pmatrix} \\ \mathbf{K}_R(\tau) = \begin{pmatrix} K_R(\tau) & 0 \\ 0 & 0 \end{pmatrix} \end{cases} \tag{6.36}$$

Linearised model

The linearised model is obtained by suppressing the quadratic viscous term, and by linearising the non-linear coupling term about the origin, thus yielding:

$$\mathbf{M}\ddot{\mathbf{x}} + \mathbf{C}'\dot{\mathbf{x}} + \mathbf{S}\mathbf{x} + \int_{\tau=0}^{\infty} \mathbf{K}_R(\tau)\dot{\mathbf{x}}(t-\tau)d\tau = \mathbf{e} \tag{6.37}$$

where

$$\mathbf{C}' = \begin{pmatrix} 0 & -J_g\dot{\varphi}_{pto} \\ J_g\dot{\varphi}_{pto} & c_{pto} \end{pmatrix} \tag{6.38}$$

and all other matrices are defined as in the non-linear model of Eq. (6.34).

6.2.5 Power calculations

Before proceeding further, the method employed to calculate the WEC power must be specified. In the four examples described in Sections 6.2.1 to 6.2.4, the internal dynamics of the PTO system are not fully described; therefore, only the power *absorbed* by the PTO system is used to measure the WEC performance (as opposed to the power *delivered* to the grid). Assume that power is transmitted to the PTO system through one of the modes of motion of the WEC, noted d_{pto}. The average absorbed power can be calculated over one period of the simulated signal as follows:

$$P = -\frac{1}{T}\int_{t=0}^{T} f_{pto}(t)\dot{x}_{d_{pto}}(t)dt \tag{6.39}$$

$x_{d_{pto}}$ is obtained from the vector $\mathbf{x}(t)$, comprising the totality of the system DoFs, through an output matrix $\mathbf{C}_{pto}$ of size $D \times 1$, consisting of zeros except for a unity coefficient at index d_{pto}. The vector of the Fourier expansion of x_{pto} is obtained from $\hat{\mathbf{x}}$ as $\hat{\mathbf{x}}_{pto} = \mathbf{M}_{pto}\hat{\mathbf{x}}$, where $\mathbf{M}_{pto} \in \mathbb{R}^{(2N+1)\times(2N+1)D}$ is defined as follows:

$$\mathbf{M}_{pto} = \begin{pmatrix} \mathbf{C}_{pto} & \mathbf{0} & \cdots & \mathbf{0} \\ \mathbf{0} & \mathbf{C}_{pto} & \mathbf{0} & \mathbf{0} \\ \mathbf{0} & \cdots & \ddots & \mathbf{0} \\ \mathbf{0} & \cdots & \mathbf{0} & \mathbf{C}_{pto} \end{pmatrix} \tag{6.40}$$

Accordingly, the PTO force is represented in the frequency domain as

$$\hat{f}_{pto} = -b_{pto}\mathbf{M}_{pto}\Omega\hat{\mathbf{x}} - k_{pto}\mathbf{M}_{pto}\hat{\mathbf{x}} \tag{6.41}$$

Finally, from Eqs. (6.39) and (6.41), it is easy to show that P can be obtained from the HB solution $\hat{\mathbf{x}}$ as follows:

$$P = b_{pto}\hat{\mathbf{x}}^T\mathbf{Q}_{pto}\hat{\mathbf{x}} \tag{6.42}$$

where

$$\mathbf{Q}_{pto} = \Omega^T\mathbf{M}_{pto}^T\mathbf{M}_{pto}\Omega \tag{6.43}$$

Note that k_{pto} does not appear in the power calculation: this is because the mechanical work of the static term, $-k_{pto}x_{pto}$, cancels out over each period of a periodic signal.

6.2.6 Design sea states

Table 6.1 summarises the main characteristics of the WEC models under study. For each case, a design sea state is identified, which will be subsequently used throughout the validation study in the remainder of this chapter. The natural period of each system is identified by considering the corresponding linearised model, based on which the wave elevation-to-position transfer function is calculated, and the resonant period is identified.

The two systems having the larger natural periods (the flap-type WEC and the cylindrical HPAs) are studied in a JONSWAP [52] sea state with parameters $(H_{m_0} = 2\text{m}, T_p = 12\text{s}, \gamma = 3.3)$. In such a sea state, the cylindrical HPAs, which have a resonant period smaller than that of the typical incident waves, will be reactively controlled with a negative stiffness coefficient k_{pto}, while the flap-type device will be reactively controlled with a positive stiffness coefficient.

The two devices having the smaller natural periods (the spherical HPA and the ISWEC device) are studied in a less energetic JONSWAP sea state with $(H_{m_0} = 1\text{m}, T_p = 7\text{s}, \gamma = 2)$. Such a sea state is typical at the ISWEC design location, off the coast of Pantelleria island [13], or at a small-scale wave energy test site such as the one in Galway Bay studied in [57], which would be suitable for a small device like the spherical HPA. The different value for γ, employed for the smaller devices, is chosen because wave spectra in less energetic locations, such as Pantelleria or Galway Bay, are usually less sharply concentrated around their peak frequency, as reported in [57]; it is therefore meaningful to include a wave spectrum with a broader frequency content in the analysis.

Table 6.1: Summary table of the main characteristics of the studied WEC models

	Flap	**Spherical HPA**	**Cyl. HPA array**	**ISWEC**
Natural period	25s	3.3s	5.9s	4.6s *(hull)*
Design sea state	$\begin{cases} T_p = 12s \\ H_{m_0} = 2m \\ \gamma = 3.3 \end{cases}$	$\begin{cases} T_p = 7s \\ H_{m_0} = 1m \\ \gamma = 2 \end{cases}$	$\begin{cases} T_p = 12s \\ H_{m_0} = 2m \\ \gamma = 3.3 \end{cases}$	$\begin{cases} T_p = 7s \\ H_{m_0} = 1m \\ \gamma = 2 \end{cases}$
Nb. of DoFs	1	1	4	2
Nb. of hyd. DoFs	*1*	*1*	*4*	*1*
Non-linear effects	Quad. visc. drag	Froude-Krylov forces; Quad. visc. drag	Quad. visc. drag	PTO dynamics; Quad. visc. drag

6.3 Calibration of the HB method

As outlined in Section 5.7 and in the introduction to this chapter, tuning the HB method essentially consists of choosing pertinent values for T and f_c, ensuring a satisfactory trade-off between computation time and accuracy. To that end, each WEC model is simulated using the HB method in its design sea state, under a reasonably large range of (f_c, T) parameters, and with 20 independent HDA sea state realisations. For all cases, the HB algorithm is initialised using the linearised WEC model, and a simple Newton algorithm is then chosen to reach the non-linear HB solution. For each (f_c, T) pair, the central processing unit (CPU) time is averaged over the 20 independent realisations. For all devices, b_{pto} is first manually tuned by quickly trying a range of values. k_{pto} is set to zero, except for the ISWEC device, for which $k_{pto} = 0$ results in ill-defined steady-state dynamics[6], thus making it preferable to set k_{pto} to an arbitrary small value.

At this preliminary stage, as with any simulation method (HB or other), the values chosen for k_{pto} and b_{pto} need not be finely tuned, and should only be of a sensible order of magnitude. When the WEC models are subsequently run over a wider range of conditions, it will become clearer what values for k_{pto} and b_{pto} are of specific interest.

6.3.1 Problem size and HB computation time

First, the link between computation time and problem size is examined empirically. In Fig. 6.6, for each pair of (f_c, T) settings, the problem size N_{HB} is calculated as $N_{HB} = T \times f_c \times D$, where D is the number of DoFs, and the corresponding calculation time t_{cpu} is shown as a dot in the scatter plot. The Newton method is used to solve the HB equation. All computation times are obtained from a Matlab implementation, run on a 3.50 GHz, 8-core Intel® processor, as will be the case for all other numerical results, presented in the remainder of this thesis.

As discussed in Section 5.7, because the HB algorithm involves inverting matrices of size N_{HB}, the computation time is expected to be, at best, proportional to N_{HB}^{α}, where $2 < \alpha < 3$. It is found empirically that, with the available Matlab software, for large problem sizes (beyond roughly $N_{HB} \approx 2000$), the CPU time indeed seems to be dominated by the matrix inversion at each Newton iteration, with a cost, in seconds, proportional to N_{HB}^{β}, where β is found to lie between 2.3 and 2.5. In Fig. 6.6, the dotted lines represent a fitted curve in $N_{HB}^{2.4}$. The trend identified remains relatively consistent across the four cases studied.

Note that, for each WEC considered, the number of iterations to reach the solution was found to present very little variability across the range of problem sizes explored: between 3 and 4 iterations were necessary for three of the devices: the flap-type device, the spherical HPA and the ISWEC device, while generally only 2 iterations were necessary for the array case study. As a

[6] In the model of Eq. (6.34), the only stiffness contribution for the second degree of freedom, i.e. ε, is k_{pto}. This means that the linearised ISWEC model is ill-defined, in the sense that the matrix $\mathbf{L}'$ in Eq. (5.71) is singular. In physical terms, there are an infinity of steady-state solution, each of which having an arbitrary average precession angle ε_0.

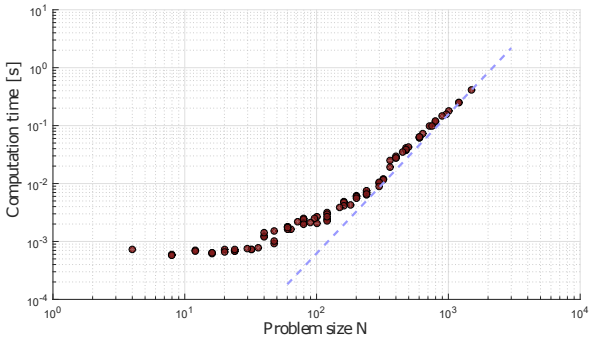

(a) Flap-type WEC

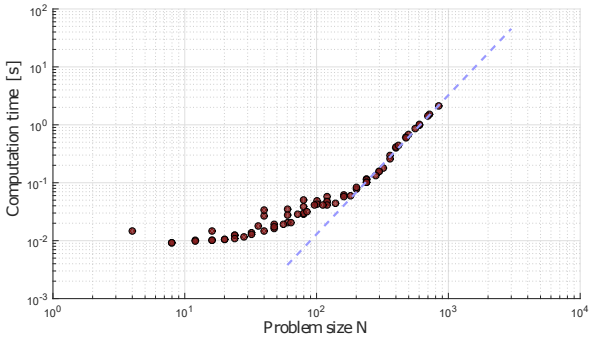

(b) Spherical HPA

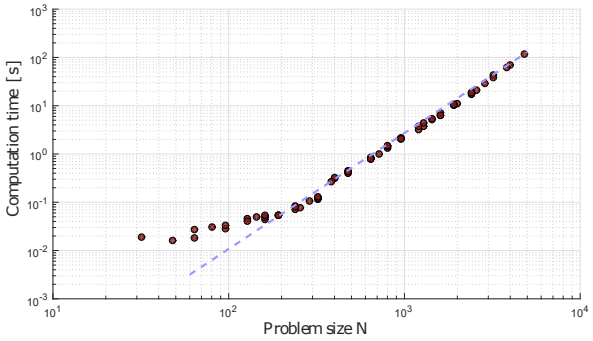

(c) Array of 4 cylindrical HPAs

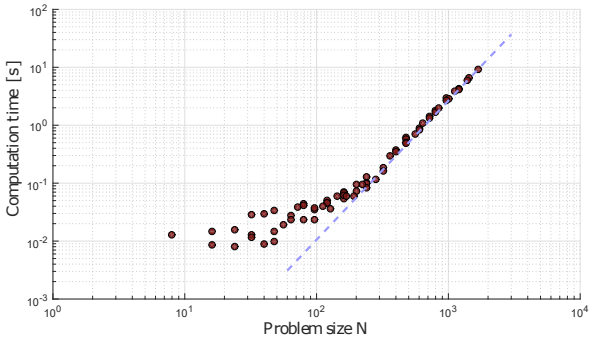

(d) ISWEC device

Figure 6.6: HB computation time *vs* problem size, for the four WEC models under study. The dotted lines represent a fitted curve in the form N_{HB}^{β}, where N_{HB} is the problem size and $\beta = 2.4$.

consequence, there is no doubt that the trends, observed in Fig. 6.6, in terms of CPU time, are accounted for by the problem size alone, *not* by the number of Newton iterations. The results of Fig. 6.6 thus empirically illustrate the fundamental fact that the HB solution cost is more than proportional to the problem size and, in fact, increases more than quadratically with the problem size. The next subsection explores how a trade-off can be found between T and f_c.

6.3.2 Tuning the cut-off frequency and simulation period

As discussed in Section 5.7, a pertinent indicator for computational performance consists of the calculation time per second of signal simulated. Therefore, the raw average computation time t_{cpu} is normalised by the simulated time $t_{sim} = T$. As far as accuracy is concerned, and based on the considerations developed in Section 5.5, it is pertinent to use the norm of the last Fourier coefficient of the HB solution as a qualitative measure of the HB solution error. However, the system variables considered for the various case studies do not have the same magnitude. Thus, for a comparable error measure, for each case the norm of the last harmonic (of order N_ω) is normalised by the norm of the solution (involving all the terms of the expansion up to N_ω):

$$error \approx \sqrt{\frac{\|\hat{\mathbf{x}}_{2N_\omega}\|^2 + \|\hat{\mathbf{x}}_{2N_\omega+1}\|^2}{\sum_{n=0}^{2N_\omega+1} \|\hat{\mathbf{x}}_n\|^2}} \tag{6.44}$$

In addition to the normalised solution accuracy, which quantifies how accurate the HB solution is *for a given wave input signal*, it is important to ensure that the chosen period T is sufficient for a satisfactory *statistical characterisation* of the WEC outputs, as discussed in Section 5.7. In particular, the period T should be long enough to avoid any significant distortion in the WEC output power calculations. Therefore, for each (f_c, T) pair, the average power (over the 20 realisations) is calculated using Eq. (6.42), and normalised by the 'reference' power P^*, calculated with the largest f_c and largest T values.

Flap-type device

Figure 6.7 shows the results obtained, over the chosen range of (f_c, T) settings, in terms of the three criteria identified (numerical accuracy as estimated through the magnitude of the last harmonic of the solution; statistical accuracy of the average power; computation time).

As shown in the bottom-left graph (in logarithmic scale) of Fig. 6.7, the numerical accuracy of the solution improves more than linearly with the cut-off frequency. It is possible to define an *'acceptable zone'* where the numerical accuracy remains below a given threshold. Choosing, for example, 10^{-4}, it is ensured that the changes in the solution, induced by the addition of more harmonics, are insignificant (less than 10^{-4} times the magnitude of the solution).

The top-right graph of Fig. 6.7 shows a similar contour plot, this time not on a logarithmic scale, where the accuracy in terms of power calculations is measured: a value of 100% means that the calculated power is virtually the same as the most accurate power calculation available, while a value of, for example, 110%, represents a 10% power overestimation. It can be seen that power accuracy has little sensitivity to the frequency range (because the vast majority of the wave energy content is concentrated within relatively low frequencies), but largely depends on the simulation period T, when T is particularly small. From the top-right graph of Fig. 6.7, another acceptable zone can be identified, within which the error committed in terms of power calculations is below, for example, 1%.

Finally, the bottom-right contour plot in Fig. 6.7 shows, in logarithmic scale, the computation time per second of signal simulated. The intersection of the two previously-defined 'acceptable zones' allows for determining an (f_c, T) pair (represented by a thick purple dot), which ensures that the chosen criteria, in terms of numerical and statistical accuracies, are satisfied at the smallest

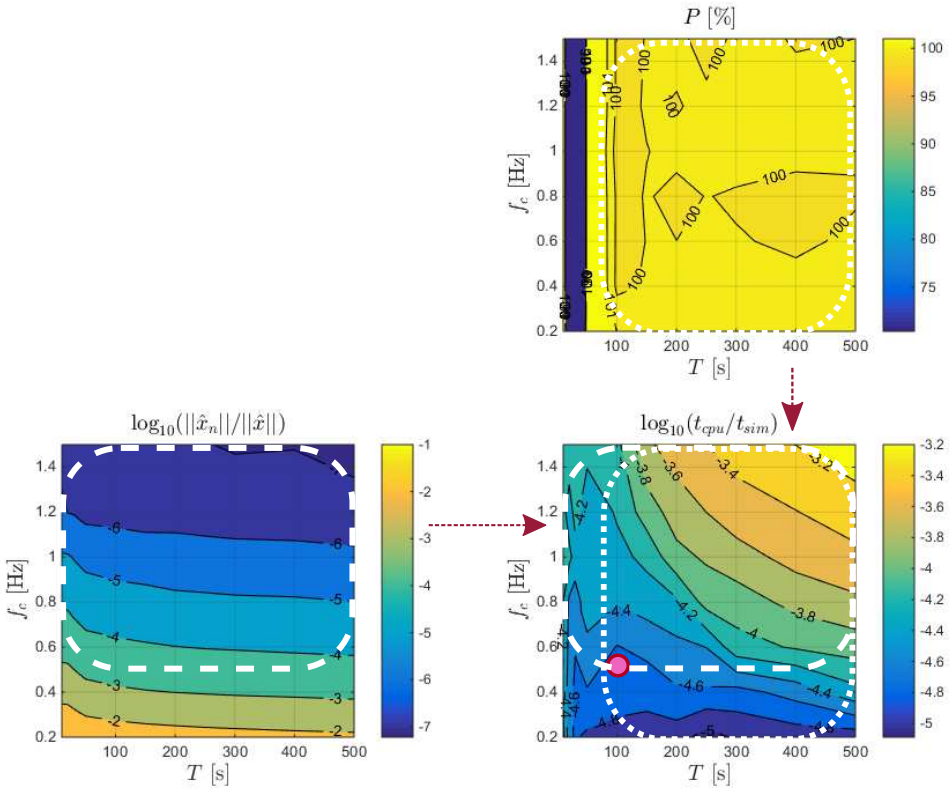

Figure 6.7: Flap-type WEC

possible computation cost. From the contour lines, it can be clearly seen in which direction, in the (f_c, T) space, the computation time increases the most. For example, increasing T (moving the purple dot to the right) is less costly, in comparison to increasing f_c (moving the purple dot upwards).

For the flap-type device, a cut-off frequency $f_c = 0.5$Hz and a simulation period $T = 100$s are found to be an appropriate compromise. In any case, throughout the rest of this chapter, the HB method will be further validated, and it will be possible to adjust, ex-post, the settings approximately carried out here.

Spherical HPA

The same procedure is repeated for the spherical HPA, in its design sea state, as shown in Fig. 6.8. On the one hand, from the bottom-left contour plot, the cut-off frequency necessary to achieve the chosen threshold of 10^{-4} is significantly larger than for the flap-type device. On the other hand, from the top-right contour plot, too small a cut-off frequency does not only affect the accuracy of the solution, but also introduces significant errors in the estimated power - in fact, the peak wave frequency is $f_p = 1/T_p \approx 0.14$Hz, so that a cut-off frequency of 0.2Hz is barely larger than f_p, and thus leaves a significant fraction of the incoming spectrum energy out of the frequency discretisation. However, the power accuracy improves rapidly with the cut-off frequency. As far as the simulation time T is concerned, the requirements are even less stringent for the spherical HPA than for the flap-type device, to fall within 1% of the reference power value. However, as seen in the bottom-right plot, increasing T from 50 to, say, 100s, does not significantly increase the computation time, so that $T = 100$s is chosen (like for the flap-type WEC), while f_c is set to a value of 0.8Hz.

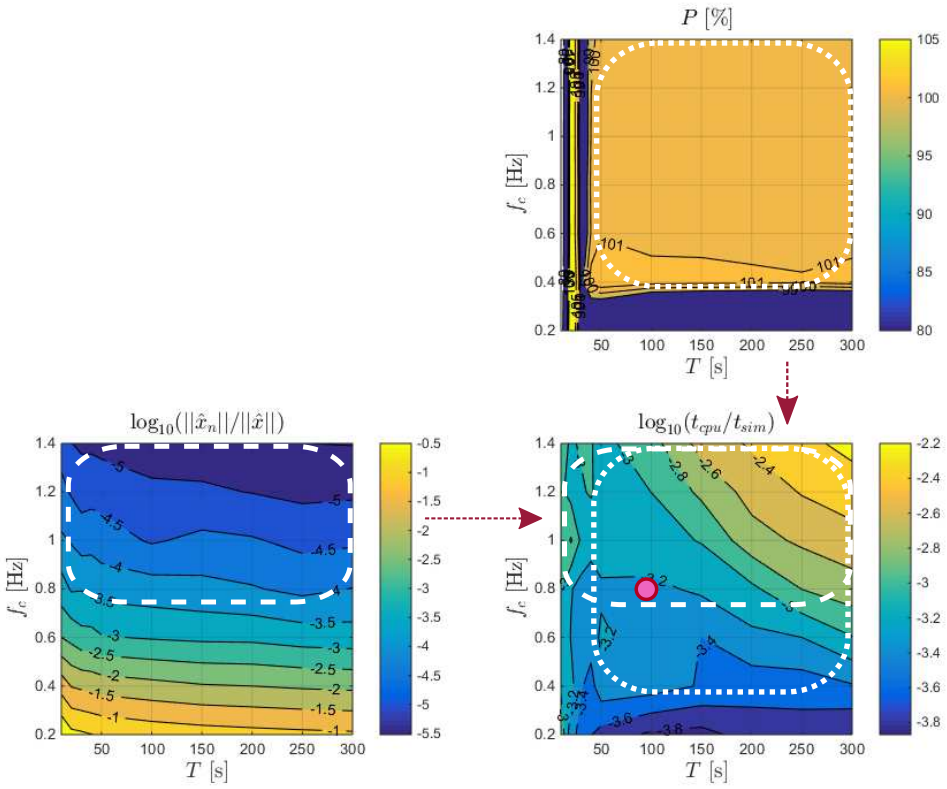

Figure 6.8: Spherical heaving point absorber

Array of 4 cylindrical HPAs

Fig. 6.9 shows the same contour plots, for the array of cylindrical HPAs. The requirements, in terms of f_c and T, to meet the chosen requirements, are similar to those for the flap-type device, with $f_c = 0.5$Hz, $T = 100$s being an acceptable choice.

ISWEC

Finally, considering Fig. 6.10, the requirements, in terms of (f_c, T) for the ISWEC device are similar to those which are obtained for the spherical HPA. Therefore, the same settings $f_c = 0.8$Hz, $T = 100$s, are adopted.

6.4 Validation and computational performance of the HB simulation method

As outlined in the introduction to this chapter, after f_c and T have been chosen, for each case study, HB simulations are run over a wide range of (k_{pto}, b_{pto}) PTO parameters, in order to identify resonance conditions around which the HB performance can be further assessed. Three strategies to initialise the HB algorithm are investigated:

- *'Linear initialisation':* In this strategy, the starting guess of the HB algorithm is the solution for the linearised WEC model dynamics - which is obtained through a simple matrix inversion, as in Eq. (5.71);

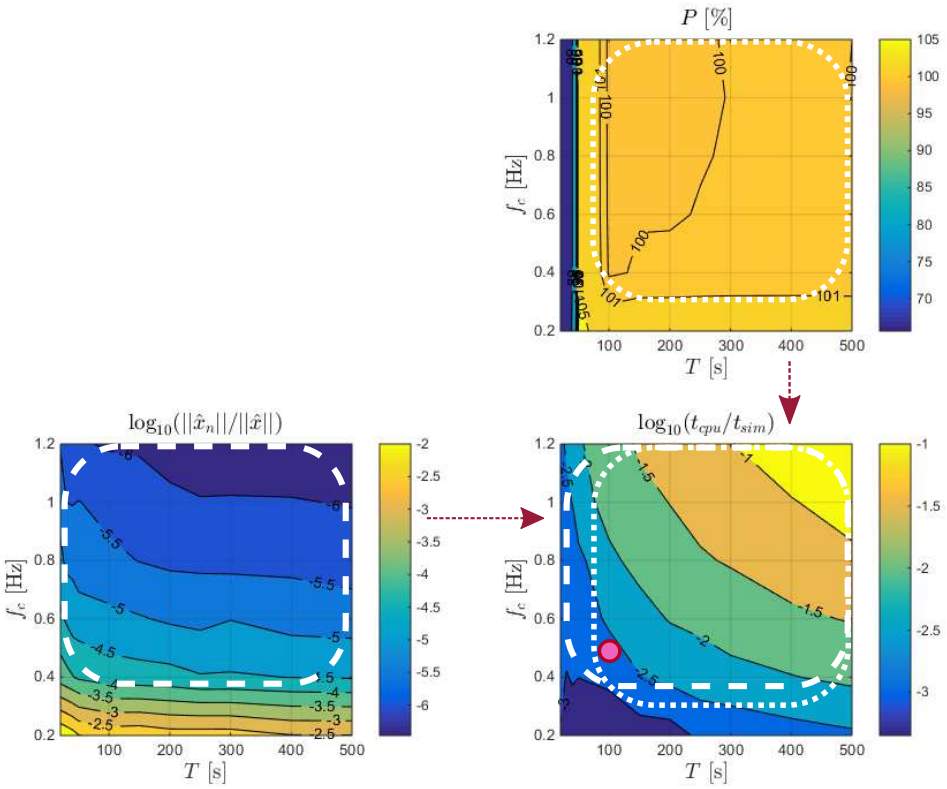

Figure 6.9: Array of four cylindrical heaving point absorbers

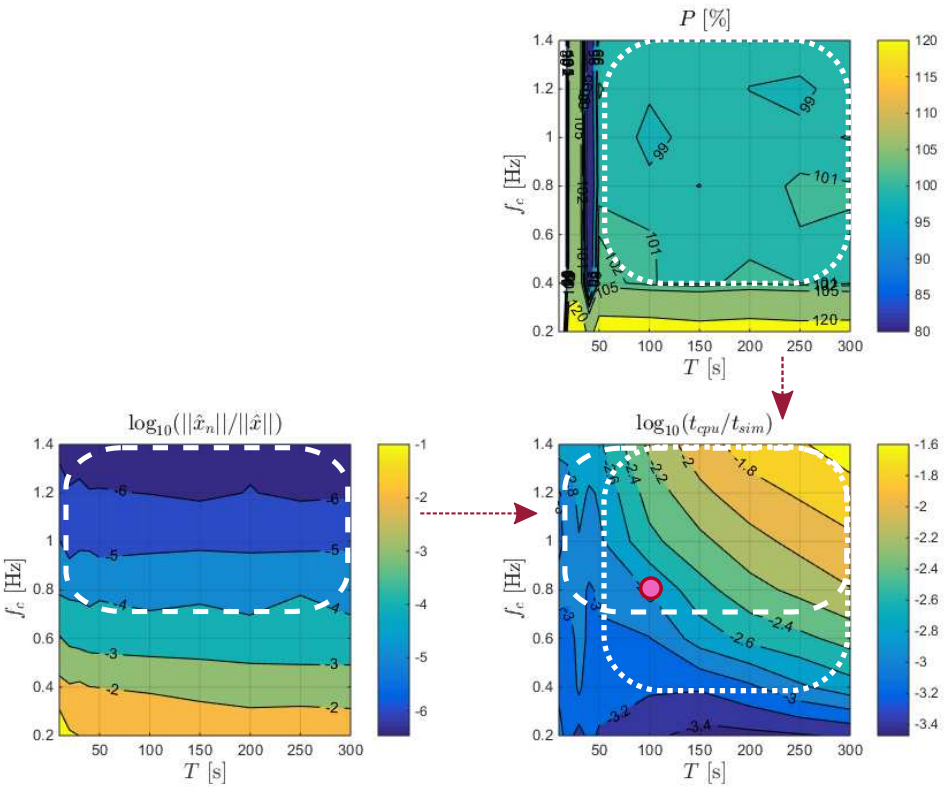

Figure 6.10: ISWEC device

- *'Neighbour-based initialisation':* This strategy takes advantage of the likely similarities between HB solutions for neighbouring choices of PTO parameters. More specifically, the HB equation is solved sequentially over a range of PTO parameter values (k_{pto_i}, b_{pto_j}). Denote $\hat{\mathbf{x}}(i,j)$ as the HB solution, obtained for (k_{pto_i}, b_{pto_j}). For every i, $\hat{\mathbf{x}}(i,1)$ is solved using the linearised solution as the initial guess, but for every $j > 1$, $\hat{\mathbf{x}}(i,j)$ is found using $\hat{\mathbf{x}}(i,j-1)$ as a starting guess.

- *'Sensitivity-based initialisation':* Like the neighbour-based initialisation, this strategy exploits the similarity between the solution obtained for adjacent pairs of PTO parameters, but also uses the sensitivity equation in order to provide a more accurate initial guess. Note

$$\alpha_{pto} := \begin{pmatrix} k_{pto} \\ b_{pto} \end{pmatrix} \tag{6.45}$$

  At the end of the HB algorithm, the derivative of the solution with respect to α_{pto}, $\frac{\partial \hat{\mathbf{x}}}{\partial \alpha_{pto}}$, can be evaluated by solving the sensitivity equation, as detailed in Section 5.6. The initial guess for $\hat{\mathbf{x}}(i,j)$ is then calculated as

$$\hat{\mathbf{x}}^{(0)}(i,j) = \hat{\mathbf{x}}(i,j-1) + \frac{\partial \hat{\mathbf{x}}}{\partial \alpha_{pto}} [\alpha_{pto_{i,j}} - \alpha_{pto_{i,j-1}}] \tag{6.46}$$

RK2 time-domain simulations are also carried out, using different time steps, in order to validate the proposed HB approach by comparison with a well-known technique, and to understand the relative properties of the RK2 and HB methods, in terms of accuracy and computation time. Of particular interest is the trend followed by the error magnitude between HB and RK2 results, when the RK2 time step tends to zero. A comparison is also provided in terms of computation time per second of the simulated signal. Because of their relatively high computation cost when the time step becomes small, RK2 simulations are only run over a restricted range of (k_{pto}, b_{pto}) conditions, which is further detailed in the following subsections.

6.4.1 Flap

The flap-type WEC model is examined first. Fig. 6.11 shows the average power P over a wide range of k_{pto}, b_{pto} parameters. An optimal pair k^*_{pto}, b^*_{pto} can be clearly identified, which maximises power absorption within the parametric control space.

Having set b_{pto} to its optimal value b^*_{pto}, the performance of the HB method is examined more closely in comparison to RK2 integration, by varying k_{pto} only, as illustrated by the thick purple dots in Fig. 6.11. This allows both non-resonant (when k_{pto} is far from k^*_{pto}) and resonant conditions (when k_{pto} is close to k^*_{pto}) to be encountered. RK2 simulations are run for the same wave input, by adding an appropriately long transient time, as illustrated in Fig. 6.12. Different RK2 time steps are investigated, between $\Delta t = 0.05$s and $\Delta t = 0.002$s.

It is useful to start with a visual comparison of the solutions obtained using HB and TD simulations. Fig. 6.12 shows an example of solutions obtained with the HB method (purple lines) and RK2 (green lines; the time step is set to 0.005s) for the same wave input. The solid lines represent the case where the PTO damping is set to b^*_{pto} while there is no reactive control term; the dotted lines represent the results obtained by using the two optimal PTO parameters, b^*_{pto} and k^*_{pto}.

The signal period is $T = 100$s, as per the HB settings determined in Section 6.3. Note however, in Fig. 6.12, the 50s additional simulation time allowed in addition to the signal period T. This is to allow the transient dynamics to fade out in the RK2 simulation. The excitation signal $e(t)$ (upper graph), over the time interval $[-50;0]$, is simply the repetition of $e(t)$ over the interval $[50;100]$. Unlike RK2, the HB method only solves for the steady-state dynamics (and therefore the HB solution over $[-50;0]$ is a repetition of the solution over $[50;100]$). In contrast, the RK2

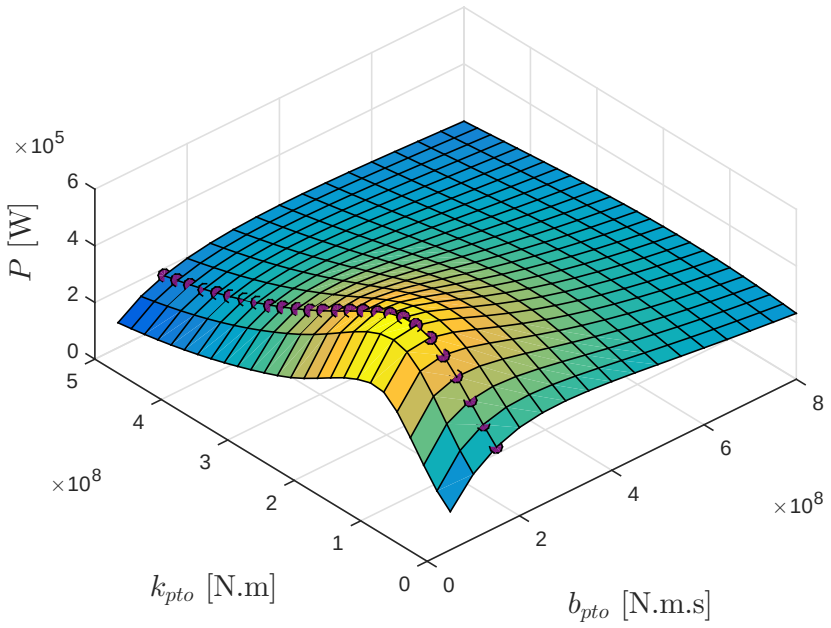

Figure 6.11: Average absorbed power in a wide range of (k_{pto}, b_{pto}) parameters, for the flap-type WEC, in a 100-s wave input generated from a JONSWAP spectrum with $H_{m_0} = 2$m, $T_p = 12$s and $\gamma = 3.3$.

solution has transient dynamics, only visible in the first few tens of seconds. The accuracy of the two techniques (RK2 and HB methods) are only compared over the time interval $[0;T]$, where RK2 simulation results are assumed to be in steady-state, as highlighted in Fig. 6.12.

As can be appreciated in Fig. 6.12, except for the transient time, HB and RK2 results seem virtually identical, which is encouraging as a first comparison of the HB method with a well-established technique. Also note how the reactive control term strongly amplifies the device dynamics and absorbed power. In fact, it can be verified that, with k^*_{pto}, the velocity and excitation are in phase with each other, which is the well-known goal which power-maximising WEC control strategies aim to achieve [9].

The difference between RK2 and HB results must be analysed more thoroughly than through simple visual examination of the time-domain trajectories. Fig. 6.13 shows the average absorbed power obtained with the HB method, and with the RK2 method using different time steps, when k_{pto} varies, while b_{pto} is fixed to its optimal value b^*_{pto}. RK2 results seem to converge towards HB results when Δt decreases. Too coarse a time step results in significant error in terms of estimated absorbed power and, remarkably, that error is more significant close to the optimal settings (k^*_{pto}, b^*_{pto}), where the device is in resonance. Recall that, with the RK2 method, it is ensured that the numerical solution tends to the exact mathematical solution, when the time step approaches zero. Therefore, when it is observed that, as the RK2 time step approaches zero, RK2 results tend to the HB solution, the latter can then be safely considered to be so close to the exact solution, that it can be used as a baseline (as an extension of the methodology, presented in Section 5.5.6, where the WEC model was linear). That is why the difference between HB and RK2 results is termed 'error' while, strictly speaking, both method yield approximation errors.

The accuracy of RK2 results, with respect to HB results, are further examined in Fig. 6.14 for different time steps, along with the computational cost associated with each time step. The relative error, in terms of absorbed power, is calculated as follows:

$$e_P = 100 \times \frac{P_{RK2} - P_{HB}}{P_{HB}} \tag{6.47}$$

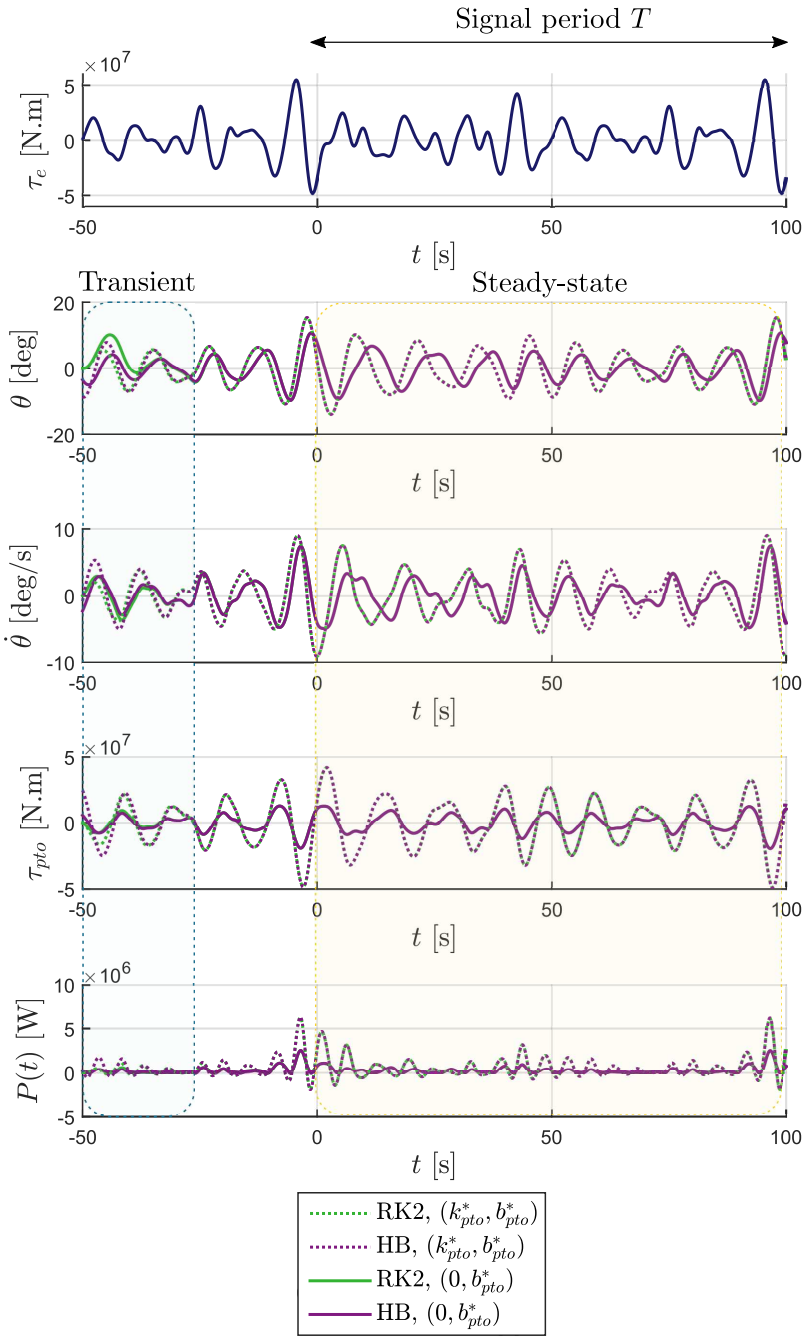

Figure 6.12: Example of time-domain trajectories obtained with the HB and RK2 solution techniques, for the flap-type WEC, in a 100-s wave input generated from a JONSWAP spectrum with $H_{m_0} = 2$m, $T_p = 12$s and $\gamma = 3.3$.

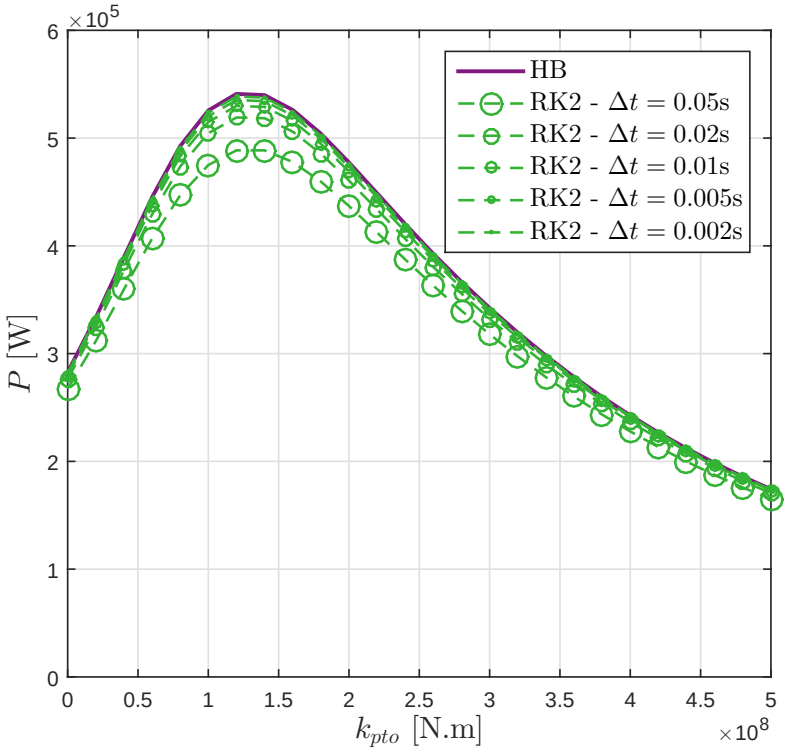

Figure 6.13: Absorbed power from simulation results, using HB and RK2 with several different time steps, over a range of k_{pto} values (b_{pto} is set to b^*_{pto}), for the flap-type WEC, in a 100-s wave input generated from a JONSWAP spectrum with $H_{m_0} = 2$m, $T_p = 12$s and $\gamma = 3.3$.

where P_{RK2} is the absorbed power calculated from RK2 simulations using Eq. (6.39), and P_{HB} is the absorbed power calculated from HB simulations using Eq. (6.42). e_P is averaged over the range of k_{pto} values shown in Fig. 6.13.

A normalised root-mean-square error value measures the relative difference between solutions obtained using the RK2 and HB methods, as follows:

$$e_{RMS} = 100 \times \frac{\sqrt{\frac{1}{T}\int_{t=0}^{T} (x_{RK2} - x_{HB})^2 \, dt}}{\sqrt{\frac{1}{T}\int_{t=0}^{T} x_{HB}^2 \, dt}} \tag{6.48}$$

where x_{RK2} (resp. x_{HB}) is the system variable for which the relative error is measured (θ, in the case of the flap-type WEC). The numerator of Eq. (6.48) is obtained through numerical integration with the time step of the RK2 method, as in Eq. (5.90), while the denominator can be obtained directly as the Euclidean norm of the HB solution:

$$\sqrt{\frac{1}{T}\int_{t=0}^{T} x_{HB}^2 \, dt} = \sqrt{\sum_{k=1}^{2N_\omega+1} \hat{x}_k^2} \tag{6.49}$$

e_{RMS} is averaged over the range of k_{pto} values shown in Fig. 6.13.

As can be appreciated in Fig. 6.14, both relative errors (in terms of absorbed power and solution trajectory) tend to zero linearly as the RK2 time step decreases. This suggests that the HB solution is so accurate, that it can be seen as the limit of the RK2 solution, when the RK2 time

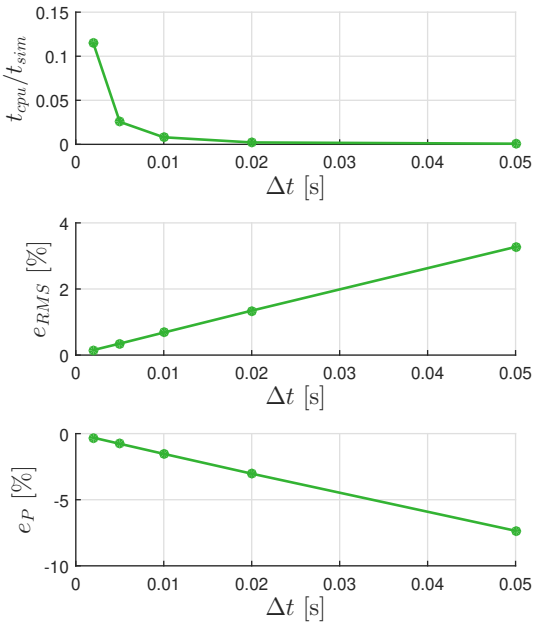

Figure 6.14: Computation time (top graph) and accuracy (middle and bottom graph) of RK2 simulations with different time steps, for the flap-type WEC, in a 100-s wave input generated from a JONSWAP spectrum with $H_{m_0} = 2$m, $T_p = 12$s and $\gamma = 3.3$. Results are averaged over the range of k_{pto} values shown in Fig. 6.13.

step tends to zero. The top graph of Fig. 6.14 indicates that the RK2 computation cost increases rapidly when Δt is reduced. A closer examination of the relative magnitude of the computation time for the different time steps indicates that the computational costs increases at a rate between $1/\Delta t$ and $1/\Delta t^2$, due to the radiation convolution term, as discussed in Section 4.3.3.6.

Finally, the computational performances of RK2 and HB methods are more closely investigated in Fig. 6.15. Unlike RK2 simulations, which are only run with varying k_{pto} values while b_{pto} is set to b^*_{pto}, HB simulations are run while varying both k_{pto} and b_{pto} parameters. Therefore, for each $k_{pto,i}$ value, the HB computation time is averaged over the range of $b_{pto,j}$ conditions. The relative merits of the three proposed HB initialisation methods are also assessed.

From Fig. 6.15, it can be seen that, unsurprisingly, the RK2 computation time remains consistent across the full range of PTO settings. In contrast, for the HB method, different PTO settings can result in problems which are more or less 'difficult' to solve, in the sense that they necessitate a larger or smaller number of iterates to reach the solution. In particular, close to the optimal PTO stiffness term k^*_{pto}, which makes the device resonate and hence magnifies the effect of non-linearities, the number of iterations (and hence the HB method computation time) tends to increase slightly, regardless of the HB initialisation strategy.

From the two graphs in Fig. 6.15, different HB initialisation strategies results in slightly different computational performance. Clearly, the neighbour-based initialisation does not reduce the average number of HB iterations, with respect to the linear initialisation strategy, which indicates that, in this specific case study, the solution of the linearised WEC model, with b_{pto_j}, is a slightly better starting point than the (non-linear) HB solution with the adjacent setting $b_{pto_{j-1}}$. However, unlike linear initialisation, the neighbour-based initialisation does not necessitate any additional numerical operation (while the linear initialisation necessitates the solution of a linear system). Therefore, the overall computational performance of the HB method with the linear and neighbour-based initialisation strategies remain similar, as seen in the top graph of Fig. 6.15. In contrast, the sensitivity-based initialisation brings a noticeable reduction of the average number of

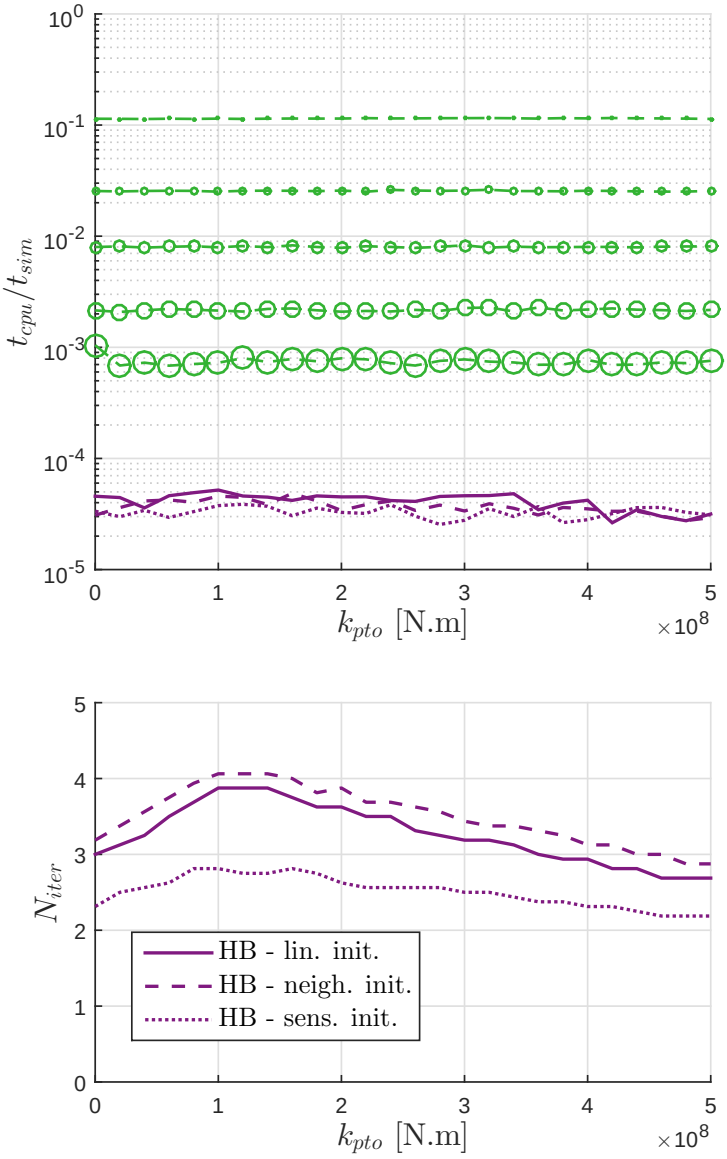

Figure 6.15: Computation time per second of the simulated signal (top graph) using the HB method with three different initialisation methods, and RK2 with different time steps (from the largest to the smallest marker size: Δt =0.05s, 0.02s, 0.01s, 0.005s, 0.002s), for the flap-type WEC, in a 100-s wave input generated from a JONSWAP spectrum with $H_{m_0} = 2$m, $T_p = 12$s and $\gamma = 3.3$. The bottom graph shows the number of HB iterations for the three different initialisation strategies. All computation times are obtained from a Matlab implementation, run on a 3.50 GHz, 8-core Intel® processor.

HB iterations, thus resulting in a slightly better computational performance.

However, the changes in computational performance induced by the different HB initialisation strategies are marginal, compared to the gap between RK2 and HB computational cost. Overall, the computation gain obtained by using the HB technique is large: with respect to RK2 integration, the HB method is between approximately 20 times faster (when the RK2 time step is set to 0.05s) and 3000 times faster (when the RK2 time step is set to 0.002s). For a 'reasonable' RK2 time step of 0.01s, which ensures that power absorption is assessed with a 1% error, the RK2 method is 250 times slower than the HB method.

Finally note that, for the RK2 results, the measured computation time per second of signal simulated does not take into account the requirement of simulating additional time for allowing transient dynamics to fade out. Therefore, in practice, the RK2 computation time should be slightly larger than the values shown in Figs. 6.14 and 6.15.

6.4.2 Spherical HPA

The same comparison procedure, presented for the flap-type WEC in Section 6.4.1, is implemented for the spherical HPA, using $T = 100$s and $f_c = 0.8$Hz, as per Section 6.3. Unlike the HB results for the flap-type WEC, which were obtained using a simple Newton method, with the spherical HPA, the HB algorithm convergence can be problematic for a couple of PTO combinations close to resonance; therefore a more robust zero-finding procedure is chosen, namely the trust-region dogleg algorithm, readily implemented in the Matlab *fsolve* function, as discussed in Section 5.4.3.

Fig. 6.16 shows the power absorbed across the chosen range of PTO parameters. In contrast to the flap-type WEC, which necessitates positive k_{pto} values to achieve optimal power absorption, the spherical HPA requires negative k_{pto} values to be tuned to the incoming waves. An optimal combination k^*_{pto}, b^*_{pto} can be clearly identified, resulting in a threefold increase in power absorption, with respect to settings where no reactive control term is allowed. Note, however, that 9 data points are missing - for the lowest b_{pto} values and the largest k_{pto} magnitude. This is because the HB algorithm failed to converge in those configurations within the chosen maximum number of iterations (set to 200). This point will be further examined at the end of this subsection.

Comparison of HB results with RK2 results is carried out over the restricted range of PTO conditions, represented by the thick purple dots in Fig. 6.16. As shown in Fig. 6.17, the difference between RK2 and HB results, in terms of power absorption, although smaller than for the flap-type WEC, shows a qualitatively similar behaviour, with a reduced difference as the RK2 time step tends to zero.

Similarly to the flap-type WEC, the accuracy and speed of the RK2 simulations are further assessed in Fig. 6.18, where it is seen that the relative error between RK2 and HB results also decreases, when the RK2 time step tends to zero. However, compared to the flap-type WEC, the magnitude of the relative error is significantly smaller, even with the coarser RK2 time step. In addition, a small residual RMS difference (in the order of 0.1%) seems to persist when the RK2 time-step tends to zero. It was found that increasing the HB cut-off frequency by a small quantity (from 0.8 to 1Hz) suppresses the residual difference, which means that this difference must be interpreted as the inaccuracies, introduced by the HB solution being cut-off at f_c. Such a small error, however, is deemed negligible, and thus f_c is maintained at a value of 0.8Hz.

The computational performance of both HB and RK2 methods are shown in Fig. 6.19. As for the flap-type WEC, HB simulations are run for varying k_{pto} and b_{pto} parameter values and, for each k_{pto} value, the HB computation time is averaged over the range of b_{pto} conditions. Those cases, where the algorithm did not converge, are not included in the calculated average computational time and number of iterations.

From Fig. 6.19, concerning the HB method with linear initialisation, there is an increase

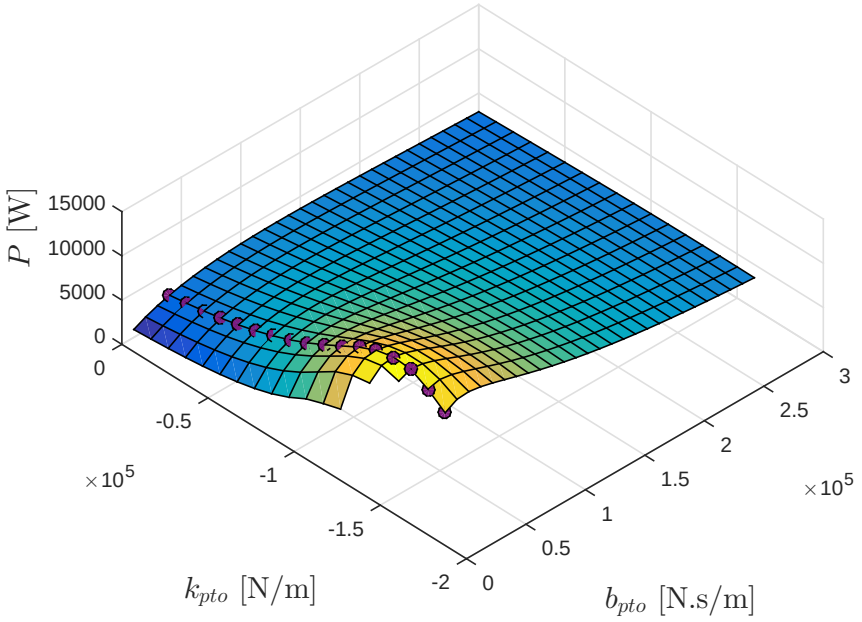

Figure 6.16: Average absorbed power in a wide range of (k_{pto}, b_{pto}) parameters, for the spherical HPA, in a 100-s wave input generated from a JONSWAP spectrum with $H_{m_0} = 1$m, $T_p = 7$s and $\gamma = 2$.

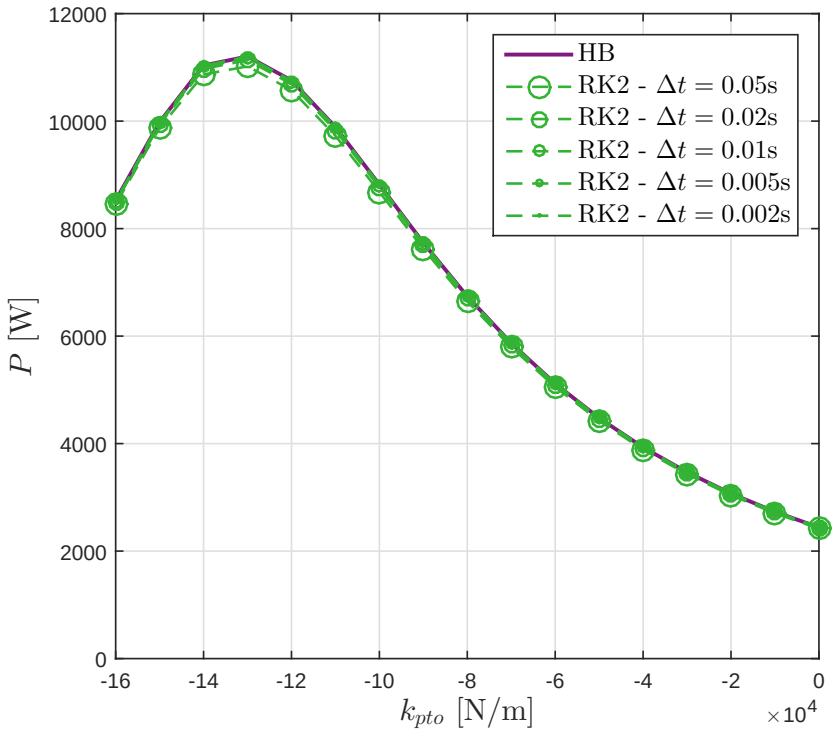

Figure 6.17: Absorbed power from simulation results, using the HB method and RK2 integration with several different time steps, over a range of k_{pto} values (b_{pto} is set to b^*_{pto}), for the spherical HPA, in a 100-s wave input generated from a JONSWAP spectrum with $H_{m_0} = 1$m, $T_p = 7$s and $\gamma = 2$.

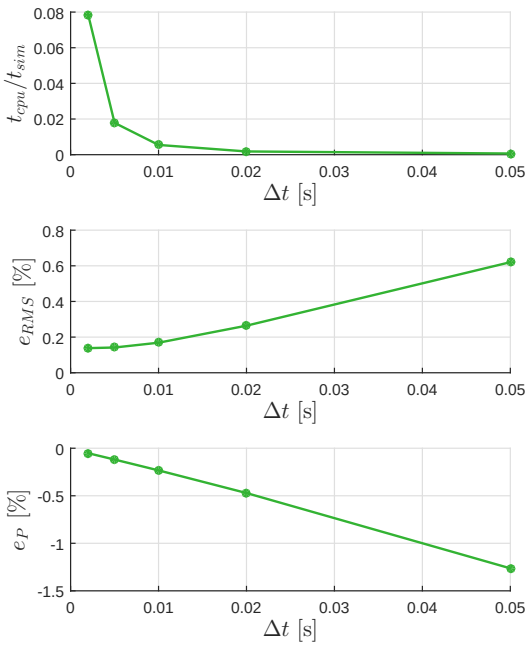

Figure 6.18: Computation time (top graph) and accuracy (middle and bottom graph) of RK2 simulations with different time steps, for the spherical HPA, in a 100-s wave input generated from a JONSWAP spectrum with $H_{m_0} = 1$m, $T_p = 7$s and $\gamma = 2$. Results are averaged over the range of k_{pto} values shown in Fig. 6.17.

in the number of iterations around and beyond resonance, i.e. when $|k_{pto}|$ becomes close to, or larger than, $|k^*_{pto}|$. This results in an increase in the HB computation cost for such k_{pto} values. In contrast, using either the neighbour-based or sensitivity-based initialisation approaches give a consistent number of iterations, and hence computation cost, across k_{pto} values.

In spite of similar numbers of iterations for the flap-type WEC and spherical HPA, when the neighbour- and sensitivity-based initialisation strategies are employed, the HB method is approximately 2 times slower for the sphere than it is for the flap-type WEC. This is because the (f_c, T) combination adopted for the spherical HPA in Section 6.3 is less favourable, in view of the considerations developed in Sections 5.7 and 6.3, since T is identical for both WECs, while f_c is 60% larger for the spherical HPA than for the flap-type WEC. The computational gain, with respect to RK2 simulations, however, remains significant; the HB method is between 10 and 1500 times faster, depending on the RK2 time step.

Finally, it is interesting to examine more closely the conditions in which the HB algorithm does not converge. To that end, Fig. 6.20 shows the solution trajectories obtained with both HB and RK2 methods. In Fig. 6.20a, the time-domain trajectory z_G as well as the instantaneous absorbed power $P(t)$, obtained with (k^*_{pto}, b^*_{pto}), are shown for both HB and RK2 methods. There is no distinguishable difference between RK2 and HB results. For comparison, the solution for the *linearised* model is also plotted, in order to highlight how strongly the non-linearities affect the WEC dynamics. Furthermore it can be seen that the WEC motion amplitude is significantly greater than the wave elevation (also plotted on the figure): this is because the reactive control term k^*_{pto} allows the device to resonate in incoming waves.

Fig. 6.20b shows the simulation results for the same wave input, when b_{pto} is set to a smaller value (1×10^4) than b^*_{pto} (4×10^4), which corresponds to one of the cases of Fig. 6.16 where the HB method does not converge. Since the HB method does not converge, only RK2 results are plotted. It can be seen that the WEC dynamics become unstable from $t \approx 45$s: At that instant, the

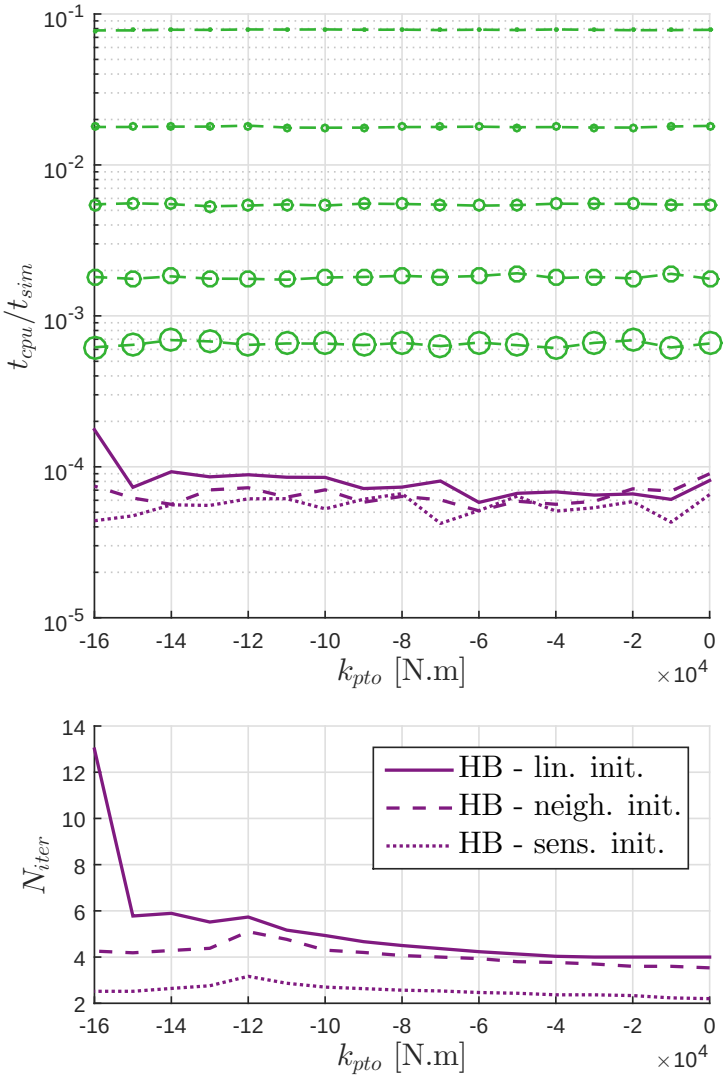

Figure 6.19: Computation time per second of the simulated signal (top graph) using the HB method with three different initialisation methods, and RK2 with different time steps (from the largest to the smallest marker size: Δt =0.05s, 0.02s, 0.01s, 0.005s, 0.002s), for the spherical HPA, in a 100-s wave input generated from a JONSWAP spectrum with $H_{m_0} = 1$m, $T_p = 7$s and $\gamma = 2$. The bottom graph shows the number of HB iterations for the three different initialisation strategies. All computation times are obtained from a Matlab implementation, run on a 3.50 GHz, 8-core Intel® processor.

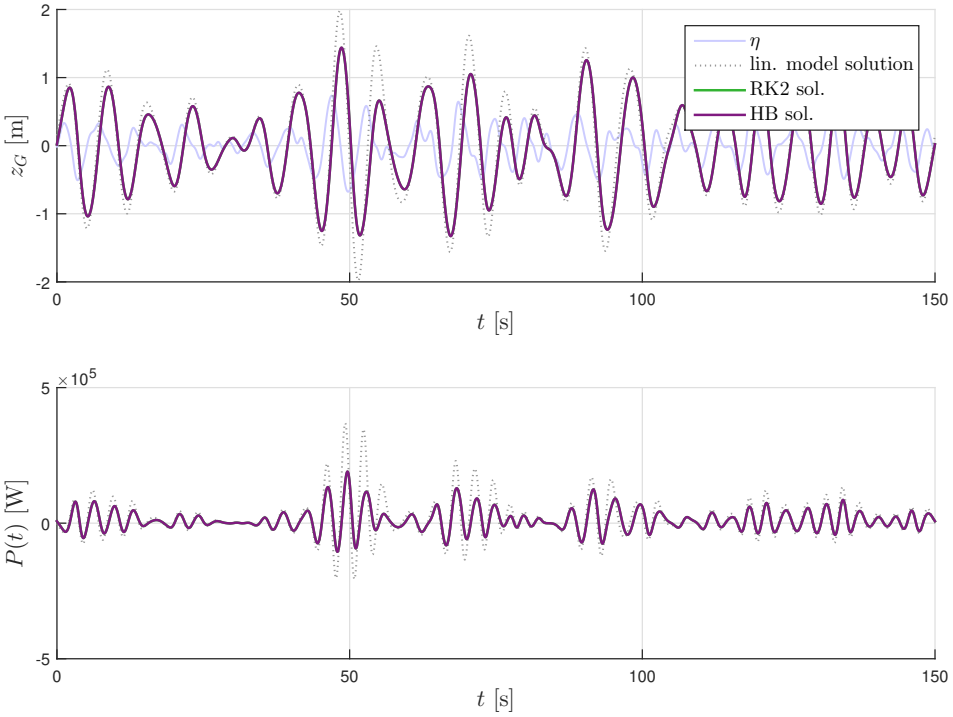

(a) $k_{pto} = k^*_{pto}, b_{pto} = b^*_{pto} = 4 \times 10^4$

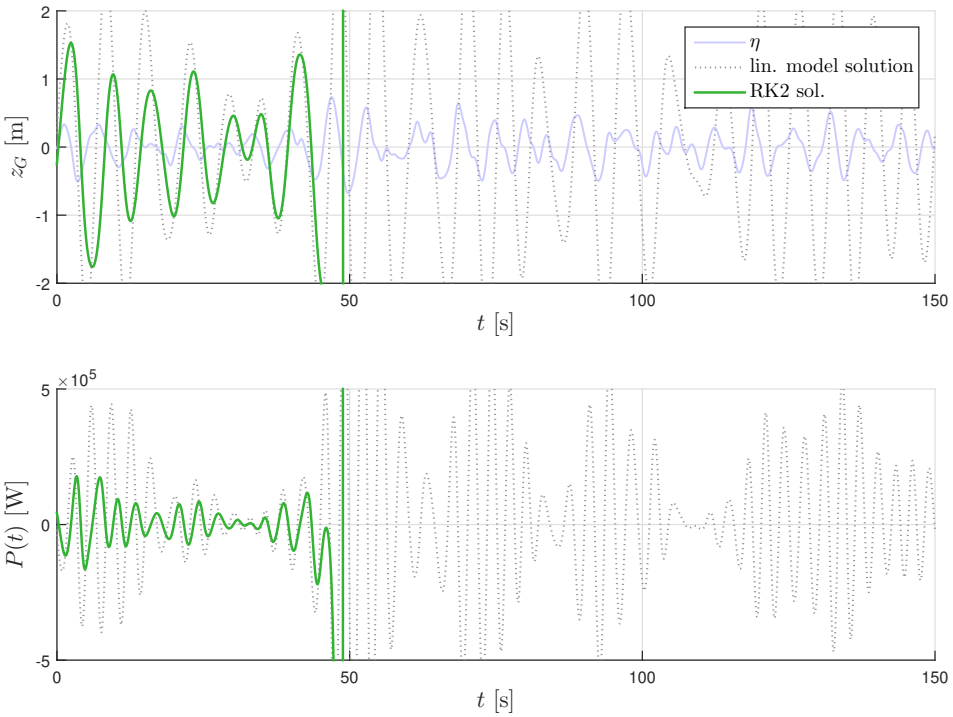

(b) $k_{pto} = k^*_{pto}, b_{pto} = 1 \times 10^4$

Figure 6.20: Solution of the dynamical equation for $k_{pto} = k^*_{pto}$ and two different b_{pto} values, using HB and RK2 methods, for the spherical HPA, in a 150-s wave input generated from a JONSWAP spectrum with $H_{m_0} = 1$m, $T_p = 7$s and $\gamma = 2$.

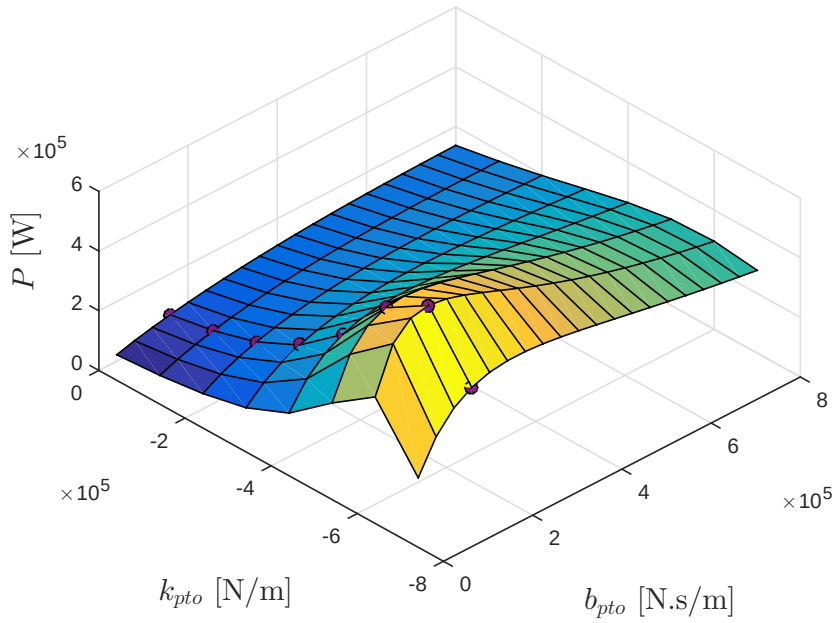

Figure 6.21: Average absorbed power in a wide range of (k_{pto}, b_{pto}) parameters, for the array of four cylindrical HPAs, in a 100-s wave input generated from a JONSWAP spectrum with $H_{m_0} =$ 2m, $T_p = 12$s and $\gamma = 3.3$.

WEC becomes fully submerged, and the proposed dynamical model of Eq. (6.16) is not physically consistent any more. Schematically, while the non-linear static term starts decreasing, the linear reactive control term continues pushing the device downwards. Of course, the model could be modified for more realism, by correcting the expression for the pressure integral when the WEC becomes fully submerged or fully dry, and by modifying the reactive control term in a non-linear way (as in [57] and [152]) in order to reduce the occurrence of unstable motion. However, as reported in [152], even such modifications do not ensure that the WEC motion is stable regardless of the choice of k_{pto}.

Also note, from Fig. 6.20b, that, while the non-linear WEC model has unstable dynamics, the linearised WEC model has a stable periodic solution. This illustrates the complexity of employing non-linear dynamical models, of which the properties in terms of stability and existence of periodic solutions [97] are difficult to predict *a priori*, but are nevertheless important, and may be masked by the use of a linear approximation.

6.4.3 Array of 4 cylindrical HPAs

Fig. 6.21 shows the absorbed power calculated using the HB method, for the array of 4 cylindrical HPAs, across the chosen range of PTO parameters. Again, a clear optimum can be found, and the PTO damping is set to its optimal value b^*_{pto} for further comparison between RK2 and HB results. Note that b_{pto} and k_{pto} are set to an identical value for each of the four devices.

For this case study, RK2 simulations, calculating the full convolution product, were so slow that the range of RK2 time steps investigated was limited to only three values, namely 0.05s, 0.02s and 0.01s. Those three values are sufficient for a meaningful comparison between HB and RK2 results, similar to that already presented for the flap-type WEC and for the spherical HPA.

Fig. 6.22 compares the absorbed power, calculated using the HB method, and with RK2 integration using different time steps, with the full convolution calculation and with the two different state-space approximations. From Fig. 6.22, HB and RK2 results yield nearly identical power

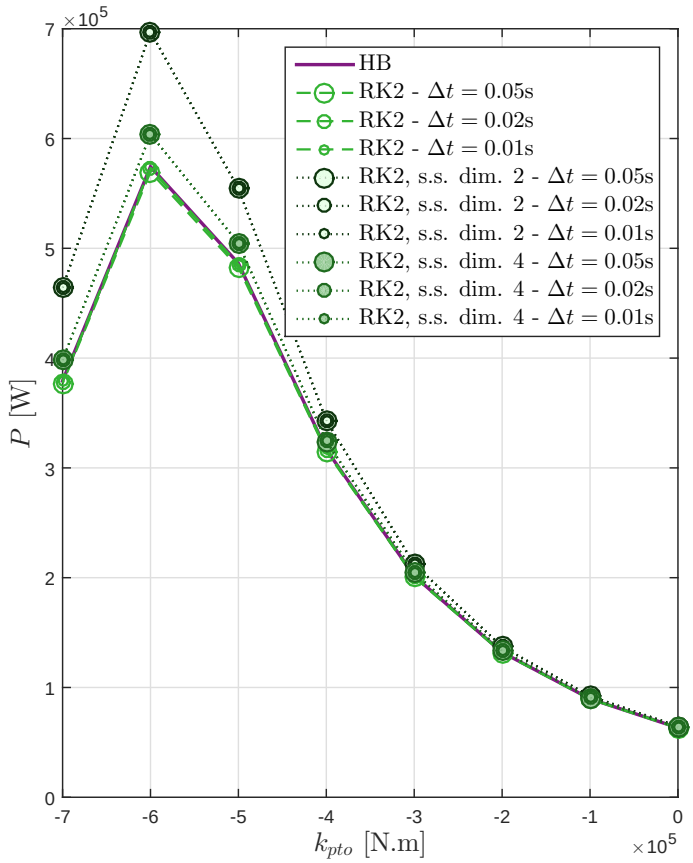

Figure 6.22: Absorbed power from simulation results, using the HB and RK2 methods with several different time steps, over a range of k_{pto} values (b_{pto} is set to b^*_{pto}), for the array of four cylindrical HPAs, in a 100-s wave input generated from a JONSWAP spectrum with $H_{m_0} = 2$m, $T_p = 12$s and $\gamma = 3.3$. For the RK2 simulations, the full convolution is compared with two state-space approximations.

absorption values, when the full convolution product is calculated in the RK2 simulation. This is examined in more detail in Fig. 6.23 which shows that, similarly to the previous case studies, RK2 results converge to the HB results when the RK2 time step decreases. In magnitude, however, the HB/RK2 difference is smaller than for the flap-type WEC; even with a relatively coarse 0.05s time-step, RK2 produces a 0.6% error only, in terms of power absorption.

In contrast to RK2 using the full convolution calculation, state-space approximations - which do not change the *simulation method*, but the *model*, following the terminology specified in the introduction to Chapter 4 - introduce significant errors which are larger in magnitude, than those introduced by the use of a large time-step. From Figs. 6.22 and 6.24, the relative error, in terms of power absorption, is larger close to resonance; while the state-space approximation introduces relatively modest errors when k_{pto} is set to zero (P being overestimated by approximately 1% only, for $D_R = 4$, and 3% for $D_R = 2$), the relative error reaches as much as 5% with $D_R = 4$ (22% with $D_R = 2$) when k_{pto} is set to its optimal value.

The errors introduced by the state-space approximation are further examined in Fig. 6.25, without any reactive control term ($k_{pto} = 0$, Fig. 6.25a), and then with the optimal reactive control parameter ($k_{pto} = k^*_{pto}$, Fig. 6.25b). Given the symmetry of the problem (see Fig. 6.4), the

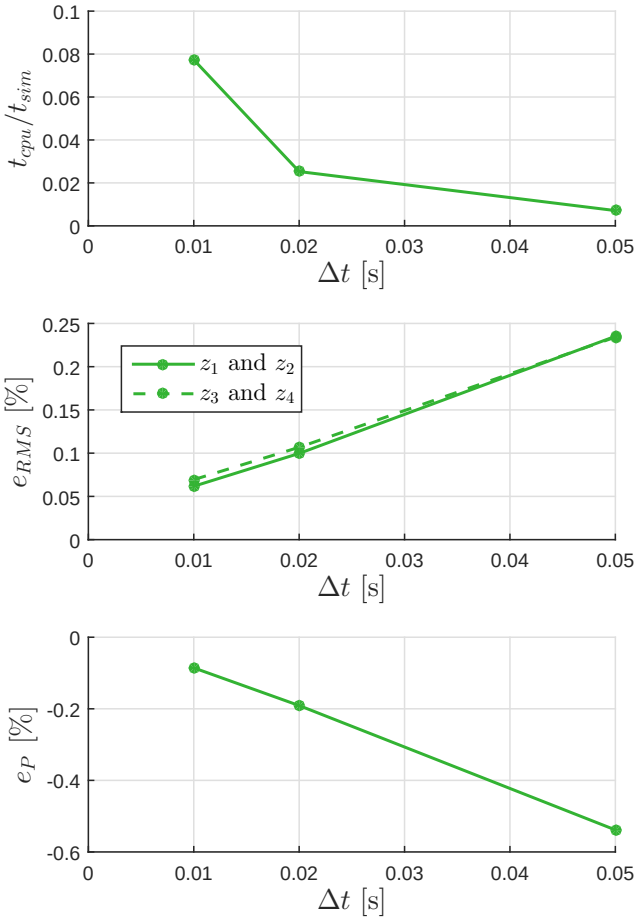

Figure 6.23: Computation time (top graph) and accuracy (middle and bottom graph) of RK2 simulations with different time steps, for the array of four cylindrical HPAs, in a 100-s wave input generated from a JONSWAP spectrum with $H_{m_0} = 2$m, $T_p = 12$s and $\gamma = 3.3$. Results are averaged over the range of k_{pto} values shown in Fig. 6.13.

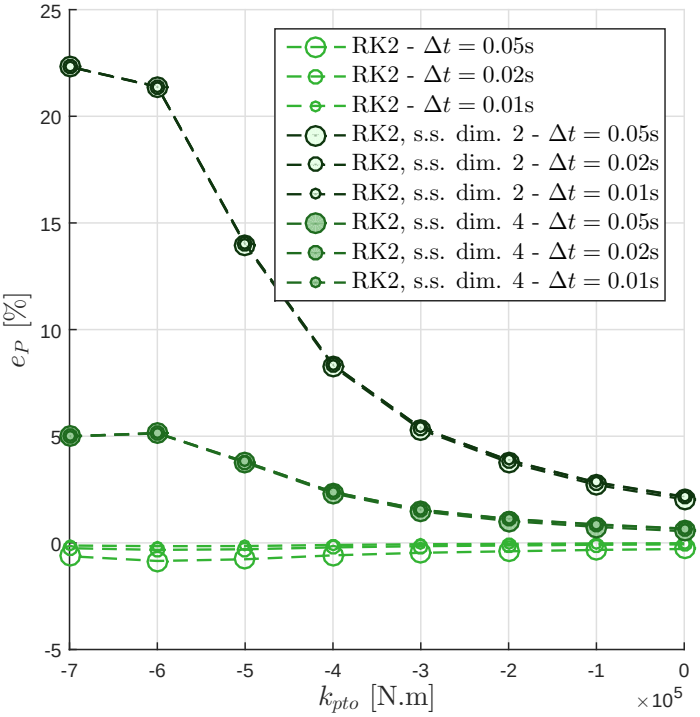

Figure 6.24: Error in average absorbed power from RK2 simulation results, using several different time steps and state-space approximations, over a range of k_{pto} values (b_{pto} is set to b^*_{pto}), for the array of four cylindrical HPAs, in a 100-s wave input generated from a JONSWAP spectrum with $H_{m_0} = 2$m, $T_p = 12$s and $\gamma = 3.3$.

solutions for z_1 and z_2 are identical to each other, and the solutions for z_3 and z_4 are identical to each other as well. Therefore, it is sufficient to visualise the solution for z_1 and z_3 only. In the case where $k_{pto} = 0$, as seen in Fig. 6.25a, each device simply follows the waves, and it is barely possible to visually detect any difference between the solution obtained with the HB method, that obtained with the RK2 method using full convolution summation, and those obtained using RK2 with the state-space approximations. In contrast, when k_{pto} is set to k^*_{pto}, as seen in Fig. 6.25b, the motion of each device is significantly amplified. This time, while the RK2 solution, using the full convolution, remains virtually identical to the HB solution, the RK2 simulations, using the two state-space approximations, present visible inaccuracies.

As yet, the author of this thesis has no definitive explanation to account for the increase in relative errors, when the WEC approaches optimal control conditions. It could be interesting to see if such results extend to other devices and state-space approximation techniques, but the focus of this thesis is on the simulation method, rather than on the modelling itself. The beginning of an answer might be the fact that, under optimal or close-to-optimal power-maximising WEC control, the control forces tend to cancel the hydrostatic terms [116], thus making the velocity-dependent terms, such as radiation forces, of primary importance in the resonant WEC dynamics. Thus, under optimal or close-to-optimal control conditions, the simulation results may be significantly more sensitive to any modelling error in the velocity-dependent terms, including radiation forces.

In terms of computational performance, both state-space approximation techniques yield a significant reduction in the RK2 computation time; for $\Delta t = 0.01$s, the two state-space approximations allow for approximately 20 times faster simulations than with the full convolution calculation. However, RK2 simulations, with both state-space approximation techniques, remain significantly slower than the HB method, between 2 times slower if a coarse time step of $\Delta t = 0.05$s is employed, and 10 times slower with $\Delta t = 0.01$s.

The HB method, in contrast, has a smaller computation time, while ideally preserving the solution accuracy. It can be seen, in Fig. 6.26, that there is little difference between the computational efficiency of the HB method, run with the three different initialisation strategies: Although the sensitivity-based strategy does modestly reduce the average number of iterations, this benefit is partly offset by the cost of solving the sensitivity equation.

Also, note that the dimension of the radiation state vector $\mathbf{x}_R$ is $4 \times 4 \times D_R$, as seen in Section 6.2.3, and that the physical state vector is of size 8 (for the four position and velocity values). Therefore, the size of the complete state vector for RK2 simulations is $8 + 16 \times 2 = 40$ with $D_R = 2$, and $8 + 16 \times 4 = 72$ (nearly twice as large) for $D_R = 4$. If the cost of each RK2 iteration is assumed to be roughly proportional to the square of the state vector size, one could expect an almost fourfold increase in computation time, between $D_R = 2$ and $D_R = 4$. However, examining Fig. 6.26, the difference in computation time between the two approximations seems modest, of the order of 10%. This is because, when the convolution term is absent from the calculations, the computational cost of RK2 simulations is dominated by the cost of executing a loop over the large number of RK2 iterations, rather than by the cost of the individual operations carried out at each iteration. As a consequence, it is worth noting that little additional computational benefit can be expected from reducing the size of the radiation state vector. Conversely, increasing the size of the state vector, by increasing the order of the state-space approximation, may improve the result accuracy, with little additional overhead.

6.4.4 ISWEC device

For the ISWEC device, similarly to the spherical HPA, convergence issues were observed under a small number of PTO parameter values (with large reactive control terms and low damping values), when the Newton method was used to solve the HB equation. However, using the trust-region dogleg algorithm, instead of the simple Newton method, allowed the HB method to converge for almost all the PTO settings considered. The only exception occurred for $k_{pto} = 1.2 \times 10^5$ and

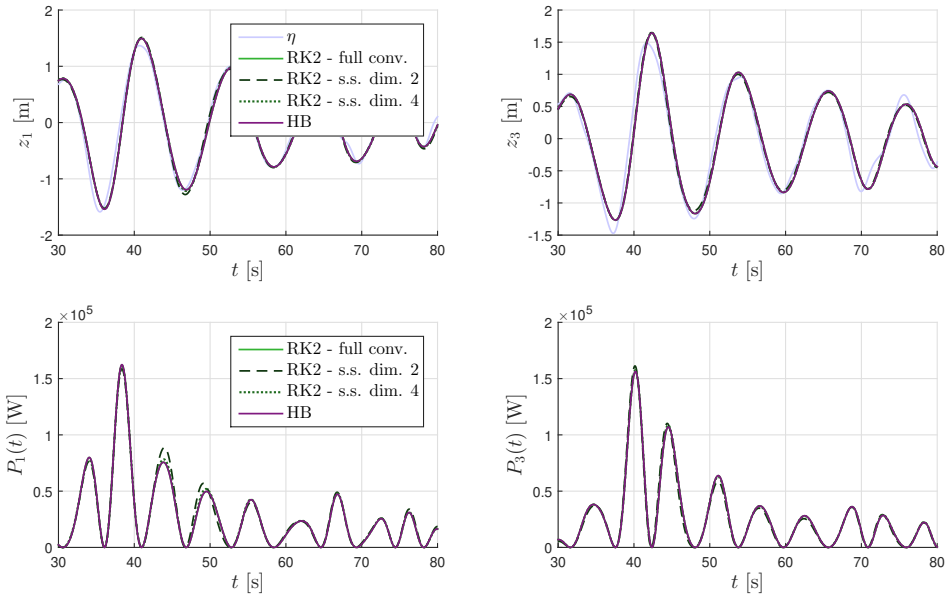

(a) $b_{pto} = b^*_{pto}, k_{pto} = 0$

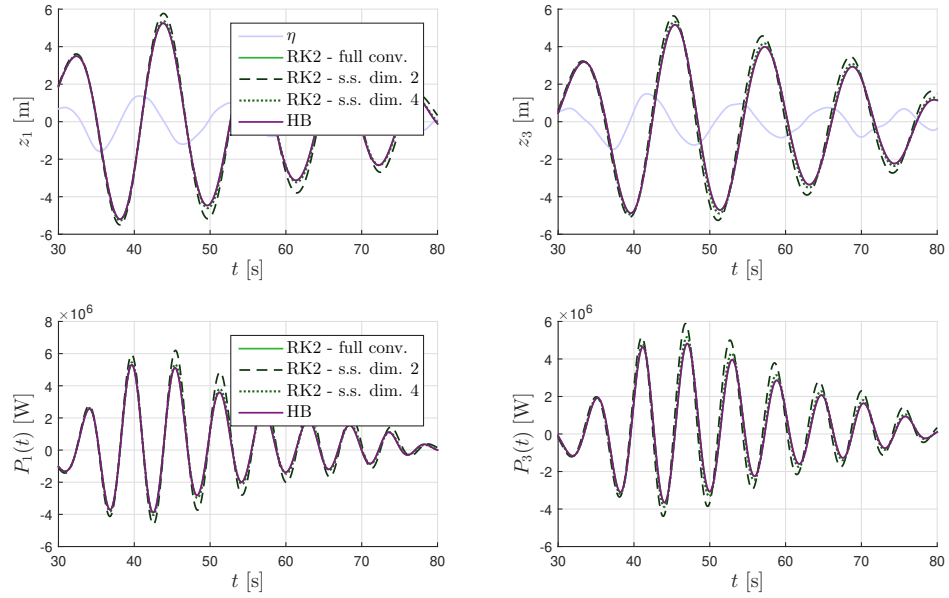

(b) $b_{pto} = b^*_{pto}, k_{pto} = k^*_{pto}$

Figure 6.25: Example of solution trajectories in terms of position and instantaneous power for the array of four cylindrical HPAs, off-resonance and in resonant conditions, obtained from the HB method, RK2 with a full convolution calculation, and RK2 with state-space radiation approximations using $D_R = 2$ and $D_R = 4$. The time series are generated from a JONSWAP spectrum with $H_{m_0} = 2$m, $T_p = 12$s and $\gamma = 3.3$.

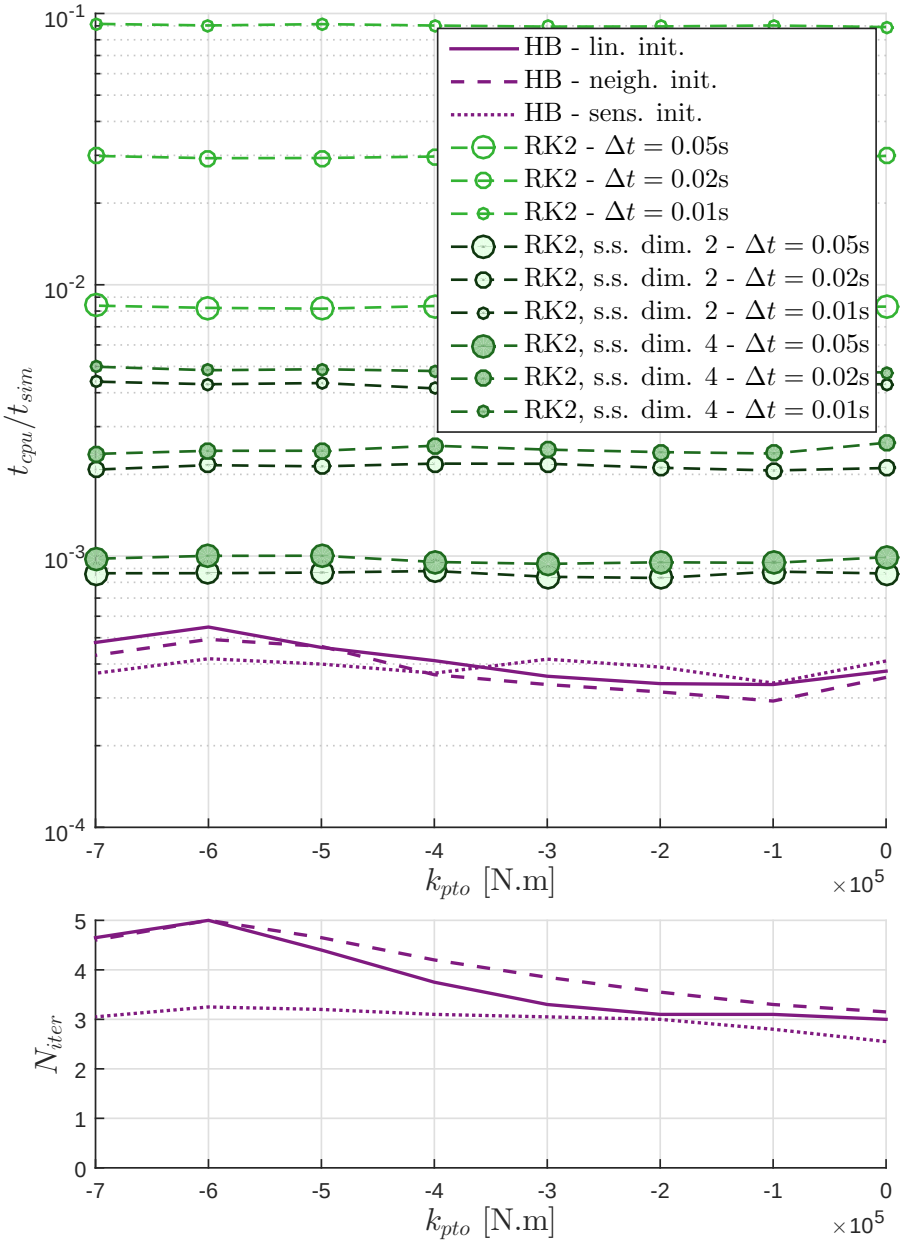

Figure 6.26: Computation time per second of the simulated signal (top graph) using the HB method with three different initialisation methods, and RK2 with different time steps (from the largest to the smallest marker size: Δt =0.05s, 0.02s, 0.01s, 0.005s, 0.002s), for the array of four cylindrical HPAs, in a 100-s wave input generated from a JONSWAP spectrum with $H_{m_0} = 2$m, $T_p = 12$s and $\gamma = 3.3$. The bottom graph shows the number of HB iterations for the three different initialisation strategies.
All computation times are obtained from a Matlab implementation, run on a 3.50 GHz, 8-core Intel® processor.

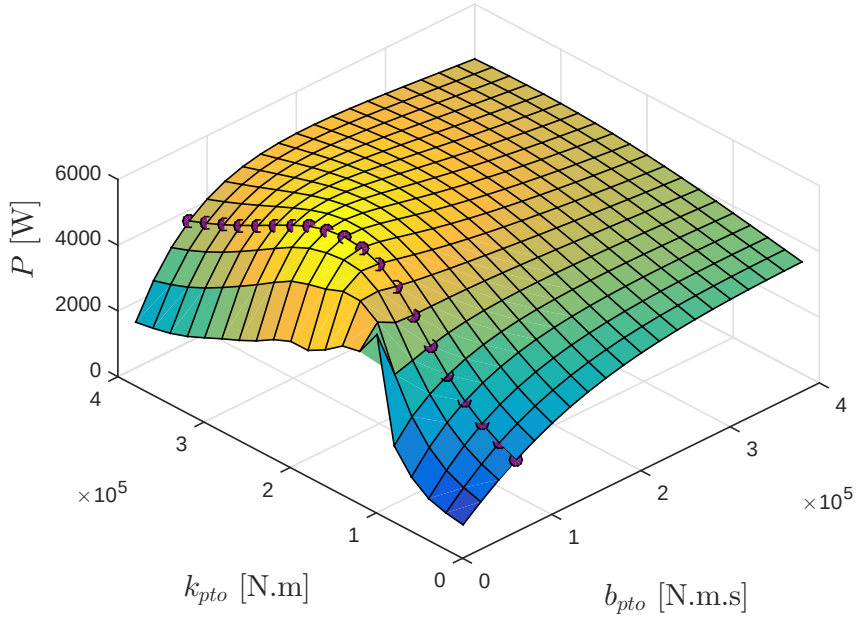

Figure 6.27: Average absorbed power in a wide range of (k_{pto}, b_{pto}) parameters, for the ISWEC device, in a 100-s wave input generated from a JONSWAP spectrum with $H_{m_0} = 1$m, $T_p = 7$s and $\gamma = 2$.

the smallest b_{pto} value, for which the HB method with the neighbour-based initialisation did not converge, which illustrates the sensitivity of the HB method to the choice of initial solution.

Fig. 6.27 shows the absorbed power for the range of PTO settings considered, with a clearly identifiable optimal setting for k_{pto} and c_{pto}. Note that the ISWEC device has a third tunable PTO parameter, namely the gyroscope rotational speed $\dot{\varphi}_{pto}$. However, such a possibility is not investigated in this chapter, and $\dot{\varphi}_{pto}$ is simply set to its maximum allowed value of 1000 rpm [13]. A more detailed comparison of HB and RK2 results is carried out in the range of settings represented with thick purple dots in Fig. 6.27

Similarly to the results of the spherical HPA, differences between RK2 and HB results are smaller than for the flap-type WEC, as can be seen in Fig. 6.28. Measuring the relative error in solution trajectories and in absorbed power, as shown in Fig. 6.28, the RK2 results seem to tend towards the HB results, when the integration time step tends to zero. However, as in the case of the spherical HPA, a close look at the middle graph of Fig. 6.28 suggests that some small residual error may remain between the HB and RK2 trajectories, even with further reduction in Δt. Such a residual error was found to be due to small inaccuracies in the HB solution, which disappear as f_c is increased. However, such inaccuracies are small enough to be acceptable, and thus do not justify increasing f_c.

The computational performance of the HB and RK2 solution methods is investigated in Fig. 6.30. As far as the HB technique is concerned, the computation cost is between 2 and 3 times larger than for the spherical HPA, due to the additional degree of freedom (the average number of Newton iterations is similar to that observed for the spherical HPA). Both the neighbour-based and sensitivity-based initialisation strategies bring a significant improvement (approximately 30%) in the HB computational performance, for large k_{pto} values. The computational gain, with respect to RK2 simulation, although more modest than for the flap-type WEC and spherical HPA, remains significant, between 4 times faster (for a coarse 0.05 RK2 time step) and 700 times faster (for a

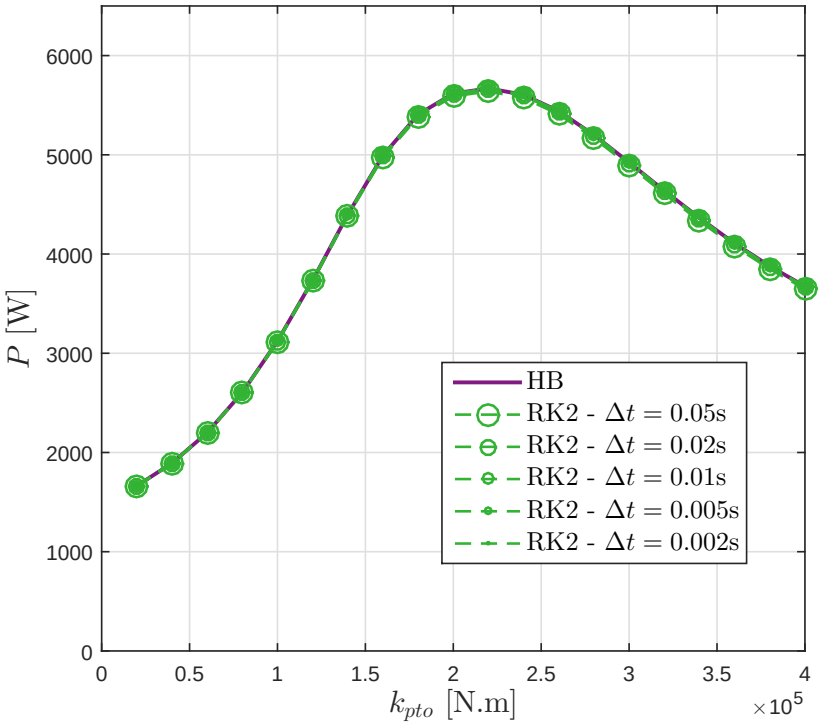

Figure 6.28: Absorbed power from simulation results, using the HB method and RK2 integration with several different time steps, over a range of k_{pto} values (b_{pto} is set to b^*_{pto}), for the ISWEC device, in a 100-s wave input generated from a JONSWAP spectrum with $H_{m_0} = 1$m, $T_p = 7$s and $\gamma = 2$.

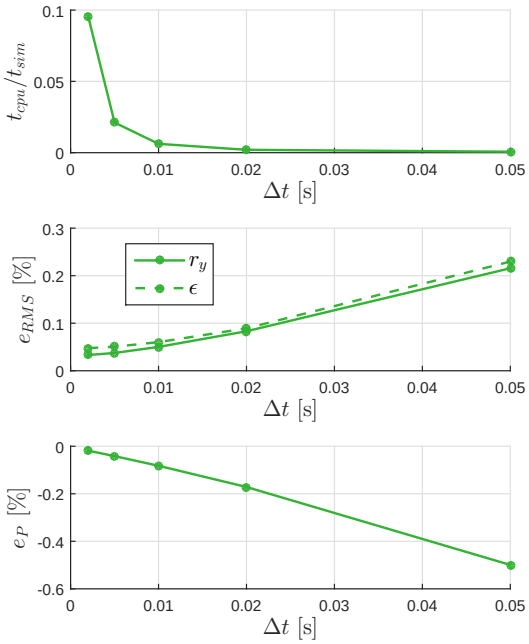

Figure 6.29: Computation time (top graph) and accuracy (middle and bottom graph) of RK2 simulations with different time steps, for the ISWEC device, in a 100-s wave input generated from a JONSWAP spectrum with $H_{m_0} = 1$m, $T_p = 7$s and $\gamma = 2$. Results are averaged over the range of k_{pto} values shown in Fig. 6.28.

refined 0.002s time step).

6.5 Ex-post validation of the HB settings

The results presented in Section 6.4 clearly confirm the numerical accuracy of the HB technique, and its appealing computational speed, compared to RK2 integration. In particular, even in resonant conditions, the cut-off frequency f_c allows the HB solution to be *at least* as accurate as a RK2 method with a refined time step of the order of 0.002s - for which RK2 is particularly slow. Therefore, the f_c values initially chosen (0.5Hz for the flap-type WEC and the array of four cylindrical HPAs; 0.8Hz for the spherical HPA and the ISWEC model) can be maintained.

Concerning the signal duration T, which governs the spectrum discretisation, it must be ensured that, in resonant conditions, the choice initially made in Section 6.3 remains pertinent, i.e. still produces accurate power estimates. Therefore, for each device, with the optimal PTO parameters (k^*_{pto}, b^*_{pto}), HB simulations are run in 20 different HDA-generated wave inputs, over a range of T settings. The results, in terms of average power absorption, are plotted in Fig. 6.31 where, similarly to Figs. 6.7 to 6.10, power is normalised by the value obtained for the largest T.

Fig. 6.31 indicates that, for the flap-type WEC, the spherical HPA and the array of four cylindrical HPAs, the average power falls within 1% of the reference value at $T = 100$s, hence confirming the choice initially made for T. Concerning the ISWEC device, it is found that $T = 100$s is slightly too short for accurate power estimates. Therefore, for the ISWEC device, the signal duration is increased to $T = 150$s.

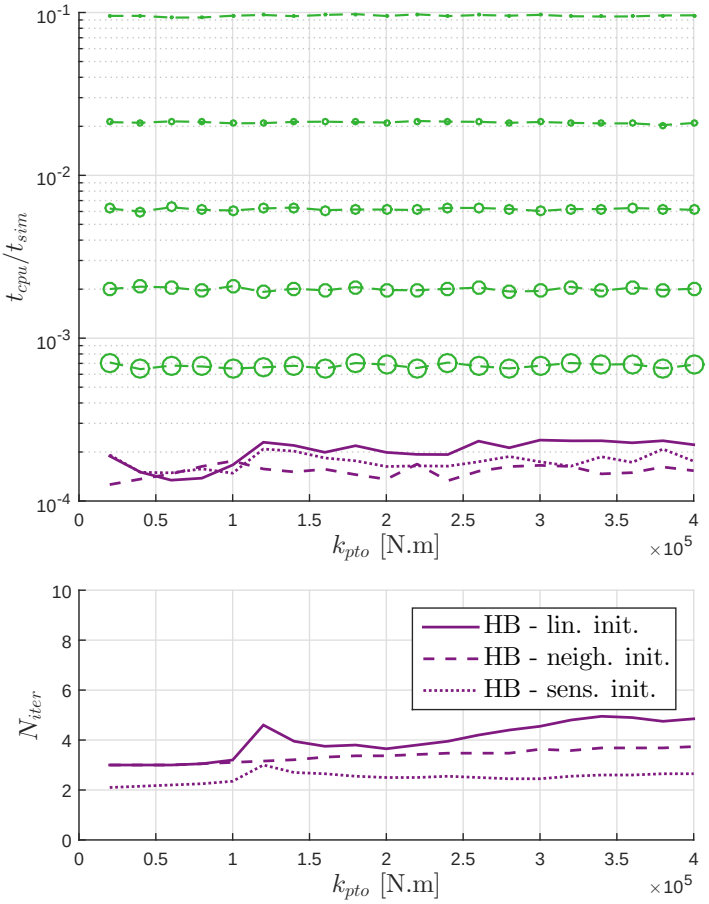

Figure 6.30: Computation time per second of the simulated signal (top graph) using the HB method with three different initialisation methods, and RK2 integration with different time steps (from the largest to the smallest marker size: Δt =0.05s, 0.02s, 0.01s, 0.005s, 0.002s), for the ISWEC device, in a 100-s wave input generated from a JONSWAP spectrum with $H_{m_0} = 1$m, $T_p = 7$s and $\gamma = 2$. The bottom graph shows the number of HB iterations for the three different initialisation strategies.
All computation times are obtained from a Matlab implementation, run on a 3.50 GHz, 8-core Intel® processor.

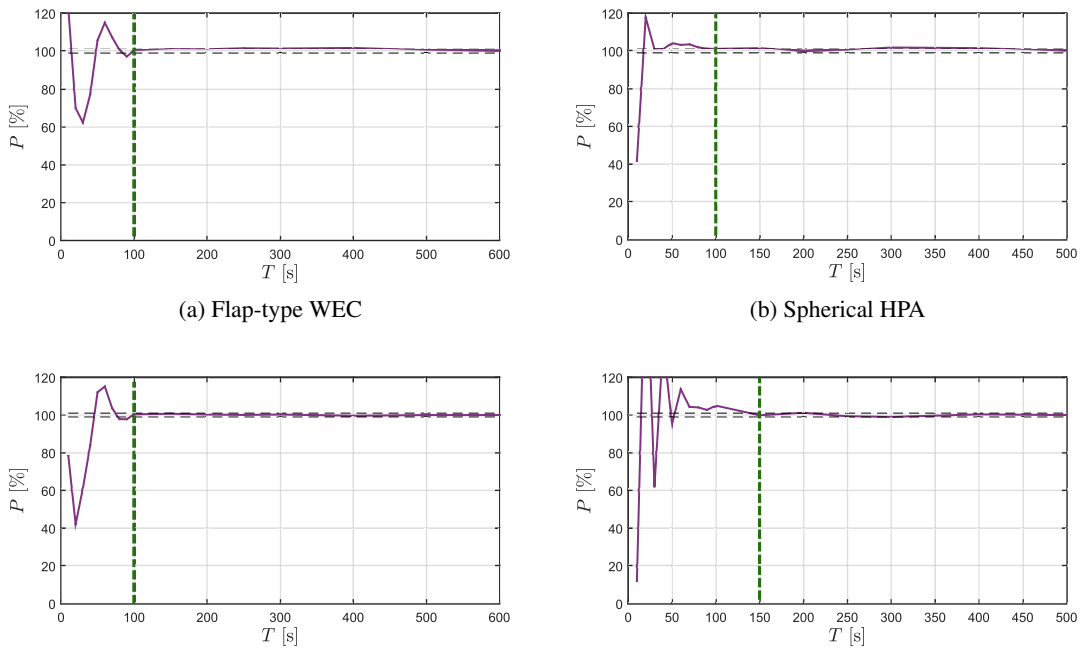

(a) Flap-type WEC

(b) Spherical HPA

(c) Array of four cylindrical HPAs

(d) ISWEC device

Figure 6.31: Effect of the simulation duration onto WEC power assessment for the four WEC case studies

6.6 Should HDA or HRA be used to generate the incident wave signals?

Previously in this chapter, only the HDA wave generation approach was used to simulate the incoming Gaussian wave elevation. In this section, based on the four WEC models identified, the validity of such an approach is discussed. It has been seen in Chapter 3 that, amongst harmonic superposition methods, only HRA allows for a realistic representation of the target Gaussian wave statistics; with HRA, every generated time-series has a variance which differs from its long-term statistical average, as observed by sampling real sea waves over short time windows. In contrast, the HDA time series all have the same variance and, more generally, statistics which present an unrealistically small variability across different generated time-series. However, as discussed in Chapter 3, using HDA for wave input generation can yield accurate statistics, such as, for example, mean power absorption or maximum amplitude, using fewer simulations than HRA, *provided that HDA results are unbiased with respect to HRA results*. Therefore, if the aim of the simulations is to quickly obtain accurate estimates of some particular statistics, HDA can be advantageous. Nevertheless, with a non-linear WEC model, it is difficult to know *a priori* if HDA results are unbiased.

In this section, a short study is carried out to examine the relative benefits of HRA and HDA. To that end, for each WEC in its design sea state, using the HB settings determined in Section 6.3 and with the optimal choice of control parameters (k^*_{pto}, b^*_{pto}), 1000 HB simulations are run[7], using both HRA and HDA to generate each $T-$length wave signal independently, where T is set to 100s, except for the ISWEC device, for which $T = 150$s. The average estimated power $\bar{P}$, and the standard deviation σ_P of the power estimate, are both calculated from the 1000 samples. σ_P quantifies how much the power, estimated from a given randomly-generated wave input of length T, fluctuates around its average.

[7]Given the high efficiency of the method, the 1000 simulations do not take more than three minutes for the array of 4 HPAs, which is the most unfavourable case

Table 6.2: Variability of power estimates using HDA and HDA, for the four WEC systems, using the HB settings determined in Section 6.3. From top to bottom: average power $\bar{P}$, standard deviation of $\bar{P}$, and number of realisations necessary to ensure that the 95% confidence interval has a half-width smaller than 5% (resp. 2.5%) of $\bar{P}$.

		Flap	**Sphere**	**Array**	**ISWEC**
$\bar{P}$ [W]	*HRA*	5.51×10^5	1.14×10^4	5.88×10^5	5.14×10^3
	HDA	5.55×10^5	1.15×10^4	5.94×10^5	5.19×10^3
σ_P [W]	*HRA*	2.35×10^5	3.33×10^3	2.90×10^5	1.65×10^3
	HDA	1.14×10^4	4.95×10^2	8.61×10^3	3.90×10^2
$N_{\pm 5\%}$	*HRA*	280	130	370	150
	HDA	< 10	< 10	< 10	< 10
$N_{\pm 2.5\%}$	*HRA*	1120	520	1500	630
	HDA	< 10	12	< 10	35

For each WEC model, Table 6.2 compares $\bar{P}$ and σ_P obtained with HDA and HRA. It is seen that, in the four case studies, using HDA does not introduce any significant bias in the power estimate $\bar{P}$. However, the standard deviation σ_P of the estimate is between 4 times larger (in the case of the ISWEC device) and 30 times larger (in the case of the array) using HRA, compared to using HDA to generate the time series.

The larger variance of the power estimates using HRA implies that more simulations are necessary, to achieve power assessment with a required level of certainty. To quantify such an effect, the number of simulations, necessary to ensure that the 95% confidence interval of the power estimate is within a 5% (resp. 2.5%) margin of the estimated average, is calculated. Indeed, for a number of simulations N_{sim} large enough (typically > 10), the distribution of $\bar{P}_{N_{sim}}$, obtained from N_{sim} simulations, approaches a normal distribution (from the Central Limit Theorem, see Chapter 2 and references therein), with mean $\bar{P}$ (the actual average power) and standard deviation $\frac{\sigma_P}{\sqrt{N_{sim}}}$. The 95% confidence interval for any N_{sim} can be calculated as $[\bar{P} \pm z^* \frac{\sigma_P}{\sqrt{N_{sim}}}]$, where z^* is the $(100-95)/2 = 2.5\%$ critical value for the standard normal distribution. Hence, it is possible to find $N_{5\%}$ (resp. $N_{2.5\%}$) such that the 95% confidence interval falls within 5% (resp. 2.5%) of the estimated average. $N_{5\%}$ and $N_{2.5\%}$ are indicated in Table 6.2. Note that, for small values of N_{sim}, the normality assumption for the distribution of $\bar{P}$ does not hold; therefore if $[\bar{P} \pm z^* \frac{\sigma_P}{\sqrt{N_{sim}}}]$ with $N_{sim} = 10$ is smaller than 5% (resp. 2.5%) of $\bar{P}$, Table 6.2 simply indicates that $N_{5\%}$ (resp. $N_{2.5\%}$) is < 10.

The difference between HDA and HRA is significant, and most particularly for the array case; while less than ten 100-s simulations are necessary with HDA, to have a 95% confidence interval within $\pm 2.5\%$ of the estimated value, 1500 simulations would be necessary with HRA. From Table 6.2, and as far as power calculations are concerned, HDA can be safely employed, in order to avoid resorting to a large number of simulations. If statistical quantities other than power absorption were of interest, a similar investigation should be carried out to ensure that HDA results are unbiased with respect to HRA results.

Finally, it should be emphasised that the considerations, presented above in this section, are not entirely specific to the HB simulation method; the question of the length and number of simulations, combined with the choice of time-series generation method, is also crucial when using any other numerical simulation technique.

6.7 Summary

Four WEC models, involving a variety of non-linear modelling terms, number and nature of degrees of freedom, and typical dynamics, have been introduced in Section 6.2, in order to assess the practical value and highlight the challenges of the HB simulation method.

An efficient use of the HB method necessitates sensible settings for the two parameters, f_c and T, of the technique. While f_c primarily governs the accuracy of the non-linear solution trajectory, obtained in a given incident wave signal, T dictates the spectrum discretisation, and thus the statistical accuracy of the methodology outlined in Section 5.7, whereby long runs are replaced with a number of shorter ones with duration T. T and f_c must be chosen so as to ensure a satisfactory solution accuracy and statistical accuracy, typically in terms of power estimates, while limiting, as much as possible, the HB computation cost, as exemplified in Section 6.3. Relatively short simulations, of the order of 100s, are found to yield accurate power estimates for all four case studies.

The proposed approach for tuning the HB settings (f_c and T) is relatively simple, and based on some *a priori* assumptions about the tuning of some parameters. This is not unreasonable because, at the stage of employing IDE models for optimisation or power assessment, the fundamental design of the WEC and typical operating conditions should be, at least approximately, understood. A possible drawback is that, when the HB method is used to further investigate the WEC design and control parameters, the settings initially chosen may not be appropriate for the new WEC dynamics, as modified for example through an optimisation procedure. However, as shown in Section 6.5, it is not difficult to carry out a quick *ex-post* validation of the HB settings initially chosen. As a general rule, as with any numerical method, a sensible route is to check the sensitivity of the results to the simulation settings. Using the HB method, such a step requires relatively little computational effort, given the method efficiency.

Unsurprisingly, WECs with faster dynamics, and in sea states with more high-frequency content, necessitate a higher cut-off frequency f_c; in such cases, $f_c = 0.8$Hz seems to be a sensible choice. For sea states with slower waves, and WECs with slower dynamics, $f_c = 0.5$Hz is sufficient to provide simulation results more accurate than RK2 numerical integration with a refined time step of 0.002s. In contrast, concerning T, from the range of WEC models employed here, and for the two different sea states considered, there does not seem to be any intuitive choice; for example, since the spherical HPA and the ISWEC device operate in a sea state with faster waves than the flap-type WEC and the array of 4 HPAs, it could have been expected that they would require a shorter simulation time T to produce accurate power estimates. Such a hypothesis is clearly not supported by empirical evidence since, to obtain accurate power estimates under reactive control, the ISWEC requires a longer simulation time than the other WEC systems. Overall, simulation lengths between 100 and 200s are probably an appropriate compromise, while shorter simulation lengths may produce significantly biased power estimates.

Section 6.4 validates both the accuracy of the HB method, and its significant practical value in terms of computational speed, in comparison to a RK2 time-domain numerical integration scheme. Depending on the RK2 time step, the HB method reduces the computation time per second of the simulated signal, by one to three orders of magnitude, while preserving a better solution accuracy than RK2 simulations with a time step of 0.002s. Throughout Section 6.4, it can also be seen that an appropriate choice of a HB starting guess can reduce the number of HB iterations, and hence the computation time. In particular, using the results of a previously-solved HB equation, with closely-related parameters, a satisfactory starting guess can be found (using either the 'neighbour-based' or 'sensitivity-based' initialisation approaches), which is generally advantageous, with respect to a linear initialisation. However, the latter approach has the merit that it does not depend on previously-solved HB problems, so that entirely dissimilar and unrelated HB problems can be solved one after the other. In contrast, the sensitivity-based, or neighbour-based, initialisation approaches assume that the solution of consecutive HB problems are close to each other which implies, in particular, that consecutive HB simulations are run using the same set of random phases (if HDA is employed) or amplitudes (if HRA is employed).

The array case study illustrates the possible dangers of using a state-space approximation for the radiation memory terms; while, with respect to the full convolution calculation, the computational gains are approximately one order of magnitude (which is consistent with the findings of [96]), the errors introduced by the model approximation seem to be larger when the WECs are

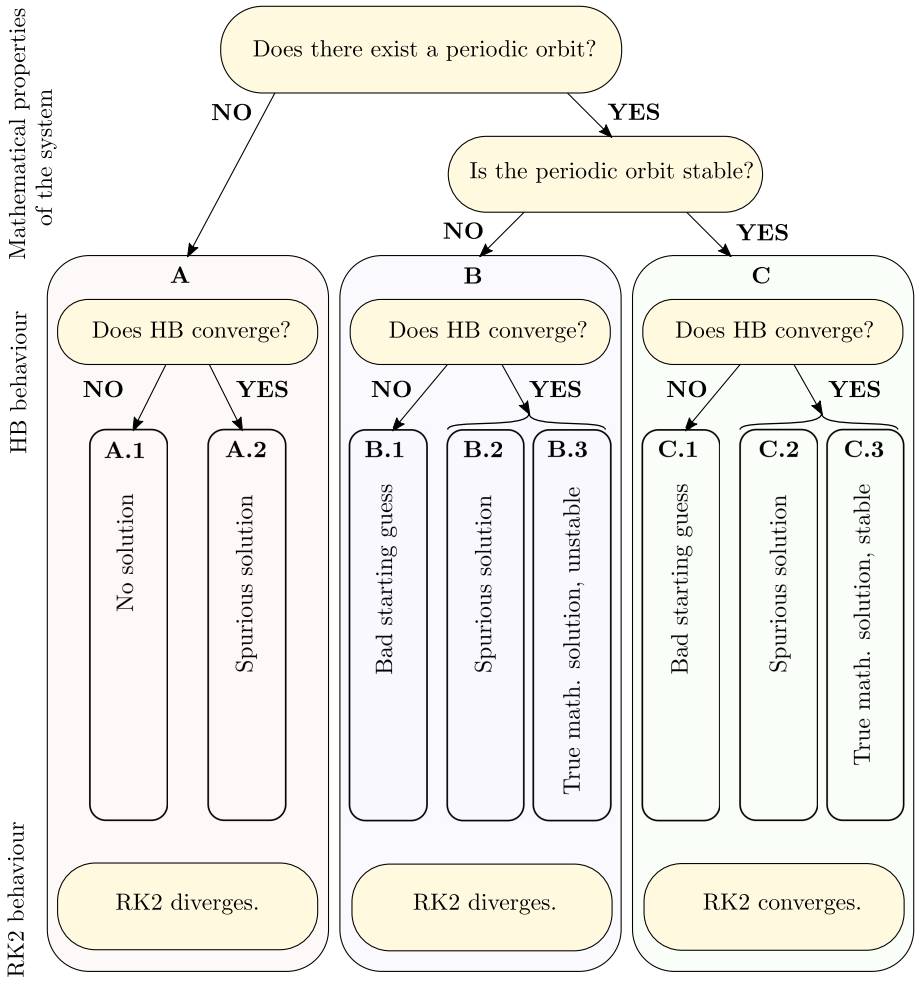

Figure 6.32: Possible numerical behaviours of the HB and RK2 simulation methods, for different scenarios concerning the mathematical properties of the WEC model

brought to resonant conditions under reactive control.

Although the bulk of the results presented in Section 6.4 supports the efficiency and accuracy claims of the HB simulation approach, the inability of the HB root-finding algorithm to find a solution, observed in several PTO configurations for the spherical HPA, and to a lesser extent for the ISWEC device, highlights convergence issues which are specific to the HB method. More specifically, a system represented by Eq. (4.90) is a non-autonomous, non-linear system. For such a system, the existence of a periodic, steady-state physical solution, for the WEC dynamics in a periodic wave input signal, can be analysed in terms of the existence (or otherwise) of *stable, periodic orbits* [97]. Fig. 6.32 schematically identifies possible configurations, in terms of the mathematical properties of *the system* represented by Eq. (4.90), for *a given periodic wave input*[8]. For each of those scenarios, it is shown that the HB method may have several types of behaviour, which are detailed in the following.

First, it must be emphasised that the HB method is known (see [149]) to sometimes converge to solutions, which are indeed an exact solution to the *discretised* residual equation (5.57), but are not close to any mathematical solution of the *exact* residual equation of Eq. (4.90); such solutions may occur in the PS version of the HB method, but *not* when the Galerkin version is employed (at least if the integrals in Eq. (5.53), to obtain the frequency-domain representation of the non-linear terms, are accurately computed). Such spurious solutions (as termed in Fig. 6.32) may

[8]With a linear system, instead of a non-linear one, the stability properties of the system would not depend on the specific input considered [97]

exist, whether or not the exact residual equation admits a mathematical solution. Furthermore, unlike mathematically-correct solutions of the residual equation, of which the Fourier coefficients quickly vanish for higher-order expansions (as detailed in Section 5.5), spurious solutions usually show large variations when modifying the frequency discretisation [149], and may even disappear when f_c is modified, or when the HB algorithm starts from a different initial guess. Therefore, in case there should be any doubt regarding the validity of HB results, it is not difficult to diagnose the spuriousness of the solution. Throughout the course of this PhD, only one example was encountered, when carrying out the work presented in [153], for a monochromatic wave input. The spurious solution disappeared with a small change in f_c.

Having addressed the pathological case of spurious solutions, it is possible to focus on the HB method behaviour for the vast majority of situations. To that end, the existence and nature of mathematical solutions to the residual equation should be first discussed. It may happen that the system of Eq. (4.90) (the *exact* residual equation) does not admit any periodic orbit, for the chosen periodic wave input (Scenario A in Fig. 6.32). This may be the case, in particular, when dissipative modelling terms, such as radiation damping, PTO damping and viscous forces, are too small. In such a scenario, the HB method generally does not converge to any solution (Case A.1); this has been illustrated with the spherical HPA example with the effect that, for some large PTO reactive terms, and low PTO damping, the HB method did not converge to any solution within the allowed numbed of iterations. Running a time-domain numerical simulation with the same wave input, e.g. using RK2, it is typically observed that the system trajectory diverges exponentially, as seen in Fig. 6.20.

Another interesting scenario may occur, where Eq. (4.90) *does* have an exact, periodic mathematical solution, which is *not* a physical solution, in the sense that the corresponding trajectory is unstable, labelled as Scenario B in Fig. 6.32. In such a case, the HB algorithm may either fail to find this mathematical solution (case B.1) (because of an initial guess outside the basin of attraction of the solution), but it may also converge to the solution (case B.3); the existence of unstable, and yet mathematically correct HB solutions [135], is well known in non-linear vibration analysis [149]. Such a solution may be approximated and visualised using the HB method, but it could never be observed using a RK2 simulation scheme (because any infinitesimal deviation from the trajectory would make the system diverge from it), and even less so in any physical experiment. Case B.3 is illustrated in Fig. 6.33 for the array of 4 cylindrical HPAs. Setting k_{pto} to a negative value, with magnitude larger than the hydrostatic stiffness s_h, the *total* stiffness of each device is negative, which would not yield any physically realistic solution. Yet, the HB algorithm converges to a solution, plotted in Fig. 6.33, which is found to be robust to changes in the HB settings (f_c in particular). In contrast, the trajectory obtained from the RK2 simulation diverges rapidly away from the origin. Non-physical solutions may be identified using, for example, Floquet stability analysis, which can be embedded within a HB framework [135].

When the WEC mathematical model is physically consistent (which is not the case in the above example with a negative total stiffness term), intuitively it is expected that the system of Eq. (4.90) admits a periodic orbit, and that this orbit is stable (Scenario C), in the sense that, in a time-domain numerical simulation or in a physical experiment, the system will gradually converge to the periodic solution as the transient response fades out. In Scenario C, the convergence of the HB algorithm, regardless of the starting guess, can unfortunately not be guaranteed. An example was provided by the ISWEC device model in Section 6.4, for which, for a given choice of k_{pto}, b_{pto} values, the HB method failed to converge when initialised using the 'neighbour-based' approach, but did find the solution when initialised using the linearised model, or the sensitivity-based approach.

Finally, the system of Eq. (4.90) may have several periodic solutions, comprising any combination of stable and unstable orbits. In such a case, while traditional time-domain simulations cannot detect the existence of those mutliple solutions, the HB method can be combined with continuation techniques [151] in order to track bifurcations (i.e. values in the model parameters, for which several possible solutions begin to emerge) [135]. For the sake of simplicity, such a case is

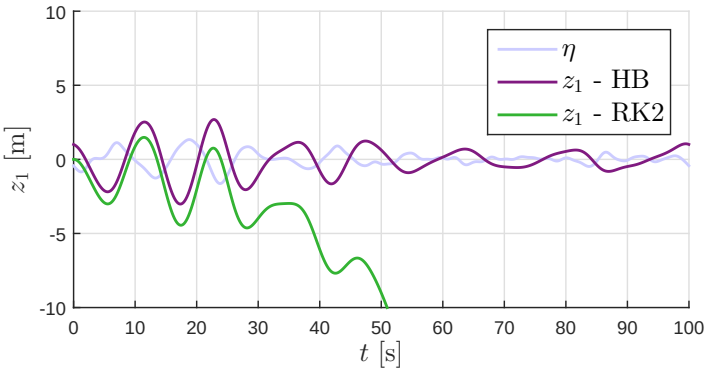

Figure 6.33: Example of unstable solution obtained using the HB method, for the array of four cylindrical HPAs, with $k_{pto} = -8 \times 10^5$ and $b_{pto} = 1.6 \times 10^5$, in a wave input generated from a JONSWAP spectrum with $H_{m_0} = 2$m, $T_p = 12$s and $\gamma = 3.3$

not detailed in Fig. 6.32.

In practice, it is difficult to know, in advance, whether or not the system considered in Eq. (4.90) has stable mathematical solutions. Convergence of the HB algorithm (A.2, B.2, B.3, C.2, C.3) does not necessarily mean that an actual physical solution has been found. In order to discriminate between exact mathematical solutions and spurious solutions, a possibility is to vary slightly the HB settings and to check if a similar solution is still found. In order to ascertain if the calculated solution is physically meaningful, stability analysis could be carried out. Conversely, there can be several possible causes for the HB method not to converge (A.1, B.1, C.1). In cases B.1 and C.1, a better choice of initial condition can be used, or a continuation technique [151] may be employed. Perhaps more pragmatically, since problematic cases seem to only represent a small fraction of the scenarios encountered in practice, running a RK2 simulation, *only* in the problematic wave inputs, could provide useful insight, as to whether the actual situation is A.1, B.1 or C.1.

In summary, 'common sense' recommendations should apply to the HB method, just as well as to other simulation techniques; when simulations are carried out to explore a broad range of configurations (such as design parameters, different sea states, or tunable control parameters), the presence of outliers, or abrupt changes in the simulation results between two neighbouring configurations, should always catch the researcher's or engineer's attention, and trigger further investigation. Conversely, continuity of the results across the range of configurations explored, and robustness of the results to changes in the HB settings (f_c, T, choice of initialisation method) should provide confidence in the mathematical and physical relevance of the simulation results.

Chapter 7

Parametric optimisation of a wave energy converter using the harmonic balance method

7.1 Introduction

Chapter 6 provides a validation of the HB method, for the numerical simulation of non-linear WEC models, in the sense that HB provides steady-state solutions with superior accuracy, with respect to standard RK2 methods with a usual 0.01s time-step, while being typically between one and two orders of magnitude faster. The general methodology associated with the use of the HB method, and which consists of simulating many, relatively short, simulations, as opposed to one, long simulation, has been shown to provide reliable power estimates. Therefore, it can already be stated that the HB method is a valuable addition to the range of techniques, available for the numerical simulation of non-linear WEC models.

However, the author feels that this thesis would not be complete, without at least one example demonstrating how the proposed HB technique can be advantageously employed, for a practical task requiring a large number of simulations. Hence, in this short chapter, a methodology is outlined, for the parametric optimisation of wave energy device models, using the HB method. As a case study, the PTO parameters of the ISWEC device, presented in Section 6.2.4, are optimised over a wide range of sea states representative of the ISWEC design location, off the island of Pantelleria [13]. The ISWEC has three PTO parameters, namely the regulated gyroscope rotational speed $\dot{\varphi}_{pto}$, a damping coefficient b_{pto}, and a stiffness coefficient k_{pto}. The benefits of employing the HB approach are discussed.

Chapter organisation

- Section 7.2 introduces the basis of a parametric optimisation methodology, employing the HB framework;
- Section 7.3 presents the chosen numerical case study, which consists of tuning the ISWEC PTO parameters;
- In Section 7.4, the outcomes and salient points of this chapter are summarised and discussed.

7.2 Parametric optimisation using the harmonic balance method

7.2.1 Parametric optimisation problem for IDE WEC models within the HB framework

In this chapter, parametric WEC models in the form of Eq. (5.91) are considered. The WEC model depends on N_α parameters, and is assumed to be continuously differentiable with respect to each parameter. The aim, in parametric optimisation, is to minimise a given cost function, noted f, which depends on the system variables $\mathbf{x}$, and possibly on α:

$$\begin{aligned} &\min_{\mathbf{x},\alpha} f(\mathbf{x},\alpha) \\ &\text{s.t. } \mathbf{r}\{\mathbf{x},\alpha,t\} = 0 \end{aligned} \tag{7.1}$$

where

$$\mathbf{r}\{\mathbf{x},\alpha,t\} := \mathcal{L}\{\mathbf{x},\alpha\} - \mathbf{n}\{\mathbf{x},t,\alpha\} - \mathbf{e}(t,\alpha) = \mathbf{0} \tag{7.2}$$

and, typically, f is specified in integral form:

$$f(\mathbf{x},\alpha) := \int_{t=0}^{T} g(\mathbf{x}(t),\dot{\mathbf{x}}(t),\alpha,t)\, dt \tag{7.3}$$

The residual equation (7.2) expresses the fact that the dynamical equation (5.91) must be satisfied at every instant. Assume, as in Chapters 5 and 6, that all inputs to the residual equation are periodic with period T, and that one wishes to minimise g (in Eq. (7.3)) over a period of the system steady-state trajectory. It is quite natural to reformulate the minimisation problem into a HB framework, assuming that all dynamical quantities in $\mathbf{x}$ are specified in terms of their Fourier expansion, following Eq. (5.25). Using Eq. (5.25), the cost function is reformulated as a function of $\hat{\mathbf{x}}$ and α:

$$f(\hat{\mathbf{x}},\alpha) := \int_{t=0}^{T} g(\Phi(t)\hat{\mathbf{x}},\Phi(t)\Omega\hat{\mathbf{x}},\alpha,t)\, dt \tag{7.4}$$

where Ω and $\Phi(t)$ are defined in Eqs. (5.28) and (5.24), respectively. Furthermore, the residual equation (7.2) is replaced with the HB equation. Considering the PS version of the HB method, Problem (7.1) is rewritten as follows:

$$\begin{aligned} &\min_{\hat{\mathbf{x}},\alpha} f(\hat{\mathbf{x}},\alpha) \\ &\text{s.t. } \mathbf{r}_{PS}(\hat{\mathbf{x}},\alpha) = \mathbf{0}_{\mathbb{R}^{DN_t}} \end{aligned} \tag{7.5}$$

where

$$\mathbf{r}_{PS}(\hat{\mathbf{x}},\alpha) = \Phi_{N_t}\mathbf{L}(\alpha)\hat{\mathbf{x}} - \mathbf{n}_{N_t}(\hat{\mathbf{x}},\alpha) - \Phi_{N_t}\hat{\mathbf{e}}(\alpha) \tag{7.6}$$

In the following, it is assumed that, for the range of parameters α considered, the system of Eq. (5.91), and hence the HB equation (7.6), have only one steady-state solution. Denote $\hat{\mathbf{x}}(\alpha)$ as the presumably unique solution of the residual equation $\mathbf{r}_{PS}(\hat{\mathbf{x}},\alpha) = 0$, for a choice of parameters α. Problem (7.1) can thus be recast as a minimisation problem, where the only variables to optimise are the components of α:

$$\min_{\alpha} f(\hat{\mathbf{x}}(\alpha),\alpha) \tag{7.7}$$

7.2.2 Gradient-based optimisation within the HB framework

If the number of parameters N_α is relatively small, typically one or two, an exhaustive search approach[1] may be employed to determine, approximately, a minimum for Problem (7.7), as was

[1] i.e. evaluating every possible PTO setting, using some discretisation of the parametric space

carried out throughout Chapter 6. However, such an approach may become intractable as N_α grows, and when the number of optimisation problems is large. For example, assuming $N_\alpha = 3$ (as will be the case in the example presented in this chapter), and assuming that each parametric dimension is discretised into 10 values, an exhaustive search approach would necessitate $10^3 = 1000$ cost function evaluations. Therefore, numerical optimisation algorithms, more powerful than the exhaustive search approach, should be used, with the aim of reducing the number of cost function evaluations.

In the present case, the cost function is assumed to be continuous and differentiable with respect to the optimisation variables. Hence, both gradient-based and gradient-free algorithms may be used. The relative benefits of gradient-free and gradient-based optimisation algorithms are discussed, and empirically investigated in [158]. Gradient-based techniques, because they use the gradient information to determine an appropriate search direction, generally converge using fewer iterations (and hence fewer cost function evaluations) than gradient-free optimisation. Furthermore, from the first-order optimality condition [146], the cost function gradient provides a clear stopping criterion, since a gradient sufficiently close to zero indicates that a local optimum has been found. However, gradient-based optimisation has the drawbacks that it is usually less straightforwardly implemented than gradient-free algorithms (for which the cost function evaluation is merely a black-box), and that there is no guarantee that the optimum found is global (while, in principle, gradient-free optimisation schemes should converge to a global optimum). In fact, methods combining a genetic algorithm (which is a global optimisation method), with a local search routine (such as gradient-based methods), are known as *memetic algorithms* and, for certain categories of problems, can produce solutions with better quality than genetic algorithms, at a significantly smaller computational cost [159], compared to simple genetic algorithms. In the remainder of this chapter, gradient-based WEC optimisation, taking advantage of the HB formalism, is investigated.

There exists a variety of gradient-based optimisation algorithms, see [146]. All of them share the same basic principle, whereby, at each iteration k of the algorithm:

1. The cost function at the current iterate, $f(\alpha^{(k)})$, is computed;
2. A search direction $\mathbf{d}^{(k)}$ is computed, using information from the cost function gradient;
3. A step length $l^{(k)}$ is determined so that $f(\alpha^{(k)} + l^{(k)}\mathbf{d}^{(k)}) < f(\alpha^{(k)})$;
4. The next iterate is calculated as $\alpha^{(k+1)} = \alpha^{(k)} + l^{(k)}\mathbf{d}^{(k)}$.

Gradient-based techniques mainly differ in the way to choose the search direction.

In the following, it is shown that, using the HB method and the sensitivity equation, the cost function and its derivative can be efficiently evaluated (which is at the core of any gradient-based optimisation algorithm). The cost function is evaluated by running the HB method; with the current parameters $\alpha^{(k)}$, the HB solution $\hat{\mathbf{x}}^{(k)} = \hat{\mathbf{x}}(\alpha^{(k)})$ is calculated as in Chapters 5 and 6, as well as the cost function $f(\hat{\mathbf{x}}^{(k)}, \alpha^{(k)})$. The cost function derivative can then be obtained as follows:

$$\frac{df}{d\alpha} = \frac{\partial f}{\partial \alpha} + \frac{\partial f}{\partial \hat{\mathbf{x}}}\frac{\partial \hat{\mathbf{x}}}{\partial \alpha} \tag{7.8}$$

Every term of Eq. (7.8) can be calculated; $\frac{\partial f}{\partial \alpha}$ and $\frac{\partial f}{\partial \hat{\mathbf{x}}}$ depend on the specific cost function considered, and $\frac{\partial \hat{\mathbf{x}}}{\partial \alpha}$ can be obtained, by solving the sensitivity equation (5.102) which, in the HB framework, takes the form of a simple linear system. Therefore, at each evaluation of the cost function, within a gradient-based optimisation algorithm, two steps are carried out:

- The cost function f is evaluated by solving the HB equation $\mathbf{r}_{PS}(\hat{\mathbf{x}}, \alpha^{(k)}) = \mathbf{0}$;
- The cost function derivative $\frac{df}{d\alpha}$ is calculated, by solving the sensitivity equation (5.102) and using Eq. (7.8).

In the example dealt with in this chapter, N_α is small, which makes the solution of the sensitivity equation (5.102) relatively fast. Note, however, that in other applications, the number of parameters in α may be large, so that solving the sensitivity equation for each component of α may become costly (in fact, more costly than solving the dynamical equation itself) [160]. In such cases, a slightly different approach is usually employed, namely the so-called adjoint method. Transposed into a HB formalism, the basic idea of the approach [160] consists of rewriting the second term in Eq. (7.8), as follows:

$$\frac{\partial f}{\partial \hat{\mathbf{x}}} \frac{\partial \hat{\mathbf{x}}}{\partial \alpha} = \lambda^{\mathrm{T}} \mathbf{B}_s \tag{7.9}$$

where λ^{T} is the solution of the following linear system, called the *adjoint problem*:

$$\mathbf{L}_s^{\mathrm{T}} \lambda = \frac{\partial f}{\partial \hat{\mathbf{x}}}^{\mathrm{T}} \tag{7.10}$$

and $\mathbf{B}_s$ and $\mathbf{L}_s$ are defined as in Section 5.6.2. Therefore, N_α linear problems, solved to calculate $\frac{\partial \hat{\mathbf{x}}}{\partial \alpha}$ explicitly, are replaced with only one linear problem, that of Eq. (7.10).

7.3 Optimisation of the ISWEC PTO settings

This section provides a numerical case study, for gradient-based optimisation of non-linear WECs within the proposed HB framework. The WEC model considered is the ISWEC device, already described in Section 6.2.4.

7.3.1 The ISWEC optimisation problem

Power-maximising control of the ISWEC device has been the subject of several studies, such as [13, 161, 162]. In particular, proportional-derivative control [161], linear-quadratic regulator [162] and stochastic optimal control [161] have been investigated. In the case of the ISWEC device, proportional-derivative control consists of implementing a control law of the form $\tau_{pto} = -k_{pto}\varepsilon - b_{pto}\dot{\varepsilon}$ (as in Chapter 6), in order to maximise power absorption. k_{pto} and b_{pto} are typically tuned on a sea state-by-sea state basis, based on an optimisation algorithm [161]. Note that, with a proportional-derivative control law, position and velocity constraints cannot be taken into account in an *exact* manner [9]; instead, such constraints can only be satisfied in a statistical sense, whereby the control parameters may be tuned to maximise power absorption, while ensuring that the probability of exceeding the constraints is below a chosen threshold. In addition to k_{pto} and b_{pto}, the ISWEC device has a third tunable parameter, $\dot{\varphi}_{pto}$, which can further enhance the ISWEC power absorption, or help in satisfying operational constraints. Throughout the rest of this chapter, proportional-derivative control will be considered, whereby three parameters ($N_\alpha = 3$) are tuned, namely the PTO stiffness coefficient k_{pto}, the PTO damping coefficient b_{pto}, and the regulated gyroscope rotational speed $\dot{\varphi}_{pto}$. Thus, α is defined as follows:

$$\alpha = \begin{pmatrix} k_{pto} \\ b_{pto} \\ \dot{\varphi}_{pto} \end{pmatrix} \tag{7.11}$$

In spite of the simplicity of the proportional-derivative control law, optimising as few as three PTO parameters (k_{pto}, b_{pto}, $\dot{\varphi}_{pto}$) is not a simple task, especially if the WEC model has non-linearities, as emphasised in [13]. Because of the significant non-linearities in the ISWEC dynamical model, commonly employed linear frequency-domain calculations may not be used for cost function evaluation. Instead, in [13], the Matlab Simulink[2] simulation platform is used for

[2] https://uk.mathworks.com/products/simulink.html

time-domain numerical integration of the ISWEC dynamical model. With such an implementation, each cost function evaluation reportedly takes at least 20 minutes [13]. This, combined with a three-dimensional parametric space, makes the PTO tuning extremely challenging [13]. In fact, as discussed in Section 7.2, if every possible PTO setting were to be evaluated, using an exhaustive search approach, and assuming that each parameter dimension is discretised into 10 values, $10^3 = 1000$ cost function evaluations would be required to optimise the PTO parameters in a given sea state, which, given the computational performance of the Simulink model reported in [13], would take almost two weeks!

There are two paths towards reducing the computational cost of the ISWEC PTO parameter optimisation: 1) improve the computational speed of each cost function evaluation, and/or 2) use an optimisation algorithm, more powerful than an exhaustive search approach, as discussed in Section 7.2, which should essentially reduce the number of cost function evaluations.

Improving the speed of each cost function evaluation could certainly be achieved, by employing a time-domain integration procedure, more efficient than those embedded within the Simulink platform documented in [13]. Regarding the number and lengths of simulations to obtain an accurate cost function evaluation, from Table 6.2, acceptable power estimates can be obtained from 10 simulations with length $T = 150$s, with waves generated using HDA. Assume that a simple RK2 numerical integration scheme, as implemented in Chapters 5 and 6, is used for each cost function evaluation. Using the results of Fig. 6.30, which show the computation time per second of simulated signal, it can be easily calculated that each cost function evaluation would take between approximately 1s (if a coarse integration step of 0.05s is chosen) and 10s (if a more accurate time step of 0.01s is chosen), to which some time should be added to allow for the transient response to fade out[3]. This is already a significant improvement, with respect to the results reported in [13].

Furthermore, as discussed in Section 7.2, using a gradient-based algorithm to carry out the optimisation is an interesting option. Calculating the cost function gradient using time domain integration would be possible, at the cost of one additional RK2 simulation, if the adjoint method is employed (see [158]), or three additional RK2 simulations, if the sensitivity equation (5.96) is explicitly solved for each component of α, which is of dimension $N_\alpha = 3$. Thus, if the cost function gradient is evaluated using time-domain simulations, at each iteration of a gradient-based algorithm, the computation time for evaluating the cost function gradient would be equal to, or three times larger than, that of evaluating the cost function itself.

However, the HB framework, proposed in Section 7.2 for evaluating the cost function and its derivatives, even more efficiently addresses all the challenges pointed out in the preceding discussion, by providing:

- A computationally-efficient method for cost function evaluation, including non-linearities, approximately 10 times faster, and more accurately than RK2 integration;
- A computationally-efficient framework for calculating the cost function gradient.

7.3.2 Problem specifications and numerical set-up

In the remainder of this chapter, the proposed HB framework is employed to determine, in each sea state of the scatter table at the ISWEC design location, off Pantelleria island, the PTO settings which maximise power absorption by the PTO system. Thus, the objective function to minimize is $f := -P$, where P is calculated as in Eq. (6.42):

$$f(\hat{\mathbf{x}}, \alpha) = -b_{pto} \hat{\mathbf{x}}^T \mathbf{Q}_{pto} \hat{\mathbf{x}} \tag{7.12}$$

The partial derivatives of f with respect to α and $\hat{\mathbf{x}}$ are given by:

$$\begin{cases} \frac{\partial f}{\partial \alpha} = \begin{pmatrix} 0 & -\hat{\mathbf{x}}^T \mathbf{Q}_{pto} \hat{\mathbf{x}} & 0 \end{pmatrix} \\ \frac{\partial f}{\partial \hat{\mathbf{x}}} = -b_{pto} \hat{\mathbf{x}}^{\mathrm{T}} \left[\mathbf{Q}_{pto} + \mathbf{Q}_{pto}^{\mathrm{T}} \right] \end{cases} \tag{7.13}$$

[3]Of course, those orders of magnitude are obtained for the specific processor, employed to produce all the other numerical results of this thesis - see Chapter 6.

The range of (H_{m_0}, T_p) conditions for the scatter table is determined from the data found in [162]. Each sea state of the scatter table is modelled using a JONSWAP spectrum with entries (H_{m_0}, T_p) corresponding to the scatter table, and $\gamma = 2$. In order to restrict the search region for the optimisation algorithm, k_{pto} and b_{pto} are allowed to take values between upper and lower bounds, which are first arbitrarily chosen, and $\dot{\varphi}_{pto}$ takes values between 0 and 1000 rpms (the upper bound is inspired by [161]). The main rationale for limiting the values, which k_{pto} and b_{pto} can take, is to avoid those situations, detailed in Section 6.7, where no solution exists (in which case the cost function is not even defined), and which are more likely to occur for small damping values, and large reactive coefficients. Therefore, the bounds are $[10-500]$ kN m s for b_{pto}, and $[10-500]$ kN m for k_{pto}.

The HB settings are those determined throughout Chapter 6: T is set to 150s, and f_c is 0.8Hz. Based on Table 6.2, the optimisation is carried out based on 10 different sets of random phases for HDA wave generation. For each sea state of the scatter table, the optimal parameters $b^*_{pto}, k^*_{pto}, \dot{\varphi}^*_{pto}$ are averaged over the 10 sets of random sea state realisations. Another, and more rigorous, approach would optimise $b_{pto}, k_{pto}, \dot{\varphi}_{pto}$ for all 10 realisations simultaneously, by considering as a cost function $\bar{f}$, which is the cost function f averaged over the 10 sets of random phases. However, running ten optimisations independently is a more careful approach since, if HB convergence issues are encountered in any of the ten realisations, such numerical issues do not contaminate the cost function, or gradient evaluation, for the other realisations. In addition, it was found that, in practice, the optimal PTO parameters showed little sensitivity to the specific set of random phases considered.

In the Matlab[4] non-linear optimisation function *fmincon*, various gradient-based algorithms are implemented, of which the working principles, and implementation details, may be found on the Matlab help web page[5]. For the sake of brevity, the various possible algorithms are not detailed here; however, a short preliminary investigation was carried out to determine the most suitable option. Assuming that the successive HB problems, which will be solved within the optimisation algorithm, are relatively close to each other, the computational performance of the HB method can be enhanced by storing the HB solution $\hat{\mathbf{x}}^{(k)}$ at each cost function evaluation k, and by using $\hat{\mathbf{x}}^{(k)}$ as a starting guess for the next cost function evaluation (as detailed in Section 6.4), at iterate $\alpha^{(k+1)}$. Therefore, it can be better to choose an optimisation strategy, which does not introduce large 'jumps' between successive iterates $\alpha^{(k)}$, $\alpha^{(k+1)}$.

Overall, the *trust-region* optimisation algorithm was found to perform the best, amongst the Matlab *fmincon* options. The fundamental idea of trust-region methods [163] is that the cost function, f, is locally approximated by a quadratic function, q, which is assumed to accurately reflect the behaviour of f in some neighbourhood (the 'trust region') of the current iterate $\alpha^{(k)}$. The quadratic approximation q is calculated using the cost function and its gradient, evaluated at $\alpha^{(k)}$, hence the interest in computing the gradient of f explicitly. q is minimised within the trust region to find the next iterate $\alpha^{(k+1)}$. If it is found that $f(\alpha^{(k+1)}) > f(\alpha^{(k)})$, then q is not an accurate approximation of f in the neighbourhood of $\alpha^{(k+1)}$; then, the trust region size is decreased, until the solution $\alpha^{(k+1)}$, which minimizes q over the trust region, also ensures that the actual cost function decreases, i.e. $f(\alpha^{(k+1)}) < f(\alpha^{(k)})$. Therefore, the trust-region algorithm will typically progress in a 'careful' way, whereby the size of each step is limited by the trust-region size. This is illustrated in Fig. 7.1, in the simplified case where $\dot{\varphi}_{pto}$ is set to its maximum allowed value, and only k_{pto} and b_{pto} are optimised; as seen in Fig. 7.1a, after one iteration with a relatively large step, the following iterates progress towards the optimum in a more careful way. Such a pattern is favourable to the HB method, since the HB solution $\hat{\mathbf{x}}^{(k)}$ for the iterate $\alpha^{(k)}$ can be successfully used as a starting guess, to solve the HB equation for the next iterate $\alpha^{(k+1)}$. For the sake of comparison, Fig. 7.1b shows how the optimisation proceeds from the same starting point, when a different algorithm (namely, sequential quadratic programming) is employed; the pattern followed

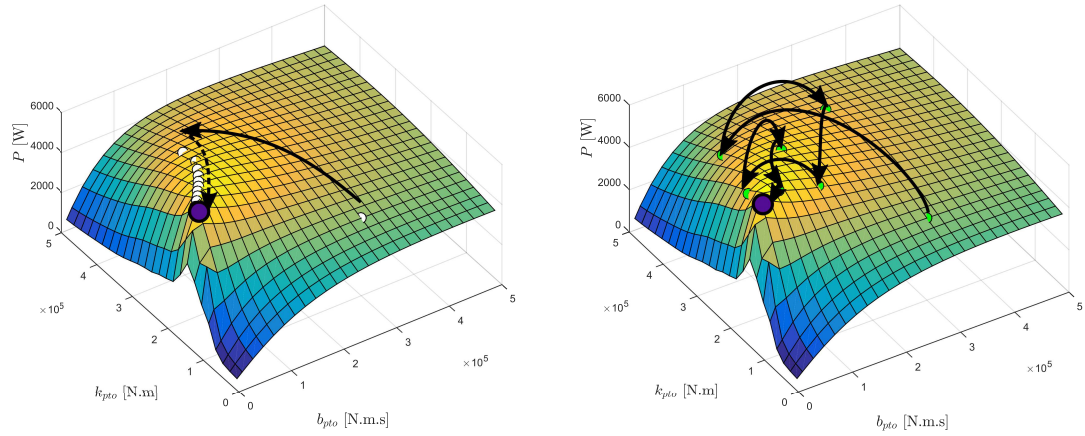

(a) Trust-region

(b) SQP

Figure 7.1: Examples of iteration patterns for the trust-region and sequential quadratic programming (SQP) algorithms, implemented within the Matlab *fmincon* function. JONSWAP sea state with $H_{m_0} = 1$m, $T_p = 7$s and $\gamma = 2$. The optimum is indicated by a thick purple dot.

by the consecutive iterates is not as favourable to the HB method as the trust-region algorithm.

Incidentally, Fig. 7.1 also illustrates the benefit of using gradient-based optimisation, compared to an exhaustive search approach. For both algorithms, the (same) optimum is reached in approximately 10 iterations. Typically, 2 or 3 cost function evaluations are necessary at each iteration (to estimate second-order derivatives), which results in approximately 30 cost function evaluations in total. In comparison, the 'exhaustive search' surface of Fig. 7.1 has been obtained using 676 cost function evaluations, and even with a significantly coarser 10×10 discretisation, 100 evaluations would have been necessary. Finally, it has been verified that, although the trust-region algorithm demonstrates the best computational performance, the optimisation results were consistent when employing a different optimisation algorithm, which Fig. 7.1 also illustrates.

7.3.3 Numerical results

Fig. 7.2 shows the optimisation results, for all sea states of the scatter table, in terms of optimal power P^*, and optimal PTO settings ($\alpha^* = (k^*_{pto}, b^*_{pto}, \dot{\varphi}^*_{pto})^T$). An optimal α^* was successfully found for each sea state. As can be appreciated in Fig. 7.2, the optimal control settings and power absorption evolve relatively continuously from one sea state to a neighbouring one, which is consistent with the fact that the ISWEC model is continuous (and, in fact, linear) in the PTO parameters. As expected, more energetic sea states (larger H_{m_0}) allow for more power absorption. For a given H_{m_0}, the maximum power absorption is achieved when T_p is close to the device natural resonance period of 4.6s (see Section 6.2.4). It is verified that the optimal choice of k_{pto} and b_{pto} is not influenced by the chosen lower and upper bounds. In contrast, the optimal settings for $\dot{\varphi}_{pto}$ reach the maximum allowed value of 1000 rpm, for T_p larger than the ISWEC resonant period. It can also be seen that the optimal b_{pto} value tends to increase, and the optimal k_{pto} value tends to decrease, as the sea state becomes more energetic. This can be interpreted by the fact that, for larger amplitude motion, the viscous dissipative terms play a more important role, and therefore it is better for the controller to somewhat mitigate the ISWEC resonance. Finally, it is worth mentioning that the starting guess for α, in all sea states, has been set to the same values of $k^{(0)}_{pto} = 100$kN.m, $b^{(0)}_{pto} = 300$kN.m, and $\dot{\varphi}^{(0)}_{pto} = 500$rpm. This provides confidence in the fact that

[4] See https:mathworks.com

[5] https://uk.mathworks.com/help/optim/ug/constrained-nonlinear-optimization-algorithms.html

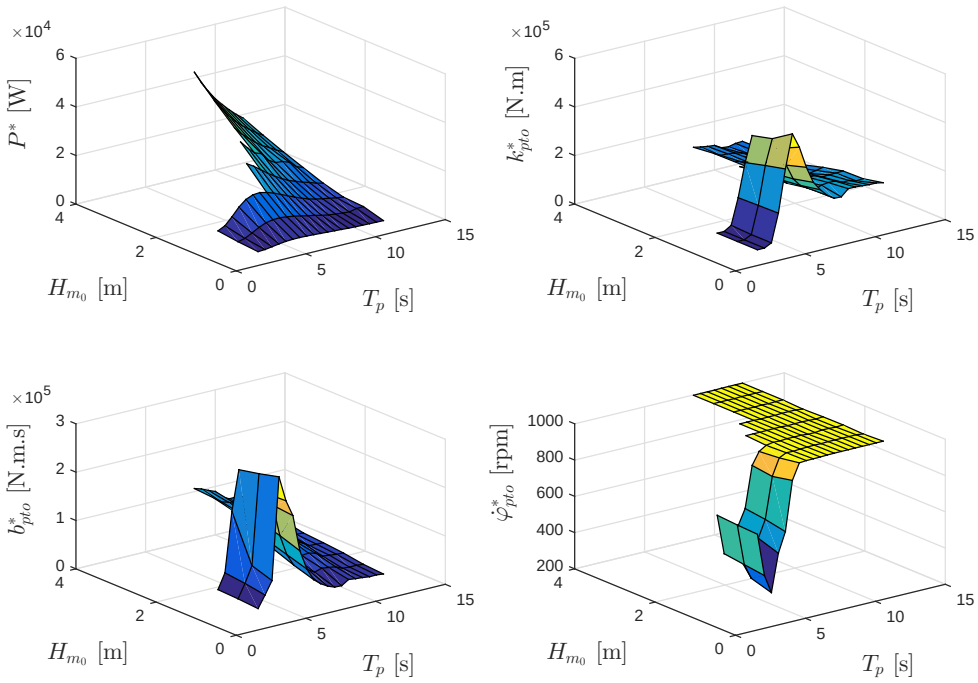

Figure 7.2: Optimisation results - non-linear ISWEC model

the results obtained, in a given sea state, are not influenced by those obtained in a neighbouring sea state.

In addition to the direct results of the optimisation procedure, it is interesting to examine whether or not the ISWEC dynamics, under optimal control settings, are physically realistic. This is done by calculating, based on the ten sets of random phases, the maximum amplitude reached by several physical variables, as plotted in Fig. 7.3. For example, it would be unrealistic to see ε (the precession angle of the gyroscope frame) take values larger than 180°, because the dynamical model of Eq. (6.34) is not compatible with overturning of the gyroscope frame. Fortunately, the maximum ε does not exceed 130°. Similarly, the maximum pitch angle is of the order of 25°, which can still be deemed compatible with linear hydrodynamic theory [161]. Interestingly, the maxima, for the different variables shown in Fig. 7.3, are found to be compatible with the operational constraints, defined in [161] within the scope of an optimal control set-up for the ISWEC device.

For the sake of comparison, Fig. 7.4 shows the optimisation results, obtained from the linearised ISWEC model. While, for low sea states, both the linear and non-linear models give similar optimisation results, in terms of optimal control parameters and optimal power, this is not the case when H_{m_0} becomes larger. In particular, the linearised model optimisation yields power absorption values up to 5 times larger than those, obtained from the non-linear model. Furthermore, it can be seen that, unlike those from the non-linear ISWEC model, the optimal PTO values are identical for all H_{m_0} values, for a fixed T_p. This is because the ISWEC dynamical model is both linear in its physical variables r_y and ε, and linear in the three optimisation variables.

Fig. 7.5 shows the maximum amplitudes reached by the different physical variables already examined in the non-linear case in Fig. 7.3. The maximum values for the pitch angle, the precession angle and the torque, are all one order of magnitude larger, compared to those obtained from the optimally-tuned non-linear system. Concerning the pitch and precession angles, such values

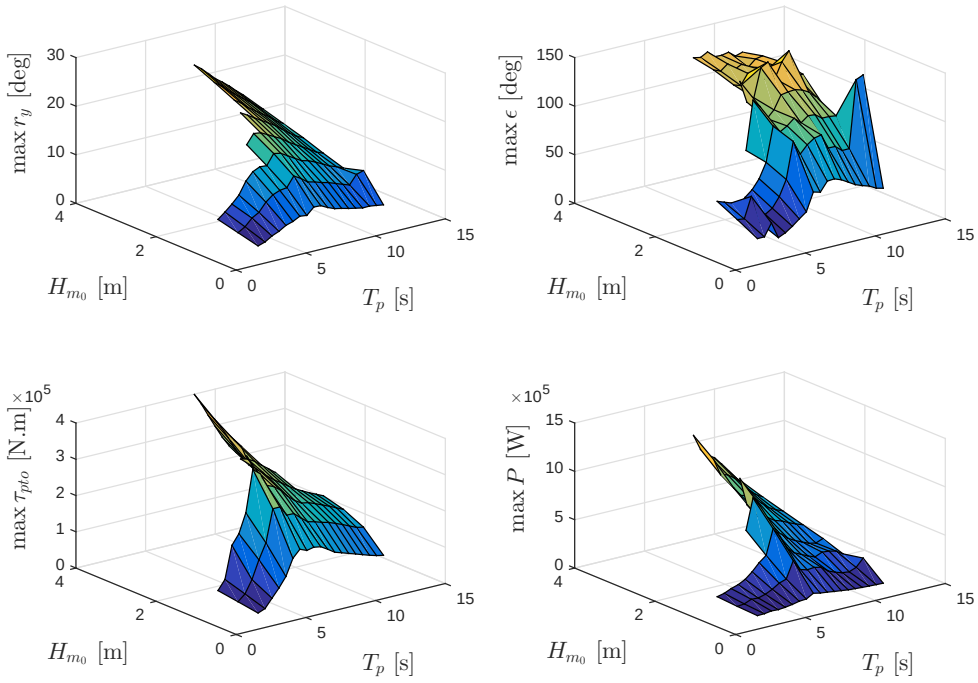

Figure 7.3: Maximum amplitude values under optimal control settings - non-linear ISWEC model

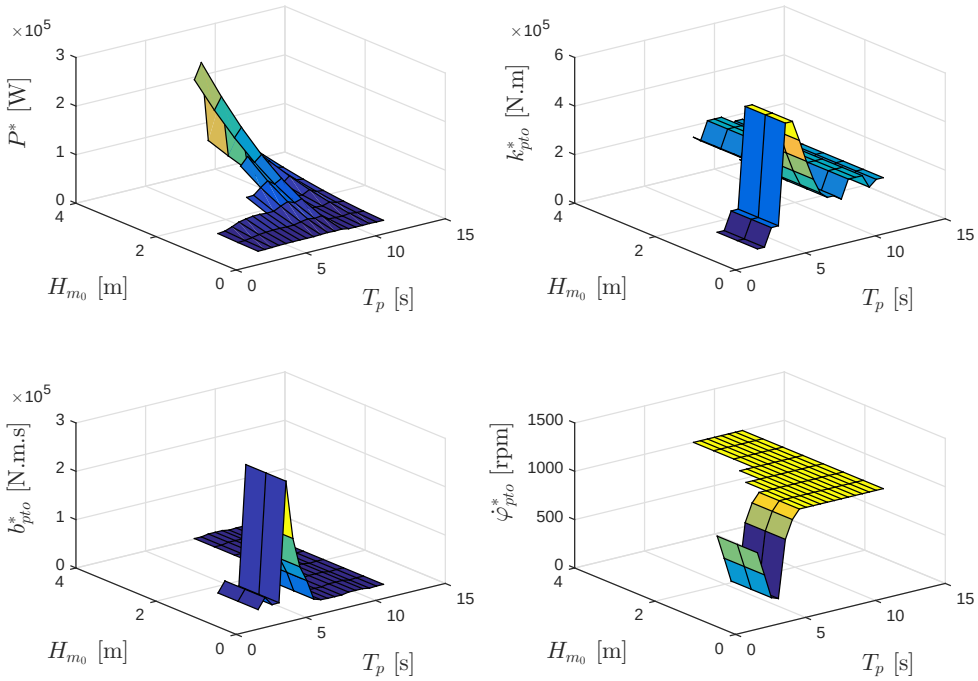

Figure 7.4: Optimisation results - linearised ISWEC model

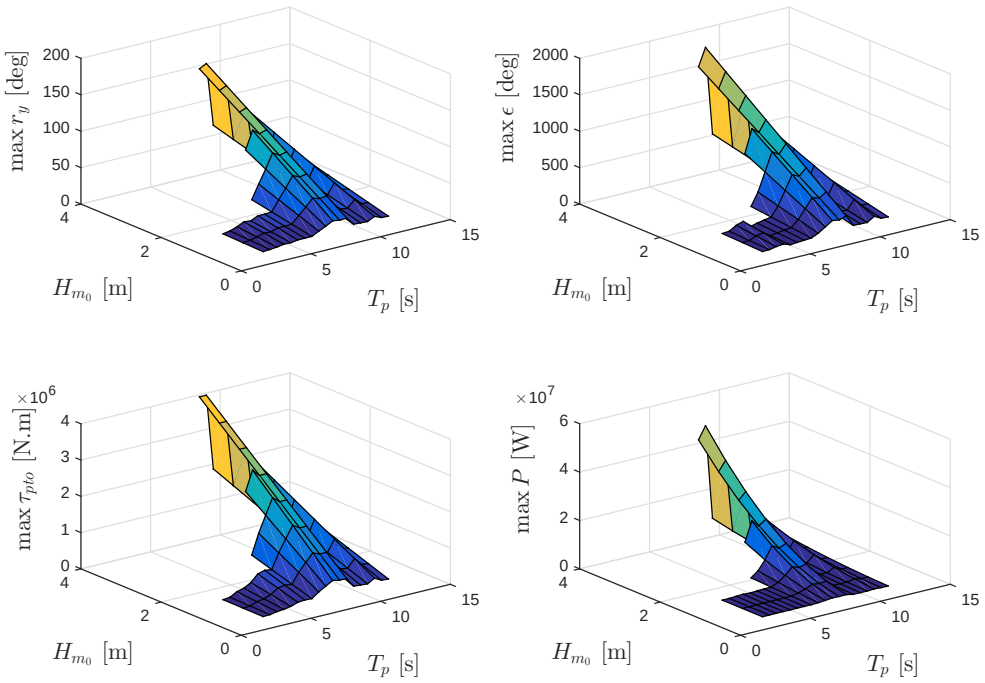

Figure 7.5: Maximum amplitude values under optimal control settings - linearised ISWEC model

are completely incompatible with the range of validity of the linearised ISWEC model.

Comparing Figs. 7.2 (resp. 7.3) on the one hand, with Figs. 7.4 (resp. 7.5) on the other hand, clearly provides further evidence, supporting the inclusion of non-linear WEC modelling, at the control design stage, as was already evoked throughout Chapter 4, following works such as [11, 113]. The proposed HB framework for gradient-based optimisation is capable of addressing this challenge, by efficiently handling non-linear IDE WEC models, as detailed further in the following.

Table 7.1 provides detailed information, concerning the computational performance of the proposed optimisation framework[6]. The total time necessary to obtain the optimal PTO settings in all 103 sea states of the scatter table was approximately 1 hour and 40 minutes, which corresponds to 1 minute per sea state. Of those 60s of computation time per sea state, on average, 24s were spent running the HB algorithm (which corresponds to the simulation, i.e. the cost function evaluation), 19s were spent solving the sensitivity equation (which corresponds to the evaluation of the cost function derivative), while the rest (approx. 16 seconds) can be accounted for by the management of the optimisation algorithm, including the update of the matrix $\mathbf{L}(\alpha)$ involved in the HB equation (5.53), when the parameter vector α is modified. On average, 130 cost function evaluations (and gradient estimations) per sea state were necessary, corresponding to 30 iterations of the trust-regions algorithm.

The average number of HB iterations per HB problem (i.e. per cost function evaluation) was low, at 2.16. This can be attributed to the fact that, within the gradient-based algorithm, most HB problems which are solved are very close to each other. Indeed, at each new iterate $\alpha^{(k)}$ of the trust-region algorithm, the cost function is evaluated on average four times (as indicated in Table 7.1), to evaluate second-order derivatives through finite differences, using neighbouring values of α sufficiently close to $\alpha^{(k)}$. Therefore, those parameter values, grouped in a neighbourhood of each iterate $\alpha^{(k)}$, are extremely close to each other, which makes the neighbour-based initialisation

[6] All computation times are obtained from a Matlab implementation, run on a 3.50 GHz, 8-core Intel® processor.

Table 7.1: Computational performance of the gradient-based optimisation methodology. Results for RK2-based cost-function evaluations are extrapolated, based on the results shown in Fig. 6.30, assuming that the cost function derivative can be obtained using only one additional RK2 simulation. c.f.e: *cost function evaluation.*

	HB	**RK2** (estimated)
Total optimisation time	1h 40min.	7h 30min - 75h
Comp. time per sea state	59s	260-2600s
incl. sim. comp. time	24s	130-1300s
incl. sens. eq. comp. time	19s	130-1300s
Av. nb. of iterations per sea state	30	30
Av. nb. of c.f.e. per sea state	130	130
Av. nb. of HB iterations per c.f.e.	2.16	—
Av. comp. time per c.f.e.	0.18s	1-10s

method particularly useful, to solve each HB equation in fewer iterations. Finally, the time spent solving the sensitivity equation is surprisingly significant, compared to the time spent on the HB solution itself. This can be explained by the fact that, as already mentioned, the HB solution only requires, on average, two iterations, i.e. two matrix inversions, while the sensitivity equation requires one matrix inversion. In other words, the computational cost of solving the sensitivity equation only seems significant because that of solving the HB equation itself is particularly low. Furthermore, the cost function gradient could perhaps be calculated more efficiently through the adjoint approach (see Section 7.2), leading to further computational savings.

It is interesting to hypothetically assess the performance of the proposed gradient-based optimisation method, where RK2 simulations are used instead of HB simulations. As discussed in Section 7.3.1, each cost function evaluation could be carried out using RK2 simulations, allowing some additional computation time for letting the transient response fade out. In addition, the cost function gradient could be evaluated, by running at least one more RK2 simulation to solve the adjoint equation[7]. Based on the results shown in Fig. 6.30, it can be estimated that each cost function evaluation would take, at least, 1s (if a 0.05s RK2 time step were used). Similarly, each cost function gradient calculation would take the same time of 1s. Thus, assuming that, in all sea states, the RK2-based trust-region optimisation algorithm would produce the very same iterations as the HB-based trust-region algorithm, it can be estimated that the optimisation would take between approximately 7h30, if a coarse 0.05s RK2 time step were used, and 75h, if a more refined 0.01s RK2 time step were employed.

7.4 Summary

In this chapter, the problem of parametric WEC optimisation has been formulated in a HB framework, assuming that the WEC model is described by an IDE, and that all terms of the model are continuously differentiable in the parameters. It has been emphasised that gradient-based optimisation techniques are particularly suitable for such optimisation problems, since they generally require fewer cost function evaluations, compared to their gradient-free competitors.

The proposed numerical example, whereby the ISWEC PTO parameters are optimised over a wide range of sea states, confirms the computational efficiency of the HB-based optimisation framework. It takes, on average, one minute to carry out the 3-variable optimisation in a given sea state. In fact, such computational performance suggests that the PTO tuning could be carried out in real time, on a sea state-by-sea state basis, using wave spectrum forecasts available in real-time, as opposed to the present approach which essentially constructs a look-up table assuming a

[7]It should be ascertained, in particular, that the inaccuracy of RK2 methods, relatively to HB, does not affect the accuracy of the cost function gradient calculation.

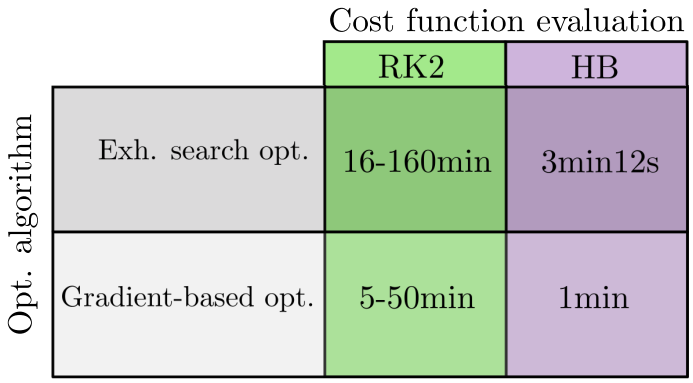

Figure 7.6: Average computation time for parametric optimisation in a given sea state, using an exhaustive search approach *vs* a gradient-based optimisation algorithm (such as the trust-region algorithm), and using RK2 *vs* HB to calculate the cost function and its derivative.
For RK2, the smaller computation time indicated is for $\Delta t_{RK} = 0.05$s, and the larger computation time is for $\Delta t_{RK} = 0.01$s. Concerning the exhaustive search approach, 10 discrete values are assumed for each of the three parameter dimensions.

JONSWAP spectral shape.

There does not seem to be any fundamental obstacle to the use of RK2 simulations, to replace the HB-based cost function and gradient evaluation, within the optimisation algorithm. In fact, the proposed gradient-based optimisation approach is relatively independent from the method employed, for cost function evaluation. Regardless of whether RK2 or HB is used, the results of this case study suggest that the number of cost function evaluations per sea state drops from at least 1000, if an exhaustive search approach is used, to approximately 130, using gradient-based optimisation. Fig. 7.6 provides estimates for the computational time, which would be necessary to solve the same optimisation problem as in this chapter, using either an exhaustive search approach or gradient-based optimisation, combined with either RK2 or HB integration techniques, to evaluate the cost function and its derivative. Combining the HB approach with a gradient-based optimisation algorithm is, unsurprisingly, the most efficient option, with computational gains between 1 and 2 orders of magnitude with respect to a simple exhaustive search approach combined with RK2 simulations. Furthermore, it should be recalled that the exhaustive search approach can only provide sub-optimal results, since the PTO parameters are chosen amongst a discrete set of possible values - as opposed to gradient-based algorithms, which explore a continuum of optimisation variables.

In Fig. 7.6, further computational gains could be expected from the gradient-based/HB approach, by using the adjoint approach for the evaluation of the cost function gradient. In addition, the time indicated for the exhaustive search/HB approach does not include the time necessary to update the system parameters and execute the loop (which, from the results presented in Table 7.1, can represent more than 30% of the time, dedicated to cost function and gradient evaluation). Finally, concerning RK2 results, the computation time indicated does not include the necessity for transient response expiry. Therefore, the relative differences between the four variants of Fig. 7.1 would likely be amplified, if those additional contributions could be accurately quantified.

Chapter 8

Conclusion

For the development of wave energy technologies, several applications require extensive numerical simulation, such as parametric optimisation, power assessment, and structural design. Such tasks must rely on a well-understood statistical characterisation of ocean waves, which represent the forcing input to the WEC system, and must employ computationally efficient simulation methods, through which the WEC output, most often power production or absorption, but also possibly other statistics of interest, can be quickly evaluated.

Wave input modelling and simulation

The Gaussian wave model, characterised by its wave spectrum, has been identified as the fundamental framework to analyse, and numerically simulate, the external forcing input to WEC systems, as emphasised in Chapter 2. Concerning the numerical simulation of such forcing inputs, it must be recalled that the usual representation of a specific wave time-series realisation, employing the superposition of a finite number of sinusoids, does *not* mean that the sea state is *actually* composed of a finite number of sinusoidal waves. In fact, the Gaussian sea state representation relies on the combination of infinitely many, infinitesimal, contributions.

Throughout Chapter 3, it is highlighted that wave simulation methods, relying on the superposition of non-harmonic sinusoids, present more drawbacks than benefits, with respect to harmonic superposition methods. Amongst the two variants of harmonic superposition methods, Chapter 3 insists on the fact that the HDA method (the approach most commonly employed in the wave energy community) is not statistically consistent, in the sense that HDA-generated signals do not follow a Gaussian law, and do not represent the short-term variability, observed in actual ocean waves. On the contrary, perfectly realistic wave statistics can be obtained, using a properly tuned HRA superposition method. Yet, paradoxically, it is the HDA method which has been employed in the vast majority of the numerical examples, presented throughout the rest of the thesis. This is because it can be ensured that, for the applications considered, the simulation output of interest, namely the average absorbed power, is calculated with no bias using the HDA method, while requiring a significantly smaller number of numerical simulations than if the HRA method was employed. Therefore, it may well be the case that, for some applications such as power estimation, the HDA method has more practical value than the theoretically-correct HRA method. However, one should never loose sight of the implications of using the HDA method and, for each specific output evaluated, numerical verifications, such as that presented in Section 6.6, should be systematically considered, either at a preliminary stage or ex-post, to determine whether the HDA method results in unbiased estimates, with respect to the HRA method. In other words, choosing the HDA method, over the HRA method, should be the result of a conscious and informed decision.

The harmonic balance method for the numerical simulation of non-linear WEC models

To improve the computational efficiency of WEC numerical simulations, two routes may be identified:

- Structure the WEC physical model to obtain a mathematical form amenable to the most efficient numerical solution methods. Typical examples include linearisation techniques (which allow the WEC response to be calculated in the frequency domain), and state-space approximations for the linear radiation memory term (which allow the WEC response to be calculated in the time domain, without evaluating a convolution integral at each time step). The drawback of these approaches is the loss of fidelity incurred, respectively, by ignoring non-linearity and by the finite-order approximation of the memory term.

- Extend the range of numerical simulation methods, considered by wave energy researchers and engineers. This is the route followed in this thesis, by proposing the harmonic balance method for the simulation of some non-linear WEC model types, for which time-domain integration routines were previously considered to be the only viable simulation techniques.

With wave inputs, simulated using a harmonic superposition method (HDA or HRA), the forcing terms of WEC dynamical models are periodic. The HB method constitutes a pertinent mathematical technique to calculate the steady-state response of such systems. In this thesis, the HB implementation is detailed for those WEC models which take the form of non-linear integro-differential equations (IDEs). As discussed throughout Chapter 4, non-linear IDEs can represent a variety of non-linear WEC models which combine two challenging components: a linear convolution term, and forces which are non-linear in the system variables.

The benefits of the HB approach, in terms of numerical accuracy, can be anticipated from the mathematical foundations of the method, and from the nature of the non-linearities present in a specific WEC model, as discussed throughout Chapter 5. In contrast, the practical value of the HB framework, which is determined by the performance trade-off which the method allows (between numerical accuracy and computation time) can only be determined by means of numerical experiments, including a comparison with a more standard method. The approach retained, and thoroughly developed in Chapter 6 of this thesis, consists of comparing the results and computational performance of the HB method with a second-order Runge-Kutta (RK2) method, using various time-steps. The choice of a RK2 method is based on two factors. Firstly, the method is governed by only one parameter, i.e. the time step length, and it is guaranteed that the RK2 results tend to the exact mathematical solution, as the RK2 time step tends to zero. Secondly, the method employs a constant time step, which makes it straightforward to numerically calculate the full convolution product, corresponding to the linear memory terms in the WEC model IDEs.

The results, shown in Chapter 6 of this thesis, suggest that the HB method can reduce the computation time (per second of simulated signal) by one to three orders of magnitude, compared to those RK2 schemes where the radiation terms are calculated from the full convolution product. Furthermore, the fact that the RK2 solutions converge to the HB solutions, as the RK2 time-step tends to zero, provides strong evidence to support the accuracy of the HB method, particularly when it comes to calculating the radiation memory terms.

RK2, however, is by no means a universal solution for time-domain numerical integration in general. Other constant time-step routines, such as the fourth-order Runge-Kutta method, are more accurate than the RK2 approach for a given time step length, but also require more function evaluations at each time step. Alternatively, numerical schemes with adaptive time-steps may provide a more favourable trade-off than RK2 methods, between computation time and accuracy. However, in such numerical schemes, the calculation of the full convolution integral is problematic, because simulation results are not stored at equally-spaced sampling instants. Therefore, such methods are more suitable for cases where the convolution product is avoided, i.e. when the memory term is approximated by means of a state-space representation. Yet, in Chapter 6, the example of the

four cylindrical HPAs illustrates the possible dangers associated with state-space approximations. Although the inaccuracies, introduced by the approximation, may seem negligible in some operational conditions, especially away from resonance, the results of Chapter 6 also suggest that in resonant conditions, the inaccuracies may be exaggerated, and result in significant errors, for example in power estimates. In fact, the inaccuracies, introduced by the state-space approximation, are one order of magnitude larger than those, resulting from the numerical integration scheme.

The benefits of the HB method are not limited to the accuracy and computational efficiency achieved. The approach also provides an interesting framework to explore the sensitivity of the steady-state solution of a WEC model, as some WEC parameters vary. Since the solutions are stored as a set of Fourier coefficients, their manipulation is easier than that of time-domain integration routines, which must be specified at each time-step (which, in the case of adaptive time-step routines, may become particularly impractical). Using the HB method, the similarity between the solutions of neighbouring problems (i.e. problems where the parameter values are close to each other) can be exploited, to further reduce the computation time. Furthermore, the sensitivity equation can be solved easily and efficiently, and used within the scope of WEC parametric optimisation.

In this thesis, all the WECs considered have models which lend themselves reasonably well to the HB method, since their non-linear terms are continuous, with continuous first-order derivatives (but discontinuous second-order derivatives, because of the quadratic drag term). The smoothness of the non-linearities is a major determining factor in the HB performance, in terms of computation time and accuracy. Non-smooth non-linearities, such as discontinuous forces and motion which may occur due to Coulomb damping, negatively affect the HB performance, because they require the addition of many more harmonics to achieve a satisfactory accuracy, and because the residual derivatives are not well-defined. Such cases have been briefly investigated by the author [152]. In [152], the discontinuities (characterised by a step function) can be approximated by means of smooth functions, but when the approximation becomes more accurate, the HB computational cost becomes comparable to, if not larger than, that of TD integration. Conversely, infinitely-smooth non-linearities (i.e. non-linearities of which the derivatives of any order exist and are continuous), such as polynomial functions, enhance the performance of the HB method. In summary, it is not true to say that the HB method, as shown in this thesis, would work equally well for any type of WEC model non-linearities.

Overall, the comparison with RK2 results, presented in this thesis, cannot be considered to provide a complete overview of how the HB competes with time-domain integration in general. However, the method is doubtlessly an interesting addition to the range of simulation techniques, usually considered for the numerical simulation of non-linear WEC models.

Bibliography

[1] A. Babarit, *Ocean Wave Energy Conversion: Resource, Technologies and Performance*. Elsevier, 2017.

[2] A. Falcão, "Wave energy utilization: A review of the technologies," *Renewable Sustainable Energy Rev.*, vol. 14, no. 3, pp. 899–918, 2010.

[3] M. Folley, *Numerical Modelling of Wave Energy Converters: State-of-the-Art Techniques for Single Devices and Arrays*. Academic Press, 2016.

[4] A. De Andrés, R. Guanche, J. Weber, and R. Costello, "Finding gaps on power production assessment on WECs: Wave definition analysis," *Renewable Energy*, vol. 83, pp. 171–187, 2015.

[5] A. Mérigaud, V. Ramos, F. Paparella, and J. V. Ringwood, "Ocean forecasting for wave energy production," *J. Mar. Res.*, vol. 75, no. 3, pp. 459–505, 2017.

[6] M. K. Ochi, *Ocean Waves: the Stochastic Approach*, vol. 6. Cambridge University Press, 2005.

[7] J. Falnes, *Ocean Waves and Oscillating Systems: Linear Interactions Including Wave-Energy Extraction*. Cambridge University Press, 2002.

[8] M. Penalba, G. Giorgi, and J. V. Ringwood, "Mathematical modelling of wave energy converters: A review of nonlinear approaches," *Renewable Sustainable Energy Rev.*, vol. 78, pp. 1188–1207, 2017.

[9] J. V. Ringwood, G. Bacelli, and F. Fusco, "Energy-maximizing control of wave-energy converters: The development of control system technology to optimize their operation," *IEEE Control Systems*, vol. 34, no. 5, pp. 30–55, 2014.

[10] N. Faedo, S. Olaya, and J. V. Ringwood, "Optimal control, MPC and MPC-like algorithms for wave energy systems: An overview," *IFAC Journal of Systems and Control*, vol. 1, pp. 37–56, 2017.

[11] M. Penalba, A. Mérigaud, J.-C. Gilloteaux, and J. Ringwood, "Nonlinear froude-krylov force modelling for two heaving wave energy point absorbers," in *Proceedings of the 11th European Wave and Tidal Energy Conference (EWTEC 2015), Nantes, France*, 2015.

[12] S. A. Sirigu, G. Vissio, G. Bracco, E. Giorcelli, B. Passione, M. Raffero, and G. Mattiazzo, "ISWEC design tool," *Int. J. Mar. Energy*, vol. 15, pp. 201–213, 2016.

[13] G. Vissio, G. Bracco, E. Giorcelli, G. Mattiazzo, D. Valério, and P. Beirão, "ISWEC control tuning: Lessons learned," in *Progress in Renewable Energies Offshore: Proceedings of the 2nd International Conference on Renewable Energies Offshore (RENEW2016), Lisbon, Portugal, 24-26 October 2016*, p. 427, CRC Press, 2016.

[14] S. D. Conte and C. W. De Boor, *Elementary Numerical Analysis: an Algorithmic Approach*. McGraw-Hill Higher Education, 1980.

[15] W. J. Pierson, "Wind generated gravity waves," *Advances in Geophysics*, vol. 2, pp. 93–178, 1955.

[16] S. R. Massel, *Ocean Surface Waves: Their Physics and Prediction*, vol. 36. World Scientific, 2013.

[17] M. St Denis and W. J. Pierson Jr, "On the motions of ships in confused seas," *Trans. Soc. Nav. Archit., N.Y.,*, no. 65, pp. 1–65, 1953.

[18] G. B. Whitham, *Linear and Nonlinear Waves*, vol. 42. John Wiley & Sons, 2011.

[19] A. D. Craik, "The origins of water wave theory," *Annu. Rev. Fluid Mech.*, vol. 36, pp. 1–28, 2004.

[20] W. J. Pierson, "A Unified Mathematical Theory for the Analysis, Propagation, and Refraction of Storm Generated Ocean Surface Waves. Parts I and II," tech. rep., Research Division, College of Engineering, New York University, 1952.

[21] S. O. Rice, "Mathematical analysis of random noise," *Bell System Technical Journal*, vol. 23, no. 3, pp. 282–332, 1944.

[22] N. Wiener, *The Extrapolation, Interpolation, and Smoothing of Stationary Time Series*. John Wiley and Sons, 1949.

[23] A. M. Yaglom, *Correlation Theory of Stationary and Related Random Functions, Vol. I; Basic Results*. Springer Science & Business Media, 1989.

[24] H. Cramér, *Random Variables and Probability Distributions*, vol. 36. Cambridge University Press, 1937.

[25] A. Papoulis and S. U. Pillai, *Probability, Random Variables, and Stochastic Processes*. Tata McGraw-Hill Education, 2002.

[26] IAHR Working Group on Wave Generation and Analysis, "List of sea-state parameters," *Journal of Waterway, Port, Coastal, and Ocean Engineering*, vol. 115, no. 6, pp. 793–808, 1989.

[27] K. Hasselmann, "Nonlinear interactions treated by the methods of theoretical physics (with application to the generation of waves by wind)," *Proc. R. Soc. Lond. A*, vol. 299, no. 1456, pp. 77–103, 1967.

[28] F. Fedele, J. Brennan, S. P. De León, J. Dudley, and F. Dias, "Real world ocean rogue waves explained without the modulational instability," *Sci. Rep.*, vol. 6, p. 27715, 2016.

[29] S. Elgar, T. H. C. Herbers, V. Chandran, and R. T. Guza, "Higher-order spectral analysis of nonlinear ocean surface gravity waves," *Journal of Geophysical Research: Oceans*, vol. 100, no. C3, pp. 4977–4983, 1995.

[30] A. D. Craik, *Wave Interactions and Fluid Flows*. Cambridge University Press, 1988.

[31] O. Phillips, "On the dynamics of unsteady gravity waves of finite amplitude Part 1. The elementary interactions," *J. Fluid Mech.*, vol. 9, no. 2, pp. 193–217, 1960.

[32] O. Phillips, "On the dynamics of unsteady gravity waves of finite amplitude Part 2. Local properties of a random wave field," *J. Fluid Mech.*, vol. 11, no. 1, pp. 143–155, 1961.

[33] J. Hammack and D. Henderson, "Resonant interactions among surface water waves," *Annu. Rev. Fluid Mech.*, vol. 25, no. 1, pp. 55–97, 1993.

[34] S. Nazarenko and S. Lukaschuk, "Wave turbulence on water surface," *Annual Review of Condensed Matter Physics*, vol. 7, pp. 61–88, 2016.

[35] K. Hasselmann, "On the non-linear energy transfer in a gravity-wave spectrum Part 1. General theory," *J. Fluid Mech.*, vol. 12, no. 4, pp. 481–500, 1962.

[36] K. Hasselmann, "On the non-linear energy transfer in a gravity wave spectrum Part 2. Conservation theorems; wave-particle analogy; irrevesibility," *J. Fluid Mech.*, vol. 15, no. 2, pp. 273–281, 1963.

[37] K. Hasselmann, "On the non-linear energy transfer in a gravity-wave spectrum. Part 3. Evaluation of the energy flux and swell-sea interaction for a neumann spectrum," *J. Fluid Mech.*, vol. 15, no. 3, pp. 385–398, 1963.

[38] A. Babarit, J. Hals, M. Muliawan, A. Kurniawan, T. Moan, and J. Krokstad, "Numerical benchmarking study of a selection of wave energy converters," *Renewable Energy*, vol. 41, pp. 44–63, 2012.

[39] L. Rusu and F. Onea, "Assessment of the performances of various wave energy converters along the European continental coasts," *Energy*, vol. 82, pp. 889–904, 2015.

[40] L. Rusu and F. Onea, "The performance of some state-of-the-art wave energy converters in locations with the worldwide highest wave power," *Renewable Sustainable Energy Rev.*, vol. 75, pp. 1348–1362, 2016.

[41] E. Rusu and F. Onea, "Estimation of the wave energy conversion efficiency in the Atlantic Ocean close to the European islands," *Renewable Energy*, vol. 85, pp. 687–703, 2016.

[42] D. Silva, E. Rusu, and C. G. Soares, "Evaluation of various technologies for wave energy conversion in the portuguese nearshore," *Energies*, vol. 6, no. 3, pp. 1344–1364, 2013.

[43] R. Carballo and G. Iglesias, "A methodology to determine the power performance of wave energy converters at a particular coastal location," *Energy Convers. Manage.*, vol. 61, pp. 8–18, 2012.

[44] B. Robertson, C. Hiles, E. Luczko, and B. Buckham, "Quantifying wave power and wave energy converter array production potential," *Int. J. Mar. Energy*, vol. 14, pp. 143–160, 2016.

[45] R. Carballo, M. Sánchez, V. Ramos, J. Fraguela, and G. Iglesias, "The intra-annual variability in the performance of wave energy converters: A comparative study in N. Galicia (Spain)," *Energy*, vol. 82, pp. 138–146, 2015.

[46] E. B. Mackay, A. S. Bahaj, and P. G. Challenor, "Uncertainty in wave energy resource assessment. Part 2: Variability and predictability," *Renewable Energy*, vol. 35, no. 8, pp. 1809–1819, 2010.

[47] S. C. Parkinson, K. Dragoon, G. Reikard, G. García-Medina, H. T. Özkan-Haller, and T. K. Brekken, "Integrating ocean wave energy at large-scales: A study of the US pacific northwest," *Renewable Energy*, vol. 76, pp. 551–559, 2015.

[48] D. A. Halamay, T. K. Brekken, A. Simmons, and S. McArthur, "Reserve requirement impacts of large-scale integration of wind, solar, and ocean wave power generation," *IEEE Trans. Sustain. Energy*, vol. 2, no. 3, pp. 321–328, 2011.

[49] F. J. Harris, "On the use of windows for harmonic analysis with the discrete Fourier transform," *Proc. IEEE*, vol. 66, no. 1, pp. 51–83, 1978.

[50] W. J. Pierson and L. Moskowitz, "A proposed spectral form for fully developed wind seas based on the similarity theory of S.A. Kitaigorodskii," *J. Geophys. Res.*, vol. 69, no. 24, pp. 5181–5190, 1964.

[51] C. Bretschneider, "Wave Variability and Wave Spectra for Wind Generated Gravity Waves," Tech. Rep. 118, Beach Erosion Board, US Army Corps of Eng., Washington, DC, 1959.

[52] K. Hasselmann, T. Barnett, E. Bouws, H. Carlson, D. Cartwright, K. Enke, J. Ewing, H. Gienapp, D. Hasselmann, P. Kruseman, *et al.*, "Measurements of Wind-Wave Growth and Swell Decay During the Joint North Sea Wave Project (JONSWAP)," tech. rep., Deutches Hydrographisches Institut, 1973.

[53] Y. Goda, "Overview on the applications of random wave concept in coastal engineering," *Proceedings of the Japan Academy, Series B*, vol. 84, no. 9, pp. 374–385, 2008.

[54] "Marine Energy-Wave, Tidal and Other Water Current ConvertersPart 101: Wave Energy Resource Assessment and Characterization; IEC TS 62600-101," standard, International Electrotechnical Commission, Geneva, Switzerland, 2015.

[55] V. Ramos and J. V. Ringwood, "Exploring the utility and effectiveness of the IEC (International Electrotechnical Commission) wave energy resource assessment and characterisation standard: A case study," *Energy*, vol. 107, pp. 668–682, 2016.

[56] S. Gallagher, R. Tiron, E. Whelan, E. Gleeson, F. Dias, and R. McGrath, "The nearshore wind and wave energy potential of Ireland: A high resolution assessment of availability and accessibility," *Renewable Energy*, vol. 88, pp. 494 – 516, 2016.

[57] A. Mérigaud and J. V. Ringwood, "Power production assessment for wave energy converters: Overcoming the perils of the power matrix," *Proceedings of the Institution of Mechanical Engineers, Part M: Journal of Engineering for the Maritime Environment*, vol. 232, no. 1, pp. 50–70, 2018.

[58] M.-A. Kerbiriou, M. Prevosto, C. Maisondieu, A. Clément, and A. Babarit, "Influence of sea-states description on wave energy production assessment," in *Proceedings of the 7th European Wave and Tidal Energy Conference (EWTEC 2007), Porto, Portugal*, pp. 11–13, 2007.

[59] J.-B. Saulnier, A. Clément, F. d. O. António, T. Pontes, M. Prevosto, and P. Ricci, "Wave groupiness and spectral bandwidth as relevant parameters for the performance assessment of wave energy converters," *Ocean Eng.*, vol. 38, no. 1, pp. 130–147, 2011.

[60] R. Pascal, G. Payne, C. Theobald, and I. Bryden, "Parametric models for the performance of wave energy converters," *Appl. Ocean Res.*, vol. 38, pp. 112–124, 2012.

[61] J.-B. Saulnier, *Refined wave climatology as a contribution to the design of wave energy conversion systems*. PhD thesis, Ecole Centrale de Nantes, France, and Instituto Superior Técnico, Lisbon, Portugal, 2009.

[62] A. Mérigaud and J. V. Ringwood, "Incorporating ocean wave spectrum information in short-term free-surface elevation forecasting," *IEEE J. Ocean. Eng.*, pp. 1–14, 2018.

[63] A. Mérigaud, J. Herterich, J. Flanagan, J. V. Ringwood, and F. Dias, "Incorporating wave spectrum information in real-time free-surface elevation forecasting: Real-sea experiments," in *Proceedings of the 11th IFAC Conference on Control Applications in Marine Systems, Robotics, and Vehicles, Opatija, Croatia, 2018 (CAMS 2018)*, 2018.

[64] P. D. Spanos and B. A. Zeldin, "Monte Carlo treatment of random fields: A broad perspective," *Appl. Mech. Rev.*, vol. 51, no. 3, pp. 219–237, 1998.

[65] P. D. Spanos and M. Mignolet, "ARMA Monte Carlo simulation in probabilistic structural analysis," *Shock Vibration Digest*, vol. 21, pp. 3–14, 1989.

[66] A. Papoulis, "Levinsons algorithm, Wolds decomposition, and spectral estimation," *SIAM Rev.*, vol. 27, no. 3, pp. 405–441, 1985.

[67] M. Shinozuka and G. Deodatis, "Simulation of stochastic processes by spectral representation," *Appl. Mech. Rev.*, vol. 44, no. 4, pp. 191–204, 1991.

[68] H. Kobayashi, B. L. Mark, and W. Turin, *Probability, Random Processes, and Statistical Analysis: Applications to Communications, Signal Processing, Queueing Theory and Mathematical Finance*. Cambridge University Press, 2011.

[69] H. Tuah and R. T. Hudspeth, "Comparisons of numerical random sea simulations," *Journal of the Waterway, Port, Coastal and Ocean Division*, vol. 108, no. 4, pp. 569–584, 1982.

[70] Y. Goda, "Numerical experiments on the statistical variability of ocean waves," *Rep. Port and Habour Research Institute*, vol. 16, pp. 3–26, 1977.

[71] M. Tucker, P. Challenor, and D. Carter, "Numerical simulation of a random sea: a common error and its effect upon wave group statistics," *Appl. Ocean Res.*, vol. 6, no. 2, pp. 118 – 122, 1984.

[72] D. B. Percival, "Simulating Gaussian random processes with specified spectra," *Computing Science and Statistics*, vol. 24, pp. 534–534, 1993.

[73] E. Funke and E. Mansard, "A rationale for the use of the deterministic approach to laboratory wave generation," *Selected Papers on Two-Dimensional Wave Generation and Analysis, Report NRCC*, no. 28750, pp. 1–44, 1987.

[74] S. Elgar, R. T. Guza, and R. J. Seymour, "Wave group statistics from numerical simulations of a random sea," *Appl. Ocean Res.*, vol. 7, no. 2, pp. 93 – 96, 1985.

[75] J. R. Medina and C. R. Sanchez-Carratala, "Comparisons of numerical random wave simulators," in *Proceedings of the 21st International Conference on Coastal Engineering, June 20-25, Costa del Sol-Malaga, Spain*, 1988.

[76] E. Mansard, "Towards a better simulation of sea states for modelling of coastal structures," *Berm breakwaters, proceedings of a workshop at NRC, Ottawa, Canada, ISBN 0872626636*, 1988.

[77] Det Norske Veritas, "Modelling and Analysis of Marine Operations, Tech. Rep. DNV-RP-H103," tech. rep., Det Norske Veritas, 2011.

[78] MARINET, "Deliverable 2.8 EC - Best Practice Manual for Wave Simulation," tech. rep., Marine Renewables Infrastructure Network for emerging Energy Technologies, 2015.

[79] J.-B. Saulnier, P. Ricci, A. Clément, and A. d. O. Falcão, "Mean power output estimation of WECs in simulated sea," in *Proceedings of The 8th European Wave and Tidal Energy Conference (EWTEC 2009), Uppsala, Sweden*, vol. 710, 2009.

[80] L. E. Borgman, "Ocean wave simulation for engineering design," *Journal of the Waterways and Harbors Division*, vol. 95, no. WW4, Proc. Paper 6925, pp. 557–583, 1969.

[81] M. Shinozuka and C.-M. Jan, "Digital simulation of random processes and its applications," *J. Sound Vib.*, vol. 25, no. 1, pp. 111–128, 1972.

[82] V. Belenky, "Risk evaluation at extreme seas," in *Proc. of 7th International Ship Stability Workshop, Shanghai, China,*, 2004.

[83] Y. Goda, *Random Seas and Design of Maritime Structures: Third Edition*, vol. 33. World Scientific Publishing Company, 2010.

[84] E. Bækkedal, "Alternative methods of realizing the sea spectrum for time-domain simulations of marine structures in irregular seas," Master's thesis, NTNU, Norway, 2014.

[85] L. Isserlis, "On a formula for the product-moment coefficient of any order of a normal frequency distribution in any number of variables," *Biometrika*, vol. 12, no. 1/2, pp. 134–139, 1918.

[86] J. Dale, "Estimation of the variance of a stationary Gaussian random process by periodic sampling," *Bell System Technical Journal*, vol. 46, no. 6, pp. 1283–1287, 1967.

[87] J.-N. Yang, "On the normality and accuracy of simulated random processes," *J. Sound Vib.*, vol. 26, no. 3, pp. 417–428, 1973.

[88] M. D. Miles and E. R. Funke, "Numerical comparison of wave synthesis methods," in *Proceedings of the 21st International Conference on Coastal Engineering, Malaga*, pp. 91–105, 1988.

[89] A. Mérigaud and J. V. Ringwood, "Free-surface time-series generation for wave energy applications," *IEEE J. Ocean. Eng.*, vol. 43, no. 1, pp. 19–35, 2018.

[90] A. Mérigaud, J.-C. Gilloteaux, and J. V. Ringwood, "A nonlinear extension for linear boundary element methods in wave energy device modelling," in *ASME 2012 31st International Conference on Ocean, Offshore and Arctic Engineering (OMAE 2012)*, pp. 615–621, American Society of Mechanical Engineers, 2012.

[91] S. Giorgi, *Linear and nonlinear parametric hydrodynamic models for wave energy converters identified from recorded data*. PhD thesis, Maynooth University, 2017.

[92] M. Penalba and J. V. Ringwood, "A review of wave-to-wire models for wave energy converters," *Energies*, vol. 9, no. 7, p. 506, 2016.

[93] J. Davidson and J. V. Ringwood, "Mathematical modelling of mooring systems for wave energy converters a review," *Energies*, vol. 10, no. 5, pp. 666–732, 2017.

[94] J. Katz, *Introductory Fluid Mechanics*. Cambridge University Press, 2010.

[95] W. E. Cummins, "The impulse response function and ship motions," *Schiffstechnik*, vol. 9, pp. 101–109, 1962.

[96] J. A. Armesto, R. Guanche, F. Del Jesus, A. Iturrioz, and I. J. Losada, "Comparative analysis of the methods to compute the radiation term in Cummins equation," *Journal of Ocean Engineering and Marine Energy*, vol. 1, no. 4, pp. 377–393, 2015.

[97] H. K. Khalil, *Nonlinear Systems*. Prentice-Hall, New Jersey, 1996.

[98] J. Henriques, L. Gato, J. Lemos, R. Gomes, and A. Falcão, "Peak-power control of a grid-integrated oscillating water column wave energy converter," *Energy*, vol. 109, pp. 378–390, 2016.

[99] B. Molin, *Hydrodynamique des Structures Offshore*. Editions Technip, 2002.

[100] H. A. Wolgamot and C. J. Fitzgerald, "Nonlinear hydrodynamic and real fluid effects on wave energy converters," *Proceedings of the Institution of Mechanical Engineers, Part A: Journal of Power and Energy*, vol. 229, no. 7, pp. 772–794, 2015.

[101] J. Palm, C. Eskilsson, L. Bergdahl, and R. E. Bensow, "Assessment of scale effects, viscous forces and induced drag on a point-absorbing wave energy converter by CFD simulations," *Journal of Marine Science and Engineering*, vol. 6, no. 4, 2018.

[102] J. P. Boyd, *Chebyshev and Fourier Spectral Methods*. Courier Corporation, 2001.

[103] T. Ogilvie, "Recent progress toward the understanding and prediction of ship motions.," in *Sixth Symposium on Naval Hydrodynamics*, 1964.

[104] A. Kurniawan, J. Hals, and T. Moan, "Assessment of time-domain models of wave energy conversion systems," in *Proceedings of the 9th European Wave and Tidal Energy Conference (EWTEC 2011), Univ. of Southampton, Southampton, U.K., 2011*, 2011.

[105] J. Morison, J. Johnson, S. Schaaf, *et al.*, "The force exerted by surface waves on piles," *Journal of Petroleum Technology*, vol. 2, no. 05, pp. 149–154, 1950.

[106] G. Bacelli, *Optimal control of wave energy converters*. PhD thesis, Maynooth University, 2014.

[107] K. Ruehl, C. Michelen, B. Bosma, and Y.-H. Yu, "WEC-Sim phase 1, validation testing: Numerical modeling of experiments," in *ASME 2016 35th International Conference on Ocean, Offshore and Arctic Engineering (OMAE 2016)*, pp. V006T09A026–V006T09A026, American Society of Mechanical Engineers, 2016.

[108] J.-C. Gilloteaux, *Mouvements de grande amplitude d'un corps flottant en fluide parfait. Application à la récupération de l'énergie des vagues.* PhD thesis, Ecole Centrale de Nantes; Université de Nantes, 2007.

[109] J. Wheeler *et al.*, "Methods for calculating forces produced by irregular waves," in *Offshore Technology Conference*, Offshore Technology Conference, 1969.

[110] G. Ducrozet, F. Bonnefoy, D. Le Touzé, and P. Ferrant, "HOS-ocean: Open-source solver for nonlinear waves in open ocean based on High-Order Spectral method," *Comput. Phys. Commun.*, vol. 203, pp. 245–254, 2016.

[111] J. D. Fenton, "Nonlinear wave theories," *The Sea*, vol. 9, pp. 1–18, 1962.

[112] M. Rienecker and J. Fenton, "A Fourier approximation method for steady water waves," *J. Fluid Mech.*, vol. 104, pp. 119–137, 1981.

[113] G. Giorgi and J. V. Ringwood, "Relevance of pressure field accuracy for nonlinear Froude–Krylov force calculations for wave energy devices," *Journal of Ocean Engineering and Marine Energy*, vol. 4, no. 1, pp. 57–71, 2018.

[114] A. Babarit, H. Mouslim, A. Clément, and P. Laporte-Weywada, "On the numerical modelling of the non linear behaviour of a wave energy converter," in *ASME 2009 28th International Conference on Ocean, Offshore and Arctic Engineering (OMAE 2009), Honolulu, Hawai, US*, pp. 1045–1053, American Society of Mechanical Engineers, 2009.

[115] G. Giorgi and J. V. Ringwood, "Computationally efficient nonlinear Froude–Krylov force calculations for heaving axisymmetric wave energy point absorbers," *Journal of Ocean Engineering and Marine Energy*, pp. 1–13, 2016.

[116] A. Mérigaud and J. V. Ringwood, "Optimal trajectories, nonlinear models and constraints in wave energy device control," in *Proceedings of the 20th IFAC world congress 2017, Toulouse, France*, pp. 15645–15650, 2017.

[117] M. Lawson, Y.-H. Yu, A. Nelessen, K. Ruehl, and C. Michelen, "Implementing nonlinear buoyancy and excitation forces in the WEC-Sim wave energy converter modeling tool," in *ASME 2014 33rd International Conference on Ocean, Offshore and Arctic Engineering (OMAE 2014), San Francisco, California, US*, pp. V09BT09A043–V09BT09A043, American Society of Mechanical Engineers, 2014.

[118] C. W. Rowley and S. T. Dawson, "Model reduction for flow analysis and control," *Annu. Rev. Fluid Mech.*, vol. 49, pp. 387–417, 2017.

[119] M. I. Ahmad, P. Benner, P. Goyal, and J. Heiland, "Moment-matching based model reduction for Navier–Stokes type quadratic-bilinear descriptor systems," *ZAMM-Journal of Applied Mathematics and Mechanics/Zeitschrift für Angewandte Mathematik und Mechanik*, vol. 97, no. 10, pp. 1252–1267, 2017.

[120] A. Mérigaud and J. V. Ringwood, "Condition-based maintenance methods for marine renewable energy," *Renewable Sustainable Energy Rev.*, vol. 66, pp. 53–78, 2016.

[121] M. Penalba, N. Sell, H. A.J., and J. V. Ringwood, "Validating a wave-to-wire model for a wave energy converter – Part I: The hydraulic transmission system," *Energies*, vol. 10, no. 7, pp. 977–998, 2017.

[122] M. Penalba, J. Cortajarena, and J. V. Ringwood, "Validating a wave-to-wire model for a wave energy converter – Part II: The electrical system," *Energies*, vol. 10, no. 7, pp. 1002–1025, 2017.

[123] M. Penalba and J. V. Ringwood, "A reduced wave-to-wire model for controller design and power assessment of wave energy converters," in *Advances in Renewable Energies Offshore: Proceedings of the 3rd International Conference on Renewable Energies Offshore (RENEW 2018), October 8-10, 2018, Lisbon, Portugal* (C. Press, ed.), 2018.

[124] M. Penalba, *Design, validation and application of wave-to-wire models for wave energy converters*. PhD thesis, Maynooth University, 2018.

[125] M. Penalba, J. Davidson, C. Windt, and J. V. Ringwood, "A high-fidelity wave-to-wire simulation platform for wave energy converters: Coupled numerical wave tank and power take-off models," *Appl. Energy*, vol. 226, pp. 655–669, 2018.

[126] G. Vissio, B. Passione, M. Hall, and M. Raffero, "Expanding ISWEC modelling with a lumped-mass mooring line model," in *Proceedings of the 11th European Wave and Tidal Energy Conference (EWTEC 2015), Nantes, France*, pp. 6–11, 2015.

[127] F. Cerveira, N. Fonseca, and R. Pascoal, "Mooring system influence on the efficiency of wave energy converters," *Int. J. Mar. Energy*, vol. 3, pp. 65–81, 2013.

[128] R. Pascoal, S. Huang, N. Barltrop, and C. G. Soares, "Equivalent force model for the effect of mooring systems on the horizontal motions," *Appl. Ocean Res.*, vol. 27, no. 3, pp. 165–172, 2005.

[129] A. Mérigaud and J. V. Ringwood, "A non-linear frequency-domain approach for numerical simulation of wave energy converters," *IEEE Trans. on Sustainable Energy*, vol. 9, no. 1, pp. 86–94, 2018.

[130] S. Gunawardane, M. Folley, and S. Sanjaya, "Spectral-domain modelling of the non-linear hydrostatic stiffness of a heaving-sphere wave energy converter," in *Proc. of the 28th International Symposium on Transport Phenomena, 22-24 September 2017, Peradeniya, Sri Lanka*, 2017.

[131] B. A. Finlayson, *The Method of Weighted Residual and Variational Principles*. Academic Press, New York, 1972.

[132] O. J. Nastov, *Spectral Methods for Circuit Analysis*. PhD thesis, Massachusetts Institute of Technology, 1999.

[133] J. S. Hesthaven, S. Gottlieb, and D. Gottlieb, *Spectral Methods for Time-Dependent Problems*, vol. 21. Cambridge University Press, 2007.

[134] A. M. Davies, "Application of the Galerkin method to the formulation of a three-dimensional nonlinear hydrodynamic numerical sea model," *Appl. Math. Modell.*, vol. 4, no. 4, pp. 245–256, 1980.

[135] T. Detroux, L. Renson, L. Masset, and G. Kerschen, "The Harmonic Balance method for bifurcation analysis of large-scale nonlinear mechanical systems," *Comput. Methods Appl. Mech. Eng.*, vol. 296, pp. 18–38, 2015.

[136] M. Urabe, "Galerkin's procedure for nonlinear periodic systems," *Arch. Ration. Mech. Anal.*, vol. 20, no. 2, pp. 120–152, 1965.

[137] A. Stokes, "On the approximation of nonlinear oscillations," *Journal of Differential Equations*, vol. 12, no. 3, pp. 535–558, 1972.

[138] J. D. García-Saldaña and A. Gasull, "A theoretical basis for the Harmonic Balance method," *Journal of Differential Equations*, vol. 254, no. 1, pp. 67–80, 2013.

[139] R. Bouc and M. Defilippi, "A Galerkin multiharmonic procedure for nonlinear multidimensional random vibration," *Int. J. Eng. Sci.*, vol. 25, no. 6, pp. 723 – 733, 1987.

[140] P. D. Spanos, M. Di Paola, and G. Failla, "A Galerkin approach for power spectrum determination of nonlinear oscillators," *Meccanica*, vol. 37, no. 1-2, pp. 51–65, 2002.

[141] G. Failla, P. Spanos, and M. Di Paola, "Response power spectrum of multi-degree-of-freedom nonlinear systems by a Galerkin technique," *J. Appl. Mech.*, vol. 70, no. 5, pp. 708–714, 2003.

[142] A. LaBryer and P. J. Attar, "A Harmonic Balance approach for large-scale problems in nonlinear structural dynamics," *Computers & Structures*, vol. 88, no. 17-18, pp. 1002–1014, 2010.

[143] K. S. Kundert and A. Sangiovanni-Vincentelli, "Simulation of nonlinear circuits in the frequency domain," *IEEE Trans. Comput.-Aided Design Integr. Circuits Syst.*, vol. 5, no. 4, pp. 521–535, 1986.

[144] L. Mukundan, *Convergence Analysis of the Harmonic Balance Method*. PhD thesis, Harvard University, 1991.

[145] L. Hai, M. Göteman, and M. Leijon, "A methodology of modelling a wave power system via an equivalent RLC circuit," *IEEE Trans. Sustain. Energy*, vol. 7, no. 4, pp. 1362–1370, 2016.

[146] M. S. Bazaraa, H. D. Sherali, and C. M. Shetty, *Nonlinear Programming: Theory and Algorithms*. John Wiley & Sons, 2013.

[147] B. Cochelin and C. Vergez, "A high order purely frequency-based Harmonic Balance formulation for continuation of periodic solutions," *J. Sound Vib.*, vol. 324, no. 1-2, pp. 243–262, 2009.

[148] S. Karkar, B. Cochelin, and C. Vergez, "A high-order, purely frequency based Harmonic Balance formulation for continuation of periodic solutions: The case of non-polynomial nonlinearities," *J. Sound Vib.*, vol. 332, no. 4, pp. 968–977, 2013.

[149] L. Liu, J. P. Thomas, E. H. Dowell, P. Attar, and K. C. Hall, "A comparison of classical and high dimensional Harmonic Balance approaches for a Duffing oscillator," *J. Comput. Phys.*, vol. 215, no. 1, pp. 298–320, 2006.

[150] S. Karkar, B. Cochelin, and C. Vergez, "A comparative study of the Harmonic Balance method and the orthogonal collocation method on stiff nonlinear systems," *J. Sound Vib.*, vol. 333, no. 12, pp. 2554–2567, 2014.

[151] E. L. Allgower and K. Georg, *Numerical Continuation Methods: An Introduction*, vol. 13. Springer Science & Business Media, 2012.

[152] A. Mérigaud and J. V. Ringwood, "Nonlinear frequency-domain WEC simulation: Numerical case studies and practical issues," in *Proceedings of the 12th European Wave and Tidal Energy Conference (EWTEC 2017), Cork, Ireland*, 2017.

[153] R. Novo, A. Mérigaud, G. Bracco, S. Sirigu, G. Mattiazzo, and J. V. Ringwood, "Non-linear simulation of a wave energy converter with multiple degrees of freedom using a Harmonic Balance method," in *Proceedings of the 37th International Conference on Ocean, Offshore & Arctic Engineering (OMAE 2018), Madrid, Spain, June 2018*, 2018.

[154] T. Cameron and J. Griffin, "An alternating frequency/time domain method for calculating the steady-state response of nonlinear dynamic systems," *J. Appl. Mech.*, vol. 56, no. 1, pp. 149–154, 1989.

[155] G. Giorgi, M. Penalba Retes, and J. V. Ringwood, "Nonlinear hydrodynamic force relevance for heaving point absorbers and oscillating surge converters," in *Proceedings of the Asian Wave and Tidal Energy Conference (AWTEC 2016), Singapore, 2016*, 2016.

[156] N. Faedo, Y. Peña-Sanchez, and J. V. Ringwood, "Finite-order hydrodynamic model determination for wave energy applications using moment-matching," *Ocean Eng.*, vol. 163, pp. 251 – 263, 2018.

[157] G. Vissio, *ISWEC toward the sea: development, optimization and testing of the device control architecture*. PhD thesis, Politecnico di Torino, 2017.

[158] D. W. Zingg, M. Nemec, and T. H. Pulliam, "A comparative evaluation of genetic and gradient-based algorithms applied to aerodynamic optimization," *European Journal of Computational Mechanics/Revue Européenne de Mécanique Numérique*, vol. 17, no. 1-2, pp. 103–126, 2008.

[159] C. Grosan and A. Abraham, "Hybrid evolutionary algorithms: methodologies, architectures, and reviews," in *Hybrid Evolutionary Algorithms*, pp. 1–17, Springer, 2007.

[160] G. Allaire, "A review of adjoint methods for sensitivity analysis, uncertainty quantification and optimization in numerical codes," *Ingénieurs de l'Automobile*, vol. 836, pp. 33–36, 2015.

[161] M. Raffero, M. Martini, B. Passione, G. Mattiazzo, E. Giorcelli, and G. Bracco, "Stochastic control of inertial sea wave energy converter," *The Scientific World Journal*, vol. 2015, 2015.

[162] G. Vissio, D. Valério, G. Bracco, P. Beirão, N. Pozzi, and G. Mattiazzo, "ISWEC linear quadratic regulator oscillating control," *Renewable Energy*, vol. 103, pp. 372–382, 2017.

[163] M. A. Branch, T. F. Coleman, and Y. Li, "A subspace, interior, and conjugate gradient method for large-scale bound-constrained minimization problems," *SIAM J. Sci. Comput.*, vol. 21, no. 1, pp. 1–23, 1999.